Geodetic Measurement of Deformation in Southern California

Thesis by

Shawn Christian Larsen

In Partial Fulfillment of the Requirements

for the Degree of

Doctor of Philosophy

California Institute of Technology

Pasadena, California

1991

(submitted October 26, 1990)

Abstract

The Global Positioning System (GPS) has rapidly become one of the most important geodetic tools for studying tectonic deformation. With potential 3-dimensional relative positioning accuracies better than 1 cm, GPS can monitor secular deformation as well as rapid strain fluctuations due to seismic and volcanic activity. A 1970/1971 trilateration survey and 1987/1988 GPS observations suggest uniaxial convergence of 6.4 mm/yr oriented N25.1 °E in the eastern third of the Santa Barbara channel, and a combination of convergence and left-lateral shear to the west. GPS surveys have been conducted in the Imperial Valley during 1986, 1988, 1989, and 1990. About 5 ± 1 cm/yr plate-boundary displacement is observed across the valley, somewhat larger than rates obtained through conventional geodesy. These GPS observations have been influenced by the 1987 Superstition Hills earthquake sequence, the first occurrence of a large earthquake within a preexisting GPS network. The measurements suggest 130 cm right-lateral slip along the northwest trending Superstition Hills fault, and 30 cm left-lateral slip along the conjugate northeast trending Elmore Ranch fault. Imperial Valley leveling surveys conducted in 1931, 1941, 1974, 1978, and 1980, are integrated with seismic, geomorphic, and sub-surfacial structural data, to suggest the northern segment of the Imperial fault formed within the last 80,000 years, and support the hypothsis that the Gulf of California rift system is propagating northwestward into the North American continent.

Table of Contents

Chapter 1

Introduction: Geodetic Measurements and Crustal Deformation

1.1 Introduction

Geodetic measurements have been used since the beginning of the century to monitor crustal motions [e.g., *Reid*, 1910; *Brown and Reilinger*, 1983; *Stein*, 1987]. Crustal strains are often related to tectonic processes such as seismic (aseismic) and/or volcanic activity [e.g., *Reilinger and Larsen*, 1986; *Savage and Clark*, 1982]. In most instances the observed and suspected tectonic movements are associated with plate-boundary deformation, although large intra-continental strains of tectonic origin have been observed [e.g., *Brown et al.*, 1978; *Larsen et al.*, 1986; *Ward and Barrientos*, 1986]. In addition, geodetic measurements often detect non-tectonic movements such as crustal subsidence due to fluid withdrawal [e.g., *Chi et al.*, 1980; *Larsen et al.*, 1983]. While these observations can be used to evaluate near-surface economic problems, they often act as "experimental noise" in tectonic studies. Effects such as monument instability and measurement error strongly influence the use of geodetic observations to monitor crustal motions [e.g., *Reilinger and Brown*, 1981; *Holdahl*, 1982].

In this study geodetic measurements in southern California are examined in terms of their tectonic significance and specifically the potential for resolving geophysical parameters such as the slip distribution on a seismic rupture plane. The bulk of the data reported here are measurements utilizing the space-based Global Positioning System (GPS), the newest and perhaps

most revolutionary development in geodetic analysis.

Chapters 1 and 2 are introductions, whereas Chapters 3-6 represent independent research papers to be submitted for publication. As a result, some redundancy exists throughout the thesis. In the remainder of this chapter the methods of land-based (conventional) and space-oriented surveying techniques are briefly discussed, as well as examples of crustal deformation problems in southern California. In Chapter 2 the focus is on the Global Positioning System, including a brief introduction, theoretical aspects, and processing techniques used to obtain geodetic coordinates from GPS data. In Chapter 3, the strain accumulation across the Santa Barbara channel determined from GPS and trilateration observations over the last two decades is associated with plate deformation occurring off the coast of southern California. GPS computed station displacements in the Imperial Valley from 1986 to 1989 are presented in Chapters 4 and 5. These measurements are examined in terms of 1) the seismic effects of the 1987 Superstition Hills earthquake sequence (the first occurrence of a large earthquake within a preexisting GPS network), and 2) the secular deformation across the valley due to the relative motion between the North American and Pacific plates. In Chapter 6, leveling observations between 1931 and 1980 in the Imperial Valley are integrated with other geophysical data to conclude that the northern segment of the Imperial fault is extremely young compared to the age of the Imperial Valley, and suggest the northwestward migration of the Gulf of California rift system into the North American continent.

1.2 Geodetic Measurements

Geodetic surveying techniques used for crustal motion research are divided into two categories: 1) land-based or conventional geodesy, and 2) those relying on satellite/lunar ranging or extraterrestrial transmissions. Conventional geodesy is sub-divided into triangulation, trilateration, and leveling, although other types of geophysical measurements such as creep-meter recordings, tidal monitoring, and surface slip along an activated fault trace can be considered forms of geodetic observation. Modern space-related techniques have been in use over the last three decades and include Very Long Baseline Interferometry (VLBI), Satellite Laser Ranging (SLR), and the Global Positioning System (GPS). Although not discussed here, astronomic positioning methods (navigational astronomy) are probably the oldest geodetic technique and they were used in crustal motion research at least back to the turn of the century (for studying changes in azimuth).

Two concepts are fundamental for utilizing geodetic measurements in crustal deformation research. The first is repeated observations. In order to establish regional strain or monument displacement, it is necessary to obtain multiple geodetic observations at different times. Depending on measurement accuracy and the magnitude of the tectonic signal, the reobservation interval may be anywhere from a few hours to tens of years. The second fundamental is the concept of relative positioning. High-precision geodesy inherently measures the *relative* position (or change in relative position) between two or more monuments. It is difficult, and to some degree impossible, to accurately constrain geodetic coordinates in an absolute sense (point positioning).

Conventional geodetic measurements

The angles constructed by line-of-sight observations between geodetic monuments through a reference monument are measured with triangulation, usually with a theodolite [*Bomford*, 1971]. Although this type of measurement is not very precise by modern standards ($\sim$ 10 parts per million), it has the advantage that data are available from well over 100 years of observation. In fact, triangulation measurements dating back to the 1880's have been integrated with modern techniques to investigate deformation in the offshore of southern California [*Webb*, 1991].

The slope distance between two monuments is determined through trilateration, often with an Electronic Distance Measurement device (EDM) or geodimeter. For simplicity this process can be thought of as timing a light signal generated at one site, reflected at another, and recorded back at its origin. (The actual technique involves the phase comparison of a modulated carrier light signal.) The measurements can be supplemented by end-point meteorological data, which are used to correct for the atmospheric refraction along the ray-path. For the highest accuracy it is necessary to record atmospheric conditions along the ray-path, usually with the aid of an aircraft. For high-precision EDM surveying, such as that conducted by the U.S. Geological Survey [e.g., *Savage and Prescott*, 1973; *Slawson and Savage*, 1983], the measurement accuracy is a function of baseline length and can be written $\sigma^2 = a^2 + b^2L^2$, where a is 0.3—0.6 cm and b is $2—5 \times 10^{-7}$. For baselines of 10 and 50 km length, the corresponding uncertainties are 0.5—0.8 cm and 1.2—2.6 cm, respectively.

Strains computed from repeated triangulation and trilateration measurements are primarily a function of horizontal deformation, with little

influence from vertical movements (assuming relatively flat topography). The observables (angle and length changes) are often generalized into lateral station displacements, although these measurements are inherently non-unique requiring a priori positioning assumptions. [*Prescott*, 1981; *Guohua and Prescott*, 1986; *Segall and Matthews*, 1989].

Vertical deformation is obtained through multiple leveling surveys [e.g., *Brown and Oliver*, 1976]. By sighting elevation differences to leveling rods, relative vertical positions are determined with high precision. For crustal deformation studies benchmark spacing is typically on the order of 1 km, although $\sim$ 100 m sight-lengths are observed in succession at multiple temporary marks between the permanent monuments. In first-order surveying, the formal measurement uncertainties across 10 and 100 km leveling transects are approximately 0.3 and 1.0 cm, respectively, although systematic errors can severely distort elevation changes [*Jackson et al.*, 1981; *Stein*, 1981; *Strange*, 1981; *Holdahl*, 1982].

Conventional geodesy has the disadvantage that single observations are restricted in length. Horizontal measurements rarely exceed 50 km. While larger networks are surveyed by integrating individual observations, this is at the expense of errors propagating into the solution. Another disadvantage is the necessity of locating stations on topographic highs (for intersite visibility). Space geodesy is generally not limited by these constraints. Measurements can span entire continents to infer rates of global plate motions, or they can be confined to smaller zones for local geophysical studies.

Space Geodesy

Although positioning from space is a multidisciplined field [e.g., *Wells et al.*, 1987], representative of the many techniques are SLR (Satellite Laser Ranging), VLBI (Very Long Baseline Interferometry), and GPS (Global Positioning System). All space positioning techniques involve the detection of electromagnetic radiation either emitted or reflected from an object in orbit about the earth or at some greater distance.

Satellite laser ranging utilizes a simple principle where a light-pulse emitted from a ground-based laser is reflected by a dedicated earth-orbiting satellite and then recorded at the transmission site. The range to the satellite is calculated from the elapsed 2-way signal transit time. At present there are about 25 fixed SLR sites worldwide, while NASA has deployed over 10 mobile systems [*Cohen and Smith*, 1985]. Intersite (continental-scale) baselines are measured to precisions of 3-5 cm by simultaneously solving for up to one month of data from several stations.

Very Long Baseline Interferometry may be the most accurate geodetic technique for long baselines ($>$ 100 km). Signals from extraterrestrial radio sources such as quasars are recorded at fixed or mobile radio antennas. The data from two or more stations are transported to a central processing site, where they are cross-correlated to obtain the signal delay between different receivers. After carefully modeling several nuisance parameters such as atmospheric refraction, the delay can be mapped into the geodetic baseline between the antennas. Processing VLBI observations is extremely computation-intensive due to the enormous volume of data, but the end results are intersite baseline vectors accurate to better than a few centimeters.

The majority of data presented in this study were obtained with the Global Positioning System, which utilizes signals from earth-orbiting satellites to calculate highly accurate 3-dimensional relative positions between geodetic monuments. For geophysical problems in southern California where station spacings are typically less than 100 km, with proper data collection and processing techniques the accuracy with GPS is better than 1 cm in the horizontal baseline components and about 3 cm in the vertical component [*Dong and Bock*, 1989; *Davis et al.*, 1989]. The system is highly mobile and relatively inexpensive. A more detailed description about GPS is presented in Chapter 2, and complete discussions are given in *King et al.* [1985], *Wells et al.* [1987], and *Rocken* [1988].

1.3 Crustal Deformation in Southern California

Santa Barbara channel

It has been recognized for some time that a sizable portion of the estimated relative motion between the North American and Pacific plates can not be accounted for by the observed slip along the San Andreas fault and deformation elsewhere in North America [*Bird and Rosenstock*, 1984; *Minster and Jordan*, 1986; *Weldon and Humphreys*, 1986; *DeMets et al.*, 1990]. Approximately 5 mm/yr fault parallel and 7 mm/yr fault normal deformation is needed to explain the observed plate motion rate. Termed the San Andreas discrepancy, it has been speculated that this missing deformation may be occurring off the coast of southern California.

At the western edge of the Transverse Ranges lies the Santa Barbara

channel. The channel exhibits high seismicity and has been the site of several large earthquakes during the period of historical record (since 1812) [*Yerkes*, 1985]. Most of the recorded seismicity occurs in the eastern channel where earthquake focal mechanisms suggest north to northeast convergence along east-west trending faults [*Lee et al.*, 1979]. This region may represent a transition between the active deformation associated with the San Andreas fault zone to the east and the stable Pacific plate to the west. It has been suggested that some or all of the missing motion attributed to the San Andreas discrepancy may be occurring across the Santa Barbara channel. Geodetic measurements of crustal strain are used to test this hypothesis.

Imperial Valley

The Imperial Valley of southern California represents a transition zone between crustal spreading in the Gulf of California and right-lateral transform motion along the San Andreas fault [*Lomnitz et al*, 1970; *Elders et al.*, 1972]. The valley is one of the most seismically prone regions in California with much of the activity occurring along the Imperial fault and within the Brawley Seismic Zone [e.g., *Johnson and Hill*, 1982]. A significant fraction of the relative motion between the North American and Pacific plates is accommodated across the valley. This region has been the site of considerable scientific interest [e.g., *U. S. G. S.*, 1982].

Important geophysical problems pertaining to the Imperial Valley which can be studied through geodetic measurements are centered around the anomalous number of large earthquakes which have occurred in this region since the beginning of the century [e.g., *Savage et al.*, 1974; *Thatcher*, 1979;

Snay et al., 1982; *Langbein et al.*, 1983; *Reilinger*, 1984; *Slade et al.*, 1984; *Reilinger and Larsen*, 1986; *Snay and Drew*, 1988]. In fact, a 1987 earthquake sequence near the Superstition Hills occurred in the middle of a preexisting GPS network. The coseismic station displacements are used to infer rupture properties of the Superstition Hills and conjugate Elmore Ranch faults. Of equal importance are the magnitude and distribution of secular movements throughout the Imperial Valley. The differential velocity across this region must somehow be accommodated on each of the valley's fault segments, the particulars of which define the strain accumulation along any given fault. Although the deformation in this region is undoubtedly complex, geodetic measurements have resolved some of these problems.

1.4 Seismic Slip Distribution and Network Geometry

From an earth scientist perspective, an important objective of geodetic observation is to utilize measurements of crustal deformation to reach some geophysical conclusion. Examples are surveys conducted near earthquake fault zones. Geodetic measurements have been used successfully to determine slip distribution along seismic rupture planes [*Ward and Barrientos*, 1986; *Harris and Segall*, 1987; *Segall and Harris*, 1987; *Snay*, 1989]. However, these studies generally utilized a fairly limited number of observations.

With the development of low-cost high-precision surveying techniques such as that provided with the Global Positioning System, it is possible to establish relatively dense geodetic networks in regions which are subject to seismic activity. Geodetic network design can be optimized to maximize the information needed to establish reliable estimates of slip distribution and the

extent of seismic rupture. Covariance analysis is used to determine the effect different network geometries and station densities have on resolving seismic parameters. Proper geodetic monitoring will allow an increased understanding of the earthquake cycle.

References

Bird, P., and R. W. Rosenstock, Kinematics of present crust and mantle flow in southern California, *Geol. Soc. Am. Bull.*, *95*, 946-957, 1984.

Bomford, G., *Geodesy*, Oxford University Press, London, 731 pp., 1971.

Brown, L. D., and J. E. Oliver, Vertical crustal movements from leveling data and their relation to geologic structure in the eastern United States, *Rev. Geophys. and Space Phys.*, *14*, 13-35, 1976.

Brown, L. D., R. E. Reilinger, and J. R. Hagstrom, Contemporary uplift of the Diablo Plateau, West Texas, from leveling measurements, *J. Geophys. Res.*, *83*, 5465-5471, 1978.

Brown, L. D., and R. E. Reilinger, Crustal movement, *Rev. Geophys. and Space Phys.*, *21*, 553-559, 1983.

Chi, S. C., R. E. Reilinger, L. D. Brown, and J. E. Oliver, Leveling circuits and crustal movements, *J. Geophys. Res.*, *85*, 1469-1474, 1980.

Cohen, S. C., and D. E. Smith, LAGEOS scientific results: Introduction *J. Geophys. Res.*, *90*, 9217-9220, 1985.

Davis, J. L., W. H. Prescott, J. L. Svarc, and K. J. Wendt, Assessment of global positioning system measurements for studies of crustal deformation, *J. Geophys. Res.*, *94*, 13,635-13,650, 1989.

DeMets, C., R. G. Gordon, D. F. Argus, and S. Stein, Current plate motions, *Geophys. J. Inter.*, *101*, 425-478, 1990.

Dong, D. Y. Bock, Global Positioning System network analysis with phase ambiguity resolution applied to crustal deformation studies in California, *J. Geophys. Res.*, *94*, 3949-3966, 1989.

Elders, W. A., R. W. Rex, T. Meidav, P. T. Robinson, and S. Biehler, Crustal spreading in southern California, *Science*, *178*, 15-24, 1972.

Guohua, G., and W. H. Prescott, Discussion on displacement analysis: Detection of crustal deformation, *J. Geophys. Res.*, *91*, 7439-7446, 1986.

Harris, R. A., and P. Segall, Detection of a locked zone at depth on the Parkfield segment of the San Andreas fault, *J. Geophys. Res.*, *92*, 7945-7962, 1987.

Holdahl, S. R., Recomputation of vertical crustal motions near Palmdale, California, 1959-1975, *J. Geophys. Res.*, *87*, 9374-9388, 1982.

Jackson, D. D., W. B. Lee, C. C. Liu, Height dependent errors in southern California leveling, in *Earthquake Prediction: An International Review, Maurice Ewing Ser.*, vol. 4, edited by D. W. Simpson and P. G. Richards, AGU, Washington, D. C., 457-472, 1981.

Johnson, C. E., and D. P. Hill, Seismicity of the Imperial Valley, *U. S. Geol. Surv. Prof. Pap.*, *1254*, 14-24, 1982.

King, R. W., E. G. Masters, C. Rizos, A. Stolz, and J. Collins, *Surveying with GPS, Monograph 9*, School of Surveying, The University of New South Wales, Kensington, Australia, 128 pp., 1985.

Langbein, J., A. McGarr, M. J. S. Johnston, and P. W. Harsh, Geodetic

measurements of postseismic crustal deformation following the 1979 Imperial Valley earthquake, California, *Bull. Seismol. Soc. Am.*, *73*, 1203-1224, 1983.

Larsen, S. C., and R. E. Reilinger, Geodetic evidence for tectonic deformation in the Rio Grande rift: Socorro, New Mexico and west Texas, *Eos Trans. Abst*, American Geophysical Union, 1983.

Larsen, S. C., R. E. Reilinger, L. D. Brown, Evidence for ongoing crustal deformation related to magmatic activity near Socorro, New Mexico; *J. Geophys. Res.*, *91*, 6283-6292, 1986.

Lee, W. H. K., R. F. Yerkes, and M. Simirenko, Recent earthquake activity and focal mechanisms in the western Transverse Ranges, California, *U. S. Geol. Surv. Circ.*, *799a*, 1-15, 1979.

Lomnitz, C., F. Mooser, C. R. Allen, J. N. Brune, and W. Thatcher, Seismicity and tectonics of northern Gulf of California region, Mexico: Preliminary results, *Geofis. Int.*, *10*, 34-48, 1970.

Minster, J. B., and T. H. Jordan, Present-day plate motions, *J. Geophys. Res.*, *83*, 5331-5354, 1978.

Prescott, W. H., The determination of displacement fields from geodetic data along a strike slip fault, *J. Geophs. Res.*, *86*, 6067-6072, 1981.

Reid, H. F., The mechanics of the earthquake, The California Earthquake of April 18, 1906, *Rep. II*, State Earthquake Invest. Comm., Carnegie Inst. of Washington, Washington, D.C., 192 pp., 1910.

Reilinger, R. E., and L. D. Brown, Neotectonic deformation near surface movements and systematic errors, in *Earthquake Prediction: An International Review, Maurice Ewing Ser.*, vol. 4, edited by D. W. Simpson and P. G. Richards, AGU, Washington, D. C., 422-440, 1981.

Reilinger, R., Coseismic and postseismic vertical movements associated with the 1940 M7.1 Imperial Valley, California, earthquake, *J. Geophys. Res.*, *89*, 4531-4537, 1984.

Reilinger, R. E., and S. C. Larsen, Vertical crustal deformation associated with the 1979 M = 6.6 Imperial Valley, California earthquake: Implications for fault behavior, *J. Geophys. Res.*, *91*, 14,044-14,056, 1986.

Rocken, C., The global positioning system: A new tool for tectonic studies; Ph.D. Thesis, University of Colorado, Boulder, 365 pp., 1988.

Savage, J. C., and W. H. Prescott, Precision of geodolite distance measurements for determining fault movements, *J. Geophys. Res.*, *75*, 6001-6008, 1973.

Savage, J. C., D. D. Goodreau, and W. H. Prescott, Possible fault slip on the Brawley Fault, Imperial Valley, California, *Bull. Seismol. Soc. Amer.*, *64*, 713-716, 1974.

Savage, J. C., and M. M. Clark, Magmatic resurgence in Long Valley Caldera, California: Possible cause of the 1980 Mammoth Lakes earthquakes, *Science*, *217*, 56-58, 1982.

Segall, P., and R. A. Harris, Earthquake deformation cycle on the San

Andreas fault near Parkfield, California, *J. Geophys. Res.*, *93*, 10,511-10,525, 1987.

Segall, P., and M. V. Matthews, Displacement calculations from geodetic data and the testing of geophysical deformation models, *J. Geophys. Res.*, *93*, 14,954-14,966, 1988.

Slade, M. A., G. A. Lyzenga, and A. Raefsky, Modeling of the surface static displacements and fault plane slip for the 1979 Imperial Valley earthquake, *Bull. Seismol. Soc. Am.*, *74*, 2413-2433, 1984.

Slawson, W. F., and J. C. Savage, Deformation near the creeping and locked segments of the San Andreas fault, Cholame Valley, California (1970-1980), *Bull. Seismol. Soc. Amer.*, *73*, 1407-1414, 1983.

Snay, R. A., M. W. Cline, M. W. and E. L. Timmerman, Horizontal deformation in the Imperial Valley, California, between 1934 and 1980, *J. Geophys. Res.*, *87*, 3959-3968, 1982.

Snay, R. A., and A. R. Drew, Supplementing geodetic data with prior information for crustal deformation in the Imperial Valley, California, Technical Report Series, University of Stuttgart, 30 pp., 1988.

Snay, R. A., Enhancing the geodetic resolution of fault slip by introducing prior information, *Manuscripta Geodaetica*, *14*, 391-403, 1989.

Stein, R. S., Discrimination of tectonic displacement from slope-dependent errors in geodetic leveling from southern California, 1953-1979, in *Earthquake Prediction: An International Review, Maurice Ewing Ser.*, vol.

4, edited by D. W. Simpson and P. G. Richards, AGU, Washington, D. C., 441-455, 1981.

Stein, R. S., Contemporary plate motion and crustal deformation, *Rev. of Geophys. and Space Phys.*, *25*, 855-863, 1987.

Strange, W. E., The impact of refraction correction on leveling in southern California, *J. Geophys. Res.*, *86*, 2809-2824, 1981.

Thatcher, W., Horizontal crustal deformation from historic geodetic measurements in southern California, *J. Geophys. Res.*, *84*, 2351-2370, 1979.

U. S. G. S., The Imperial Valley, California, earthquake of October 15, 1979, *U. S. Geol. Surv. Prof. Pap.*, *1254*, 451 pp., 1982.

Ward, S. N., and S. E. Barrientos, An inversion for slip distribution and fault shape from geodetic data observations of the 1983, Borah Peak, Idaho, earthquake, *J. Geophys. Res.*, *91*, 4909-4919, 1986.

Webb, F. H., Geodetic measurement of deformation in the offshore of southern California, Ph.D. Thesis, California Institute of Technology, Pasadena, 1991.

Weldon, R., and G. Humphreys, A kinematic model of southern California, *Tectonics*, *5*, 33-48, 1986.

Wells, D., N. Beck, D. Delikaraoglou, A. Kleusberg, E. J. Tranquilla, and P. Vanicek, *Guide to GPS Positioning*, Canadian GPS Associates, Fredericton, N. B., Canada, 1987.

Yerkes, R. F., Geologic and seismologic setting, in Evaluating earthquake hazards in the Los Angeles region -- An earth-science perspective, *U. S. Geol. Surv. Prof. Pap., 1360*, 25-41, 1985.

Chapter 2

The Global Positioning System

2.1 Introduction

The NAVSTAR (Navigation Satellite Time and Ranging) Global Positioning System (GPS) is a satellite based positioning system currently under development in the United States [e.g., *Wells*, 1986]. By measuring radio transmissions from earth orbiting satellites, 3-dimensional positioning as well as accurate time synchronization will be available almost anywhere on earth at all times. In its final configuration scheduled for the mid 1990's, 21 satellites will be deployed in 6 orbital planes, with 3 additional satellites used as active spares. At an altitude of approximately 26,000 km, each satellite will orbit the earth every 12 hours. With this geometry 4 to 10 satellites will be continuously in view anywhere around the globe.

Between 1978 and 1985 eleven prototype Block I satellites were launched for the purpose of GPS testing and evaluation, although they have been used in real applications. Launch of the Block II satellites, which will make up the final GPS constellation, was initiated in February 1989. As of December 1989, 7 Block I and 4 Block II satellites were in use.

Although the scheduled satellite coverage is only partially complete, the present configuration is optimized for North America. In California, for example, a 6 to 8 hour observation window is available each day in which enough satellites are in view to make high precision geodetic positioning

feasible. For the past several years, GPS observations have been collected in California in an effort to establish networks for crustal motion research. Other states and countries including Alaska, Idaho, Montana, Oregon, Washington, Wyoming, Greece, Japan, the South Pacific, and Turkey have been the sight of GPS occupation. These observations are often integrated with historical geodetic data (conventional surveying) in order to investigate tectonic deformation.

The Global Positioning System was initiated by the U.S. Department of Defense in 1973 in an effort to satisfy both military and civilian needs for real-time positioning. The system consists of 3 segments: the control system, the satellites, and the users. The satellite and user segments are self explanatory. The control system is composed of ground-based sites throughout the world, as well as a master control station at the Consolidated Space Operations Center in Colorado Springs (Colorado). These sites are used to monitor the health of each satellite, calculate satellite orbits and the behavior of their atomic clocks, and update the broadcast message transmitted by each satellite.

Positioning modes

The primary purpose of the Global Positioning System is for civilian and military navigation. The time-biased satellite range is determined by aligning a receiver generated code with that of an incoming pseudo-random signal (see below). The "range" measurement is computed by differencing the time of signal transmission at the satellite from the time of signal reception at the receiver (multiplied by the speed of light). It is time biased because the

satellite and receiver clocks are not synchronized. The 3-dimensional receiver position and the receiver-satellite time offset are calculated from the range measurement to at least 4 satellites and their orbital coordinates. Depending on the type of pseudo-random signal received, whether it be the "precise" P-code or the "course acquisition" C/A-code (previously referred to as the "secondary" S-code), accuracies for real-time positioning (planes, boats, automobiles) are on the order of 10 to 100 meters. If a stationary receiver continuously tracks data for several hours, post-processing can yield pseudo-range positioning accuracies of several meters (the term pseudo-range refers to the time-biased range).

Soon after GPS technology was conceived, it was recognized that by using the satellite carrier phase signal(s) (see below) high precision differential geodetic measurements could be achieved. This procedure is usually conducted in a static mode, where two or more receivers are left stationary, while they continuously collect and record the GPS phase and other relevant information. For GPS measurements in California during the last several years, daily observation sessions usually lasted between 4 to 8 hours each day. Several hours of observation are required for data redundancy as well as better geometrical coverage (the satellites move across the sky during each data collection period). Alternate observation scenarios are required in different parts of the world due to changing satellite geometry and coverage. The GPS phase data are later post-processed to obtain receiver position differences. Station coordinates, or more precisely coordinate differences between stations, can be determined at the sub-centimeter level. This high degree of refinement allows GPS to be used for crustal motion research where

typical movements are on the order of several millimeters to a few centimeters per year.

Another surveying technique using the carrier signal is kinematic positioning. With this approach a stationary receiver held fixed at a site with known coordinates is used together with one or more roving instruments. After the phase signals observed by all receivers are initially calibrated (at the fixed site), the roving instrument is transported to the first site in the network. The receiver must maintain continuous lock on the GPS phase signals during transit. The roving receiver is usually left at the new monument to collect data for several minutes to an hour. If the instrument maintains continuous phase lock on each satellite, the phase difference between the stationary and roving receiver (initially null at calibration) is used to determine the relative coordinates between the two sites. The roving instrument is then transported to each subsequent station and the process is repeated. If the receiver does not continuously observe the phase, however, the roving instrument must be transported back to the original site (or one previously occupied) for recalibration with the stationary receiver. The principal advantage of kinematic positioning compared with static GPS is that a greater number of monuments can be occupied over the span of an experiment. The chief disadvantage is each receiver must continuously track all satellites with no interruption. Kinematic positioning can not be used in the presence of obstructions (buildings, trees, topography, etc.). Another disadvantage is that kinematic results may be significantly less precise than those from static positioning, particularly for the vertical component or in the presence of multipath. No kinematic survey results are included in this study.

The Department of Defense initiated Selective Availability (SA) on March 25, 1990. With SA the GPS signal is purposely degraded by introducing clock errors (dithering) as well as errors to the broadcast orbits. The military and other selected users have access to special error-decoding information transmitted with the broadcast message enabling them to reconstruct the original signal. Non-authorized or civilian users are denied this access and thus their positioning ability will be significantly degraded. Real-time positioning using the C/A code without SA is accurate to about 30 meters. With SA applied to the signal the accuracy is reduced to over 100 meters. (Actually, since the GPS constellation is not yet complete the present accuracy with SA is 200-300 meters.) Another option which reportedly will only be used in the event of a national emergency (except for testing purposes) is known as anti-spoofing (AS). With AS the military will utilize the Y-code, which is an encrypted version of the P-code. This will prevent any hostile group from spoofing (corrupting) the GPS signal. Generally, SA will only affect navigational GPS (pseudo-range). High precision surveying using the carrier phase will not be seriously altered, except that SA will inject some "nuisance" terms into the data processing. Even with navigational GPS differential positioning techniques should largely counter the affect of SA.

2.2 Theoretical Aspects

A brief introduction to some of the terminology and theory behind the Global Positioning System is given here. The methodologies presented are based on the analyses used in this study, and utilize some of the principles behind the Bernese GPS analysis software. Although to some degree these

principles are generalized, minor and major differences exist in the way different software packages handle GPS data. It is not the intent to provide a rigorous formulation, but rather outline some of the important concepts and techniques. Complete discussions are found in *King et al.* [1985], *Wells et al.*, [1987], and *Rocken* [1988].

Signal Structure

The signal structure broadcast from each GPS satellite consists of two carrier phase signals modulated by a navigational message as well as pseudo-random codes. Pseudo-random means that the codes are seemingly random modulations, yet repeat themselves every 1 millisecond (C/A code) to 267 days (P code). The two carrier frequencies, known as L1 and L2, are broadcast at 1575.42 Mhz (L1) and 1227.60 Mhz (L2). This is equivalent to wavelengths of about 19 cm for the L1 and 24 cm for the L2. It is the carrier phase observables which are used for highly accurate geodetic positioning. Usually these measurements are utilized in a post-processing environment, where data collected in the field are brought back to the office or laboratory for analysis with a fairly robust computer software system.

The pseudo-random codes contain time marks which allow GPS receivers to determine the transmission time of the signal. Comparison of the transmit and receipt times, when multiplied by the speed of light, produces the pseudo-range, or the time-biased satellite-receiver distance. If measurements to at least 4 GPS satellites can be made, and if the satellite coordinates are known, the 3-dimensional receiver position as well as the satellite-receiver clock error can be determined. The clock error is due to the fact that the

satellite and receiver clocks are not synchronized. Satellite coordinates are broadcast with the navigational message (broadcast ephemeris). Both the P (precise) and C/A (S or secondary) pseudo-random codes are modulated onto the L1 carrier frequency, while only the P code is available with the L2 signal. Ionospheric corrections (see below) can be determined by accessing both carrier frequencies (with the P code). The absence of the less precise C/A code on the L2 phase is intended to allow non-authorized users (civilians) access to the L1 component only, resulting in positioning degradation. The P code is generated at a frequency of 10.23 Mhz (30 meters) and is repeated every 267 days. The C/A code is generated at a frequency of 1.023 Mhz (300 meters) and is repeated every millisecond. The accuracy obtainable for the pseudo-range is about 1 to 100 m, depending on which code is used, the receiver type, length of observation, and the static or kinematic behavior of the instrument. It is the pseudo-range which is used for civilian and military navigation.

The navigational message, a 1500-bit data stream modulated on both carrier frequencies and transmitted at 50 bps (bits per second), contains the satellite coordinates (broadcast ephemeris), clock parameters (describing the stability and drift of the satellite clocks), satellite health, and general system status. The final 300 bits in each stream contain information specific to a particular satellite, thus 25 30-second message transmissions are required to rotate through all satellites. Individual components of the broadcast message are periodically updated, nominally every hour or each day depending on the data block.

Pseudo-range Coordinates

As an example of how GPS data are utilized to obtain geodetic positions, we examine how coordinates are determined by navigational GPS using the pseudo-range. In general terms, the pseudo-range R^k, or the distance between the GPS receiver and the *k*th satellite, is calculated from the difference in transmission time of the P or C/A code from the *k*th satellite and the time of signal reception at the receiver (multiplied by the speed of light). The observable can be written

$$R^k = r(x,y,z,X^k,Y^k,Z^k,\Delta t) \tag{2.1}$$

where (x,y,z) are the 3-dimensional coordinates of the receiver (in some reference frame), (X^k,Y^k,Z^k) are the 3-dimensional coordinates of the *k*th satellite, and *r* is some function relating the geometrical position between the satellite and receiver. Because the satellite and receiver clocks are not synchronized, the pseudo-range depends on an additional unknown Δt, which is the offset or error between the receiver-clock time and GPS (satellite) time. This time offset is often referred to as the clock error. The actual pseudo-range function is slightly more complicated, as it depends on transmission effects through the atmosphere. If the coordinates of the kth satellite are known (usually with the broadcast ephemeris), then (2.1) is written

$$R^k = s(x,y,z,\Delta t) \tag{2.2}$$

where the receiver coordinates and time offset are determined by inverting multiple observations of R in a least-squares sense, or

$$(x,y,z,\Delta t) = R^{-1} \tag{2.3}$$

For real-time positioning 4 satellites are required to determine all unknown components in the function. The coordinate uncertainties determined from the pseudo-range are on the order of meters.

Each satellite has a highly accurate and stable atomic clock. The GPS receivers on the other hand, utilize quartz oscillators which are fairly inaccurate and unstable (drift with time). However, the use of quartz crystals allow the receivers to be highly mobile and less expensive. (Most receivers can be connected to an external timing standard if one is available; typically found at radio observatories.) It is the relatively poor receiver clocks which necessitates the calculation of the time offset Δt in (2.3). If all clocks were perfectly synchronized, then only the 3-dimensional receiver position would need be determined.

Pseudo-range analyses does not yield the centimeter-level accuracy required for crustal motion research. However, the pseudo-range is often integrated with high-precision (carrier phase) GPS surveying, as it provides initial station coordinates as well as the satellite-receiver time offset.

Phase Observable

The fundamental GPS observable for high-precision surveying is Φ_i^k, the carrier phase from the kth satellite recorded at the ith receiver. The phase is a distance or range measurement when factored by its period. If the satellite-receiver distance changes by 19 cm (the wavelength of the L1 carrier), for example, the L1 phase observable will change by 1 cycle. It is this information, along with knowledge of the time-dependent satellite coordinates, which allow the receiver position to be determined analogous to (2.3). For static positioning, several hours of continuous phase monitoring from multiple satellites are required for the highest precisions.

The phase observable can be written

$$\Phi_i^k = r(x_i,y_i,z_i,X^k,Y^k,Z^k) + \bar{c}(t_i,t^k) + d_{ion} + d_{trop} + \lambda N \qquad (2.4)$$

where r is a geometrical function of receiver and satellite coordinates, $\bar{c}$ is a clock-error function dependent on the difference between the receiver and satellite clocks, d_{ion} and d_{trop} are signal propagation delays through the ionosphere and troposphere, and N is the unknown number of integer cycles between the satellite and receiver often referred to as the ambiguity or bias (λ is the wavelength). The issues which remain in order to evaluate (2.4) in terms of receiver position (x,y,z), are to constrain, eliminate, or model the additional parameters (the satellite orbits, $\bar{c}$, d_{ion}, d_{trop}, and N).

GPS phase analysis can be considered from the perspective of understanding and removing the various error and ambiguity terms affecting the observations. Clock errors are nearly eliminated by differencing the phase measurement between different receivers and satellites. This is known as double differencing and is discussed below. The ionospheric signal delay d_{ion} is frequency dependent, and is virtually eliminated by taking an appropriate linear combination of the L1 and L2 carrier signals. The tropospheric delay d_{trop} is not frequency dependent and needs to be modeled from observed or assumed meteorologic data. In addition, a tropospheric delay adjustment is usually solved as a parameter in the final estimation. If the broadcast ephemerides are used, the largest uncertainty is contributed by errors in the satellite coordinates (X,Y,Z).

Three other error sources are worth mentioning: cycle slips, multipath, and blunders. Optimally, the receiver needs to continuously track the carrier phase signal transmitted from each satellite (phase-lock). When the receiver loses lock on the carrier signal, a break is recorded in the phase measurement.

These breaks are known as cycle slips and for TI-4100 instruments are normally of an integer number of cycles. Cycle slips can usually be corrected or fixed through proper (albeit tedious) data processing; detection and removal techniques are discussed below. Multipath is caused when the signal does not travel directly from the satellite to receiver, but is reflected off some secondary object (tree, fence, etc.). Blunders are usually generated from poor surveying techniques and include mis-measuring the antenna height, not centering over the monument, centering over the wrong monument, etc. Multipath and blunders are not considered here.

Double differencing

Clock errors are nearly eliminated through single and double differencing. Let the clock error from (2.4) be written

$$\overline{c}(t_i,t^k) = t^k - t_i \tag{2.5}$$

(when phase is written as a distance measurement it is necessary to include the speed of light). A single difference phase observable formed by differencing the phase measurements from two stations i and j is given by

$$\delta\Phi_{i,j}^{k} = \Phi_i^k - \Phi_j^k \tag{2.6}$$

Double difference phase observables are formed by differencing two single difference combinations between satellites k and l and is written

$$\Delta\Phi_{i,j}^{k,l} = \delta\Phi_{i,j}^{k} - \delta\Phi_{i,j}^{l} \tag{2.7}$$

Double differencing the clock terms from (2.5) yields

$$\Delta t_{i,j}^{k,l} = (t^k - t_i) - (t^k - t_j) - (t^l - t_i) + (t^l - t_j) = 0 \tag{2.8}$$

The explicit clock terms cancel by receiver-satellite double differencing so this bias is eliminated from (2.4). A more rigorous formulation would show that higher order clock terms remain in the double difference phase observable so

that clock stability is still an important consideration [e.g., *King et al.*, 1985].

It is the double difference phase observable which is utilized by most software systems, where the analog to (2.4) is

$$\Delta\Phi_{i,j}^{k,l} = \Delta r(x_{i,j},y_{i,j},z_{i,j},X^{k,l},Y^{k,l},Z^{k,l}) + \Delta d_{ion} + \Delta d_{trop} + \lambda\Delta N \qquad (2.9)$$

where Δ implies double differencing. There are separate phase combinations for the L1 and L2 carrier frequencies.

It is still necessary in high precision surveying to determine the nature of the clocks, nominally the receiver clock. Equation (2.9) is non-linear so its time-derivative linear approximation is computed for introduction into a least-squares formulation. The satellite coordinates (X,Y,Z) are strong functions of time, and in order to correctly evaluate the partial derivatives it is necessary to accurately model the clock behavior. The receiver timing standard is usually calibrated with a quartz oscillator (the satellites use atomic clocks), which tends to drift over a several hour observation interval. For the analysis incorporated in this study, the drift and the initial satellite-receiver clock offset are modeled as a polynomial of specified degree (quadratic or cubic terms usually suffice). The polynomial coefficients are often calculated from the pseudo-range. In many software systems the clocks are modeled as white noise, that is, independent clock terms are estimated at every measurement epoch. This is necessary due to the clock behavior of many GPS receivers.

The geometric (r), atmospheric (d_{ion}, d_{trop}), and ambiguity terms (N) in (2.9) are vector parameters relating the 3-dimensional satellite-receiver position, and subsequently do not cancel by differencing the phase. The signal

noise is greatly reduced through differencing, however, since potential error sources are often strongly correlated between stations. This is especially true for short baselines.

One final differencing concept is mentioned. GPS phase observations are usually recorded at predetermined epochs, perhaps once every 30 seconds (time-tags). The triple difference observable is the change in the receiver-satellite double difference from one epoch to the next. Cycle slips will affect only one point in the triple difference phase observable so this approach is frequently used for data editing. Another advantage is that correlated errors are further removed from the signal. The primary disadvantage of triple differencing, as is true with any differencing scheme, is that a significant amount of information will be lost.

Tropospheric delay model

An electromagnetic pulse propagating through a non-vacuum medium is refracted or slowed. Consequently, the troposphere creates a delay or an equivalent range error on the transmitted GPS signal. The result in an apparent increase in the receiver-satellite range measurement, and this bias will distort geodetic positioning. The equivalent zenith delay is about 2 m, but for satellites near the horizon the range error is as great as 20 m. The dry component of the atmosphere (nitrogen, oxygen, etc.) accounts for most of the zenith delay, while water-vapor content contributes anywhere from 0-5 cm (southern California) up to 30 cm (tropical climates).

The tropospheric range-error is easily modeled using surface measurements of temperature, pressure, and relative humidity. Frequently the delay d_{trop} is

computed with a Saastamoinen model [*Saastamoinen*, 1973], which is given (in seconds) by

$$d_{trop} = 7.595 \times 10^{-12} \sec z \left[p + \left(\frac{1255}{T} + 0.05 \right) e - \tan^2 z \right] \qquad (2.10)$$

where z is the zenith angle of the satellite, p is the atmospheric pressure in millibars, T is the temperature in °K, and e is the partial pressure of water vapor in millibars given by

$$e = 6.108 H_r \exp \left[\frac{17.15T - 4684}{T - 38.45} \right] \qquad (2.11)$$

where H_r is the relative humidity. The part of the model accounting for the dry atmospheric component is easily determined through surface pressure measurements and is accurate to about 1 cm. The wet component (water vapor) is not easily modeled since surface readings of relative humidity do not accurately reflect the water content throughout the atmosphere; the usefulness of these weather measurements is questionable. Default (or assumed) meteorologic values do not significantly influence geodetic positioning, especially for short baselines. It is usually necessary for high precision surveying to solve for an adjustment to the modeled tropospheric zenith delay, in addition to station coordinates and other unknowns. This technique frequently improves measurement precision [e.g., *Blewitt et al.*, 1986].

Ionospheric-free L3 phase observable

The ionized gas molecules in the upper 50-1000 km of the atmosphere (ionosphere), have the effect of creating a 5-150 m equivalent range error on the transmitted GPS signal. The ionospheric delay d_{ion} is frequency dependent (dispersive) and given (in seconds) by

$$d_{ion} = -\frac{1.35 \times 10^{-7} N_e}{f^2} \tag{2.12}$$

where f is the signal frequency and N_e is a function of the ionospheric electron density, elevation angle of the satellite, latitude, time of day, season of the year, and 11-year sunspot cycle [*King et al.*, 1985]. The ionospheric bias is eliminated by an appropriate linear combination of the L1 and L2 phase (or double differenced) observables. The L3, or ionosphere-free phase combination is given by

$$\Phi_{L3} = \Phi_{L1} - \frac{f_1 f_2}{f_1^2 - f_2^2}\left(\Phi_{L2} - \frac{f_2}{f_1}\Phi_{L1}\right) \tag{2.13a}$$

or

$$\Phi_{L3} = \Phi_{L1} - 1.984(\Phi_{L2} - 0.779\Phi_{L1}) \tag{2.13b}$$

[*King et al.*, 1985]. The L3 phase combination is a differenced measurement free of ionospheric distortions, and in fact, the primary purpose of providing 2 carrier frequencies with the GPS signal structure is to eliminate this bias.

Alternatively, if only single frequency measurements are available, either intentionally (some receivers record only the L1 carrier) or because of poor observing conditions (high solar activity, etc.), the ionosphere can be modeled with an appropriate correction. However, ionospheric models are still in the early stages of development and their use will likely result in significantly degraded solutions compared with multifrequency observations.

One drawback for using the L3 phase combination is that data noise is somewhat larger than that of the L1 or L2 measurements. For longer baselines the ionospheric error predominates so the L3 phase will provide optimum results, but for baselines less than $\sim$ 10 km the ionospheric

component is so strongly correlated between stations (and thus removed when differencing) that the L1 observable yields better solutions [*Davis et al.*, 1989; *Prescott et al.*, 1989].

GPS solution

Once all bias and error terms have been modeled or eliminated, Equations (2.4) and (2.9) are written

$$\Delta\Phi_{i,j}^{k,l}(t_m) = F(x_{i,j},y_{i,j},z_{i,j},X^{k,l},Y^{k,l},Z^{k,l},N_{i,j}^{k,l},f) \qquad (2.14)$$

where $(x_{i,j},y_{i,j},z_{i,j})$ are the relative baseline coordinates between stations i and j, $(X_{k,l},Y_{k,l},Y_{k,l})$ are the relative coordinates between satellites k and l, $N_{i,j}^{k,l}$ is the unknown double differenced phase ambiguity between stations i and j and satellites k and l, f represents additional/optional parameters to solve, and F is some function relating all terms. The double differenced phase observable at time t_m, where m is the measurement epoch, is either the L1, L2, or ionosphere-free L3 phase combination (the L3 is generally used in practice). The satellite coordinates are also functions of time.

The solution to (2.14) can be determined by some least-squares parameterization. Since the problem is non-linear, adjustments to a priori values are estimated. Data are usually processed in a network mode, where all double difference phase combinations from each station-station and satellite-satellite pair for the daily observation session are integrated into one solution. (In less rigorous methods each station pair is solved separately and a network adjustment is applied to all baselines). For an observation session of 7 hours and a data collection rate of 30 seconds (epoch), there are typically 2000 observables for each station-station pair, depending on the tracking

interval for each satellite. For a network of 6 stations, this will correspond to 10,000 data. For the most robust positioning, several days of observation are combined into a single solution with the aid of multi-day orbital arcs [e.g., *Lichten and Border*, 1987].

In the simplest case, the only unknown parameters in (2.14) are the station coordinates (x,y,z) and the double differenced phase ambiguities (N). In principle the relative coordinates between stations are computed, although in practice one or more stations are held fixed so the solved positions are relative to these sites. Satellite coordinates can be constrained by the broadcast ephemeris or some other orbit service, although they may be modified from force modeling considerations. For the most precise positioning it is necessary to adjust or solve for satellite orbits in addition to station coordinates.

Additional unknowns f can be included in the solution. Although the tropospheric delay is almost always determined by atmospheric models, since it is difficult to estimate water-vapor content from surface measurements alone, a tropospheric zenith delay adjustment is often solved at each station. This allows additional leeway in the computed tropospheric range-error. If the pseudo-range measurements do not yield adequate clock corrections, clock coefficients are estimated with the station coordinates. Ionospheric models applied to single frequency observations can be improved by calculating adjustments to the ionospheric parameters.

Estimating Satellite Orbits

Three types of parameterizations are used in GPS orbit analysis: the

broadcast, precise, and improved orbits. The broadcast ephemeris is included with the satellite message modulated on the GPS signal. Satellite coordinates are held fixed in (2.14) to orbital elements determined from the broadcast ephemeris. Depending on the software scheme there may be some adjustment due to force-modeling considerations. The same is true with post-processed or precise ephemerides available from agencies such as the Naval Surface Weapons Center (NSWC). The broadcast and precise orbits yield comparable repeatabilities [*Remondi and Hofmann-Wellenhof*, 1989], with typical baseline accuracies anywhere from 1 to 0.1 ppm (parts per million). For short baselines ($\sim$ 50 km), this is equivalent to 0.5-5 cm. Broadcast orbits have the advantage that they are available in real-time so that GPS analysis can begin immediately once the data are collected, while with the precise ephemerides there is a delay before they are available.

When sub-centimeter surveying accuracy is required, it is necessary to utilize orbit improvement techniques (improved or solved orbits). With this method the parameters which define the satellite coordinates in (2.14) are estimated along with station coordinates and other terms. Satellite orbits can be defined by 6 Keplerian elements, as well as 0-2 radiation pressure terms. Satellite motions are not solved at each epoch, but rather adjustments to a set of Keplerian parameters (plus radiation terms) are estimated for each orbital arc lasting from several hours to several days.

In order to solve for station coordinates it is necessary to constrain the phase observations. When using the broadcast or precise ephemerides the data are constrained by the satellite orbits. However, when solving for orbits as free parameters it is necessary to hold the positions of at least three GPS

sites fixed to coordinates well determined by other means (such as VLBI or SLR). The coordinates and phase observations from these fiducial sites constrain the satellite orbits which in turn define the coordinates of the unknown GPS stations.

A continuously monitoring worldwide GPS network has been established to provide phase observations at sites with well determined coordinates. Known as the Cooperative International GPS Network (CIGNET) [*Chin*, 1988], North American fiducial sites are located at Mojave (California), Westford (Massachusetts), Richmond (Florida), Kokee Park (Hawaii), and Yellowknife (Canada). Data from these sites are often integrated with local and regional GPS measurements to provide orbit improvement.

The horizontal positioning accuracy utilizing orbit improvement techniques are on the order of a few parts in 10^{-8}, corresponding to the millimeter level for 50 km baselines. Station coordinates obtained with the broadcast ephemeris (50 km lines) yield solutions 1 to 3 cm different in the horizontal components than those computed with improved orbits.

Ambiguity Resolution

The phase ambiguity N (2.4) is the unknown number of cycles (or wavelengths) between satellite and receiver. Without loss of generality this concept is extended to the double difference observable in (2.14). Initially, the ambiguity (or biases) are usually estimate as a real number in the GPS solution. The L1 and L2 phase ambiguities are integers, while the L3 ambiguity is constrained to specified values (not necessarily integers). The solution will improve if the bias can be fixed or optimized to its integer or

specified value. This is known as ambiguity resolution, bias fixing, or bias optimization; more detailed discussions are found in *Blewitt* [1989] and *Dong and Bock* [1989].

Unfortunately, resolving ambiguities is not always easy. For example, suppose the estimated L1 phase bias equals 4.02. It would be reasonable to suggest that the true ambiguity, which must be an integer, is 4.00. Recomputing the solution with the bias fixed at 4.00 will yield a more accurate result. However, suppose the computed ambiguity is 4.40. Now it is questionable whether the true bias is 4.00 or 5.00. Fixing the ambiguity to the wrong value will distort the solution.

2.3 GPS Data Collection

GPS data used for crustal motion research are collected in well planned surveys often referred to as campaigns. These experiments usually last anywhere from several days to a few weeks, with several months of full-time preliminary preparation. Described here are some of the aspects involved in GPS data collection.

Site selection

Site selection from a tectonic standpoint is considered from 3 perspectives: 1) geophysics, 2) gps constraints, and 3) logistics. The geophysical objective is straightforward; a tectonic problem is defined and a network is designed which maximizes the geophysical information. The crustal motions sought must be experimentally obtainable with the given GPS accuracy and technology. This surprisingly has been overlooked on a number of not-to-be-

mentioned instances. It is also possible to over-design an experiment. It is not necessarily true that more measurements will significantly improve the intended geophysical result. Some specific GPS considerations include baseline length (short lines are more accurate), baseline orientation (north-south lines are more accurate), strength of network (determined through covariance analysis), receiver type (best to use same type of equipment), and fiducial coverage (used for orbit improvement). Also under consideration are previous site occupations, either from GPS or conventional surveys. In addition, as is true for most geodetic measurements, site stability is an important gps constraint. Sites must be located where near surface effects such as subsidence, frost heave, or soil creep will not significantly influence the tectonic signal. This is all the more true considering the accuracy of GPS. That is, the detection of increasingly smaller tectonic motions anticipated from improved measurement accuracy, will require greater site stability. (It is noted that for some engineering applications, geodetic measurements are made to monitor subsidence.)

The logistics behind designing an experiment are immense; this is all the more true for foreign experiments (Can the survey crew rent camels to transport the equipment up a mountain? Will the military provide local villagers with weapons to protect the personnel from anti-government rebels? Will equipment go through customs?) Usually each survey crew is highly independent, with one or two days allotted for equipment transfer between remote sites.

Two types of station occupation methods are used. In the first, multiple observations of the same network are made over 3-5 consecutive (or nearly

consecutive) days. This has an advantage from a statistical viewpoint, in that day-to-day baseline repeatability can be examined. Outlyers in the data are detected and discarded if necessary. Because of multiple observations the uncertainty in the mean measurement is decreased. The second method is often referred to as the leap-frog approach, in which site-occupations change on a daily basis. Frequently each station is observed at least twice during the experiment, but the GPS network geometry is usually different each day. One or two stations may be continuously observed. This type of occupation scenario has the advantage that more stations can be occupied over the course of a campaign. The disadvantage is that day-to-day experimental precision is difficult to ascertain since redundant baselines are less common.

Instrumentation

Dual frequency GPS receivers are necessary for crustal motion research. For baselines longer than $\sim$ 10 km the large ionospheric signal distortion must be eliminated by utilizing the L3 ionosphere-free phase combination. The first commercially available dual frequency P and C/A code instrument was the TI-4100 NAVSTAR Navigator. This unit decodes the pseudo-random signals to measure the carrier phase (code-correlation) and is able to track up to 4 satellites at a time. Both the P (L1, L2) and C/A (L1) codes can be recorded, along with the broadcast message. Although portable, this instrument is somewhat bulky with a total surveying weight of about 200 pounds (including tripod, cables, etc.). The TI-4100 was the primary instrument used for crustal deformation measurements in the 1980's. Typical of newer and lighter models is the Trimble 4000SDT GPS Surveyor. This dual frequency unit is code-correlating on the L1 frequency, records the C/A

code and broadcast message, and is able to track up to 8 satellites at a time (16 in single frequency mode). The first use of this instrument for geophysical purposes was in Turkey during the summer of 1989.

Equipment set-up

Set-up time for a mobile GPS instrument takes anywhere from 20 minutes to 2 hours, depending on the type of equipment, the speed of the operator, and the ease of leveling and centering a tripod at the monument. After arriving at the site, the vehicle is usually parked at least 100 feet and preferably downhill from the observation point to prevent signal-multipath interference. All equipment (except the tripod, tribrach, antenna, and cable) should remain in the vehicle or some other weather-proof structure. The operator powers up the receiver $\sim$ 1 hour before the measurement start time to allow the internal oscillator to stabilize (for the TI-4100 instrument). A standard surveying tripod and tribrach is leveled over the monument, and the GPS antenna is secured to the top. For consistent phase center measurements, a reference mark on the antenna is oriented to some predefined azimuth (e.g., north). At least two measurements of the antenna height above the geodetic monument are recorded (as a consistency check). A RF cable is connected from the antenna to the receiver, and the GPS instrument is programmed to track GPS transmissions either automatically or from a predefined scenario. At the end of the observation session, the antenna height is remeasured and recorded.

Observation approach

Most daily GPS observations for crustal motion research in California

have lasted between 5 and 8 hours. Due to the motion of the earth around the sun, the observation scenario is shifted 4 minutes earlier each day. Data are usually collected at 15 to 30 second epochs. GPS receivers of the same type and internal software record the phase measurements at the same time-tag (according to the internal oscillator), while receivers of different types will not. Meteorologic measurements of surface temperature, barometric pressure, and relative humidity (usually computed from wet and dry bulb temperature readings) are recorded periodically throughout the experiment. These data are used to constrain the tropospheric delay model in the processing.

2.4 GPS Data Processing

Bernese software

Most of the GPS data presented here have been processed with the Bernese GPS analysis software (version 3.0) from the University of Bern, Switzerland [*M. Rothacher*, unpublished documentation, 1988]. (Some preliminary processing such as data translation were made with an earlier version of the Bernese software.) The Bernese GPS analysis package allows 3-dimensional station coordinates to be determined from the integration of carrier phase, pseudo-range, and orbital data [e.g., Gurtner et al., 1985; Beutler et al., 1985; Rocken, 1988]. In addition to estimating station coordinates, the double difference algorithm can solve for adjustments to six Keplerian elements and two radiation pressure coefficients for each satellite, an atmospheric zenith delay parameter at each station, a clock error term at each station, ionospheric model coefficients, and cycle ambiguity terms. Observations spanning several days are either processed individually (day by

day) or integrated into one simultaneous solution. While the L1 or L2 phase observables can be used, in practice for all but the shortest lines ($\sim$ 10 km) the ionosphere-free L3 phase measurement is utilized. Auxiliary information such as surface meteorological measurements, polar motion and Earth rotation data, gravity potential coefficients, and a priori site coordinates help constrain the solution. Introductions to GPS and data processing methods are found in *King et al.* [1985] and *Wells et al.* [1987].

Routine GPS data processing with the Bernese software is grouped into two categories: 1) preprocessing and 2) parameter estimation. The preprocessing phase is sub-divided into several steps: 1) data translation, 2) initial orbit generation, 3) pseudo-range processing, 4) single difference formation, and 5) data editing (cycle slip detection and elimination). While some procedures are relatively transparent to the user, others require knowledge of GPS to utilize proficiently. In general, the processing techniques employed are similar for all data analyzed; the "typical" processing scheme is outlined below.

Data translation

After data collection in the field, the phase, pseudo-range, and ephemeris observations are translated or transcribed into Bernese format from the raw GESAR, NAVDAPT, FICA, or CIGNET (ARGO) formatted data. With the exception of cycle slip detection and elimination, this is surprisingly the most time consuming step. Although there are several utilities within the Bernese software for translating raw and pre-transcribed GPS data of different formats (from different receivers, receiver software, etc.), it was necessary to

develop FICA and CIGNET translation routines as nothing previously was available. It was also necessary to make minor changes to the GESAR and NAVDAPT transcription algorithms to account for slight modifications in the raw data.

Orbits

After data translation, initial orbital parameters are created from the broadcast ephemeris. Approximately once an hour, a message is recorded which contains for each satellite: 6 Keplerian elements (from which satellite position and velocity are computed), perturbations of these elements (mostly from the non-sphericity of the earth, solar and lunar gravitational attractions, and solar radiation pressure), and coefficients of satellite clock errors. The broadcast parameters are given in an earth-centered, earth-fixed, reference system (rotating with the earth). The ephemeris is currently given in the WGS-84 reference frame [*Defense Mapping Agency*, 1987], although previous to January 17, 1987, the WGS-72 coordinate system was used. The broadcast ephemeris is computed from the extrapolation of a postprocessed orbit into the future and up-loaded to each satellite and is intended for use only during the $\sim$ 1 hour period to which it refers. Extrapolation significantly beyond this interval will yield large orbital errors.

After checking for outlyers in the broadcast parameters (few were detected) a tabular orbit file consisting of satellite positions every 1000 seconds in a Cartesian system is created by fitting and interpolating between the hourly broadcast elements. In addition, a transformation is made between the earth-fixed broadcast coordinate system (e.g., WGS-72, WGS-84),

into an inertial reference frame (i.e., system 1950.0). A priori standard orbits are created once a tabular ephemeris is generated. The tabular orbit file positions are treated as "observations" and used to find the solution to the equations of motion that best fit these positions. These are solutions to the equations of motion for each satellite computed by numerical integration, and represented by polynomial coefficients. Specific details for orbit modeling with the Bernese software is found in *Beutler et al.* [1985]. Standard orbits are used in the GPS coordinate adjustment; they can, however be updated or improved in the solution.

Pseudo-range

The pseudo-range measurements (essentially the receiver-satellite distance) are checked for obvious outlyers (typically 0 to 5 bad pseudorange data were found for each station per day). These observations, together with the broadcast ephemeris, are used to estimate initial station coordinates (accurate to 1-5 meters) and polynomial coefficients for corrections to the receiver clocks (Equation 2.3). In the Bernese software, the receiver-satellite clock offset is modeled as a polynomial of selected degree over time. We used a polynomial of order 3 for all data, and found that changing the degree did not significantly affect the results. Generally, errors in clock offset estimates should be eliminated by the double difference algorithm used in the solution [e.g., *King et. al.*, 1985]. The pseudo-range measurements can be used for cycle slip editing and aid in the resolution of the phase ambiguities.

Differencing

Single difference phase observables are formed by differencing the phase

measurements between two stations. If n stations are occupied on a given day, then $n-1$ single difference combinations can uniquely define the observation set without redundancy. The general strategy used to determine the single difference combinations, is to minimize the sum of the baseline lengths between all station pairs. Additional constraints are considered, such as data quality at a given site. Differences are made separately for the L1 and L2 phase signals. The double difference phase observables (between satellites) are automatically computed during the GPS solution phase, as are the ionosphere-free L3 combinations (if requested).

Cycle slips

Once the minimum number of single difference combinations are formed, cycle slips are interactively removed from the L1 and L2 phase observables. This has proven to be the most time consuming step of GPS data processing. Although there have been vast improvements over the last few years in the ability of GPS software to handle this problem [e.g., *G. Blewitt*, JPL interoffice memorandum, 1988; *Rocken*, 1988], with bad data or large data gaps, cycle slip correction can be extremely tedious. The Bernese software uses a triple difference algorithm to delete bad data and correct cycle slips. A polynomial is first fit to the each single difference phase combination to detect large slips (interpreted as large residuals between the polynomial and data). After the observations are prescreened in this way, triple difference solutions using the a priori standard orbits are iteratively improved by leaving out large residuals. Once a satisfactory solution is obtained (usually after 1-2 iterations), the large residuals are interpreted as cycle slips and removed (the residuals should be near integers). This operation is performed first on the L1

and L2 phase observables, then the ionospheric-free linear combination (referred to as L3 in the Bernese software) and the wide-lane combination (referred to as L5) are inspected as a check for uncorrected slips. If successful, there should be no cycle slips remaining in the double difference phase observables for each of the single difference phase combinations. Finally, the residuals from a GPS solution are examined for slips not removed.

For reasonably good data (perhaps 4 out of 5 stations), and for baselines under 1000 km, this technique is all but automatic. Cycle slip correction for a 10 station regional network observed 7 hours, for example, will optimally take 1-2 man hours. However, it can be significantly more difficult when using baselines of continental length or particularly bad data. For the longer lines, errors in the a priori standard orbits produce residuals which are often too large to detect all cycle slips, or at the very least, to ascertain whether all slips have been removed. Therefore, it is necessary to use an iterative process by adjusting the orbital parameters through the estimation program to form a set of improved standard orbits, and reemploying the above steps to edit any remaining slips. One to three iterations are usually sufficient to remove all slips in continental-length baselines. In general, data from the continental (CIGNET) sites has been of poorer quality than those collected from the regional GPS networks.

If data for any baseline is particularly bad (numerous slips or large data gaps in the phase observables), the time required to repair cycle slips is greatly increased. In several instances, up to 6 hours are necessary for a single baseline. We point out that most editing was done using older versions of the cycle slip correction routines available with the Bernese software. Completely

automatic modules recently made available in the Bernese package are said to correct cycle slips in bad data much more proficiently.

Although the option is available in the software, half cycle slips are never repaired. It is found that half slips either occurred at the beginning of a satellite double difference arc, in which case the first epoch is simply removed, or in pairs, in which case the first observation of the pair is deleted resulting in either a single slip or no slip. However, almost all data reported here were collected with TI-4100 instruments. Half cycle slips are common for newer GPS receivers, such as the Trimble, Ashtech, and Minimac models.

Parameter estimation -- GPS solution

Once all single difference station-station phase observables are free of cycle slips at the double difference level (preprocessing), site coordinates and other parameters are estimated in the GPS solution. In many respects, the estimation approach is similar for each survey with the notable exception regarding the handling of satellite orbits. The "typical" solution is briefly discussed, as well as specifics concerning the methods of orbit utilization.

Each epoch of the 30 second data collection rate are used as observables. Smoothing or non-unity sampling criteria are not applied to data. The L3, or ionospheric-free phase observable is used for all observations. A Saastamoinen meteorological zenith delay model, constrained by surface measurements of temperature, pressure, and humidity (usually computed from wet and dry bulb temperature readings), is used to calculate the atmospheric signal delay, which is adjusted by estimating a tropospheric delay parameter at each station. An a priori sigma of 5 cm at each site is used to constrain

the tropospheric adjustment (typical adjustments are less than 10 cm). Data from satellite elevations lower than 20 degrees are not used. Bias fixing and optimization techniques, which have been demonstrated to improve measurement repeatability are not incorporated [Blewitt, 1989; Dong and Bock, 1989]. While ambiguities are resolvable for most baselines under 50 km length, only partial success is achieved on the longer lines. Because the line-lengths involved for this study are relatively short, only marginal improvement from bias fixing is expected, therefore the ambiguities are left unresolved. All observations for a given campaign are combined to form a single multi-day simultaneous solution. This involved integrating anywhere from 3 to 9 days of observation. In some instances, single-day solutions are obtained to investigate day to day repeatability.

Two methods are imposed to handle satellite orbits. If GPS data are available from at least 3 sites with well determined coordinates, the satellite orbits are simultaneously adjusted by holding these fiducial sites fixed, and solving for the coordinates of the remaining stations as free parameters. The estimated station positions are computed in the reference frame defined by the fixed coordinates. The fiducial stations are constrained to SV-3 coordinates predetermined by VLBI and Satellite Laser Ranging [*Murray and King*, unpublished memo, 1988]. For each satellite, 6 Keplerian elements and two radiation pressure terms are estimated. We find experimental solutions excluding the Y-bias scale term [*Fliegel et al.*, 1985] have negligible influence on the results.

Continental fiducial phase observations are made available from the CIGNET tracking network, or obtained as part of a particular GPS

campaign. Data from CIGNET sites are frequently of poor quality, however. In fact, many times there are no data available, or at least insufficient data to adequately estimate satellite orbital parameters. When this is the case it is necessary to utilize the broadcast ephemeris with no orbital adjustment. The coordinates of one station are held fixed, and the remaining site coordinates estimated relative to the fixed station.

Computer constraints

All coordinate solutions obtained with the Bernese GPS software are processed on a Sun-4 UNIX-based computer. A typical GPS campaign involved 50 station-days of observation, each about 7 hours in length. The raw receiver data from such an experiment requires $\sim$ 15 Mbytes of disk storage (in binary), or 40 Mbytes for a standard exchange format such as FICA (ASCII). Preliminary processing requires an additional 40 Mbytes of hard storage, but the differenced phase observables and other relevant data needed for the parameter estimation can be maintained in about 15 Mbytes. The executable software has a 10 Mbyte hard disk requirement.

Once cycle slips have been edited from the differenced phase observables, a single baseline GPS solution takes approximately 1 minute of CPU time. In the network mode, coordinates for 7 stations are determined in $\sim$ 10 CPU minutes, while a 14 station network may require an hour of computation. In the largest solution performed in this study, a 5-day orbit adjusted simultaneous estimation with approximately 14 stations per day, required 25 hours of CPU time. The core-memory requirement for this solution of 110,000 observables and 469 estimated parameters was a few Mbytes. If

computations become too intensive, non-unity sampling criteria can be applied to the observations.

2.5 GPS Coordinates and Error Analysis

Coordinate systems

Geodetic positions obtained through conventional surveying are usually tied to some local coordinate system. It is often difficult to correlate geodetic measurements from different regions. With the advent of space-based surveying technology, it is prudent to speak of a world coordinate system, where geodetic positions are described in a Cartesian reference frame given by $\vec{X}=(x,y,z)$. The origin is often constrained to the earth's center, and the axes are defined in an earth-fixed sense (rotating with the earth). In modeling satellite orbits it is necessary that the origin of the coordinate system be at the center of mass of the earth (and satellite system). Satellite coordinate are often relative to some inertial system. The shape of the earth is approximated by an ellipsoid centered around the Cartesian system, and defined in terms of the semi-major axis and flattening coefficient [e.g., *Stacey*, 1977]. It is straightforward to transform between the Cartesian system and a geographic system defined on the ellipsoid (latitude, longitude, height above ellipsoid). When manipulating 3-dimensional Global Positioning System coordinates, it is easiest to refer to the Cartesian system. However, when referencing crustal motion measurements such as the orientation of station displacement, it is more intuitive to speak in terms of geographical coordinates (east-west, north-south, up-down).

The GPS reference frame is in the World Geodetic System (WGS) [e.g., *Defense Mapping Agency*, 1987]. The broadcast ephemeris after January 17, 1987, is defined in the WGS-84 system. Before this time satellite orbits were reported in WGS-72. Other space geodetic measurements are usually made relative to some other reference frame, such as the VLBI/SLR based SV-3 or NAD-83 (North American Datum). It is generally *assumed* that the WGS-84, NAD-83, and SV-3 coordinate frames are equivalent. However, there are undoubtedly differences among the different coordinate systems and a future problem will be to relate geodetic parameters computed in different reference frames.

A transformation is necessary from WGS-72 to WGS-84 for GPS station coordinates obtained with the broadcast ephemeris before January, 1987 (to be consistent with the most recent system). The transformation of a set of Cartesian coordinates from WGS-72 to WGS-84 is given by

$$\vec{X}_{84} = \Delta\vec{X} + (1 + \Delta s)\mathbf{R}\vec{X}_{72} \tag{2.15}$$

where $\vec{X}_{84}$ are site coordinates in WGS-84 (meters), $\vec{X}_{72}$ are site coordinates in WGS-72 (meters), $\Delta s = 2.263 \times 10^{-7}$, and the translation vector $\Delta\vec{X}$ (meters) and rotation matrix **R** are given by

$$\Delta\vec{X} = \begin{bmatrix} 0 \\ 0 \\ 4.5 \end{bmatrix}$$

$$\mathbf{R} = \begin{bmatrix} 1 & -r_z & 0 \\ r_z & 1 & 0 \\ 0 & 0 & 1 \end{bmatrix}$$

with $r_z = 2.686 \times 10^{-6}$.

GPS coordinates

Three Cartesian coordinates $\vec{X}_i = [x_i, y_i, z_i]$ are estimated for each station not held fixed in the GPS solution (for fixed stations $\vec{X}_i$ is equal to the a priori coordinates). The baseline vector from station i to station j is given simply by

$$d\vec{X}_{ij} = \vec{X}_j - \vec{X}_i = \begin{bmatrix} x_j - x_i \\ y_j - y_i \\ z_j - z_i \end{bmatrix} = \begin{bmatrix} dx_{ij} \\ dy_{ij} \\ dz_{ij} \end{bmatrix} \tag{2.16}$$

Station coordinates are often listed as a set of baseline vectors, each made relative to the same reference station. For $n+1$ stations with known coordinates, there are n independent baseline vectors.

For geophysical purposes it is often convenient to refer to the baselines in a local reference frame. Instead of $d\vec{X}_{ij} = [dx_{ij}, dy_{ij}, dz_{ij}]$, we speak of $d\vec{X}'_{ij} = [de_{ij}, dn_{ij}, dv_{ij}]$ where *de*, *dn*, and *dv*, are the east, north, and vertical baseline components as defined at station i. Cartesian vectors are rotated into a local frame by

$$d\vec{X}'_{ij} = \mathbf{R}_i d\vec{X}_{ij} \tag{2.17}$$

where

$$\mathbf{R}_i = \begin{bmatrix} -\sin(\theta_{lon}) & \cos(\theta_{lon}) & 0 \\ -\sin(\theta_{lat})\cos(\theta_{lon}) & -\sin(\theta_{lat})\sin(\theta_{lon}) & \cos(\theta_{lat}) \\ \cos(\theta_{lat}) & \cos(\theta_{lat})\sin(\theta_{lon}) & \sin(\theta_{lat}) \end{bmatrix}$$

and θ_{lat} and θ_{lon} are the latitude and longitude of station i, respectively. It is stressed that unless stations i and j are identical then $d\vec{X}'_{ij} \neq d\vec{X}'_{ji}$.

If a particular baseline $d\vec{X}'_{ij}$ is observed on N consecutive (or nearly consecutive) days, the day to day repeatability (scatter) in the baseline components measured in the local reference frame is determined by

$$\vec{\sigma} = \begin{bmatrix} \sigma_e \\ \sigma_n \\ \sigma_v \end{bmatrix} = \left[\sum_{k=1}^{N} (\Delta \vec{X}'^{\,k}_{ij}) / (N-1) \right]^{\frac{1}{2}} \tag{2.18}$$

where the difference between the average ($d\bar{X}_{ij}$) and the kth ($d\vec{X}'^{\,k}_{ij}$) baseline observation is given in a Cartesian frame by

$$\Delta \vec{X}_{ij} = d\vec{X}^{k}_{ij} - d\bar{X}_{ij} \tag{2.19}$$

and in the local frame by

$$\Delta \vec{X}'^{\,k}_{ij} = \mathbf{R}_i \Delta \vec{X}^{k}_{ij} \tag{2.20}$$

where $\mathbf{R}_i$ is given above.

Coordinate adjustment

For multiple days of repeated observations, a "best" or weighted average set of coordinates relative to some reference station is obtained through an adjustment of the baseline vectors (note that this is not necessary for multi-day simultaneous solutions). Analogously, an adjustment is necessary to determine the weighted average coordinates between multiple independent surveys, assuming no deformation has occurred between observations.

If the number of non-redundant baselines observed on the kth day of a N day experiment is given by $m_k = n_k$, where $n_k + 1$ is the number of stations observed on the kth day, then the number of independent baselines m observed during the multi-day experiment of $n+1$ stations, is given by

$$m = \sum_{k=1}^{N} m_k$$

Note that dependency requires only that the non-redundancy condition hold each day; baselines can be repeated, if observed on different days. The adjusted solution $d\vec{A}$, where

$$d\vec{A} = \begin{bmatrix} d\vec{X}^{a}_{(n+1)1} \\ d\vec{X}^{a}_{(n+1)2} \\ \cdot \\ \cdot \\ d\vec{X}^{a}_{(n+1)n} \end{bmatrix}$$

are the adjusted baseline vectors relative to station $n+1$ (here assumed to be the reference station), is given by the simple least squares inversion

$$d\vec{A} = \left[\mathbf{A}^{T}\mathbf{W}^{T}\mathbf{W}\mathbf{A}\right]^{-1}\mathbf{A}^{T}\mathbf{W}^{T}\mathbf{W}d\vec{X}^{m} \qquad (2.21)$$

where $d\vec{X}^{m}$ is the data observation array containing the m independent baseline vectors, $\mathbf{W}$ is the inverse of the covariance matrix of baseline uncertainties and correlations ($\mathbf{W} = [\mathrm{cov}]^{-1}$), and $\mathbf{A}$ is the mxn model matrix of the geometrical relationship between the observations and the model parameters. If all observations $d\vec{X}^{m}$ are made relative to station $n+1$, then $\mathbf{A}$ is given simply by

$$\mathbf{A} = \left[\delta_{ij}\right]$$

where $i = j$ if the ith observation was made between stations $n+1$ and j.

An adjustment is useful when determining an optimal coordinate or vector solution for multiple observations of the same baselines, in addition to evaluating measurement repeatability. In practice, if the number of consecutive days of measurement is relatively small, all observations and coordinate parameters are evaluated simultaneously in the GPS solution. In this case no adjustment is necessary since only one set of station coordinates is estimated. However, each day of observation can be evaluated independently to examine measurement repeatability.

Error analysis

In this section we discuss the formal aspects regarding the calculation of GPS baseline errors. In general, we use an integrated approach which combines formal estimates of baseline uncertainty with measurement precision. Unless specifically mentioned, we include both variances and covariances in all analyses. All errors are considered at the one standard deviation level.

With each estimation, the Bernese software creates a covariance matrix listing formal uncertainties for station coordinates in a Cartesian reference frame. The covariance matrix **C** can be written

$$\mathbf{C} = \left[\mathbf{c}_{ij}\right] \tag{2.22}$$

where

$$\mathbf{c}_{ij} = \begin{bmatrix} \nu_{x_i x_j} & \nu_{y_i x_j} & \nu_{z_i x_j} \\ \nu_{x_i y_j} & \nu_{y_i y_j} & \nu_{z_i y_j} \\ \nu_{x_i z_j} & \nu_{y_i z_j} & \nu_{z_i z_j} \end{bmatrix}$$

If $i = j$, then $\mathbf{c}_{ij}$ are the coordinate covariances of station i, where the diagonal components of $\mathbf{c}_{ij}$ are the variances or the square of the one sigma errors ($\sigma^2 = \nu$). If $i \neq j$, then $\mathbf{c}_{ij}$ are the interstation covariances. For example, $\nu_{x_i x_j}$ is the covariance in the x coordinate between stations i and j, while the error σ_y in the y coordinate of station i is given by $\sigma_y^2 = \nu_{y_i y_i}$.

The baseline error between stations i and j (j minus i) is computed from

$$\hat{\mathbf{c}}_{ij} = \mathbf{G}\hat{\mathbf{C}}\mathbf{G}^{\mathrm{T}} \tag{2.23}$$

where

$$\mathbf{G} = \begin{bmatrix} -1 & 0 & 0 & 1 & 0 & 0 \\ 0 & -1 & 0 & 0 & 1 & 0 \\ 0 & 0 & -1 & 0 & 0 & 1 \end{bmatrix}$$

and

$$\hat{\mathbf{C}} = \begin{bmatrix} \mathbf{c}_{ii} & \mathbf{c}_{ij} \\ \mathbf{c}_{ji} & \mathbf{c}_{jj} \end{bmatrix}$$

The transpose of $\mathbf{G}$ is given by $\mathbf{G}^T$. The off-diagonal terms of $\hat{\mathbf{c}}_{ij}$ are the covariances for the Cartesian baseline components between stations i and j, while the diagonal elements are the variances.

The error in the baseline length L, where $L=(x^2+y^2+z^2)^{1/2}$, is computed from

$$\sigma_L^2 = \nu_x \left(\frac{\partial L}{\partial x}\right)^2 + \nu_y \left(\frac{\partial L}{\partial y}\right)^2 + \nu_z \left(\frac{\partial L}{\partial z}\right)^2 + 2\nu_{xy}\left(\frac{\partial L}{\partial x}\right)\left(\frac{\partial L}{\partial y}\right) + 2\nu_{xz}\left(\frac{\partial L}{\partial x}\right)\left(\frac{\partial L}{\partial z}\right) + 2\nu_{yz}\left(\frac{\partial L}{\partial y}\right)\left(\frac{\partial L}{\partial z}\right) \qquad (2.24)$$

or

$$\sigma_L^2 = \frac{\nu_x x^2 + \nu_y y^2 + \nu_z z^2 + 2\nu_{xy} xy + 2\nu_{xz} xz + 2\nu_{yz} yz}{x^2+y^2+z^2}$$

Once the baseline covariance matrix $\hat{\mathbf{c}}_{ij}$ is calculated, the Cartesian coordinates are rotated into a local reference frame. We use a north-east-up system, so that the local covariances are given by

$$\mathbf{c'}_{ij} = \mathbf{R}_i \hat{\mathbf{c}}_{ij} \mathbf{R}_i^{-1} \qquad (2.25)$$

[e.g., *Goldstein*, 1980, p. 146], where

$$\mathbf{R}_i = \begin{bmatrix} \cos(\theta_{lat})\cos(\theta_{lon}) & \cos(\theta_{lat})\sin(\theta_{lon}) & \sin(\theta_{lat}) \\ -\sin(\theta_{lon}) & \cos(\theta_{lon}) & 0 \\ -\sin(\theta_{lat})\cos(\theta_{lon}) & -\sin(\theta_{lat})\sin(\theta_{lon}) & \cos(\theta_{lat}) \end{bmatrix}$$

and θ_{lat} and θ_{lon} are the latitude and longitude at station i, respectively. The

local covariances $\mathbf{c'}_{ij}$ are given by

$$\mathbf{c'}_{ij} = \begin{bmatrix} \nu_{uu} & \nu_{ue} & \nu_{un} \\ \nu_{eu} & \nu_{ee} & \nu_{en} \\ \nu_{nu} & \nu_{ne} & \nu_{nn} \end{bmatrix}$$

(u: up, e: east, n: north). The local terms are defined at station i only, although for baselines of relatively short length (less than a few hundred kilometers) $\mathbf{c'}_{ij} \approx \mathbf{c}_{ji}$. In general, GPS errors are natural to the local coordinate system; that is, the local covariance matrix is nearly diagonal.

Up to this point we have considered only formal estimates of measurement uncertainty, which are derived from the GPS solution. However, simple tests of baseline precision such as the day to day measurement repeatability, show that formal uncertainties computed with the Bernese software almost always underestimate real error. A better definition of error is to include a comparison with real observations. The method we impose, albeit somewhat ad-hoc, integrates the structure of the formal covariances with short-term measurement repeatability. The formal covariance matrix is multiplied by a variance factor, which represents how well the estimated uncertainties predict the day to day scatter in the measurements. If the difference between day to day scatter and the formal error estimate is small, then the variance factor will be near unity. However, as is generally the case with GPS data, if the formal uncertainties are smaller than the day to day repeatability the variance factor will be greater than 1.

The variance factor is computed by adjusting a group of independent GPS observations to obtain a weighted average set of coordinates or baseline vectors. Usually, this requires multiple days of repeated measurements. The

variance factor σ_0 is defined by

$$\sigma_0^2 = \frac{\sum_{i=1}^{m}((b_i - c_i)/\sigma_i)^2}{m - n} \tag{2.26}$$

[*Bevington*, 1969; *Snay*, 1986], where m is the number of independent observations, n is the number of adjusted parameters ($m - n$ are the degrees of freedom), b_i and c_i are the observed and adjusted (calculated) values of the ith baseline, and σ_i is the a priori standard error for the ith observation. Normally 3 baseline components are considered for each term.

The method above uses short-term repeatability as the criteria to scale formal measurement uncertainties. However, error sources such as tropospheric refraction, ionospheric conditions, benchmark stability, multipath, and satellite/receiver clock behavior, may be highly correlated from one day to the next. Thus, the long-term measurement variations over several months or years (ignoring tectonic effects) may be somewhat greater than that from a single experiment lasting only a few days. Davis *et al.* [1989] have found that by including long-term repeatability, precision estimates for a 223 km baseline between Palos Verdes and Vandenberg worsened by 20-40 % in the horizontal components. Unfortunately, in this study there are no non-tectonic baselines with short *and* long term redundancies, so no comparisons are made. Therefore, long term error sources are ignored.

References

Beutler, G., W. Gurtner, I. Bauersima, and R. Langley, Modeling and estimating the orbits of GPS satellites, paper presented at First International Symposium on Precise Positioning with the Global Positioning System, Int. Assoc. of Geod., Rockville, Md., April 15-19, 1985.

Bevington, P. R., *Data Reduction and Error Analysis for the Physical Sciences*, McGraw-Hill, 336 pp., 1969.

Blewitt, G., S. C. Larsen, J. M. Davidson, and B. H. Hager, GPS-based measurement of uplift in the Long Valley caldera, *Eos Trans. Abst.*, American Geophysical Union, 1986.

Blewitt, G., Carrier phase ambiguity resolution for the Global Positioning System applied to geodetic baselines up to 2000 km, *J. Geophys. Res.*, *94*, 10,187-10,203, 1989.

Chin, M., CIGNET report, *GPS Bull.*, Global Positioning System Subcomm. of Comm. VIII, Int. Coord. of Space Tech. for Geod. and Geodyn., Natl. Geod. Surv., Rockville, Md., 1988.

Davis, J. L., W. H. Prescott, J. L. Svarc, and K. J. Wendt, Assessment of global positioning system measurements for studies of crustal deformation, *J. Geophys. Res.*, *94*, 13,635-13,650, 1989.

Defense Mapping Agency, Department of Defense World Geodetic System 1984, *DMA TR 8350.2*, 121 pp., D.M.A., Washington, D. C., 1987.

Dong, D. Y. Bock, Global Positioning System network analysis with phase ambiguity resolution applied to crustal deformation studies in California, *J. Geophys. Res.*, *94*, 3949-3966, 1989.

Fliegel, H. F., W. A. Feess, W. C. Layton, and N. W. Rhodus, The GPS radiation force model, paper presented at First International Symposium on Precise Positioning with the Global Positioning System, Int. Assoc. of Geod., Rockville, Md., April 15-19, 1985.

Goldstein, H., *Classical Mechanics*, Addison-Wesley, 672 pp., 1980.

Gurtner, W., G. Beutler, I. Bauersima, and T. Schildknecht, Evaluation of GPS carrier difference observations: The Bernese second generation software package, paper presented at First International Symposium on Precise Positioning with the Global Positioning System, Int. Assoc. of Geod., Rockville, Md., April 15-19, 1985.

Gurtner, W., G. Mader, D. MacArthur, A common exchange format for GPS data, *GPS Bull.*, *2*, 1-11, 1989.

King, R. W., E. G. Masters, C. Rizos, A. Stolz, and J. Collins, *Surveying with GPS*, *Monograph 9*, School of Surveying, The University of New South Wales, Kensington, Australia, 128 pp. 1985.

Lichten, S. M., and J. S. Border, Strategies for high-precision Global Positioning Systems orbit determination, *J. Geophys. Res.*, *92*, 12,751-12,762, 1987.

Prescott, W. H., J. L. Davis, J. L. Svarc, Global Positioning System

measurements for crustal deformation: Precision and accuracy, *Science*, *244*, 1337-1340, 1989.

Remondi, B. W., and B. Hofmann-Wellenhof, GPS broadcast orbits versus precise orbits: A comparison study, *GPS Bull.*, *2*, 8-20, 1989.

Rocken, C., The global position system: A new tool for tectonic studies; Ph.D. Thesis, University of Colorado, Boulder, 365 pp., 1988.

Saastamoinen, J., Contributions to the theory of atmospheric refraction, *Bull. Geodes.*, *107*, 13-34, 1973.

Snay, R. A., Horizontal deformation in New York and Connecticut: Examining contradictory results from the geodetic evidence, *J. Geophys. Res.*, *91*, 12,695-12,702, 1986.

Stacey, F. D., *Physics of the Earth*, John Wiley and Sons, 414 pp., 1977.

Wells, D., N. Beck, D. Delikaraoglou, A. Kleusberg, E. J. Tranquilla, and P. Vanicek, *Guide to GPS Positioning*, Canadian GPS Associates, Fredericton, N. B., Canada, 1987.

Chapter 3

Strain Accumulation in the Santa Barbara Channel: 1970-1988

Abstract

Geodetic observations between 1970 and 1988 indicate appreciable strain accumulation in the Santa Barbara channel, California. Eleven baseline strains from a 6-station geodetic network spanning the eastern two-thirds of the channel were determined from EDM measurements in 1970/1971 and GPS observations in 1987/1988. The eastern channel is modeled as near uniaxial convergence of 6.4 mm/yr oriented N25 °E. The strain field is consistent with seismicity, dominated by thrust mechanisms with P-axes directed to the northeast. Central channel strain is more poorly resolved, but appears to include a significant component of left-lateral shear. The discrepancy vector calculated between the North American-Pacific relative motion (NUVEL-1), and the observed deformation from slip along the San Andreas fault and extension within the Basin and Range, is 8 mm/yr oriented N18 °E. In light of the geodetic measurements, it appears that some or all of this missing plate motion may be occurring across the channel. These observations illustrate the importance of GPS for monitoring crustal motions. The day to day repeatabilities for 50 km baselines (typical for local geophysical studies), are found to be 0.5 cm in the length component and 3.8 cm in the vertical. GPS baselines (31-122 km) obtained with the broadcast ephemeris agree with orbit-improved solutions to 1.6 cm in the length and 2.4 cm in the vertical.

3.1 Introduction

The Santa Barbara channel is located in the southwesternmost part of the Transverse Range structure between the California coast and the islands of Santa Cruz, Santa Rosa, and San Miguel (Figure 3.1). Much of the interest of the Transverse Ranges lies in their departure from the structural style of the rest of the tectonically active region of the Pacific-North American plate boundary; rather than exhibiting northwest-southeast right-lateral strike-slip, the dominant style in the Transverse Ranges is one of east-west folds and thrust faults. Most of the deformation has developed over geologic time. However, the 1971 San Fernando and 1987 Whittier Narrows earthquakes show that such deformation is presently taking place.

Here we present measurements of strain accumulation in the eastern two-thirds of the Santa Barbara channel between 1970 and 1988. These observations were obtained by combining 3-dimensional GPS positioning and precise distance measurements from an earlier EDM survey. We evaluate the magnitude and orientation of the convergence rate across the channel, as well as non-uniformity in the strain field. The measured deformation is related to the potential for large earthquakes in this region, as well as the discrepancy between the North American and Pacific relative plate motions predicted from global models (NUVEL-1) [*DeMets et al.*, 1987; *DeMets et al.*, 1990], and the observed deformation from slip along the San Andreas fault and extension within the Basin and Range. Termed the San Andreas discrepancy (Figure 3.1a), it has been postulated that this missing motion may be accommodated by slip along faults offshore of California [e.g., *Minster and Jordan*, 1978, *Minster and Jordan*, 1984]. The discrepancy vector near Santa Barbara is

Figure 3.1a: Map of California. The Transverse Ranges extend from the San Andreas fault westward to the California coast near Santa Barbara. The San Andreas discrepancy is the difference between plate motion predicted from global plate models (NUVEL-1), and the observed deformation from slip along the San Andreas fault and extension within the Basin and Range (B+R). The discrepancy vector near the channel is about 8 mm/yr oriented east of north. Some or all of this missing motion may be accommodated by nearly north-south convergence across the channel.

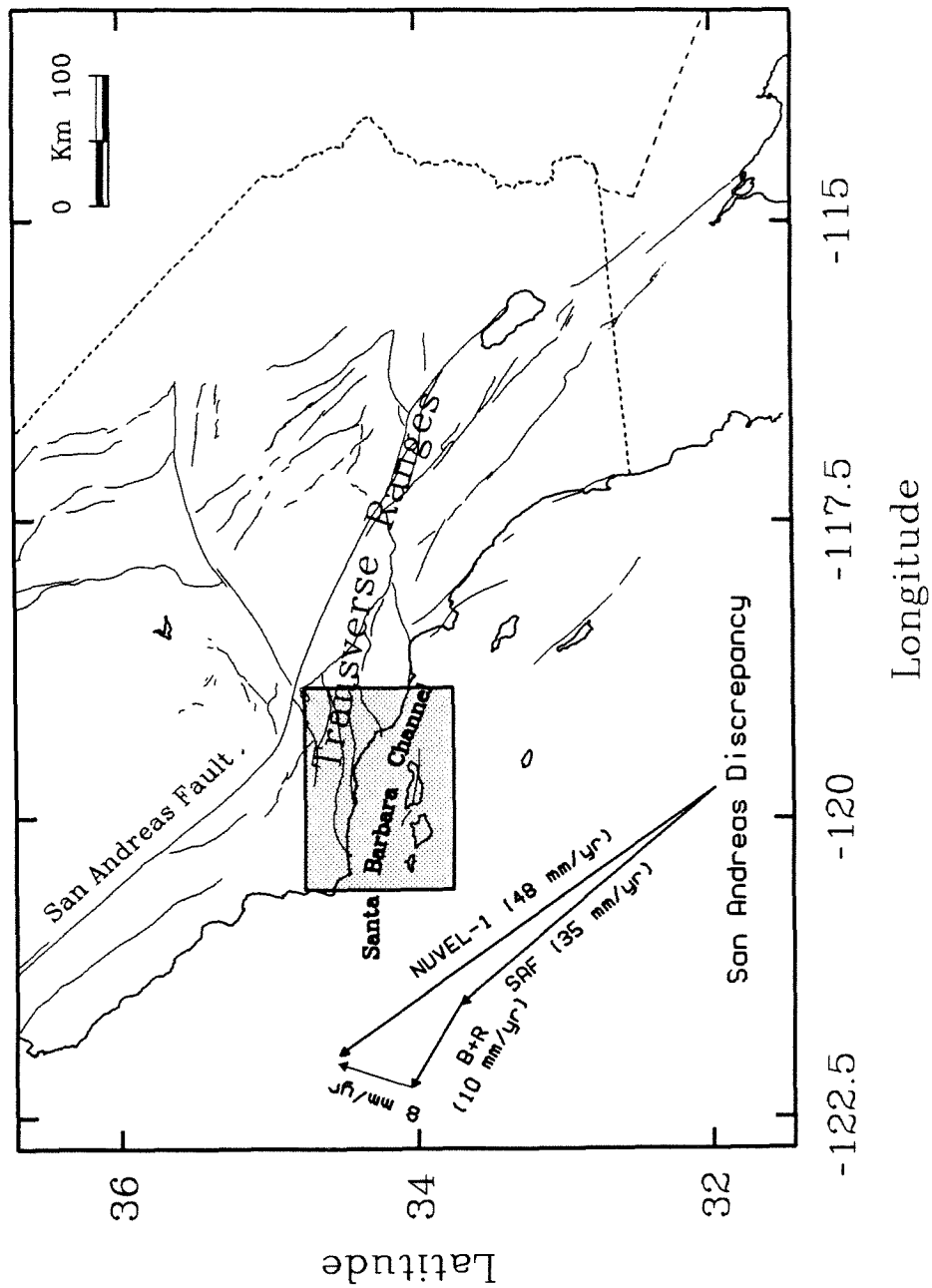
0 Km 100
Transverse Ranges
San Andreas Fault
Santa Barbara Channel
NUVEL-1 (48 mm/yr)
B+R (10 mm/yr)
SAF (35 mm/yr)
8 mm/yr
San Andreas Discrepancy
36
34
32
-122.5
-120
-117.5
-115
Latitude
Longitude

Figure 3.1b: Map of the Santa Barbara channel. The Santa Barbara channel is dominated by east-west trending faults (dark lines) and folds (light lines), indicative of convergence in the western Transverse Ranges. Geodetic measurements (reported here) have taken place on the mainland, and also on the islands of Santa Cruz and Santa Rosa.

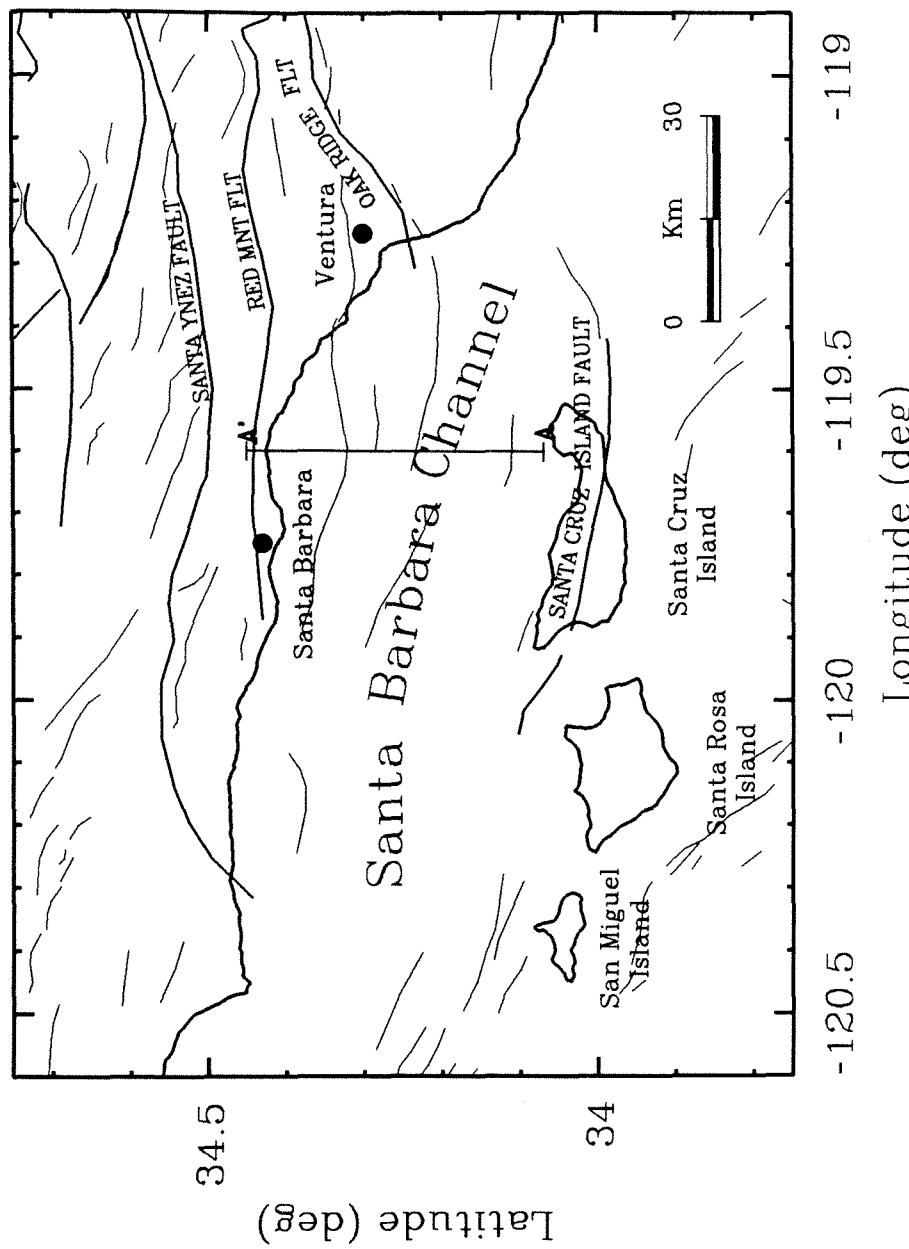
Santa Barbara Channel
SANTA YNEZ FAULT
RED MNT FLT
Ventura RIDGE FLT
OAK
A
A'
Santa Barbara
SANTA CRUZ ISLAND FAULT
Santa Cruz Island
Santa Rosa Island
San Miguel Island
0 Km 30
34.5
34
-120.5
-120
-119.5
-119
Latitude (deg)
Longitude (deg)

about 8 mm/yr oriented N18°E, and could be satisfied by northeast directed convergence across the channel. In addition, we present statistical results regarding the ability of GPS to accurately monitor tectonic motions.

3.2 Tectonic Setting

While there has been considerable controversy over the nature of deformation in the central part of the Transverse Ranges [*Bird and Rosenstock*, 1984; *Weldon and Humphreys*, 1986], there seems to be general agreement that the western Transverse Ranges are dominated by north-south compression. Both within the Santa Barbara channel and along the coast to the north, the dominant geological structures are east-west striking folds and faults (Figure 3.1b). The Santa Barbara channel is an expression of this, being the submarine part of the Ventura basin; detailed geological studies of the basin just to the east have shown very high rates of motion [*Yeats*, 1983; *Yeats*, 1988].

Yeats [1981, 1983] interpreted total horizontal convergence along three profiles in the Ventura basin. The westernmost of these was in the Santa Barbara channel (line A-A' in Figure 3.1b) and showed 1800 m of convergence in the last 1 myr. Over this same time the onshore part of the Ventura basin (at the Ventura Avenue anticline) showed 5500 m of displacement, of which 4600 m occurred in the last 0.2 myr. If we assume that the rates in the Santa Barbara channel are simply proportional to those at Ventura Avenue, the predicted rate of north-south convergence in the channel would be 7.5 mm/yr over the last 0.2 myr.

Figure 3.2 shows coastal southern California seismic activity between 1932 and 1990 (Caltech Catalog). Notable events include the Long Beach earthquake of 1933 (M_L 6.3), Kern County earthquake of 1952 (M_L 7.6), and the San Fernando earthquake of 1971 (M_L 6.6). The eastern channel appears as a region of anomalously high activity. Shown in Figure 3.3 and listed in Table 3.1 are large historic earthquakes over the past two centuries [*Yerkes*, 1985], as well as background seismicity between 1932 and 1990. Although the location and size for the pre-1932 events are not well constrained, it is clear that this region is capable of producing large earthquakes. In fact, there is evidence for an earthquake generated tsunami in the channel due to the 1927 event [*Richter*, 1958; *McCulloch*, 1985]. *Wesson et al.* [1974] and *Ziony and Yerkes* [1985] suggest a reasonable maximum magnitude of about M_L 7.5 for the Santa Barbara channel and surrounding areas, while *Patterson* [1978] attributes 3-4 meter geomorphic offsets on Santa Cruz Island to displacements from single events.

Additional evidence for contemporary north-south compression is provided by focal mechanism studies of small earthquakes. Shown in Figure 3.4 are lower hemisphere, equal area first motion projections, for earthquakes between 1970 and 1978 near the Santa Barbara channel (compressional quadrant shaded) [*Lee et al.*, 1979; *Yerkes et al.*, 1980; *Yerkes and Lee*, 1988]. Most of these events occurred in the eastern channel (east of Santa Barbara) with the majority displaying thrust mechanisms and a northeast trending P-axes, although some show a small component of left-lateral motion. Extensive study of the 1978 Santa Barbara earthquake [*Corbett*, 1982] suggests it occurred on a shallow, north-dipping thrust fault, indicative of active

Figure 3.2: Seismicity between 1932 and 1990 in coastal southern California. Earthquakes are taken from the Caltech Catalog. The Santa Barbara channel is a zone of relatively high seismicity. The region outlined by the solid box is shown in detail in Figure 3.3, which includes historic earthquakes from 1800. Focal mechanisms (1970 to 1978) located in the dashed region are shown in Figure 3.4.

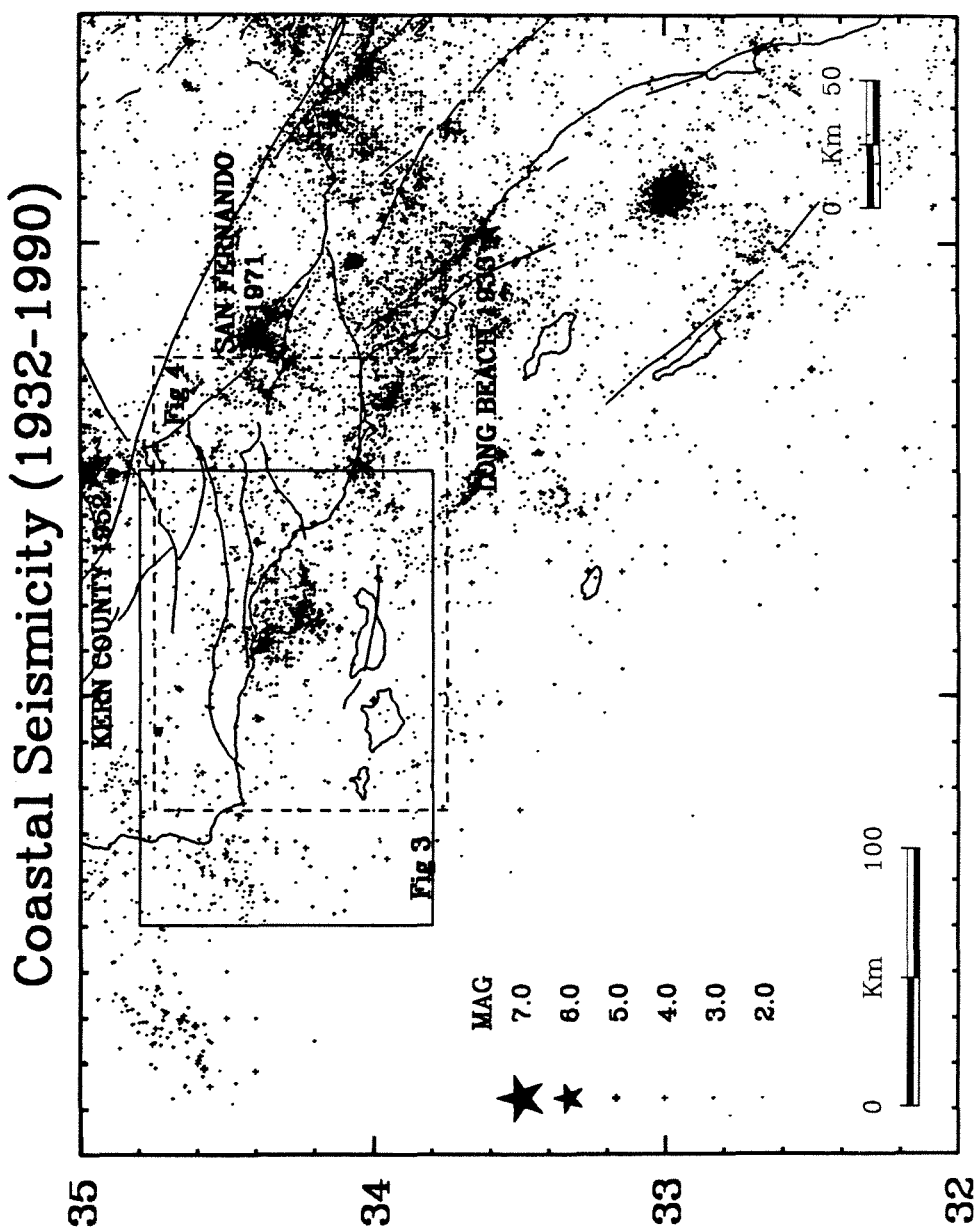
Coastal Seismicity (1932-1990)
KERN COUNTY 1952
SAN FERNANDO 1971
LONG BEACH 1933
Fig 4
Fig 3
MAG
7.0
6.0
5.0
4.0
3.0
2.0
0 Km 100
0 Km 50
35
34
33
32
-122
-120
-118

Figure 3.3: Seismicity between 1932 and 1990 (Caltech Catalog) as well as large historic events between 1800 and 1980 as given by *Yerkes* [1985]. The location and size of the 1812 event is very uncertain. Note the dominance of seismicity in the eastern section of the channel.

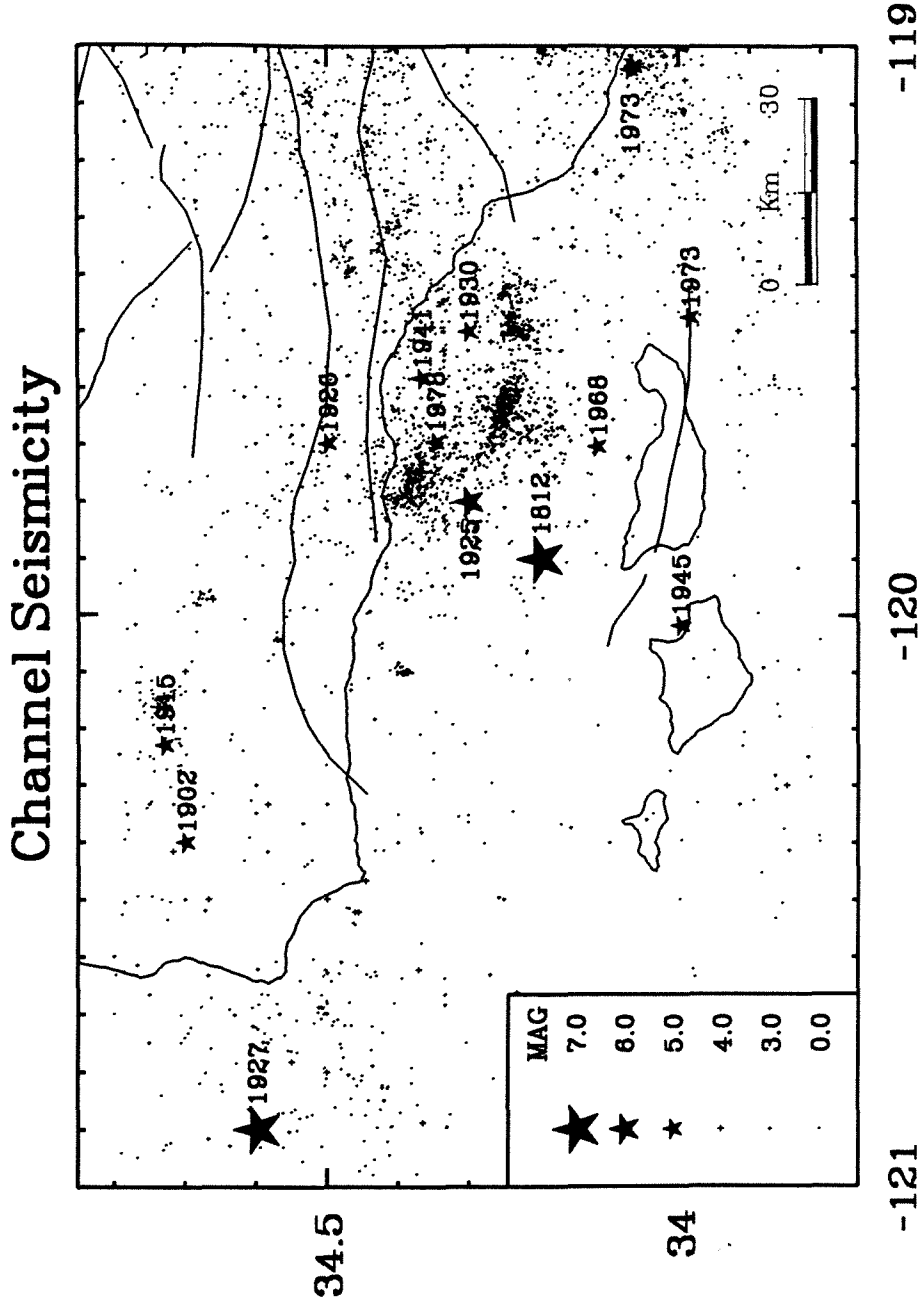
Channel Seismicity
34.5
34
-121
-120
-119
1927
1902
1916
1926
1930
1941
1978
1925
1812
1968
1945
1973
1973
MAG
7.0
6.0
5.0
4.0
3.0
0.0
0
30
km

Figure 3.4: Focal mechanisms (lower hemisphere, equal area projections) for earthquakes between 1970 and 1978 [*Lee et al.*, 1978; *Yerkes et al.*, 1980; and *Yerkes and Lee*, 1988]. Compressional quadrants are shaded. The majority of events are thrust mechanisms, with compressional P-axes oriented north to north-east.

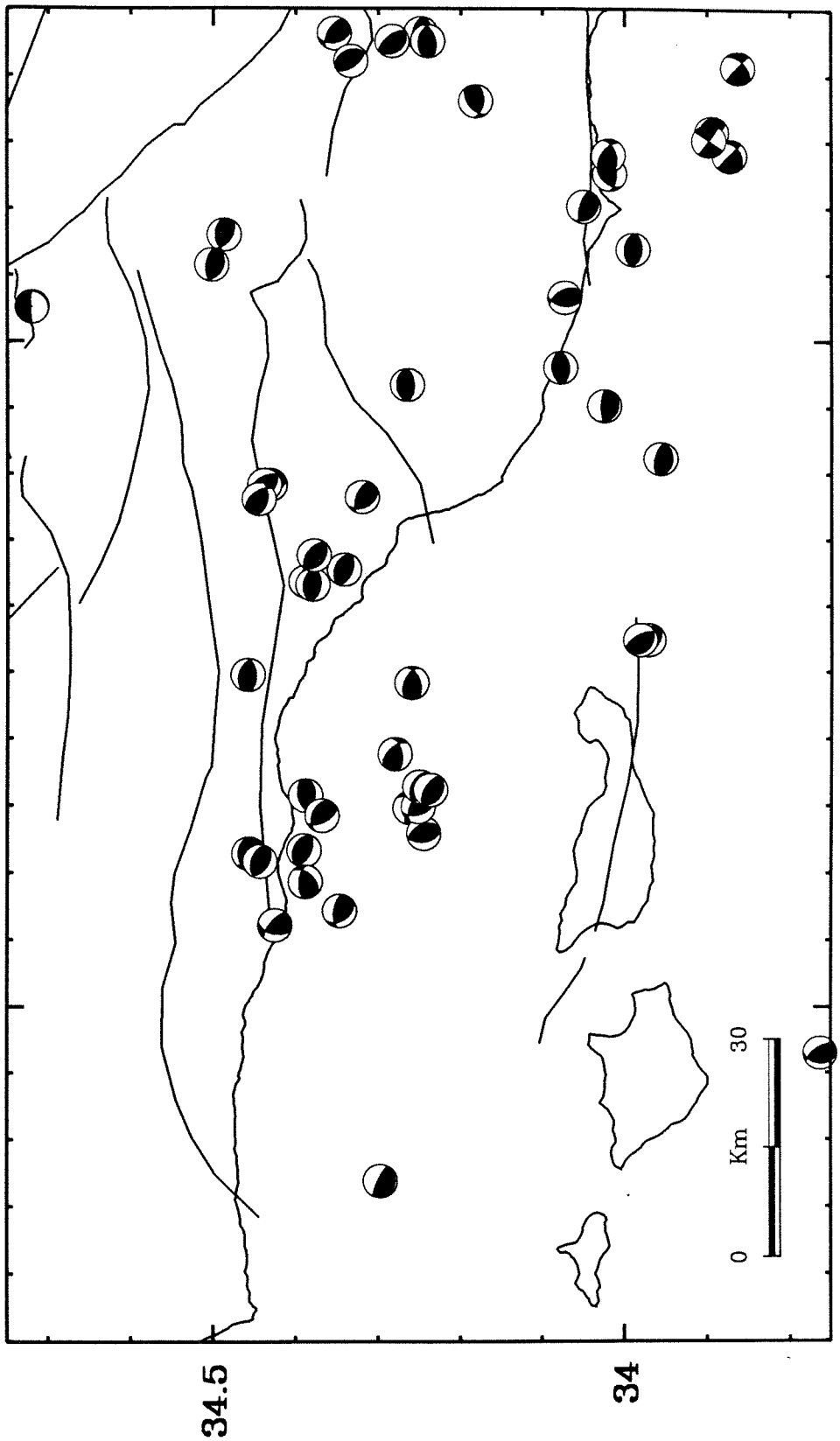
34.5
34
-120
-119
0
Km
30

Table 3.1 Santa Barbara Channel Historic Earthquakes (1800–1980)[1]

Year	Month	Day	Lat (°N)	Long (°E)	Mag	Fault
1812	12	21	34.2[2]	-119.9[2]	7.1[2]	Santa Barbara channel[2]
1893	4	4	34.3	-118.7	5.5	Santa Susana(?), Simi(?)
1902	7	28	34.7	-120.4	5.4	Los Alamos
1912	12	14	34	-119	5	Offshore(?)
1915	1	12	34.73	-120.23	5.8	Los Alamos
1925	6	29	34.3	-119.8	6.8	Santa Barbara channel
1926	6	29	34.5	-119.7	5.5	Santa Ynez(?)
1927	11	4	34.6	-120.9	7.3	Offshore Point Arguello
1930	8	5	34.3	-119.5	5	Santa Barbara channel
1930	31	31	33.95	-118.68	5.2	Anacapa
1941	7	1	34.37	-119.58	6.0	Santa Barbara channel
1971	3	31	34.29	-118.52	5.1	San Fernando
1973	2	21	34.07	-119.04	5.3	Anacapa
1978	8	13	34.40	-119.68	5.6	Santa Barbara channel

[1] *Yerkes* [1985]
[2] Earthquake parameters for the 1812 event are *very* approximate

compression in the western Transverse Ranges. Northeast directed convergence is also suggested by the seismic strain calculated from $M_L \geq 3.0$ earthquakes between 1981 and 1988 in a region of the western Transverse Ranges which includes the Santa Barbara channel [Huang *et al.*, 1990]. Although the estimated strain rate is relatively small (0.5 mm/yr), presumably this is because no large earthquakes occurred during the 7-year measurement interval.

Whereas the structural style of the Santa Barbara channel is dominated by north-south compression, there is good evidence for other types of deformation. Most notably, the Santa Cruz Island fault (running just south of the network discussed here) shows clear geomorphic evidence of left-lateral strike slip [*Patterson*, 1978]. This strongly suggests that such motion has taken place relatively recently, and could well be present in the region of our measurements.

3.3 Data Collection

In this section we describe the two sets of observations on which we base our determination of strain rates; one using EDM measurements (Electronic Distance Measurement) and the other from GPS campaigns (Global Position System). These measurements were taken over a 6 station, 11 baseline network in the eastern and central portions of the Santa Barbara channel. We refer to this as the Santa Barbara Channel Geodetic Network (SBCGN). Figure 3.5 shows the SBCGN, as well as station occupation history for each of the geodetic surveys. Additional sites in California and North America were occupied as part of the GPS campaigns (Figure 3.6). Table 3.2 lists SBCGN

Figure 3.5: Map of EDM and GPS station occupations for those sites near the Santa Barbara channel. Solid lines indicate baselines which form the SBCGN; dash lines indicate other baselines. a) 1970/1971 EDM network, b) January, 1987 GPS network, c) October, 1987 GPS network, d) May, 1988 GPS network.

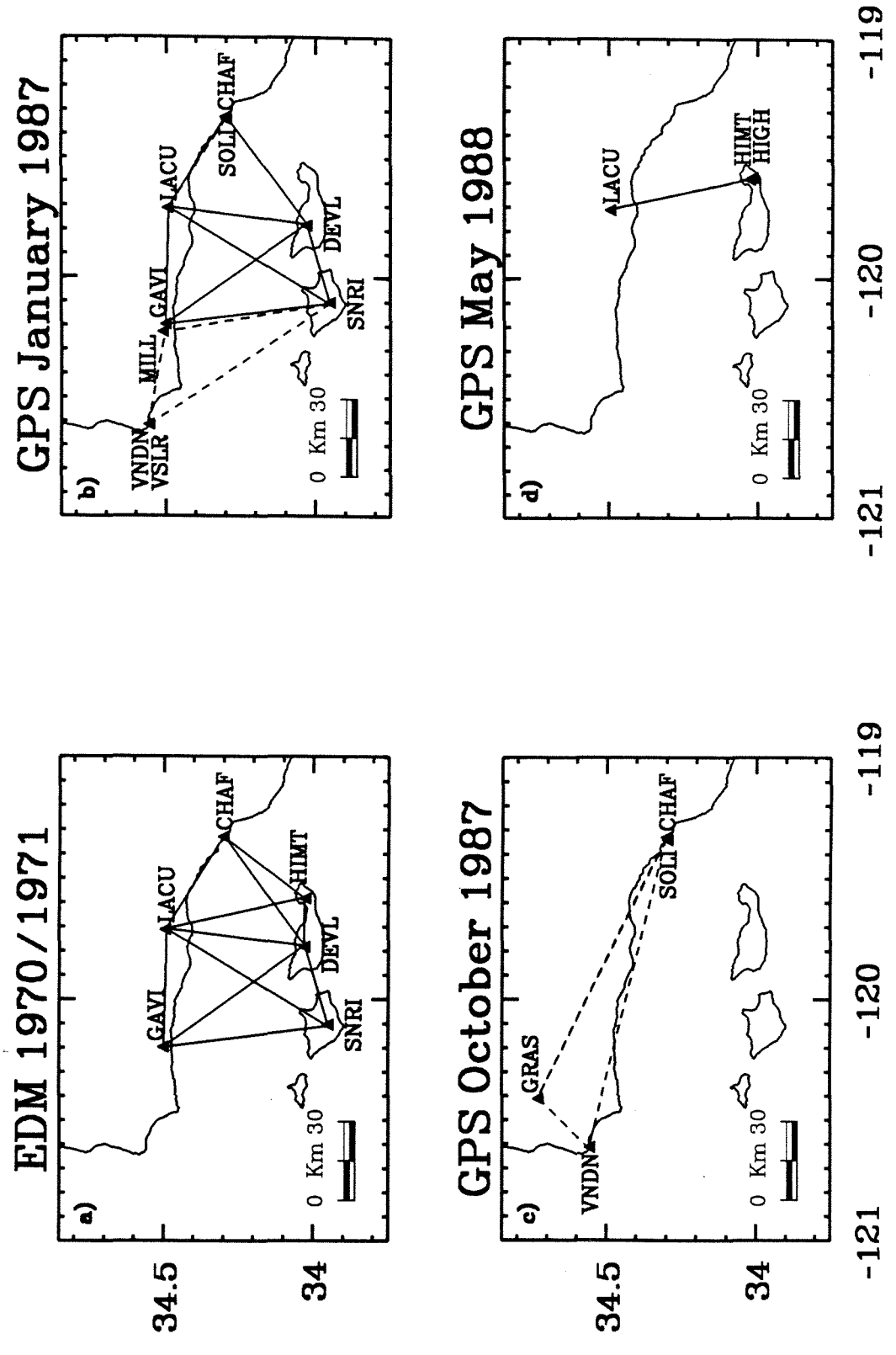
EDM 1970/1971
a)
GAVI
LACU
CHAF
HIMT
DEVL
SNRI
0 Km 30
GPS January 1987
b)
VNDN
VSLR
MILL
GAVI
LACU
SOLI
CHAF
DEVL
SNRI
0 Km 30
GPS October 1987
c)
GRAS
VNDN
SOLI
CHAF
0 Km 30
GPS May 1988
d)
LACU
HIMT
HIGH
0 Km 30
34.5
34
-121
-120
-119
Latitude (deg)
Longitude (deg)

Figure 3.6: Map showing other California and North American GPS stations occupied as part of the January and October, 1987 GPS campaigns.

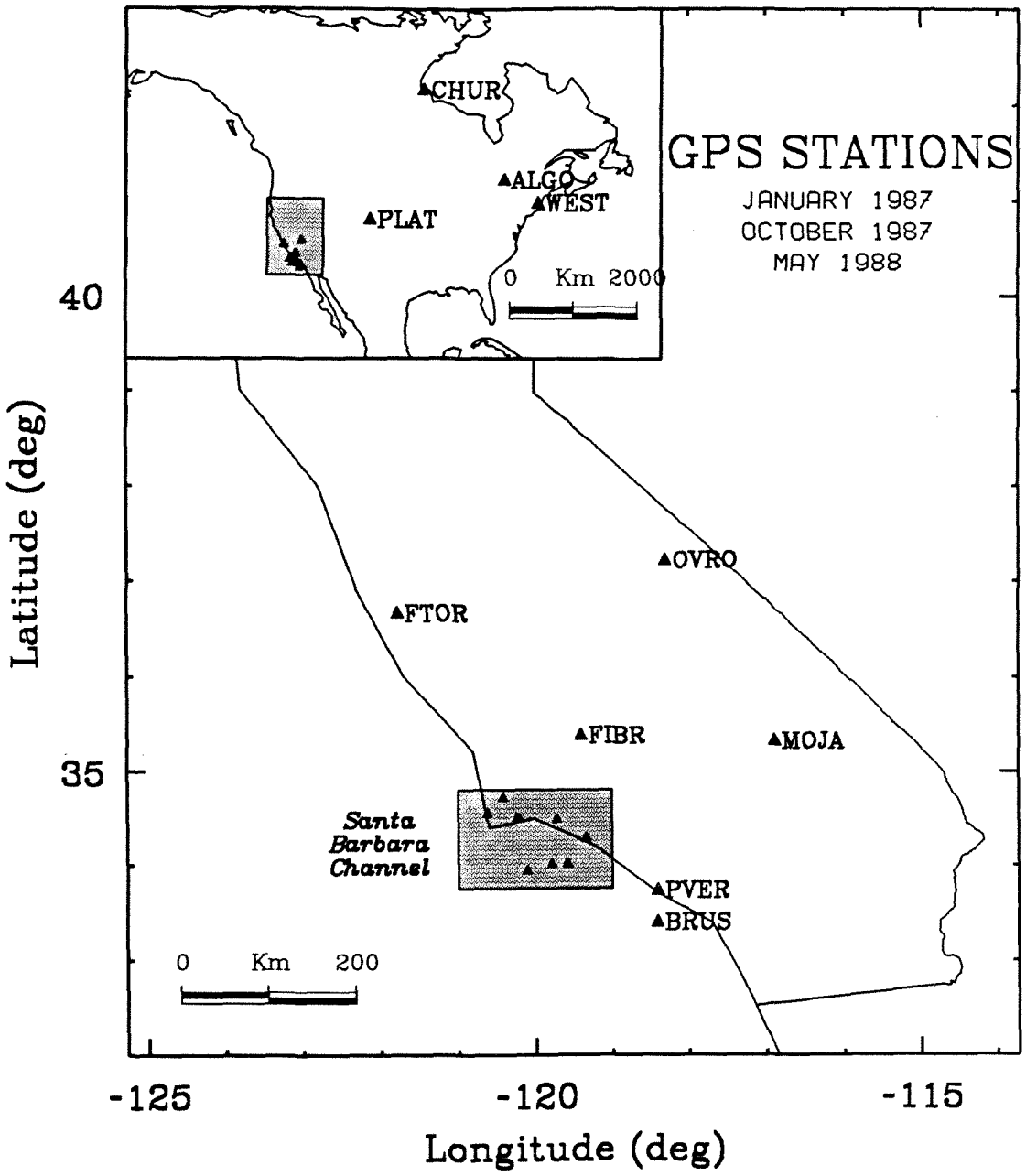
GPS STATIONS
JANUARY 1987
OCTOBER 1987
MAY 1988
CHUR
ALGO
WEST
PLAT
0 Km 2000
OVRO
FTOR
FIBR
MOJA
Santa
Barbara
Channel
PVER
BRUS
0 Km 200
40
35
-125
-120
-115
Latitude (deg)
Longitude (deg)

Table 3.2 SBCGN Survey Stations

Code	Name	Lat (°N)	Long (°E)	Elev (m)
LACU	ONI-172	34.494	-119.713	1197
GAVI	Gaviota 1873	34.502	-120.198	749
SNRI	Soledad 1872	33.951	-120.105	480
DEVL	Devil's Peak	34.029	-119.783	739
HIMT	High Mount	34.026	-119.583	482
CHAF	Chaffee 2	34.301	-119.330	343

station names (as used here, and also the more conventional names used by the NGS) and approximate coordinates. EDM surveys directly measure station to station slope distances, while GPS computes 3-dimensional site coordinates (or intersite coordinate differences), which are converted into slope distances and compared to the EDM observations. The full network was surveyed with EDM in late 1970 and early 1971, while the GPS observations were obtained through two field campaigns in 1987 (January) and 1988 (May). We also present data from a third GPS survey made in 1987 (October). While results from this experiment are not directly tied to our strain analysis, they do give some indication of the reliability of the GPS measurements.

EDM Survey (1970-71)

The initial survey between the monuments listed in Table 3.2 was done by Greenwood and Associates, under contract to the University of California, Santa Barbara. The lines LACU-HIMT, LACU-DEVL, CHAF-HIMT, and CHAF-DEVL were measured in November 1970; the other lines were measured in February 1971 (Figure 3.5a). All line lengths were obtained with a Model 8 Geodimeter; because of the great length of some lines, as many as 42 corner-cube prisms were used as reflectors. Typically, around 6 Geodimeter measurements were made over an interval of about an hour and a half. The instrument constants of this system had been determined to the millimeter level and the frequency was checked to better than 10^{-7}. The largest source of error in EDM measurements is the correction for the refractive index along the light path, which requires knowledge of the air density. To determine this, the pressure was measured at each end of the line using calibrated

Kollsman altimeters; the temperature (and in most cases the humidity) was measured using sensors mounted on the wing of an aircraft that flew along the line of sight during the Geodimeter measurements. (*Savage and Prescott* [1973] describe a similar system.) The aircraft would traverse the line two to four times during the measurement, traveling at a constant airspeed to allow the necessary correction to be applied to the temperature sensors.

GPS Surveys (1987-1988)

The GPS data used in this study were collected during 3 field campaigns in 1987 and 1988 (Figures 3.5b-d and 3.6). The station occupation history is listed in Table 3.3. Texas Instruments TI-4100 GPS receivers supporting GESAR software were used for all observations. Data were collected at 30 second intervals over 6 to 7.5 hour observation sessions, at a time when satellite coverage was optimal. Surface meteorological data (temperature, pressure, and humidity) were recorded at each site. On average, weather measurements were made once an hour, although this interval varied at each location depending on the field operator. Water vapor radiometers (WVR's) were not used.

The first GPS field campaign was made as part of a multi-university project to investigate strain accumulation along the North American-Pacific plate margin, when a network was established in southern California during December, 1986 and January, 1987. From January 3 to January 7, sites near the Santa Barbara channel were occupied to resurvey the earlier EDM monuments. In all, 5 of the 6 geodimeter marks were reoccupied with GPS during this experiment (Figure 3.5b). Stations DEVL, SNRI, and LACU were

Table 3.3 GPS Station Occupation History

	January 1987					October 1987	May 1988		
	3	4	5	6	7	1	18	19	19
LACU	•	•	•	•	•		•	•	•
CHAF	•					•			
GAVI	•	•	•						
DEVL	•	•	•	•	•				
SNRI	•	•	•	•	•				
HIMT							•	•	•
SOLI		•	•	•	•	•			
MILL					•				
HIGH								•	•
VNDN	•	•	•	•	•	•			
VSLR				•					
PVER	•	•	•	•	•				
BRUS	•	•	•	•	•				
OVRO	•	•	•	•	•				
FTOR	•	•	•	•	•				
FIBR	•	•	•	•	•				
GRAS						•			
MOJA						•			
PLAT	•	•	•	•	•				
CHUR	•	•	•	•	•				
ALGO	•	•	•	•	•				
WEST						•			

observed the full 5 days. Due to inclement weather and road conditions, GAVI was occupied 3 days and CHAF 1 day. Stations SOLI and MILL were used as backups for CHAF and GAVI, respectively. Ten additional GPS sites were operational in California and North America (Figure 3.6, Table 3.3).

The satellite tracking summary for January 3 is shown in Figure 3.7a; subsequent days are similar, except that observation times are shifted 4 minutes earlier each day due to satellite regression. A total of 6 satellites were visible during the scheduled 7.5 hour nightly observation session, lasting from 6:58 to 14:28 UTC (10:58 pm to 6:28 am PST). Any particular satellite was in view between 1.5 and 6 hours each tracking interval. Data were collected at most sites the full 7.5 hours each day, although due to equipment or operational difficulties partial data were collected at some sites. Data gaps of greater than 1 hour occurred at GAVI (January 5), VNDN (January 4 and 6), BRUS (January 4), and BRUS (January 7); tracking was stopped and restarted (multiple sessions) at SNRI (January 3 and 6), MILL (January 7), VNDN (January 4 and 6), and FTOR (January 4). In addition, because satellite coverage is not the same at widely separated points on the earth ($\sim$ 1000km), stations outside California (PLAT, ALGO, and CHUR) followed a slightly different data collection format. Satellite tracking was initiated 0.5 to 1.0 hours later than the California sites, although the stop times were the same.

The second field campaign was made on October 1, 1987 with GPS measurements at CHAF, SOLI, VNDN, and GRAS (Figure 3.5c; Table 3.3). Two days of observation were planned but the field equipment was redeployed following the October 1 (M_L 5.9) Whittier-Narrows earthquake. This network

Figure 3.7: Satellite scenarios and station coverage for all GPS sites. Times listed are for the first day of the given campaign. Times for following days are shifted 4 minutes earlier due to satellite regression. Two satellite scenarios were used for the May, 1988 campaign.

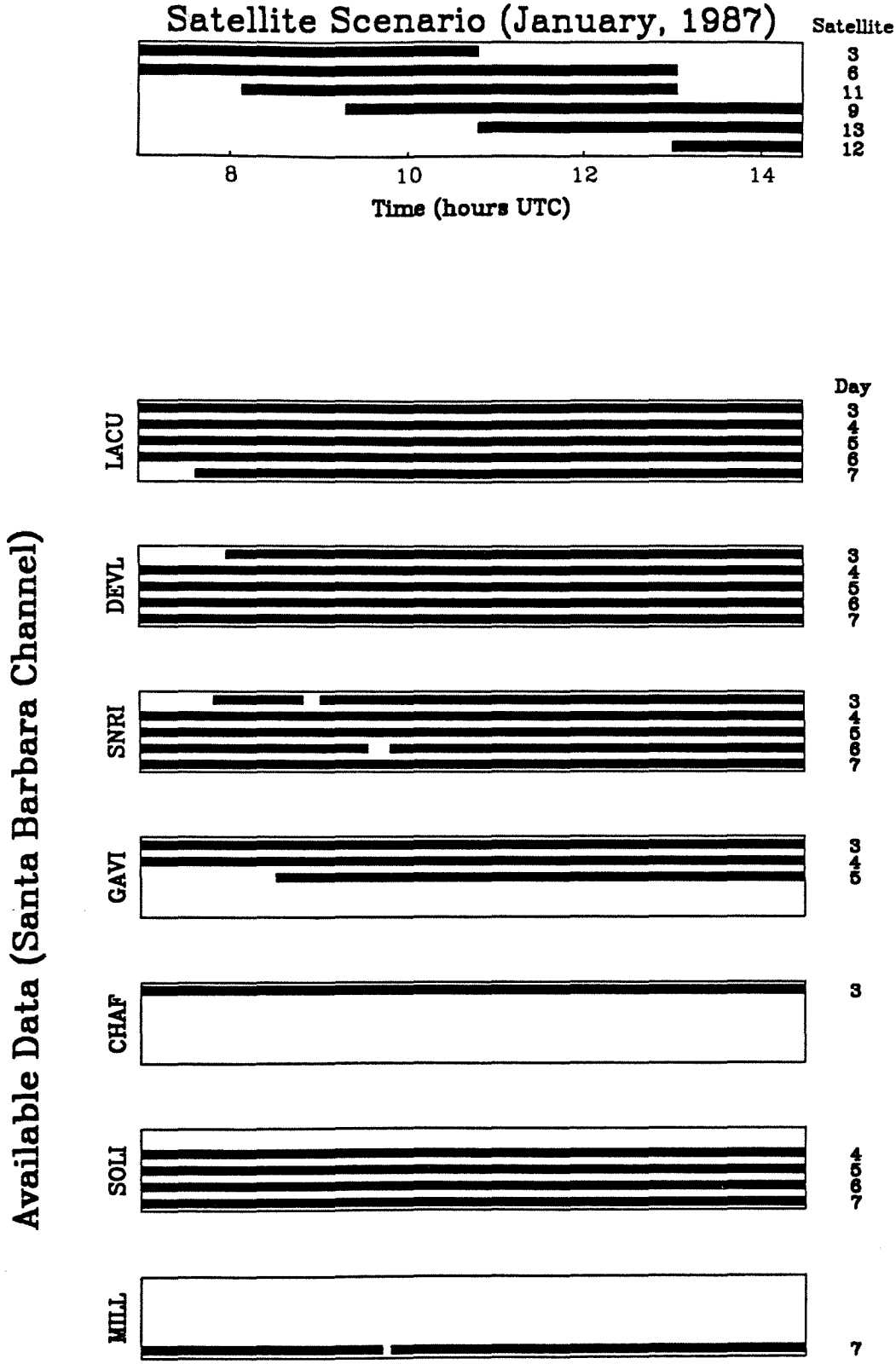
Satellite Scenario (January, 1987)
Satellite
3
6
11
9
13
12
8
10
12
14
Time (hours UTC)
Available Data (Santa Barbara Channel)
Day
LACU
3 4 5 6 7
DEVL
3 4 5 6 7
SNRI
3 4 5 6 7
GAVI
3 4 5
CHAF
3
SOLI
4 5 6 7
MILL
7

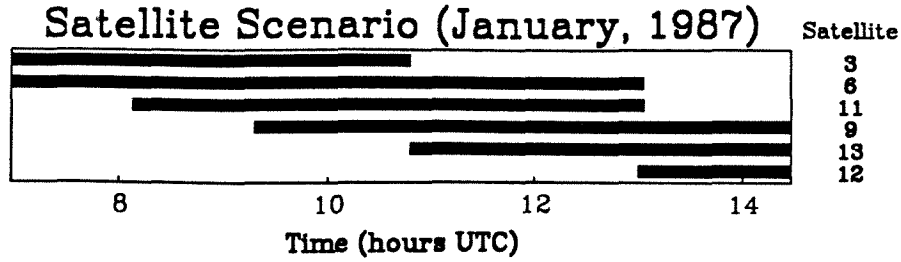
Satellite Scenario (January, 1987)
Satellite
3
6
11
9
13
12
8
10
12
14
Time (hours UTC)

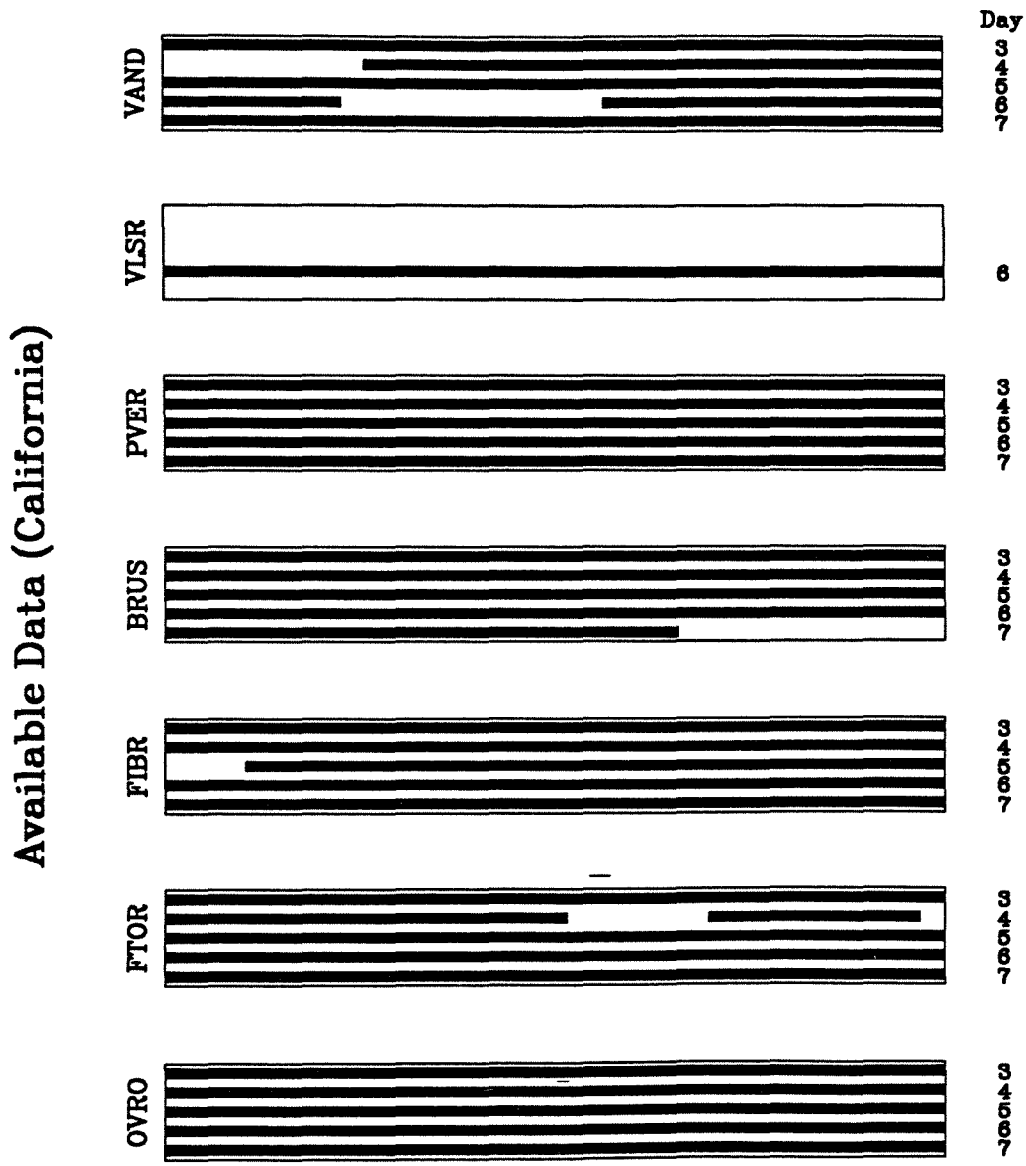
Available Data (California)
Day
VAND
3
4
5
6
7
VLSR
6
PVER
3
4
5
6
7
BRUS
3
4
5
6
7
FIBR
3
4
5
6
7
FTOR
3
4
5
6
7
OVRO
3
4
5
6
7

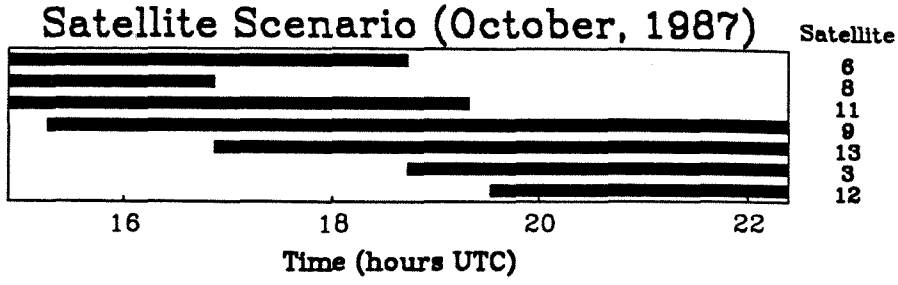
Satellite Scenario (October, 1987)
Satellite
6
8
11
9
13
3
12
16
18
20
22
Time (hours UTC)

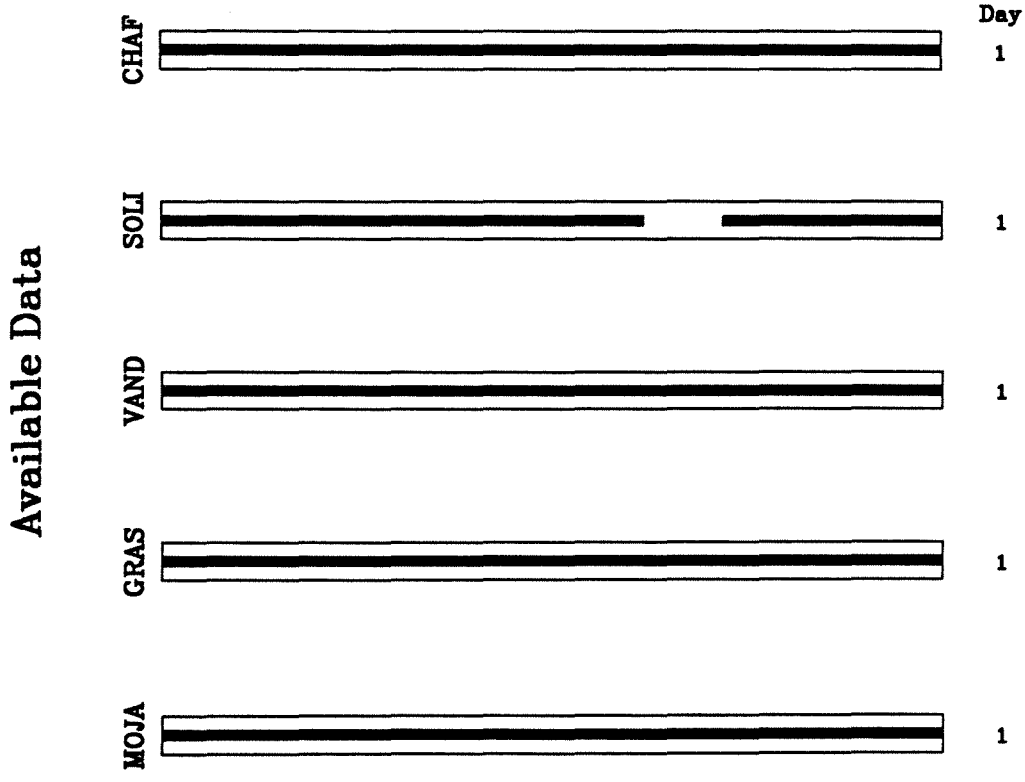
Available Data
Day
CHAF
1
SOLI
1
VAND
1
GRAS
1
MOJA
1

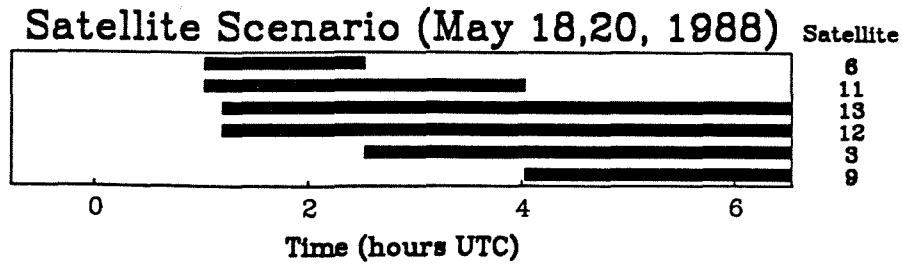
Satellite Scenario (May 18,20, 1988)
Satellite
6
11
13
12
3
9
0
2
4
6
Time (hours UTC)

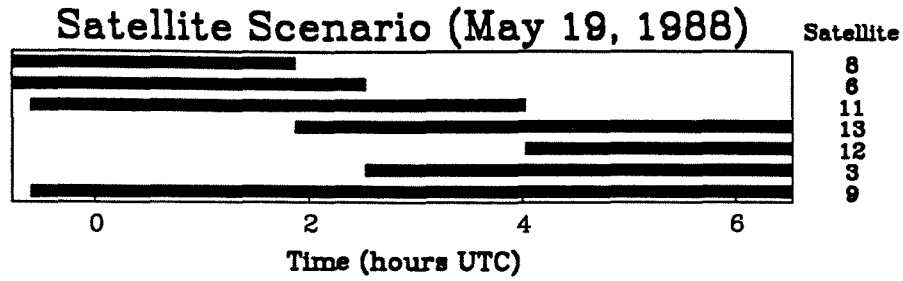
Satellite Scenario (May 19, 1988)
Satellite
8
6
11
13
12
3
9
0
2
4
6
Time (hours UTC)

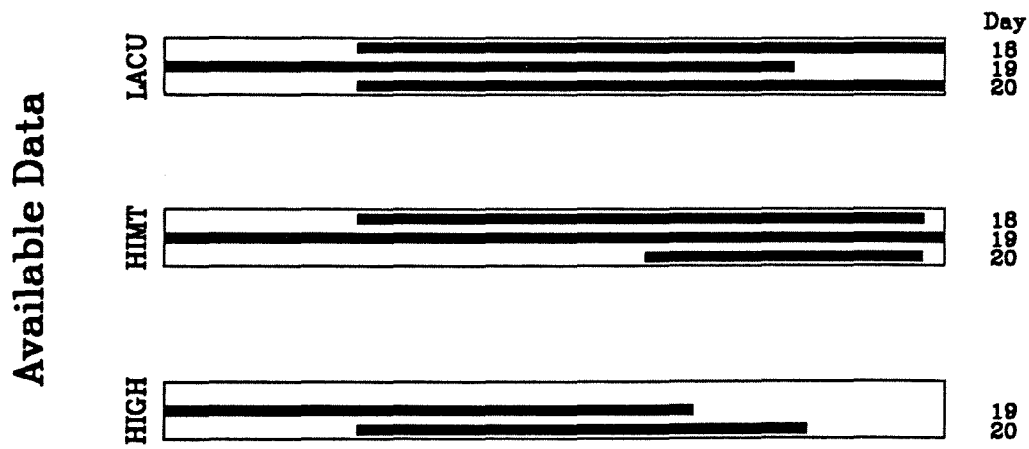
Available Data
LACU
HIMT
HIGH
Day
18
19
20
18
19
20
19
20

was occupied primarily to constrain the 3-dimensional vector between CHAF (one of the 1971 EDM monuments) and SOLI. For logistical reasons, CHAF is a difficult site for geodetic measurements. The ability to reach the mark requires a 4-wheel drive transverse along a dirt road, which is greatly hampered during bad weather (rain). Furthermore, the station is located on private property, requiring access permission from the local landowner. Such allowance previously has been difficult to obtain and future access to the site can not be guaranteed. About 1 km to the west and directly off a major highway, SOLI was selected as a permanent replacement site to CHAF. In fact, SOLI was used 4 days in January, 1987 when CHAF could not be reached because of rain. The 3-dimensional vector measurement between the two stations (station to station tie), will allow the position of SOLI to be referenced to historical geodetic measurements at CHAF.

The satellite tracking summary for October 1, 1987, is shown in Figure 3.7b. Observations lasted 7.5 hours between 14:56 to 22:24 UTC (7:56 am to 3:24 pm PDT), with 7 satellites tracked. CHAF, VNDN, and GRAS recorded data continuously the entire scenario. Due to equipment malfunction, observations at SOLI were broken into two sessions, one 4.5 hours and the other 2.1 hours in length.

Independent GPS measurements were made on October 1, 1987, at MOJA and WEST as provided by the Cooperative International GPS Network (CIGNET) [*Chin*, 1988] (Figure 3.6; Table 3.3). Observations from the CIGNET sites are used to improve satellite orbits in the data processing (see below).

The resurvey of the 1970/1971 EDM network was completed during the third GPS campaign when LACU, HIMT, and HIGH were occupied for 3 days in May, 1988 (Figure 3.5d; Table 3.3). In addition to directly measuring the LACU-HIMT baseline, these observations are integrated with the 1987 (January) GPS survey to compute the DEVL-HIMT and CHAF-HIMT baseline vectors.

The satellite tracking and data collection summaries for this final field experiment are shown in Figure 3.7c. Observations for the first day lasted 5.5 hours from 1:02 to 6:32 UTC (6:02 pm to 11:32 pm PDT), with 6 satellites tracked. The short experiment interval was necessary to accommodate the transfer of equipment onto Santa Cruz island. The TI-4100 receiver requires a 24-volt power source, which in the field is often satisfied by two 12-volt car batteries connected in series. Batteries not fully charged or those not capable of retaining a charge will not last the full experiment. Because of power problems at HIGH on the first day (May 18), no data were collected (Figure 3.7c). A scenario lasting 7.3 hours, tracking 7 satellites, was used for the second day. However, the scheduled observations from 23:10 to 6:28 UTC (4:10 pm to 11:28 pm PDT) were cut short at LUCU (5:03 UTC) and HIGH (4:07 UTC) due to power failures to the GPS receivers. The tracking scenario scheduled for the final day was the same as that used on May 18 (shifted 8 minutes earlier). Again, due to power difficulties data collection at HIGH was prematurely stopped (5:06 UTC), while observations at HIMT started late (3:36 UTC).

3.4 Data Reduction

This section (and the Appendix) describe the processing performed to get the length measurements forming the basis of our discussion in Section 3.5. This section can be skipped without loss of continuity.

EDM Data

Though the correction of EDM data for atmospheric refraction has been much examined in the geodetic literature, little of it deals with the case where air temperature is available along the line measured. This is admittedly a topic of decreasing future interest, and so while we have included a complete discussion of our data-reduction procedure, we have relegated it to an Appendix. We focus here on the uncertainties in the data.

The probable errors in other data collected using this system have been discussed by *King et al.* [1987] and by *Slawson and Savage* [1983]. Both discussions have been based entirely on the repeatability of particular line lengths, as found from the scatter about their fit to a model with a linear change in length with time. Both studies expressed the error in the form $\sigma^2 = a^2 + b^2L^2$, where σ is the distance error of a line of length L. Slawson and Savage found a to be 6 mm and b to be $5\text{x}10^{-7}$; King *et al.* found a and b to be 6 mm and $7.4\text{x}10^{-7}$, respectively. The fixed error a is comparable to that expected for the Model 8 Geodimeter. The proportional error is usually dominated by errors in the refractivity corrections; the largest errors in these come from errors in the endpoint pressures and along-line temperatures.

Because of the method we have used to reduce the data (described in the Appendix), we have an internal check on part of this: we can use the reduction process to see how closely the pressure at one end of the line agrees

with that computed from that measured at the other end, assuming a hydrostatic atmosphere. The departures observed translate into line-length changes equivalent to strains of 2×10^{-7} or less (3.7×10^{-7} for one line). This is of course a lower bound, since other errors (notably the measurement of air temperature) will also contribute. An error of only 0.1 ° C in the measured air temperatures translates into 10^{-7} in line length. We believe that the error estimate of *Slawson and Savage* [1983] is consistent with our internal estimate of error, and have therefore used it to assign errors to the EDM survey.

We are somewhat suspicious of the measured length for one baseline. During the 1971 survey, a large fraction of the resources were employed to determine the distance between GAVI and DEVL, but unfortunately this was at the expense of the GAVI-SNRI line. In fact, only 3 measurements were made for this baseline. In addition, temperature records along the GAVI-SNRI transect exhibited large scatter. It is necessary for the strain analysis in Section 3.5 to consider the possibility that the observed length for this line is in error.

GPS Data Processing

All Global Positioning System data (Figures 3.5 and 3.6; Table 3.3) are processed with the Bernese 3.0 GPS analysis software from the University of Bern, Switzerland [M. Rothacher, unpublished documentation, 1988]. The Bernese GPS analysis package allows 3-dimensional station coordinates to be determined from the integration of carrier phase, pseudo-range, and orbital data [e.g., *Gurtner et al.*, 1985; *Beutler et al.*, 1985; *Rocken*, 1988]. In addition to measuring station coordinates, the double difference estimation

algorithm can solve for adjustments to six Keplerian elements and two radiation pressure coefficients for each satellite, an atmospheric zenith delay parameter at each station, a clock error term at each station, ionospheric model coefficients, and cycle ambiguity terms [e.g., *Rocken*, 1988]. Consecutive (or nearly consecutive) days of observation are either processed individually (day by day) or integrated into one simultaneous solution. The L1, L2, or ionosphere-free L3 phase observable is used. In practice, for all but the shortest baselines (< 10 km), the L3 phase combination gives the most accurate solutions [e.g., *Davis et al.*, 1989]. Auxiliary information such as surface meteorological measurements, polar motion and Earth rotation data, gravity potential coefficients, and a priori site coordinates help constrain the solution. An introduction to GPS and data processing methods is found in *King et al.* [1985] and *Wells et al.* [1987].

Routine GPS data processing with the Bernese software can be grouped into two categories: 1) preprocessing and 2) parameter estimation. The preprocessing phase is sub-divided into several steps: 1) data translation, 2) pseudorange processing, 3) initial orbit generation, 4) single difference formation, and 5) data editing (cycle slip detection and elimination). The specific processing parameters and methods used here are listed in Table 3.4. In general, the techniques employed are similar for each of the three campaigns.

Once the raw-receiver or archived data is translated into the format utilized by the Bernese software, the receiver-satellite clock offsets and initial station coordinates are determined from the pseudorange observations. Clock offsets are modeled as polynomials of selected degree over time. We use 3rd

Table 3.4 Bernese GPS Processing Scheme

	January, 1987	October, 1987	May, 1988
FIELD COLLECTION			
Stations[1]	14/3	5/1	3/0
Days	5	1	3
Hours/Day	7.5	7.5	5.5-7.3
Instruments	TI-4100 (gesar)	TI-4100 (gesar)	TI-4100 (gesar)
Satellites	6	7	6/7
Surface Met	Y	Y	Y
Collection Rate	30	30	30
PROCESSING			
Data Format	FICA	FICA	GESAR/CIGNET
Clock Degree	3	3	3
Trophopheres	Y	Y	Y
Ambiguities	N	N	N
Cut off elevation	20	20	20
Sampling Rate	1	1	1
Parameters	469	93	41
Observations	110458	8909	6626
SOLUTIONS			
Orbits	Solved/Broadcast	Solved	Broadcast
Solution	Multiday/Single day	Single day	Multiday

[1] Total/Continental

order terms for all data and found that changing the degree does not significantly affect the results. Coordinate accuracy with the pseudorange is between 1 to 5 meters. The broadcast ephemeris is used to create standard orbits, which represent solutions to the equations of motion for each satellite computed by numerical integration, and represented by polynomial coefficients. Specific details for orbit modeling with the Bernese software is found in *Beutler et al.* [1985]. Standard orbits are used in the coordinate adjustment, although they are often updated or improved with the solution. Single difference phase observables are formed by differencing the phase measurements between two stations. If n stations are occupied on a given day, then n—1 single difference combinations can define the observation set without redundancy. The general strategy to determine which single difference combinations to use, is to minimize the sum of the baseline lengths between all station pairs. Additional constraints are considered, such as data quality at a given site. The single difference combinations chosen here are listed in Table 3.5. During the January (1987) experiment, LACU was central to the entire Santa Barbara channel network and provided good data each day. Therefore, all combinations for the California stations are made relative to LACU. For the October (1987) campaign, single differences are made relative to CHAF for those stations local to the Santa Barbara channel. Separate combinations are made between fiducial sites used in the parameter estimation (see below). During the May (1988) measurements, because of the shortness of the HIMT-HIGH baseline, the preferred combinations are HIMT to HIGH and HIMT to LACU, as was the case for May 19 (HIGH was not occupied on May 18). On May 20, however, there is only partial overlap in phase observation between HIMT and HIGH (Figure 3.7c) (differencing

Table 3.5 Single Difference Combinations

January 3-7 1987	October 1 1987	May 18 1988	May 19 1988	May 20 1988
LACU - *a*	CHAF - *b*	LACU - HIMT	LACU - HIMT	LACU - HIMT
OVRO - PLAT	VAND - MOJA		HIMT - HIGH	LACU - HIGH
ALGO - PLAT	MOJA - WEST			
ALGO - CHUR				

a All California baselines made relative to LACU
b All Santa Barbara channel baselines made relative to CHAF

requires simultaneous observation). Therefore, phase measurements at HIGH on that day are made relative to LACU. Once the minimum number of single difference combinations are formed, cycle slips are interactively removed from the L1 and L2 phase observables. This has proven to be the most time consuming step of GPS data processing. The Bernese software uses a triple difference algorithm to detect and eliminate cycle slips in the double difference phase observables.

After all single difference station to station phases combinations are free of cycle slips at the double difference level (preprocessing), site coordinates and other parameters are estimated in the GPS solution. In many respects, the solution is similar for each survey with the notable exception regarding the handling of satellite orbits. We briefly discuss the "typical" solution constraints, and specifically how satellite orbits are utilized for each campaign.

Each epoch of the 30 second data collection interval is used as an observable. We do not apply any smoothing or non-unity sampling criteria to data. The ionosphere-free L3 phase combination is used for all observations. A Saasmontonian meteorological zenith delay model, using surface measurements of temperature, pressure, and humidity (usually computed from wet and dry bulb temperature readings), is used to calculate the atmospheric signal delay, which is then adjusted by estimating a tropospheric delay parameter at each station. An a priori sigma of 5 cm is used to constrain the tropospheric adjustment (typical adjustments are less than 10 cm). Data from satellite elevations lower than 20 degrees are not used. Bias fixing and optimization techniques, which have been demonstrated to improve measurement repeatability [*Blewitt*, 1989; *Dong and Bock*, 1989], are not

incorporated. Although ambiguities were resolvable for most baselines shorter than 50 km, only partial success was achieved for the longer lines. Because the channel crossing baselines are relatively short (18 to 70 km), only marginal solution improvement is expected so the ambiguities are left unresolved.

Two methods are imposed to handle satellite orbits. If GPS data are available from at least 3 sites whose coordinates are well determined by other geodetic techniques, the data are included into the solution by holding these "fiducial" sites fixed, and simultaneously adjusting (or improving) the satellite orbits and solving for the coordinates of the other stations as free parameters. For each satellite, six Keplerian elements and two radiation pressure terms are estimated. We experimented with excluding the Y-bias scale term [*Fliegel et al.*, 1985] and found this had negligible influence on the results. The estimated station positions are computed in the reference frame defined by the fiducial coordinates. Data are available from California and continental fiducial sites for both the January and October, 1987 experiments. For the January analysis, we hold OVRO, PLAT, and ALGO fixed to SV-3 coordinates predetermined by VLBI and Laser Ranging [Murray and King, unpublished memo, 1988]. SV-3 coordinates are not significantly different than those of the WGS-84 system. For the October solution, we hold MOJA, WEST, and VNDN fixed (to SV-3 coordinates). Observations at OVRO, PLAT, and ALGO were made as part of the January (1987) experiment, while those from MOJA and WEST were obtained through the CIGNET tracking network.

Data provided by the CIGNET sites during the May, 1988 campaign

contained a significant proportion of "bad observations" as well as large time gaps in the coverage. The data were not sufficient to adequately improve satellite orbits, so the broadcast ephemeris is used in the parameter estimation. In this analysis, LACU is held fixed to coordinates determined previously from the January (1987) experiment.

To evaluate how well solutions obtained with the broadcast ephemeris compare to those utilizing orbital improvement, the January (1987) data are processed separately without estimating satellite orbits. Since the ephemerides broadcast before January 17, 1987 are given in the WGS-72 reference system, the station coordinates estimated from the solution are transformed from WGS-72 to WGS-84 [*Defense Mapping Agency*, 1987]. The transformation of a set of Cartesian coordinates from WGS-72 to WGS-84 is given by

$$\vec{X}_{84} = \Delta\vec{X} + (1 + \Delta s)\mathbf{R}\vec{X}_{72} \tag{3.1}$$

where $\vec{X}_{84}$ are site coordinates in the WGS-84 system (meters), $\vec{X}_{72}$ are site coordinates in the WGS-72 system (meters), and the translation vector $\Delta\vec{X}$ (meters), scale factor Δs, and rotation matrix $\mathbf{R}$, are given by

$$\Delta\vec{X} = \begin{bmatrix} 0 \\ 0 \\ 4.5 \end{bmatrix}$$

$$\Delta s = 2.263 \times 10^{-7},$$

$$\mathbf{R} = \begin{bmatrix} 1 & -r_z & 0 \\ r_z & 1 & 0 \\ 0 & 0 & 1 \end{bmatrix}$$

where $r_z = 2.686 \times 10^{-6}$. LACU is held fixed to coordinates determined by the satellite improved solution (transformed into WGS-72 to be consistent with the broadcast reference system). Comparing solutions obtained with the

broadcast parameters to those with orbit improvement, provides constraint on solution accuracy with the broadcast ephemerides (believed to be about 0.1 to 1.0 ppm). In Section 3.5 we show that Santa Barbara strain rates derived using broadcast orbit solutions are not significantly different than those calculated utilizing orbit improvement techniques.

Two observation sessions are believed to be in error. The vertical baseline component from all stations to FTOR on January 3, 1987 is different by about 0.30 meters from the other 4 days. We assume this to be an error in the antenna height measurement, and do not include this session in the analysis. Due to equipment problems, FTOR on January 4, 1987 was divided into two observation sessions, covering the first 4.5 hours and the final 2.0 hours of the scheduled 7.5 hour tracking session (Figure 3.7a). Incorporating the second session into the processing resulted in high residuals and large deviations in baseline length (several meters); therefore, only the first 4.5 hours of observation are used.

GPS Coordinates

Three Cartesian coordinates $\vec{X}_i = [x_i, y_i, z_i]$ are estimated for each station not held fixed in the GPS solution (for fixed stations $\vec{X}_i$ is equal to the a priori coordinates). The baseline vector from station i to station j is given simply by

$$d\vec{X}_{ij} = \vec{X}_j - \vec{X}_i = \begin{bmatrix} x_j - x_i \\ y_j - y_i \\ z_j - z_i \end{bmatrix} = \begin{bmatrix} dx_{ij} \\ dy_{ij} \\ dz_{ij} \end{bmatrix} \tag{3.2}$$

Station coordinates are often listed as a set of baseline vectors, each made relative to the same reference station. For $n+1$ stations with known

coordinates, there are n independent baseline vectors.

Many times it is convenient to refer to the baselines in a local reference frame. Instead of $d\vec{X}_{ij} = [dx_{ij}, dy_{ij}, dz_{ij}]$, we speak of $d\vec{X}'_{ij} = [de_{ij}, dn_{ij}, dv_{ij}]$ where *de*, *dn*, and *dv*, are the east, north, and vertical baseline components as defined at station *i*. Cartesian vectors are rotated into a local reference frame by

$$d\vec{X}'_{ij} = \mathbf{R}_i d\vec{X}_{ij} \tag{3.3}$$

where

$$\mathbf{R}_i = \begin{bmatrix} -\sin(\theta_{lon}) & \cos(\theta_{lon}) & 0 \\ -\sin(\theta_{lat})\cos(\theta_{lon}) & -\sin(\theta_{lat})\sin(\theta_{lon}) & \cos(\theta_{lat}) \\ \cos(\theta_{lat}) & \cos(\theta_{lat})\sin(\theta_{lon}) & \sin(\theta_{lat}) \end{bmatrix}$$

and θ_{lat} and θ_{lon} are the latitude and longitude of station *i*, respectively. It is stressed that unless stations *i* and *j* are the same, then $d\vec{X}'_{ij} \neq d\vec{X}'_{ji}$.

If a particular baseline $d\vec{X}'_{ij}$ is observed on N consecutive (or nearly consecutive) days, the day to day repeatability (scatter) in the baseline components measured in the local reference frame is determined by

$$\vec{\sigma} = \begin{bmatrix} \sigma_e \\ \sigma_n \\ \sigma_v \end{bmatrix} = \left(\sum_{k=1}^{N} (\Delta\vec{X}'^{\,k}_{ij})/(N-1) \right)^{\frac{1}{2}} \tag{3.4}$$

where the difference between the average ($d\bar{X}_{ij}$) and the kth ($d\vec{X}'^{\,k}_{ij}$) baseline observation is given in a Cartesian frame by

$$\Delta\vec{X}_{ij} = d\vec{X}^{k}_{ij} - d\bar{X}_{ij} \tag{3.5}$$

and in the local frame by

$$\Delta\vec{X}'^{\,k}_{ij} = \mathbf{R}_i \Delta\vec{X}^{k}_{ij} \tag{3.6}$$

where $\mathbf{R}_i$ is given above.

For multiple days of repeated observations, a "best" or weighted average set of coordinates relative to some reference station is obtained through an adjustment of the baseline vectors. If the number of non-redundant baselines observed on the *k*th day of a *N* day experiment is given by $m_k = n_k$, where $n_k + 1$ is the number of stations observed on the *k*th day, then the number of independent baselines *m* observed during the multi-day experiment of $n+1$ stations, is given by

$$m = \sum_{k=1}^{N} m_k$$

Note that dependency requires only that the non-redundancy condition hold each day; baselines can be repeated, if observed on different days. The adjusted solution $d\vec{A}$, where

$$d\vec{A} = \begin{bmatrix} d\vec{X}^a_{(n+1)1} \\ d\vec{X}^a_{(n+1)2} \\ \cdot \\ \cdot \\ d\vec{X}^a_{(n+1)n} \end{bmatrix}$$

are the adjusted baseline vectors relative to station $n+1$ (here assumed to be the reference station) is given by the simple least squares inversion

$$d\vec{A} = \left[\mathbf{A}^T\mathbf{W}^T\mathbf{W}\mathbf{A}\right]^{-1}\mathbf{A}^T\mathbf{W}^T\mathbf{W}d\vec{X}^m \qquad (3.7)$$

where $d\vec{X}^m$ is the data observation array containing the *m* independent baseline vectors, **W** is the inverse of the covariance matrix of baseline uncertainties and correlations ($\mathbf{W} = [\mathrm{cov}]^{-1}$), and $\mathbf{W}^T$ is the transpose of **W**. **A** is the *mxn* model matrix of the geometrical relationship between the observations and the model parameters. If all observations $d\vec{X}^m$ are made relative to station $n+1$, then **A** is given simply by

$$\mathbf{A} = \left[\delta_{ij}\right]$$

where $i = j$ if the ith observation was made between stations $n+1$ and j

An adjustment is useful when determining an optimal coordinate or vector solution for multiple observations of the same baselines, in addition to evaluating measurement repeatability. In practice, if the number of days of consecutive observations is relatively small, all observations and coordinate parameters are evaluated simultaneously to obtain a single multi-day solution. In this case, no adjustment is necessary since only one set of station coordinates is estimated. However, each day of observation can be evaluated independently to examine measurement repeatability.

GPS Error Analysis

In this section we discuss the formal aspects regarding the calculation of GPS baseline errors. In general, we use an integrated approach which combines formal estimates of baseline uncertainty with measurement precision. Unless specifically mentioned, we include both variances and covariances in all analysis. All errors are considered at the one standard deviation level.

With each estimation, the Bernese software creates a covariance matrix listing formal uncertainties for station coordinates in a Cartesian reference frame. The covariance matrix $\mathbf{C}$ can be written

$$\mathbf{C} = \left[c_{ij}\right] \tag{3.8}$$

where

$$\mathbf{c}_{ij} = \begin{bmatrix} \nu_{x_i x_j} & \nu_{y_i x_j} & \nu_{z_i x_j} \\ \nu_{x_i y_j} & \nu_{y_i y_j} & \nu_{z_i y_j} \\ \nu_{x_i z_j} & \nu_{y_i z_j} & \nu_{z_i z_j} \end{bmatrix}$$

If $i = j$, then $\mathbf{c}_{ij}$ are the coordinate covariances of station i, where the diagonal components of $\mathbf{c}_{ij}$ are the variances, or the square of the one sigma errors ($\sigma^2 = \nu$). If $i \neq j$, then $\mathbf{c}_{ij}$ are the interstation covariances. For example, $\nu_{x_i x_j}$ is the covariance in the x coordinate between stations i and j, while the error in the y coordinate of station i is given by σ_y, where $\sigma_y^2 = \nu_{y_i y_i}$.

The baseline error between stations i and j (j minus i) is computed from

$$\hat{\mathbf{c}}_{ij} = \mathbf{G}\hat{\mathbf{C}}\mathbf{G}^T \tag{3.9}$$

where

$$\mathbf{G} = \begin{bmatrix} -1 & 0 & 0 & 1 & 0 & 0 \\ 0 & -1 & 0 & 0 & 1 & 0 \\ 0 & 0 & -1 & 0 & 0 & 1 \end{bmatrix}$$

and

$$\hat{\mathbf{C}} = \begin{bmatrix} \mathbf{c}_{ii} & \mathbf{c}_{ij} \\ \mathbf{c}_{ji} & \mathbf{c}_{jj} \end{bmatrix}$$

The transpose of $\mathbf{G}$ is given by $\mathbf{G}^T$. The off-diagonal terms of $\hat{\mathbf{c}}_{ij}$ are the covariances for the Cartesian baseline components between stations i and j, while the diagonal elements are the variances.

The error in the baseline length L, where $L = (x^2+y^2+z^2)^{1/2}$, is computed from

$$\sigma_L^2 = \nu_x \left(\frac{\partial L}{\partial x}\right)^2 + \nu_y \left(\frac{\partial L}{\partial y}\right)^2 + \nu_z \left(\frac{\partial L}{\partial y}\right)^2 + 2\nu_{xy} \left(\frac{\partial L}{\partial x}\right)\left(\frac{\partial L}{\partial y}\right) + 2\nu_{xz} \left(\frac{\partial L}{\partial x}\right)\left(\frac{\partial L}{\partial z}\right) + 2\nu_{yz} \left(\frac{\partial L}{\partial y}\right)\left(\frac{\partial L}{\partial z}\right) \tag{3.10}$$

or

$$\sigma_L^2 = \frac{\nu_x x^2+\nu_y y^2+\nu_z z^2+2\nu_{xy}xy+2\nu_{xz}xz+2\nu_{yz}yz}{x^2+y^2+z^2}$$

Once the baseline covariance matrix $\hat{\mathbf{c}}_{ij}$ is calculated, the Cartesian coordinates are rotated into a local reference frame. We use a north-east-up system, so that the local covariances are given by

$$\mathbf{c'}_{ij} = \mathbf{R}_i \hat{\mathbf{c}}_{ij} \mathbf{R}_i^{-1} \tag{3.11}$$

[e.g., *Goldstein*, 1980], where

$$\mathbf{R}_i = \begin{bmatrix} \cos(\theta_{lat})\cos(\theta_{lon}) & \cos(\theta_{lat})\sin(\theta_{lon}) & \sin(\theta_{lat}) \\ -\sin(\theta_{lon}) & \cos(\theta_{lon}) & 0 \\ -\sin(\theta_{lat})\cos(\theta_{lon}) & -\sin(\theta_{lat})\sin(\theta_{lon}) & \cos(\theta_{lat}) \end{bmatrix}$$

and θ_{lat} and θ_{lon} are the latitude and longitude at station i, respectively. The local covariances $\mathbf{c'}_{ij}$, where

$$\mathbf{c'}_{ij} = \begin{bmatrix} \nu_{uu} & \nu_{ue} & \nu_{un} \\ \nu_{eu} & \nu_{ee} & \nu_{en} \\ \nu_{nu} & \nu_{ne} & \nu_{nn} \end{bmatrix}$$

(u: up, e: east, n: north), are defined only at station i. However, for baselines of relatively short length (less than a few hundred kilometers) $\mathbf{c'}_{ij} \approx \mathbf{c}_{ji}$. In general, GPS errors are natural to the local coordinate system in that the local covariance matrix is nearly diagonal.

Up to this point, we have considered only formal estimates of measurement uncertainty, which are derived from the GPS solution. However, simple tests of baseline precision, such as the measurement repeatability from one day to the next, show that formal uncertainties computed with the Bernese software almost always underestimate the real error. A better definition of error, is to include a comparison with real observations. The method we impose, albeit somewhat ad-hoc, integrates the

structure of the formal covariances with short-term measurement repeatability. The formal covariance matrix is multiplied by a variance factor, which represents how well the estimated uncertainties predict the day to day scatter in the measurements. If the difference between day to day scatter and the formal error estimate is small, then the variance factor will be near unity. However, as is generally the case with GPS data, if the formal uncertainties are smaller than the day to day repeatability, the variance factor will be greater than 1.

The variance factor is computed by adjusting a group of independent GPS observations, to obtain a weighted average set of coordinates or baseline vectors. Usually, this requires multiple days of repeated measurements. The variance factor σ_0 is defined by

$$\sigma_0^2 = \frac{\sum_{i=1}^{m}((b_i - c_i)/\sigma_i)^2}{m - n} \tag{3.12}$$

[*Bevington*, 1969; *Snay*, 1986], where m is the number of independent observations, n is the number of adjusted parameters ($m - n$ are the degrees of freedom), b_i and c_i are the observed and adjusted (calculated) values of the ith baseline, and σ_i is the a priori standard error for the ith observation. Normally 3 baseline components are considered for each of the above terms.

The method above uses short-term repeatability as the criteria to scale the formal measurement uncertainties. However, error sources such as tropospheric refraction, ionospheric conditions, bench mark stability, multipath, and satellite/receiver clock behavior, may be highly correlated from one day to the next, and the long-term measurement variations over

several months or years (ignoring tectonic effects) may be somewhat greater than that from a single experiment lasting only a few days. *Davis et al.* [1989] have found that by including long-term repeatability, precision estimates for a 223 km baseline between Palos Verdes and Vandenberg worsened by 20-40 % in the horizontal components. Unfortunately, we have no baselines with short *and* long term redundancies, so we can not make any comparisons here. Therefore, we choose to ignore long term error sources.

GPS Solutions

Each day of the January, 1987 experiment is processed independently to examine day to day baseline variation. This variation, or repeatability, is defined as the one sigma standard deviation of the baseline component and is used to constrain measurement precision, which gives an indication as to experimental accuracy. Figure 3.8 shows the day to day repeatability vs. baseline length (improved orbits). Table 3.6 lists the offset and slope of the best fit line through the scatter, weighted by the number of days of observation. For baselines under 100 km (typical of the Santa Barbara channel), the horizontal components generally give repeatabilities between 0 and 10 mm; the correlations in baseline length are 2.2×10^{-8} and 3.0×10^{-8} in the north and east components, respectively. The improved precision for the north-south component is due to the geometrical strength of the satellite orbits mapped to this axis. The vertical repeatability is about 40 mm, and is not significantly correlated with baseline length. It is stressed that the repeatabilities are calculated over a relatively short time period (days). Larger scatter is expected for precision estimates determined over longer intervals [e.g., *Davis et al.*, 1989].

Table 3.6 Baseline Repeatability ($\sigma = \alpha + \beta$ Length)

	α	β	Baseline Error (cm)		
	cm	$1x10^{-8}$	5 km	50 km	500 km
Length	0.5	0.9	0.5	0.5	0.9
North-South	0.2	2.2	0.2	0.3	1.3
East-West	0.6	3.0	0.6	0.7	2.1
Vertical	3.8	-0.9	3.8	3.8	3.4

Figure 3.8: Day to day repeatability vs. baseline length for the January, 1987 experiment. Shown are the day to day RMS scatters for the north, east, vertical, and length components of each baseline. A best-fit line has been drawn through the scatters. Shaded is the region where repeatability is better than 1×10^{-7}.

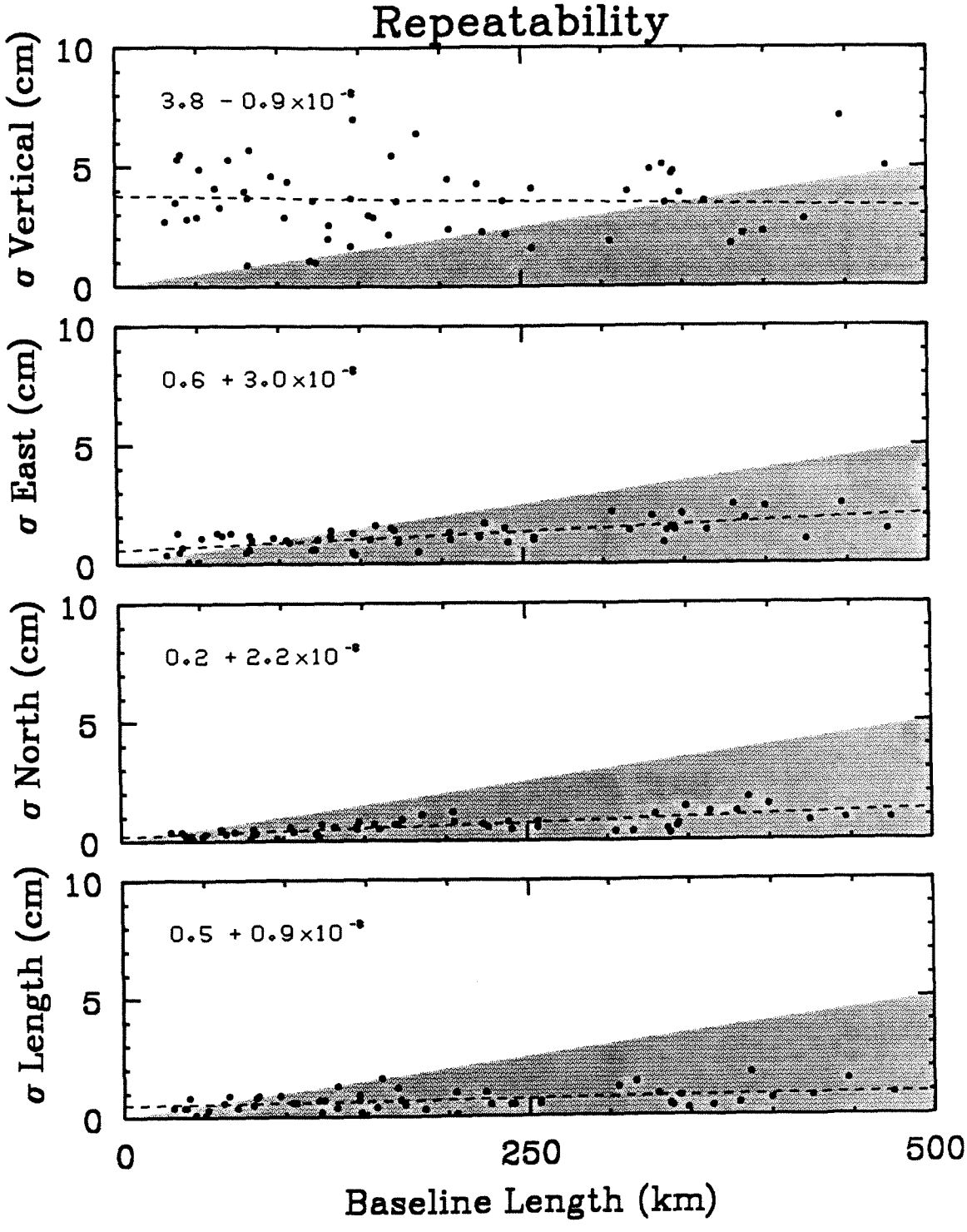
Repeatability
σ Vertical (cm)
3.8 - 0.9×10⁻⁶
σ East (cm)
0.6 + 3.0×10⁻⁶
σ North (cm)
0.2 + 2.2×10⁻⁶
σ Length (cm)
0.5 + 0.9×10⁻⁶
10
5
0
0
250
500
Baseline Length (km)

The daily baseline variation between LACU and the other stations local to the Santa Barbara channel, is shown in Figure 3.9. Plotted is the day to day scatter about the 3-5 day mean for each site. Stations with only one observation to LACU are not included (CHAF, MILL, VSLR). Also shown are the formal error ellipses from the GPS solution when scaled by the variance factor calculated above. The daily scatter agrees well with the (scaled) formal errors, suggesting our approach for estimating baseline uncertainty is sufficient, at least from a short-term repeatability perspective. The much improved precision in the north-south vs. east-west component is indicated by the eccentricity of each ellipse. The interstation correlations are most prominently seen by the SNRI and DEVL scatters. Because of this high degree of correlation, the error in the SNRI to DEVL baseline vector is significantly smaller than the baseline scatter indicates. Since all covariances are included in our error analysis, these correlations are mapped correctly into the baseline uncertainty estimates. In addition, there are up to 5 days of observation for any particular baseline. Thus, baseline error averaged over n days of observation goes as the error in the mean; that is, $\sigma_{\text{mean}} = \sigma_{\text{rms}}/\sqrt{\text{n}-1}$, where σ_{rms} are the scaled formal uncertainties.

We compare how well solutions obtained with the broadcast ephemeris compare to those obtained by applying orbital improvement techniques (holding continental tracking site coordinates fixed). Shown in Figure 3.10 is the difference between the broadcast and improved solutions (broadcast - improved) for the baseline components. The broadcast baselines were obtained by incorporating only those stations local to the Santa Barbara channel into the solution. The error bars give the standard deviation of the

daily broadcast component about its average. No error bars are shown for baselines observed only one day. The day to day scatter in the vertical component is relatively large, although the average daily value agrees fairly well with the improved results. The average differences between the two solution strategies are 1.64 cm in length, 1.19 cm in the north, 2.01 cm in the east, and 2.40 cm in the vertical. There may be a slight systematic difference in the north component between the two solutions, although in general the broadcast components seem to be evenly scattered about the improved solutions. Thus, for relatively short baselines, the use of the broadcast ephemeris does not appear to significantly degrade solution accuracy, at least above the 1 to 2 cm level. This constraint is important because the lack of fiducial coverage during May, 1988, requires the use of the broadcast orbits to determine the length of the 53.3 km LACU-HIMT baseline.

Listed in Table 3.7 are the 3-dimensional baseline components for all SBCGN baselines. All measurements except LACU-HIMT, CHAF-HIMT, and DEVL-HIMT, are obtained through a 5-day simultaneous solution of the January (1987) experiment (with orbit improvement). Formal errors are calculated by multiplying the formal covariance matrix by a variance factor, calculated from the discrepancy between the day to day repeatability and formal uncertainty estimates. The LACU-HIMT baseline length is determined through a 3-day simultaneous solution of the May (1988) data. Because of lacking fiducial coverage, the broadcast ephemeris is used. Errors are estimated from the discrepancy between orbit improved and broadcast solutions from the January experiment (Figure 3.10). Because DEVL and CHAF were not occupied during the May survey, no direct measurements are

Figure 3.9: Day to day scatter in coordinates relative to LACU for those stations local to the Santa Barbara channel during January, 1987. The shaded ellipses indicate formal errors scaled by a variance factor calculated from the day to day repeatability of the measurements. The dashed ellipses indicate the error in the data scatter for each station.

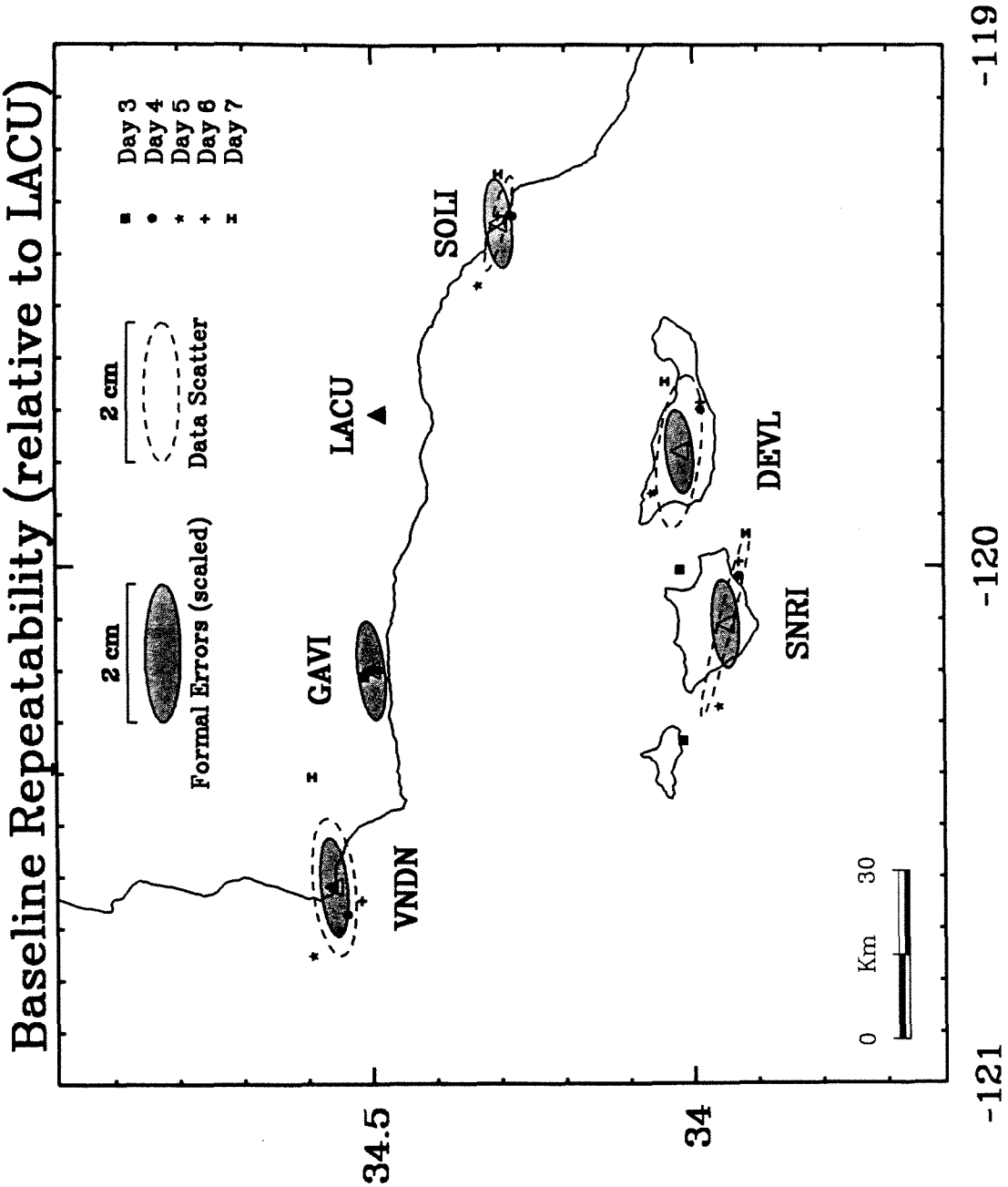
Baseline Repeatability (relative to LACU)
2 cm
Formal Errors (scaled)
2 cm
Data Scatter
Day 3
Day 4
Day 5
Day 6
Day 7
GAVI
LACU
SOLI
VNDN
DEVL
SNRI
0
Km
30
34.5
34
-121
-120
-119

Figure 3.10: Comparison between broadcast and improved orbit solutions for those lines local to the Santa Barbara channel. Shown are broadcast minus improved baseline components. The error bars indicate the day to day scatter in the broadcast measurements.

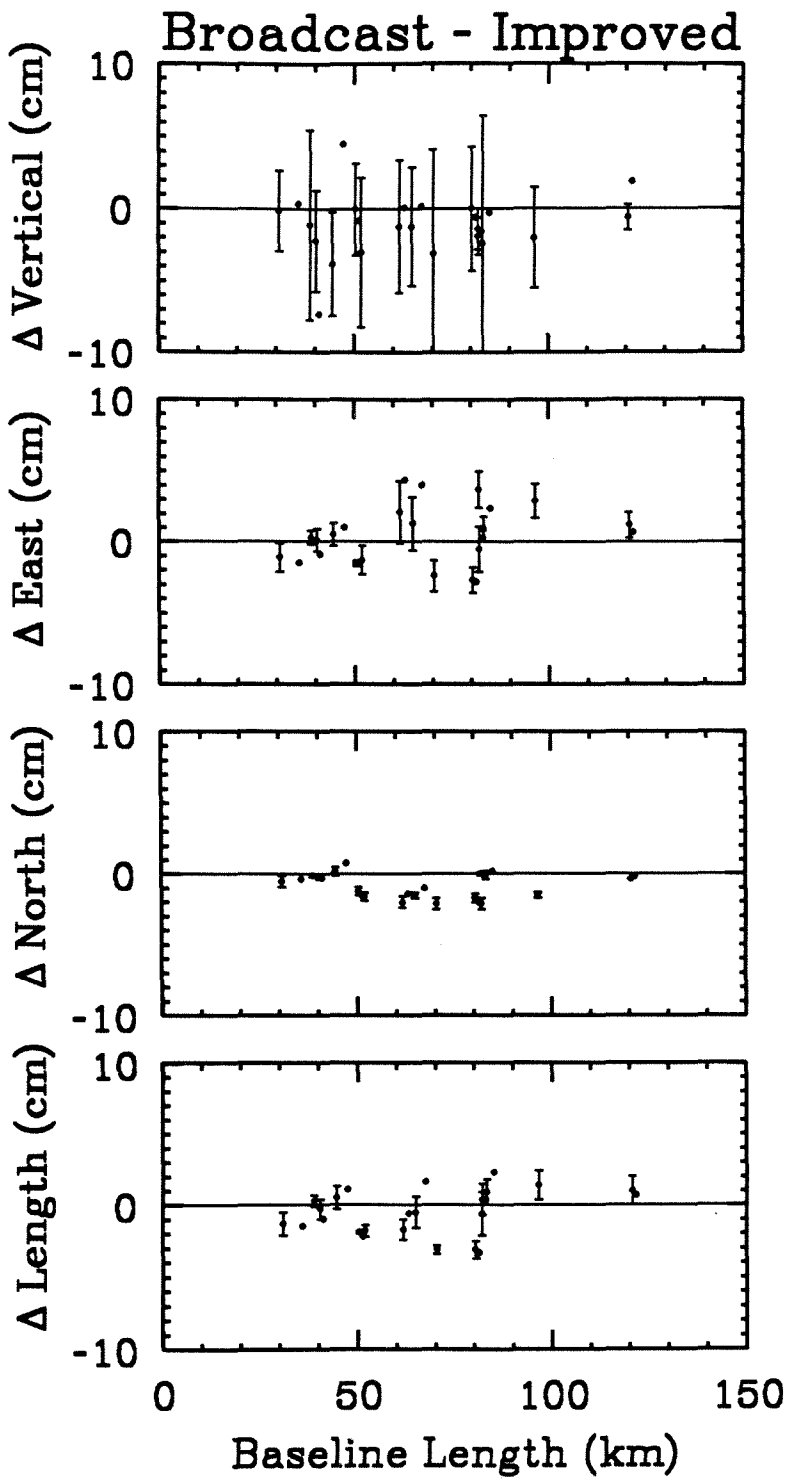
Broadcast - Improved
Δ Vertical (cm)
Δ East (cm)
Δ North (cm)
Δ Length (cm)
10
0
-10
0
50
100
150
Baseline Length (km)

Table 3.7 SBCGN baseline components

Baseline	X m	σ_x m	Y m	σ_y m	Z m	σ_z m	Length m	σ_L m
LACU-CHAF	25007.3227	0.0113	-27306.1257	0.0087	-18224.5619	0.0064	41268.9392	0.0087
LACU-DEVL	-19871.0084	0.0064	-21677.8948	0.0049	-42922.5485	0.0038	52030.1188	0.0023
LACU-GAVI	-38172.3183	0.0076	22966.2416	0.0057	421.0721	0.0042	44550.5493	0.0072
LACU-SNRI	-47908.6340	0.0068	-10877.2646	0.0053	-50266.5355	0.0038	70287.1019	0.0042
LACU-HIMT	-3784.3777	0.0202	-30795.3418	0.0207	-43316.4027	0.0167	53282.1296	0.0164
CHAF-HIMT	-28791.7004	0.0205	-3489.2161	0.0209	-25091.8408	0.0168	38350.1906	0.0156
CHAF-DEVL	-44878.3311	0.0113	5628.2309	0.0086	-24697.9866	0.0064	51533.7960	0.0094
GAVI-DEVL	18301.3099	0.0079	-44644.1364	0.0060	-43343.6206	0.0041	64859.1266	0.0045
GAVI-SNRI	-9736.3157	0.0079	-33843.5062	0.0060	-50687.6076	0.0045	61720.4368	0.0026
DEVL-HIMT	16086.6307	0.0204	-9117.4470	0.0208	-393.8542	0.0168	18494.9357	0.0202
DEVL-SNRI	-28037.6256	0.0068	10800.6302	0.0049	-7343.9870	0.0038	30930.5061	0.0060

made between these sites and HIMT. However, unlike conventional geodesy, GPS measures 3-dimensional positions. The CHAF-HIMT and DEVL-HIMT baselines are determined by subtracting from the LACU-HIMT vector, the LACU-CHAF and LACU-DEVL vectors, respectively.

Comparison with other techniques

Shown in Figure 3.11 is a comparison between GPS baseline components obtained from the January survey of 1987, and those calculated from the SV-3 coordinate system (VLBI). The difference in baseline components and length between GPS and VLBI for the 223 km VNDN-PVER and 3,286 km VNDN-CHUR baselines are shown. The error bars give the 5-day RMS scatters in the GPS components. The VNDN-PVER line compares well in length (1.3 cm), but for each horizontal component the comparison is slightly less than 3 cm. This lack of fit may be due to the predominately east-west baseline orientation, which generally results in a poorer solution. Not surprisingly, the GPS-VLBI discrepancy for the VNDN-CHUR line is considerably larger due to its continental length. In addition, Murray and King [MIT interoffice memorandum, 1988] suggest a 10 cm potential error at CHUR. Still the agreement between the two methods is on the order of $3-5\text{x}10^{-8}$ in the horizontal components and $7\text{x}10^{-8}$ in the vertical.

The October 1987 Survey

Although the GPS survey of October 1, 1987 (Figure 3.5c, Table 3.3) is not used in our strain analysis, we can compare the difference between the CHAF-VNDN and CHAF-SOLI baselines vectors obtained during this campaign and in January, 1987. The CHAF-VNDN line was measured only

Figure 3.11: Comparison between GPS and VLBI measurements (GPS minus VLBI) for two lines from the January, 1987 experiment. The error bars indicate the day to day scatter in the measurements.

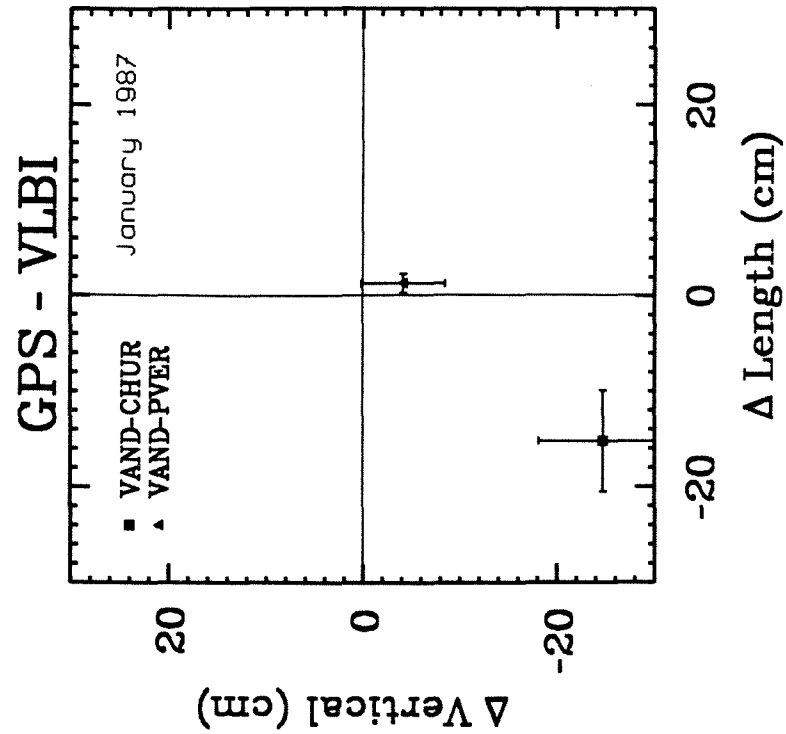
GPS - VLBI
January 1987
VAND-CHUR
VAND-PVER
Δ Vertical (cm)
Δ Length (cm)
20
0
-20
20
0
-20

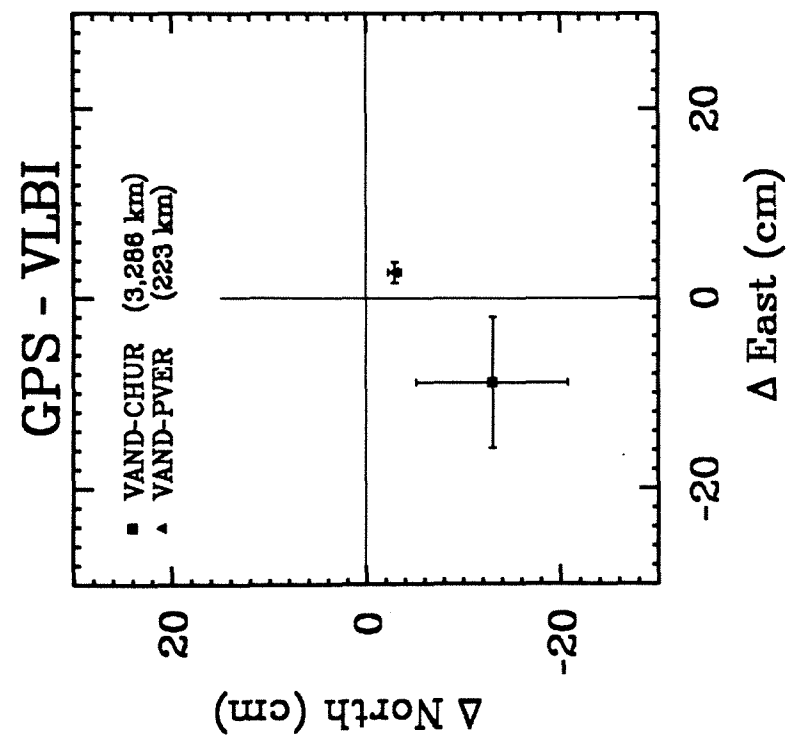
GPS - VLBI
VAND-CHUR (3,286 km)
VAND-PVER (223 km)
Δ North (cm)
Δ East (cm)
20
0
-20
20
0
-20

once during each of the two campaigns (CHAF was not occupied January 4-7, 1987). CHAF-SOLI was occupied on October 1, 1987 but there were no direct measurements of this baseline in January, 1987 (CHAF was occupied on January 3, SOLI on January 4-7). However, we obtain the baseline vector since all 5 days of the January survey were included into a single simultaneous GPS solution. Listed in Table 3.8 are the local (north, east, vertical, length) baseline component differences between the two baselines. Also shown is a 1950 EDM distance obtained between CHAF and SOLI. The CHAF-VNDN line yields relatively good agreement between the two surveys spaced 9 months apart, especially true considering the predominately east-west orientation of this 121 km baseline. The large component differences for CHAF-SOLI are somewhat disturbing, considering its length is only 1 km. However, recall that there were no direct measurements of this baseline in January, 1987; the baseline is obtained indirectly by differencing the LACU-CHAF and LACU-SOLI baseline vectors, done automatically in the 5-day simultaneous GPS solution. In addition, CHAF is located on top of a hill overlooking SOLI; the 319 meter vertical separation is a significant component of the 1154 meter baseline so an error in the vertical will significantly influence the length measurement.

Systematic Differences between EDM and GPS

Given the considerable difference in methods between the 1970/1971 and 1987/1988 measurements, we must consider the possibility of some sort of systematic difference between them. We can do this indirectly by comparing both with a common standard: the distance measurements made by the U.S. Geological Survey over other survey lines in California. These distances are

Table 3.8 Baseline Comparison (CHAF-VNDN, CHAF-SOLI)

Baseline	Length (km)	Difference (cm)			
		North	East	Vertical	Length
CHAF–VNDN[1]	121	-0.3	1.6	1.9	1.7
CHAF–SOLI[1]	1	-0.3	2.8	-4.4	1.3
CHAF–SOLI[2]	1				-0.4

[1] October, 1987 GPS - January, 1987 GPS
[2] 1950 EDM - January, 1987 GPS

determined using a different type of EDM instrument (a Geodolite), with corrections for atmospheric refraction being made in the same way as was done for the 1970/1971 survey but with different instrumentation. *Savage et al.* [1981] give the results of measurements by the USGS and by Greenwood and Associates (under contract to the California Division of Mines and Geology) over the same lines a few weeks apart. For data from the early 1970's, there is no significant difference between the two systems. This result is confirmed by the analysis of *King et al.* [1987] of line-length changes in the Parkfield area. Comparisons between GPS and USGS EDM data over three lines in Central California, as well as a GPS/EDM network near Hebgen Lake, Montana, have shown no systematic offset between these two techniques [*Davis et al.*, 1989]. In their study the difference between Geodolite and GPS baseline lengths is given by

$$\Delta L = a + bL \tag{3.13}$$

where L is the line length, a is 0.06 $\pm$ 0.05 cm, and b is 0.01 $\pm$ 0.01 cm-km^{-1}. For the 18.5 to 70.3 km baselines spanning the Santa Barbara channel, the GPS-Geodolite differences are 0.24 to 0.76 cm, which are not significantly different than 0.

3.5 Analysis

Strain Models

Baseline length and length changes for those lines spanning the Santa Barbara channel, surveyed by trilateration in 1970/1971 and GPS in 1987/1988, are listed in Table 3.9. The difference between the two epochs is a measure of the strain accumulation in the channel over this 16 year interval.

Table 3.9 EDM/GPS Baseline Lengths

Baseline	EDM m	σ_{edm} m	GPS m	σ_{gps} m	Difference m	σ_{diff} m
LACU-CHAF	41268.926	0.022	41268.9392	0.0087	0.013	0.023
LACU-HIMT	53282.202	0.027	53282.1296	0.0164	-0.072	0.032
LACU-DEVL	52030.224	0.027	52030.1188	0.0023	-0.105	0.027
LACU-SNRI	70287.175	0.036	70287.1019	0.0042	-0.730	0.036
LACU-GAVI	44550.542	0.023	44550.5493	0.0072	0.007	0.024
CHAF-HMNT	38350.273	0.020	38350.1906	0.0156	-0.082	0.025
CHAF-DEVL	51533.879	0.027	51533.7960	0.0094	-0.083	0.028
GAVI-DEVL	64859.053	0.033	64859.1266	0.0045	0.074	0.033
GAVI-SNRI	61720.369	0.031	61720.4368	0.0026	0.068	0.032
DEVL-HMNT	18494.944	0.012	18494.9357	0.0202	-0.008	0.024
DEVL-SNRI	30930.512	0.017	30930.5061	0.0060	-0.006	0.018

The one-sigma errors, which we feel are realistic estimates of baseline uncertainty (and largest for the geodimeter results), are generally smaller than the observed strains, suggesting a tectonic signature in the measurements. The accuracy for the trilateration is almost entirely a function of baseline length, while the GPS uncertainties are also dependent on baseline orientation. The error in length change is computed by assuming no correlation between the EDM and GPS surveys, that is

$$\sigma_{\text{diff}}^2 = \sigma_{\text{edm}}^2 + \sigma_{\text{gps}}^2 \tag{3.14}$$

The largest strains between the two survey epochs are observed for the channel crossing baselines. In the eastern channel, convergence is suggested by the consistent shortening of 7.2 cm (LACU-HIMT) to 10.5 cm (LACU-DEVL) measured between stations on opposite sides of the channel. The picture is more complicated in the west, where observed length changes are both positive (GAVI-DEVL, 7.4 cm; GAVI-SNRI, 6.8 cm) and negative (SNRI-LACU, -7.3 cm). It is significant that the 4 lines which do not cross the channel (mainland-mainland or island-island) all show changes which are small (between 0.6 and 1.3 cm), and in fact, significantly smaller than the baseline uncertainties. In addition to suggesting that deformation is largely concentrated across the channel, this gives some constraint on the reliability of the measurements. If "true errors" are larger than the estimated uncertainties, we would not expect each of these lines to show negligible deformation. If anything, the small magnitude of the observed movements suggests that the calculated uncertainties may be overly conservative. More importantly, this implies that the large length changes for the channel crossing baselines are real, and not simply an artifact of measurement error.

Assuming (infinitesimal) uniform strain, the change in length ΔL_i for the ith baseline is given by

$$\Delta L_i = \Big(E_{11}\sin(\theta_i) + E_{12}\sin(2\theta_i) + E_{22}\cos(2\theta_i)\Big)L_i \qquad (3.15)$$

where E_{11} and E_{22} are the east-west and north-south strain components, respectively, and E_{12} is the right-lateral shear strain across an east-west line [e.g., *Jaeger and Cook*, 1969]. We define dilatation (lengthening) as positive and contraction (shortening) as negative strain. Baseline azimuths (θ_i) are measured clockwise from north and lengths are given by L_i. It is often convenient to refer to the strain $\epsilon_i = \Delta L_i / L_i$, or the strain rate $\dot{\epsilon}_i = \epsilon_i / t_i$, where t_i is the time between measurements; thus

$$\dot{\epsilon}_i = \dot{E}_{11}\sin(\theta_i) + \dot{E}_{12}\sin(2\theta_i) + \dot{E}_{22}\cos(2\theta_i) \qquad (3.16)$$

Given in Table 3.10 is the strain and strain rate for each of the 11 Santa Barbara channel baselines. For all baselines except those to HIMT, the interval between measurement epochs is 15.9 or 16.2 years, depending on whether the EDM observations were made in November, 1970 or February, 1971. Most GPS sites were reoccupied during January, 1987. The LACU-HIMT interval is slightly longer (17.5 years), as this baseline was reoccupied with GPS in May, 1988. Since the CHAF-HIMT and DEVL-HIMT baselines are determined by integrating the January and May surveys (baseline tie), the resurvey interval for these baselines is determined by averaging the time of the two GPS campaigns. The strain rate errors are nearly constant for all but the DEVL-HIMT baseline. This is because both the strain and errors (predominately due to the EDM observations) are directly proportional to baseline length. The DEVL-HIMT GPS baseline involves a tie between two surveys, one of which was processed with the less precise broadcast ephemeris.

Table 3.10 Strain Accumulation 1970 - 1988

Baseline	Length km	Change cm	Interval yr	Strain $\mu\epsilon$	Rate $\mu\epsilon$/yr	Error $\mu\epsilon$/yr	Azimuth deg	Model[1]
LACU-CHAF	41.3	1.3	15.9	0.315	0.020	0.035	121.	1,2
LACU-HIMT	53.3	-7.2	17.5	-1.351	-0.077	0.034	167.	1,2
LACU-DEVL	52.0	-10.5	16.2	-2.018	-0.124	0.032	7.	1,2,3a,3b
LACU-SNRI	70.3	-7.3	15.9	-1.038	-0.065	0.032	31.	1,3
LACU-GAVI	44.6	0.7	15.9	0.157	0.010	0.034	91.	1,3
CHAF-HMNT	38.3	-8.2	16.8	-2.138	-0.127	0.039	38.	1,2a
CHAF-DEVL	51.5	-8.3	16.2	-1.611	-0.099	0.033	54.	1,2
GAVI-DEVL	64.8	7.4	15.9	1.141	0.072	0.032	144.	1,3
GAVI-SNRI	61.7	6.8	15.9	1.102	0.069	0.033	172.	1a,3a,3b
DEVL-HMNT	18.5	-0.8	16.6	-0.432	-0.026	0.078	91.	1,2a
DEVL-SNRI	30.9	-0.6	15.9	-0.194	-0.012	0.036	74.	1,3

[1] Model number refers to Table 3.11

This baseline is predominately east-west, which generally results in a larger uncertainty.

The strain rate measurements for the SBCGN are combined into a weighted least squares adjustment to determine the $\dot{E}_{11}$, $\dot{E}_{12}$, and $\dot{E}_{22}$ components of the strain rate tensor [e.g., *Prescott*, 1979]. Briefly, for n observables given by Equation (3.16), the tensor components are computed from

$$\dot{\mathbf{E}} = \left(\mathbf{G}^t\mathbf{W}^t\mathbf{W}\mathbf{G}\right)^{-1}\mathbf{G}^t\mathbf{W}^t\mathbf{W}\dot{\epsilon} \tag{3.17}$$

where the model parameters are given by

$$\dot{\mathbf{E}} = \begin{bmatrix} \dot{E}_{11} \\ \dot{E}_{12} \\ \dot{E}_{22} \end{bmatrix}$$

and

$$\mathbf{G} = \begin{bmatrix} \sin(\theta_1) & \sin(2\theta_1) & \cos(\theta_1) \\ \cdot & \cdot & \cdot \\ \cdot & \cdot & \cdot \\ \sin(\theta_n) & \sin(2\theta_n) & \cos(\theta_n) \end{bmatrix}$$

is the nx3 parameter matrix which depends exclusively on baseline azimuth, and

$$\mathbf{W} = \begin{bmatrix} \frac{1}{\sigma_1^2} & & & \\ & \frac{1}{\sigma_2^2} & & \\ & & \cdot & \\ & & & \frac{1}{\sigma_n^2} \end{bmatrix}$$

is the nxn diagonal error matrix where σ_i is the strain rate error of the ith

baseline, and

$$\dot{\epsilon} = \begin{bmatrix} \dot{\epsilon}_1 \\ \dot{\epsilon}_2 \\ . \\ . \\ \dot{\epsilon}_n \end{bmatrix}$$

is the n dimensioned data array containing the strain rate observables for each baseline.

We examine 3 models (and several sub-models) of deformation in the Santa Barbara channel, each differing by the area covered and baselines used in the inversion. For Model 1 the entire network is considered, while for Models 2 and 3 the channel is partitioned into its eastern and central sections, respectively, arbitrarily divided at the LACU-DEVL baseline. Separate solutions are calculated for each of the 3 models by either including all baselines or with selected lines removed. All measurements for each network (or sub-network) are incorporated into Models 1a, 2a, and 3a. Because the accuracy of the GAVI-SNRI EDM measurement is in question, this line is omitted in Model 1b and 3b. For Model 2b, the HIMT-CHAF and HIMT-DEVL baselines are excluded since the GPS lengths for these lines were determined indirectly by integrating the January, 1987 and May, 1988 surveys. Comparing Models 2a and 2b will show the effect (if any) of these baseline ties on the strain analysis. Finally, Model 3c utilizes all measurements from the central sub-network except that of LACU-DEVL. Table 3.10 lists the baselines which correspond to each model. Calculated for each model are the three components of the strain tensor, the magnitude and azimuth of the maximum and minimum principle strains, and the RMS of the

Table 3.11 Uniform Strain Models

Model	$\dot{E}_{11}$ $\mu\epsilon$/yr	$\dot{E}_{12}$ $\mu\epsilon$/yr	$\dot{E}_{22}$ $\mu\epsilon$/yr	$\dot{e}_1$ $\mu\epsilon$/yr	$\dot{e}_2$ $\mu\epsilon$/yr	$e_{1\theta}$ °	σ_{rms} cm
1a (FULL)	0.003 ± 0.020	-0.076 ± 0.016	-0.046 ± 0.017	0.058	-0.102	-53.9	4.8
1b (FULL)	0.013 ± 0.020	-0.068 ± 0.016	-0.080 ± 0.019	0.049	-0.116	-62.2	3.5
2a (EAST)	-0.009 ± 0.033	-0.060 ± 0.021	-0.109 ± 0.024	0.019	-0.137	-64.9	0.4
2b (EAST)	-0.006 ± 0.037	-0.061 ± 0.025	-0.110 ± 0.025	0.022	-0.138	-65.3	0.2
3a (CENTRAL)	0.024 ± 0.025	-0.091 ± 0.023	-0.024 ± 0.019	0.094	-0.094	-52.3	5.8
3b (CENTRAL)	0.032 ± 0.025	-0.078 ± 0.023	-0.060 ± 0.024	0.076	-0.105	-60.3	4.7
3c (CENTRAL)	0.009 ± 0.026	-0.074 ± 0.023	0.023 ± 0.024	0.091	-0.059	-42.2	2.7

$\dot{E}_{11}$ east-west strain rate
$\dot{E}_{22}$ north-south strain rate
$\dot{E}_{12}$ shear strain rate (right-lateral)
$\dot{e}_1$ maximum principle strain rate
$\dot{e}_2$ minimum principle strain rate
$e_{1\theta}$ maximum strain direction (clockwise from north)
σ_{rms} model redsidual

solution (Table 3.11). The RMS indicates of how well each model fits the data and is defined as

$$\sigma^2_{RMS} = \sum_{i=1}^{n} (\Delta L_i - \Delta L_i^c)^2 / n_{dof} \qquad (3.18)$$

where ΔL_i is the observed length change of the ith baseline, ΔL_i^c is the calculated change from the model, and n_{dof} is the number of degrees of freedom in the estimation. Since 3 strain parameters are solved, $n_{dof} = n - 3$, where n is the number of observations. The model fit (RMS) is measured in units of centimeters or line length change (as opposed to strain rate), since this is a more intuitive unit to view the model fit in terms of the accuracy of the geodetic measurements.

Model 1a (FULL network; all lines) indicates appreciable north-south convergence and left-lateral shear with insignificant east-west deformation. However, this model does not fit the data very well as is indicated by the high σ_{RMS}. Plotted in Figure 3.12 are the observed baseline strains vs orientation, as well as the model fit to the data. There are large discrepancies between the model parameters and observations for several baselines. Model 1b (FULL network; GAVI-SNRI excluded) does not yield a significantly different or improved solution. Presumably, the lack of fit is not solely explained by a (potentially) bad EDM measurement for the GAVI-SNRI baseline. Because Model 1 covers the entire SBCGN, this analysis assumes uniform strain across the network. The poor fit between model and observation may signify that strain is not homogeneous, but is spatially dependent. A much better fit is obtained when we model the eastern and central networks separately (Figure 3.12; Table 3.11). Model 2a (EAST network; all lines) indicates almost pure uniaxial convergence oriented N25.1°E. Model 2b (EAST network; HIMT-

CHAF and HIMT-DEVL excluded) is nearly identical suggesting the incorporation of the GPS baseline ties has little influence on the calculated east-channel strain. Model 3a (CENTRAL network; all lines) yields a combination of left-lateral shear strain and marginal strain along the north-south axis. The fit for Model 3a is not very good, however. In fact, the large residuals are on par with the magnitude of the observed length changes across the channel. Especially noticeable is the large deviation for the LACU-DEVL baseline (Figure 3.12). The fit for Model 3b (CENTRAL network; GAVI-SNRI excluded) is slightly improved, while Model 3c (CENTRAL network; LACU-DEVL excluded) seems to satisfy the data reasonably well. σ_{RMS} should be independent of the number of observations since it is a function of the number of degrees of freedom in the model. Admittingly, the exclusion of any particular line is somewhat ad hoc, so is difficult to ascertain which of the sub-models is preferred. The omission of the LACU-DEVL baseline in the latter model (3b) does not presume the measurement is bad, rather, the good agreement with observation mearly suggests that the LACU-DEVL transect is more representative of the deformation in the eastern channel. In any rate, the strain parameters for the CENTRAL channel do provide an important observation. For each sub-model, the shear component (left-lateral) is greater than the north-south (or east-west) strain. This is different that the uniaxial northeast trending convergence indicated to the east, and suggests a stress/strain transition between the two providences.

Elastic Rebound Effects

During the interval between the first and second surveys, the largest earthquake within the network was the Santa Barbara earthquake of 13

Figure 3.12: Comparison of strain-rate observations for each baseline of the Santa Barbara channel network with the best fit strain model. Azimuths are measured clockwise from north. The Full Network model includes all SBCGN data into the strain analysis; the East Network model includes baselines in the eastern third of the channel (from LACU-DEVL to the east); the Central Network model includes baselines in the central channel (from LACU-DEVL to the west). Solid lines indicate solutions with no excluded baselines. Dashed lines indicate solutions with excluded baselines.

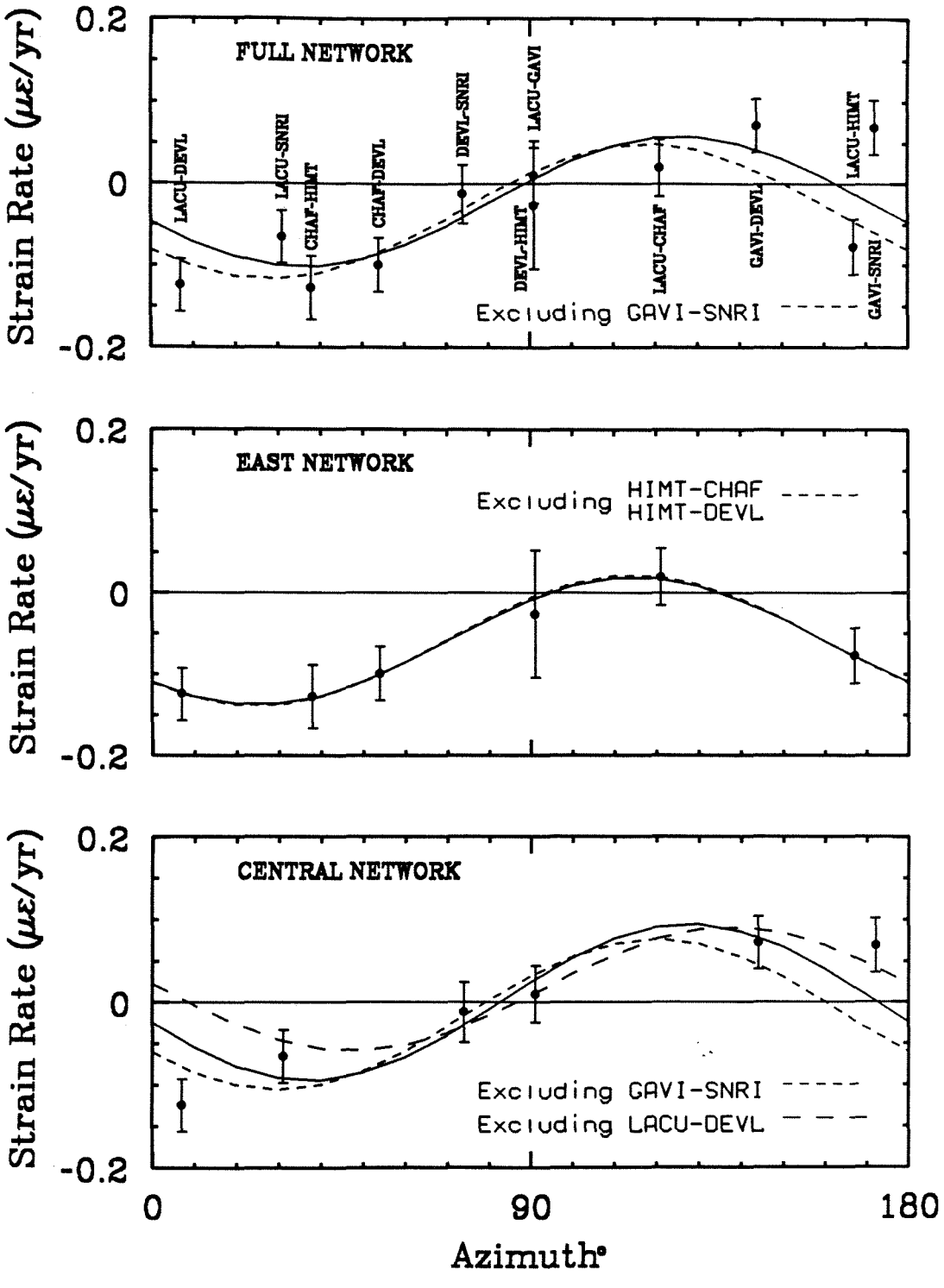
FULL NETWORK
LACU-DEVL
LACU-SNRI
CHAF-HIMT
CHAF-DEVL
DEVL-SNRI
LACU-GAVI
DEVL-HIMT
LACU-CHAF
GAVI-DEVL
LACU-HIMT
GAVI-SNRI
Excluding GAVI-SNRI
EAST NETWORK
Excluding HIMT-CHAF
HIMT-DEVL
CENTRAL NETWORK
Excluding GAVI-SNRI
Excluding LACU-DEVL
Strain Rate (με/yr)
0.2
0
-0.2
0
90
180
Azimuth°

August 1978. The study of *Corbett and Johnson* [1982] showed that the rupture plane for this event was a shallowly-dipping fault about 15 km below the city of Santa Barbara. We have computed the station displacements (and from these line-length changes) from this event assuming that the earthquake could be represented by a rectangular rupture plane in an elastic half-space. We used the fault location, orientation, and slip direction found by Corbett and Johnson, and a moment of 1.1×10^{25} dyne-cm from long-period WWSSN data [*Wallace et al.*, 1981]. Even the largest line-length change (2 mm lengthening between LACU and DEVL) is much smaller than the survey errors; we have therefore not included this effect in our computed strains.

We have also calculated line length changes from the San Fernando earthquake of February 9, 1971 with an epicentral location about 85 km east of CHAF. We use source parameters given by *Canitez and Toksoz* [1972], who found seismic and static displacements could be modeled by a fault with dimensions 14 by 14 km, oriented N70 ° W, dipping 52 ° NE, and with 280 cm slip along a vector oriented 225 ° from the horizontal (thrust mechanism with a left-lateral component). Although significantly outside the network, because of the earthquakes size (M_L 6.6), the CHAF-LACU and CHAF-DEVL baselines lengthened 6 mm, the CHAF-HIMT baseline lengthened 4 mm, while all other lines showed deformation less than 2 mm. Still, these strains are significantly inside the survey errors; therefore we have not included the effect of this earthquake in our analysis.

Equivalent Strain

As a final test for how well the GPS measurements can detect strain

accumulation across the channel, we investigate the effect of different processing schemes on the computed strains. We approach this issue by determining the difference in length for the SBCGN baselines processed by two methods, and then calculate the apparent or equivalent strain that results between the two techniques. In this way, rather than simply comparing line length changes, we can directly evaluate the effect of potential error sources on the strain analysis.

Table 3.12 lists the equivalent strain determined by two methods: 1) different GPS processing software, and 2) GPS solutions from the broadcast ephemeris. For comparison, we have included the tectonic strain between the 1970/1971 EDM and 1987 GPS observations, but have not included the 1988 GPS measurements since these were obtained using the broadcast orbits, which is one of our comparison tests. For simplicity, we have assumed that the baseline errors are equal to those given in Table 3.10. Of primary importance is the relative magnitude of the tectonic and equivalent strains, and the formal errors computed from the inversion. If the equivalent strains do not fall within the uncertainty estimates, and if they are not significantly smaller than the tectonic measurements, we can not ascertain whether the computed deformation is real or is due to measurement error.

In the first analysis (NGS), the equivalent strain is determined by differencing the Bernese GPS solutions (Table 3.7) against those obtained from the GPS22 algorithm developed at the National Geodetic Survey (NGS) [F. Webb, personal communication, 1990]. The NGS baseline lengths are calculated by adjusting the 5 consecutive days of observation from the January (1987) campaign. The equivalent strains are well within the

Table 3.12 Equivalent Strain

Model	E_{11}	E_{12}	E_{22}	e_1	e_2	$e_{1\theta}$
TECTONIC	0.02 ± 0.34	-1.26 ± 0.27	-0.40 ± 0.31	1.09	-1.47	-49.6
NGS	-0.12 ± 0.34	0.07 ± 0.27	0.08 ± 0.31	0.10	-0.14	17.5
BROADCAST	0.12 ± 0.34	0.21 ± 0.27	0.32 ± 0.31	0.46	-0.02	32.0

E_{11} east-west strain
E_{22} north-south strain
E_{12} shear strain (right-lateral)
e_1 maximum principle strain
e_2 minimum principle strain
$e_{1\theta}$ maximum strain direction (clockwise from north)

estimated uncertainties, suggesting solutions obtained with different software systems have little influence in our analysis. This is a strong indication that the strains we observe are both real and accurate. The equivalent strain between the broadcast and orbit improved solutions are also listed in Table 3.12 (BROADCAST). The comparison is on par with the error estimates for the tectonic strain. This suggests, at least for lines of relatively short length as is the case for the Santa Barbara channel (18 – 80 km), solutions obtained entirely with the broadcast ephemeris will provide results which are geophysically significant, assuming strain rates comparable to the channel and at least a 16 year measurement interval.

Geophysical Implications

The geodetic observations of baseline strain (Table 3.11) suggest non-uniform deformation in the Santa Barbara channel. Near uniaxial convergence of -0.14$\mu\epsilon$ oriented N25.1 ° E is calculated for the eastern channel (Figure 3.13). This is equivalent to an average rate of convergence between 1970 and 1988 of 6.4 mm/yr, assuming a 45 km channel width. To the west, however, the strain analysis indicates a large component of left-lateral shear suggesting a rapid change in deformation style between the eastern and central portions of the channel. Shown in Figure 3.13 are the principle strain directions calculated from Model 3a (Table 3.11). While our channel division may seem somewhat ad-hoc, it is supported by seismic and tectonic evidence.

Non-uniform deformation is consistent with seismic patterns over the last several years. Figures 3.2-3.4 show that seismicity is concentrated in the eastern part of the channel. One could argue that this is simply due to a few

Figure 3.13: Shown are the magnitudes and orientations of the principle strain axes for the East and Central Santa Barbara channel networks. The formal uncertainties are indicated by the error bars along each arrow.

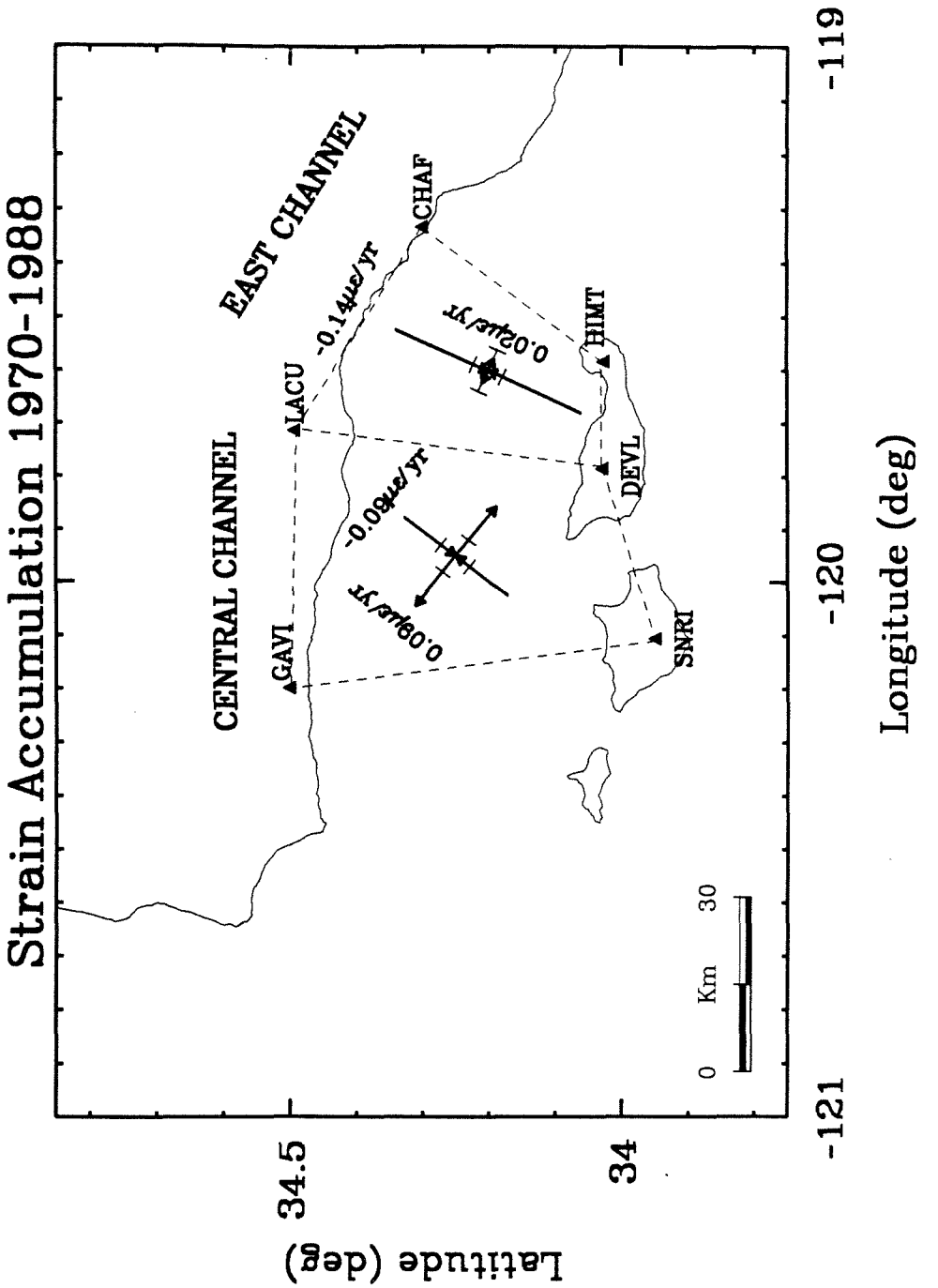
Strain Accumulation 1970-1988
EAST CHANNEL
CENTRAL CHANNEL
LACU
CHAF
HIMT
DEVL
GAVI
SNRI
-0.14με/yr
0.02με/yr
-0.09με/yr
0.08με/yr
0
Km
30
Latitude (deg)
34.5
34
Longitude (deg)
-121
-120
-119

large earthquakes and their aftershock distribution. However, seismicity plotted at 10 year intervals shows that the eastern channel has been consistently quite active (Figure 3.14). The apparent increase in activity with time is due to better station coverage. Figure 3.14 suggests a fairly dramatic change in the tectonic characteristics from the eastern to central portions of the channel.

The topographic variation along 4 channel crossing profiles is shown in Figure 3.15. The rugged topography indicated by the high elevations along profiles C-C' and D-D' formed by active north-south compression in the western Transverse Ranges. However, to the west (A-A' and B-B') the topographic gradient is significantly reduced. This suggests a considerable transition between compression in the east to some other style of deformation in the central and western portions of the channel. Presumably, this corresponds to the alternate strain patterns observed geodetically.

The observed geodetic convergence in the eastern channel favorably compares to the rate and orientation of the predicted San Andreas discrepancy vector (Figure 3.1a). This suggests that most or all of the missing plate motion may be accommodated across this region. The deformation is consistent with seismicity studies and focal parameters. In fact, the average P-axis orientation for those mechanisms within the eastern channel network is N22°E (Figure 4). Pure thrust mechanisms along northwest trending faults or thrust events with left-lateral components along east-west trending faults will satisfy the measured strain.

The calculated strain field changes from uniaxial northeast convergence to

left-lateral shear in the central channel. This deformation could be satisfied by left-lateral slip along east-west trending faults. However, there is considerable uncertainty associated with the central channel stain estimate as evident by the multiple solutions for Model 3 in Table 3.11 and the data misfit in Figure 3.12. It is difficult to ascertain how the central channel is related tectonically to the deformation observed in the east. This region may mark the western boundary between compression in the Transverse Ranges and the northwest trending motion of the Pacific plate relative to the North American continent. In the Santa Maria fold and thrust belt directly northwest of the central channel, *Feigl et al.* [1990] suggest crustal shortening of 6 mm/yr oriented N30°E, along with 3 mm/yr right-lateral shear across this axis. The convergence rate and orientation is similar to that observed in the eastern third of the Santa Barbara channel. This may mean that deformation to the west is shifted to the northwest, roughly parallel to the trend of the San Andreas fault.

The observed strain field in the eastern channel can be evaluated in terms of seismic moment release. The relationship between the seismically generated strain E_{ij} within a volume V, and the seismic moment M_{ij}^k from each earthquake within it is given by

$$E_{ij} = \frac{1}{2\mu V} \sum_{k=1}^{N} M_{ij}^k \tag{3.19}$$

[*Kostrov*, 1974; *Jackson and McKenzie*, 1988], where μ is the rigidity given here as 3.0×10^{11} dyne-cm^{-2}. The observed strain will be larger than the seismic estimate if the medium is characterized by aseismic deformation or unreleased strain energy. In the case of the eastern Santa Barbara channel, the regional volume is calculated assuming the area spanned by the network is

Figure 3.14: The temporal variation in seismic activity in the Santa Barbara channel plotted at 10-year intervals (8 years for the first). The increased seismicity with time is an artifact of station coverage. Note the consistent high activity in the eastern channel.

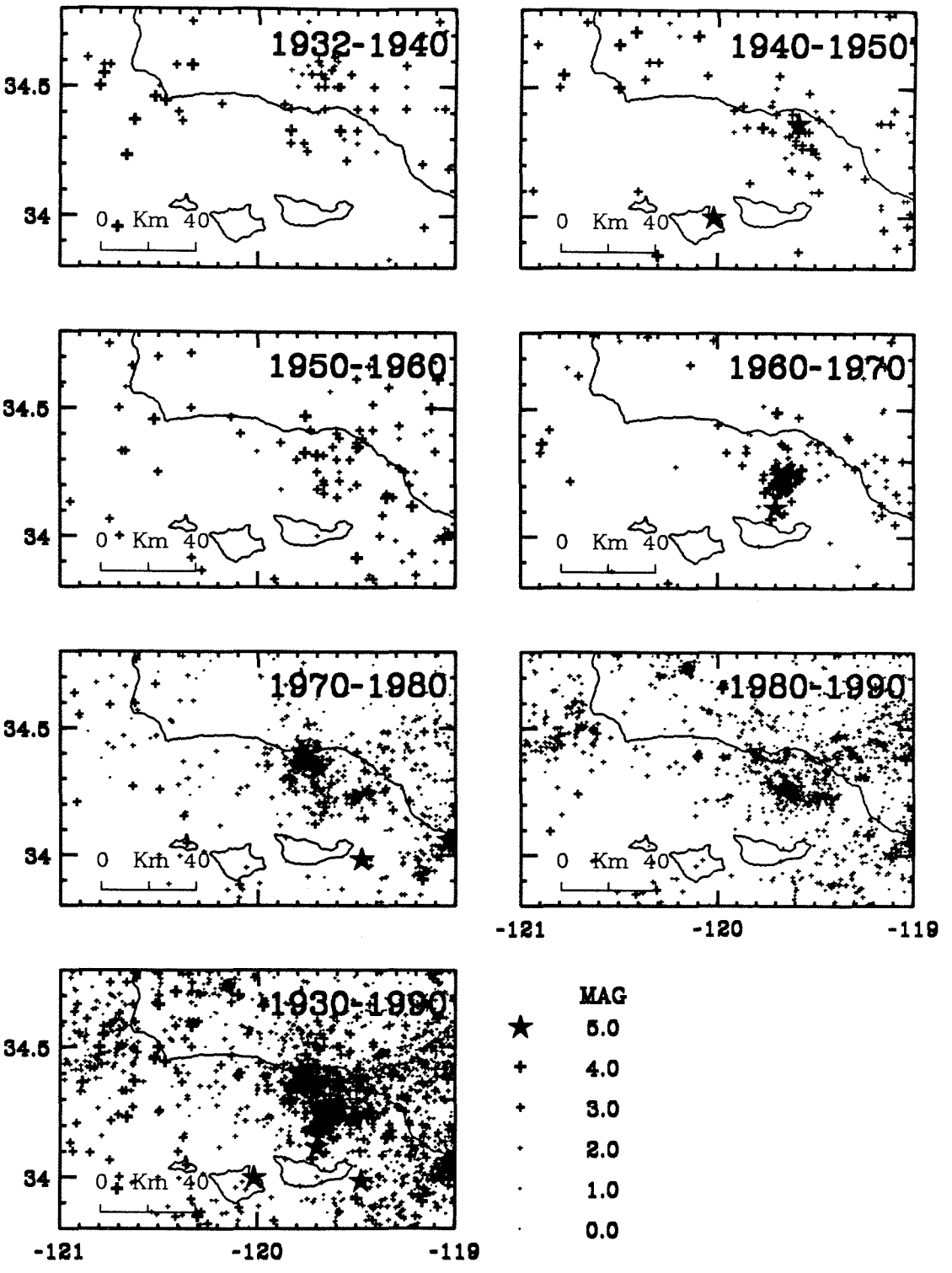
1932-1940
1940-1950
1950-1960
1960-1970
1970-1980
1980-1990
1930-1990
34.5
34
0 Km 40
-121
-120
-119
MAG
5.0
4.0
3.0
2.0
1.0
0.0

Figure 3.15: Topographic variation along 4 profiles crossing the Santa Barbara channel at different longitudes. C-C' and D-D' show uplift due to convergence across the western Transverse Ranges. The decreased topographic expression along profiles A-A' and B-B' indicate a transition between convergence to some other style of deformation.

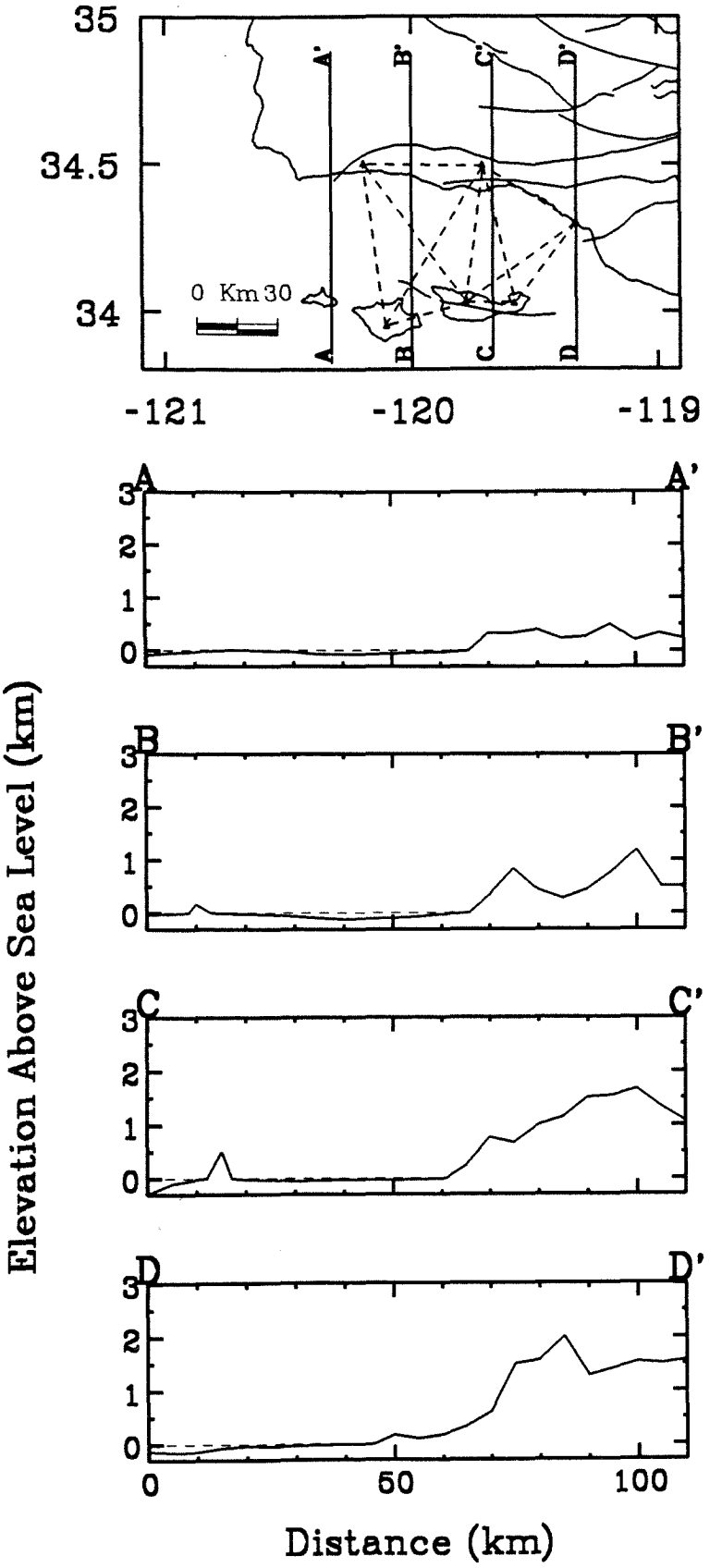
35
34.5
34
-121
-120
-119
0 Km 30
A'
B'
C'
D'
A
B
C
D
A
A'
B
B'
C
C'
D
D'
3
2
1
0
0
50
100
Elevation Above Sea Level (km)
Distance (km)

1500 km^2, and a seismogenic depth of 15 km (almost all earthquakes have shallower depths). The moment tensor is computed from the scalar moment M_0 by

$$M_{ij} = M_0(u_i n_j + u_j n_i) \tag{3.20}$$

where $\vec{u}$ and $\vec{n}$ are the outward normal vectors to the two nodal planes. We assume a coordinate system oriented along the direction of maximum convergence (N25.1 ° E). If earthquakes within this volume are dictated by pure thrust mechanisms along 30 ° dipping planes trending N64.9 ° W (perpendicular to the principle axis), the seismic convergence ϵ is thus

$$\epsilon = \frac{1}{2\mu V}(0.87M_0) \tag{3.21}$$

where M_0 is the cumulative seismic moment within the volume. Using the observed 16 year convergence rate of $-0.137\mu\epsilon$/yr, the estimated or potential moment release is $M_0 = 3.5 \times 10^{25}$ dyne-cm. Seismicity in the eastern channel during this time is dominated by the 1978 Santa Barbara earthquake, with a seismic moment of 1.1×10^{25} dyne-cm [*Wallace et al.*, 1981]. Thus, about 30 % of the accumulated strain over the last two decades has been released seismically. This is a significant percentage and suggests that moderate sized earthquakes play the dominate role for relieving tectonic stress in the eastern channel. Still, earthquakes similar in size to the 1978 event are relatively infrequent in this region (Table 3.1), suggesting that there may be considerable strain accumulation. Deformation in the central channel is not accompanied by abundant seismicity, however, indicating this region may be influenced by larger, although less frequent earthquakes.

3.6 Conclusions

A 1970/1971 EDM survey of a 6-station, 11-baseline network spanning the eastern and central Santa Barbara channel is integrated with 1987 and 1988 GPS resurveys to determine the regional strain accumulation over this 16 year period. The eastern channel is modeled by uniaxial convergence of 6 to 7 mm/yr oriented N25.1 ° E. This deformation is consistent with the north to north-east compression suggested by seismic data, as well as geomorphic evidence of 7.5 mm/yr convergence averaged over the last 0.2 myr (see above). Observed deformation in the central channel is less resolved, although it can be largely satisfied by left-lateral shear along east-west trending faults. The rapid change in tectonic style between the eastern and central thirds of the Santa Barbara channel is consistent with historical seismicity, which show activity predominately in the east, as well as a decreased topographic gradient to the west.

The precision from a 5-day (January, 1987) GPS campaign from a 14-station network in California (including 5 of the 6 Santa Barbara channel stations), gives day to day repeatabilities in the horizontal baseline components of 2.2×10^{-8} (north) and 3.0×10^{-8} (east). The vertical repeatability is 3.8 cm and is not significantly biased by the baseline length. Comparisons with VLBI measurements yield agreements on the order of a few parts in 10^{-8}. Independent solutions using the broadcast ephemeris are compared to orbit improved results for baselines between 31 and 122 km. Agreements at the 1-2 cm level are observed for the horizontal components, while the vertical comparison is 2.4 cm. In addition, solutions obtained with different GPS analysis software are comparable, and do not seriously affect the tectonic strain estimates.

Acknowledgments

Duncan Agnew (University of California at San Diego) supplied all processing and analysis of the EDM data, and provided many helpful suggestions and comments regarding the manuscript. I thank William Prescott, Kerry Sieh, Toshiro Tanimoto, and Donald Helmberger for their reviews. I especially thank my advisor Hiroo Kanamori for his wisdom and support. Financial support was provided by U.S. Geological Survey contract 14-08-0001-61679, National Science Foundation contract NSF-8618542, and NASA contract NAG-5-842.

Appendix: Data Reduction for 1970/1971 EDM Survey

In order to get the maximum accuracy for EDM measurements over long lines, we need to use a more elaborate procedure than is usual in most EDM surveys. We begin with the equation developed by *Brunner and Angus-Leppan* [1976]:

$$L = L_O - \int_0^L (n_G - 1)dx + \tfrac{1}{2}\cos^2\beta \int_0^L \left[\int_0^x \frac{dn}{dh}\zeta d\zeta\right]^2 \frac{dx}{x^2} \qquad (1)$$

where L is the true length between the endpoints (chord distance) and L_O is the optical path length; n_G is the ratio of the speed of light c to group velocity (the group index of refraction), and n is the index of refraction. The integration is carried out along the chord (not along the actual light path), this being the direction of the x-axis; this chord is inclined at angle β to the horizontal. The vertical gradient of refraction is dn/dh, h being positive upwards. The length reading given by the EDM instrument is

$$L_E = L_O/(1+N_E), \qquad (2)$$

where N_E is a constant of the instrument, being given by

$$N_E = \frac{c}{2Uf_m} - 1$$

where U is the distance assumed to correspond to a modulation frequency of f_m. For the AGA-8 Geodimeter, U is 5 m for f_m = 29.97 MHz; using the 1983 value of c gives $N_E = 3.08502\text{x}10^{-4}$.

If we define the integrated refraction correction

$$\bar{N}_G = \int_0^L (n_G - 1)\, dx$$

and note that this is $\ll 1$, we can combine (1) and (2) to get

$$L = L_E + L_E[(1-\bar{N}_G)(N_E-\bar{N}_G)] + \tfrac{1}{2}\cos^2\beta \int_0^L \left[\int_0^x \frac{dn}{dh}\zeta d\zeta\right]^2 \frac{dx}{x^2} \qquad (3)$$

as our equation to go from measured to actual length.

The data available to compute $\bar{N}_G$ are pressure records at both ends of the line, and temperature and humidity readings taken along it from an aircraft. The aircraft measurements are taken at distances from the Geodimeter f_0L, f_1L, ..., f_ML, where $f_0=0$ and $f_M=1$; we arrange the measurements in order of distance from the Geodimeter whether the aircraft is flying away from it or towards it. We assume that the aircraft flies along the chord; the actual flight path is along the light beam, but the difference between this and the chord is smaller than the error in keeping the aircraft on the beam. The height of the ith observation point is then

$$h_i = h_E + f_i(h_R-h_E) - \frac{L^2}{2} r_e(f_i-f_i^2)$$

where r_e is the radius of the Earth and h_E and h_R are the heights of the EDM instrument and reflector. The measurements at the ith point are temperature T_i and water vapor pressure e_i (easily obtained from humidity).

Our procedure is to assume that the atmosphere is in hydrostatic equilibrium; given this, we can find the pressure at different heights given the pressure at one height and the profile of temperature with height. We take this profile from the aircraft data, although in fact these sample different heights at different places. We thus can find P_1 given P_0 (which we know from the endpoint measurements), P_2 given P_1, and so on to get a complete profile of P_i's; given P_i, T_i, and e_i, we can compute $n_G(f_iL)$, which can then be integrated to give $\bar{N}_G$. In order to use the hydrostatic assumption, we first

convert the measured temperature and humidity to get the virtual temperatures (defined as the temperature for which the ideal gas law would give the correct density); including a rough correction for compressibility, this is

$$\hat{T} = 0.9996 \left(\frac{P}{P - e + \mu e} \right) T$$

where μ is the ratio of the molecular weights of dry air and water (0.62197). We assume that the temperature profile with height is

$$\hat{T} = \tfrac{1}{2}(\hat{T}_i + \hat{T}_{i+1}) + \tfrac{1}{2}\alpha(h_i + h_{i+1}) - \alpha h$$

for the ith segment; the temperature thus varies with height with a lapse rate α and also matches the interpolated temperature at the middle of the segment. (Note that to find $\hat{T}_{i+1}$ we need P_{i+1}, which we compute from a rough version of the calculation below). We can combine this temperature profile with the ideal gas law and the hydrostatic assumption

$$\rho = \frac{P}{R\hat{T}} \qquad \frac{dP}{dh} = -\rho g$$

to get, for small differences in height, that

$$P_{i+1} = P_i \left(1 - \gamma\epsilon + \frac{\gamma(\gamma-1)}{2}\epsilon^2 \right)$$

where

$$\gamma = \frac{g}{\alpha R} \qquad \epsilon = \frac{\alpha(h_i - h_{i+1})}{\tfrac{1}{2}(\hat{T}_i + \hat{T}_{i+1}) + \tfrac{1}{2}\alpha(h_i - h_{i+1})}$$

with R being the gas constant and g the acceleration of gravity. Though the value of α is not well known, the dependence of the computed pressure on this is slight; a value of $\alpha = -0.0055$ K/m was used.

Given P, T, and e along the chord, we compute n_G from the expressions

given by *Owens* [1967], and integrate it using the trapezoidal rule to get $\bar{N}_G$. Because we actually have measurements of pressure at both ends of the line, we actually can compute two profiles of P (and hence of n_G): one by starting with P_0, the other by starting with P_M. The mismatch in pressures so computed is some indication of the quality of the pressure measurements (and of our assumptions); since the pressure measurements at both ends of the line are of equal quality, we simply average the n_G profiles computed from each one to get our value of $\bar{N}_G$.

A byproduct of the computation of n_G along the path is values of n_G at different elevations; we use this to estimate dn/dh (ignoring the slight difference between n_g and n). In all but two cases the dependence of n upon h was very nearly linear; we can then regard dn/dh as constant, in which case

$$\tfrac{1}{2}\int_0^L \left[\int_0^x \frac{dn}{dh}\zeta d\zeta\right]^2 \frac{dx}{x^2} = \frac{L^3}{24}\left(\frac{dn}{dh}\right)^2$$

We obtain dn/dh by fitting a straight line to n versus h. For two lines (GAVI-SNRI and DEVL-SNRI) the dependence of n upon h was definitely nonlinear because the line ran through the inversion commonly found in this area (with warm dry air overlying a colder damp marine layer); it was however possible to approximate dn/dh by two piecewise constants (again found by linear fits to n versus h), in which case the second integral in (1) can still be evaluated analytically.

All these measurements (endpoint pressure, aircraft data, and EDM measurements), while made concurrently, are not precisely synchronized. We used linear interpolation (and extrapolation when necessary) to find the

pressure values at the times corresponding to the middle of each aircraft run; all aircraft values for that run were assumed to be at this time. The result of the computation described above was a series for $\bar{N}_G$, at the times of the aircraft runs; the values of $\bar{N}_G$ at the time of each EDM reading were then found by interpolation of this series and used in (3). The dn/dh term was assumed constant for each line).

References

Bevington, P. R., *Data Reduction and Error Analysis for the Physical Sciences*, Mcgraw-Hill, 336 p., 1969.

Bird, P., and R. W. Rosenstock, Kinematics of present crust and mantle flow in southern California, *Geol. Soc. Am. Bull.*, *95*, 946-957, 1984.

Brunner, F. K., and P. V. Angus-Leppan, On the significance of meteorological parameters for terrestrial refraction, *Unisurv G*, *25*, 95-108, 1976.

Beutler, G., W. Gurtner, I. Bauersima, and R. Langley, Modeling and estimating the orbits of GPS satellites, paper presented at First International Symposium on Precise Positioning with the Global Positioning System, Int. Assoc. of Geod., Rockville, Md., April 15-19, 1985.

Canitez, N., and M. N. Toksoz, Static and dynamic study of earthquake source mechanism: San Fernando Earthquake, *J. Geophys. Res.*, *77*, 2583-2594, 1972.

Chin, M., CIGNET report, *GPS Bull.*, Global Positioning System Subcomm. of Comm. VIII, Int. Coord. of Space Tech. for Geod. and Geodyn., Natl. Geod. Surv., Rockville, Md., 1988.

Corbett, E. J., and C. E. Johnson, The Santa Barbara, California, earthquake of 13 August 1978, *Bull. Seismol. Soc. Amer.*, *72*, 2201-2226, 1982.

Davis, J. L., W. H. Prescott, J. L. Svarc, and K. J. Wendt, Assessment of

Global Positioning System Measurements for Studies of Crustal Deformation, *J. Geophys. Res.*, *94*, 13,635-13,650, 1989.

Defense Mapping Agency, Department of Defense World Geodetic System 1984, *DMA TR 8350.2*, 121 p., D. M. A. Washington, D. C., 1987.

DeMets, C., R. G. Gordon, S. Stein, and D. F. Argus, A revised estimate of Pacific-North America motion and implications for western North America plate boundary zone tectonics, *Geophys. Res. Letts.*, *14*, 911-914, 1987.

DeMets, C., R. G. Gordon, D. F. Argus, and S. Stein, Current plate motions, *Geophys. J. Inter.*, *101*, 425-478, 1990.

Dong, D., and Y. Bock, Global Positioning System network analysis with phase ambiguity resolution applied to crustal deformation studies in California, *J. Geophys. Res.*, *94*, 3949-3966, 1989.

Feigl, K. L., R. W. King, and T. H. Jordan, Geodetic measurement of tectonic deformation in the Santa Maria fold and thrust belt, California *J. Geophys. Res.*, *95*, 2679-2699, 1990.

Fliegel, H. F., W. A. Feess, W. C. Layton, and N. W. Rhodus, The GPS radiation force model, paper presented at First International Symposium on Precise Positioning With the Global Positioning System, Int. Assoc. of Geod., Rockville, Md., April 15-19, 1985.

Goldstein, H., *Classical Mechanics*, Addison-Wesley, 672 p., 1980.

Gurtner, W., G. Beutler, I. Bauersima, and T. Schildknecht, Evaluation of

GPS carrier difference observations: The Bernese second generation software package, paper presented at First International Symposium on Precise Positioning With the Global Positioning System, Int. Assoc. of Geod., Rockville, Md., April 15-19, 1985.

Huang, W., H. Kanamori, and L. T. Silver, Seismic strain rates in southern California, *EOS Trans.*, submitted, 1990.

Jackson, J., and D. McKenzie, The relationship between plate motions and seismic moment tensors, and the rates of active deformation in the Mediterranean and Middle East, *Geophysical Journal, 93*, 45-73, 1988.

Jaeger, J. C., and N. G. W. Cook, *Fundamentals of Rock Mechanics*, Methuen, London, 1969.

King, N. E., P. Segall, and W. Prescott, Geodetic measurements near Parkfield, 1959-1984, *J. Geophys. Res., 92*, 2747-2766, 1987.

King, R. W., E. G. Masters, C. Rizos, A. Stolz, and J. Collins, *Surveying with GPS, Monograph 9*, School of Surveying, The University of New South Wales, Kensington, Australia, 1985.

Kostrov, V. V., Seismic moment and energy of earthquakes, and seismic flow of rock, *Iz. Acad. Sci. USSR Phys. Solid Earth, 1*, 23-44, 1974.

Lee, W. H. K., R. F. Yerkes, and M. Simirenko, Recent earthquake activity and focal mechanisms in the western Transverse Ranges, California, *U.S.G.S. circ. 799a*, 1-15, 1979.

McCulloch, D. S., Evaluating Tsunami Potential, in Evaluating earthquake

hazards in the Los Angeles Region – An earth-science perspective, *U. S. Geol. Surv. Prof. Pap., 1360*, 375-413, 1985.

Minster, J. B., and T. H. Jordan, Present-day plate motions, *J. Geophys. Res., 83*, 5331-5354, 1978.

Minster, J. B., and T. H. Jordan, Vector constraints on Quaternary deformation of the western United States east and west of the San Andreas Fault, in *Tectonics and Sedimentation Along the California Margin, 38*, edited by J. K. Crouch and S. B. Bachman, Society of Economic Paleontologists and Mineralogists, Pacific Section, Los Angeles, California, 1-16, 1984.

Owens, J. C., Optical refractive index of air: dependence on pressure, temperature, and composition, *Appl. Opt., 6*, 51-58, 1967.

Patterson, R. H., Neotectonics of the Santa Cruz Island Fault, California, *Earthquake Notes abst., 49*, p. 21, 1978.

Prescott, W. H., J. C. Savage, and W. T. Kinoshita, Strain Accumulation Rates in the Western United States Between 1970 and 1978, *J. Geophy. Res., 84*, 5423-5435, 1979.

Richter, C. F., *Elementary Seismology*, W. H. Freeman and Co., 768 p., 1958.

Rocken, C., The global positioning system: A new tool for tectonic studies; *Thesis*, University of Colorado, Boulder, 365 p., 1988.

Savage, J. C., and W. H. Prescott, Precision of Geodolite measurements for determining fault movements, *J. Geophys. Res., 78*, 6001-6008, 1973.

Savage, J. C., W. H. Prescott, M. Lisowski, and N. E. King, Strain accumulation in southern California, 1973-1980, *J. Geophys. Res.*, *86*, 6991-7001, 1981.

Slawson, W. F., and J. C. Savage, Deformation near the creeping and locked segments of the San Andreas fault, Cholame Valley, California (1970-1980), *Bull. Seismol. Soc. Amer.*, *73*, 1407-1414, 1983.

Snay, R. A., Horizontal Deformation in New York and Connecticut: Examining Contradictory Results From the Geodetic Evidence, *J. Geophys. Res.*, *91*, 12,695-12,702, 1986.

Wallace, T. C., D. V. Helmberger, and J. E. Ebel, A broadband study of the August 13, 1978 Santa Barbara earthquake, *Bull. Seismol. Soc. Amer.*, *71*, 1701-1718, 1981.

Weldon, R., and G. Humphreys, A kinematic model of southern California, *Tectonics*, *5*, 33-48, 1986.

Wells, D., N. Beck, D. Delikaraoglou, A. Kleusberg, E. J. Krakiwsky, G. Lachapelle, R. B. Langley, M. Nakiboglu, K. Schwarz, J. M. Tranquilla, and P. Vanicek, *Guide to GPS Positioning*, Canadian GPS Associates, Fredericton, N. B., Canada, 1987.

Wesson, R. L., R. A. Page, D. M. Boore, and R. F. Yerkes, Expectable earthquakes and their ground motions in the Van Norman reservoirs area, *U.S. Geol. Survey Cir.*, *691-B*, 1-9, 1974.

Yeats, R. S., Deformation of a 1 Ma datum, Ventura basin, California, Final

Report for Contract 14-08-0001-18283 Mod 3, U.S. Geological Survey, Menlo Park, 1981.

Yeats, R. S., Large-scale Quaternary detachments, Ventura basin, southern California, *J. Geophys. Res.*, *88*, 569-584, 1983.

Yeats, R. S., Late Quaternary slip on the Oak Ridge fault, Transverse Ranges, California: implications for seismic risk, *J. Geophys. Res.*, *93*, 12137-12150, 1988.

Yerkes, R. F., and W. H. K. Lee, Late Quaternary deformation in the western Transverse Ranges, *U.S. Geological Survey Circular 799-B*, 10 p., 1979.

Yerkes, R. F., H. G. Greene, J. C. Tinsley, and K. R. Lajoie, Seismotectonic setting of the Santa Barbara channel area, southern California, *U.S. Geol. Surv. Misc. Field Stud.*, MF-1169, 1980.

Yerkes, R. F., Geologic and seismologic setting, in Evaluating earthquake hazards in the Los Angeles Region -- An earth-science perspective, *U. S. Geol. Surv. Prof. Pap.*, *1360*, 25-41, 1985.

Yerkes, R. F., and W. H. K. Lee, Late Quaternary deformation in the western Transverse Ranges, *U.S. Geol. Surv. Prof. Pap.*, *1339*, 71-82, 1988.

Ziony, J. I., and R. F. Yerkes, Evaluating earthquake and surface-faulting potential, in Evaluating earthquake hazards in the Los Angeles Region -- An earth-science perspective, *U. S. Geol. Surv. Prof. Pap.*, *1360*, 43-91, 1985.

Chapter 4

GPS Measurements of Deformation Associated with the 1987 Superstition Hills Earthquake: Evidence for Conjugate Faulting

Abstract

Large station displacements observed from Imperial Valley GPS campaigns are attributed to the November 24, 1987 Superstition Hills earthquake sequence. Thirty sites from a 42 station GPS network established in 1986 have been reoccupied during 1988 and/or 1990. Displacements at three sites within 3 kilometers of the surface rupture approach 0.5 m. Eight additional stations within 20 km of the seismic zone are displaced at least 10 cm. This is the first occurrence of a large earthquake (M_S 6.6) within a preexisting GPS network. Best-fitting uniform slip models of rectangular dislocations in an elastic half-space indicate 130 cm right-lateral displacement along the northwest trending Superstition Hills fault and 30 cm left-lateral offset along the conjugate northeast trending Elmore Ranch fault. The geodetic moments are 9.4 x 10^{25} dyne-cm and 2.3 x 10^{25} dyne-cm for the Superstition Hills and Elmore Ranch faults, respectively. Distributed slip solutions using Singular Value Decomposition suggest near uniform displacement along the Elmore Ranch fault and concentrated slip to the northwest and southeast along the Superstition Hills fault. A significant component of non-seismic secular displacement is observed across the Imperial Valley, which is attributed to interseismic plate-boundary elastic deformation.

4.1 Introduction

The Global Positioning System (GPS) is rapidly becoming one of the most important tools to study tectonic deformation. By recording signals from earth orbiting satellites it is possible to determine 3-dimensional coordinates of geodetic monuments with high accuracy. With repeated observations the station displacement or deformation between surveys is measured. GPS can be used to monitor secular deformation such as that associated with plate motion, or to record rapid strain fluctuations such as those due to seismic and volcanic activity. In its final configuration scheduled for the mid 1990's, 18 satellites will be deployed in 6 orbital planes (with 3 additional satellites used as active spares). When GPS becomes fully operational it will be possible to continuously determine 3-dimensional positions anywhere on or near the earth. The available satellite constellation existing for the last several years, was optimized for North America making geodetic studies in California practical. The observation window in which enough satellites have been visible to obtain the high accuracies necessary to measure tectonic motion has been about 6 to 8 hours each day.

On November 24, 1987, two large earthquakes separated by 12 hours occurred in the northwest portion of the Imperial Valley region of southern California. The first event was located on a northeast trending seismic lineament and was followed 12 hours later by rupture along the northwest trending Superstition hills fault. What makes this earthquake sequence so significant from a GPS standpoint, is that it occurred spatially and temporally within a preexisting GPS network. This network was established in the Imperial Valley in 1986, with partial resurveys in 1988 and 1990.

Fifteen stations are located within 20 km of the rupture zone; three stations are within 3 km. This is the first occurrence of a large earthquake within a preexisting GPS network.

We compute GPS displacements in the Imperial Valley between 1986 and 1990. Observed movements of nearly 0.5 meters are attributed to the Superstition Hills earthquake sequence. The earthquake-induced displacements are inverted to estimate seismic slip and the corresponding geodetic moment along the rupture planes. In addition, there is a large component of deformation which can not be explained by the seismic disturbance; we assume this to be a manifestation of continuous strain accumulation across the Imperial Valley due to the relative motion of the Pacific and North American plates.

4.2 Imperial Valley Seismicity and Tectonics

The Imperial Valley region of southern California is a complex transition zone between crustal spreading in the Gulf of California and right-lateral transform motion along the San Andreas fault (Figure 4.1) [*Lomnitz et al.*, 1970; *Elders et al.*, 1972]. The valley is 4-5 million years old and has been filled by up to 5 km of late Cenozoic sediments [*Fuis et al.*, 1982]. The major fault systems and structural grain of the valley trend to the northwest, roughly parallel to the direction of plate motion. A significant fraction of the North American and Pacific relative motion may be accommodated across this region.

The valley is one of the most seismically active regions of California

(Figure 4.1) with much of the activity occurring along the Imperial fault and within the Brawley Seismic Zone [*Johnson and Hill*, 1982]. Several large earthquakes have occurred in and near the Imperial Valley since 1940 (Figure 4.1). The Imperial fault ruptured with a M_S 7.1 event in 1940 and a M_L 6.6 event in 1979 [*U.S. Geol. Surv.*, 1982]. Segments of the San Jacinto fault system broke with a M_L 6.2 earthquake in 1954 (Clark segment) and the 1968 M_L 6.5 Borrego Mountain event (Coyote Creek segment). The most GPS relevant episode of seismic activity occurred in 1987 along the Superstition Hills segment of the San Jacinto fault system, with a M_S 6.2 earthquake on a northeast trending seismic lineament followed 12 hours later by a M_S 6.6 event on the Superstition Hills fault.

Conventional geodetic measurements suggest considerable deformation across the Imperial Valley. In fact, a significant fraction of the Pacific-North American relative plate motion may be accommodated here. New global plate model estimates (NUVEL-1) [*DeMets et al.*, 1987; *DeMets et al.*, 1990] predict the rate of relative motion between the North American and Pacific plates (at Imperial Valley coordinates: 33.0°N, 115.5°W) is 4.7 cm/yr oriented N39.6°W. Triangulation measurements spanning this region have been modeled as 4.3 cm/yr of plate-boundary deformation averaged between 1941 and 1986 [*Snay and Drew*, 1988]. Trilateration measurements made by the U.S.G.S. between 1972 and 1987 indicate 3.45 cm/yr relative movement between stations on opposite sides of the valley [*Prescott et al.*, 1987b]. The orientations of the conventional geodetic displacements are approximately N40°W, although to some extent the direction is non-unique and depends upon a priori assumptions [e.g., *Prescott*, 1981]. In addition, the conventional

Figure 4.1: Seismicity and major fault systems of the Imperial Valley. The Brawley Seismic Zone is the region of anomalously high activity between the northern Imperial and southern San Andreas faults. The valley represents a transition zone between crustal spreading in the Gulf of California to the south and right-lateral transform motion along the San Andreas system.

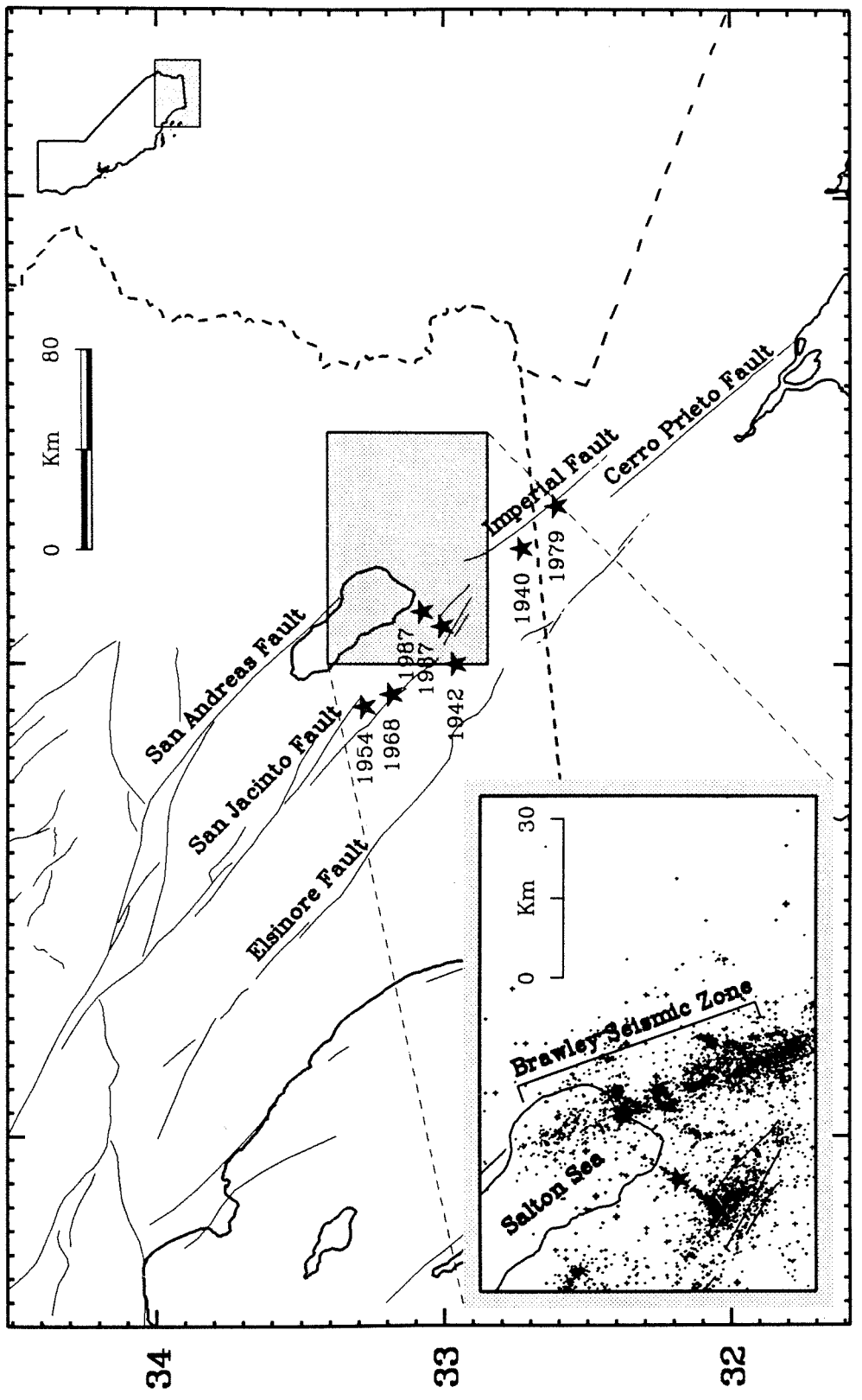
San Andreas Fault
San Jacinto Fault
Elsinore Fault
Imperial Fault
Cerro Prieto Fault
1940
1979
1942
1954
1968
1987
1987
0
Km
80
0
Km
30
Brawley Seismic Zone
Salton Sea
34
33
32
-118
-116
-114

geodetic measurements indicate that deformation is concentrated in a narrow 20 km wide zone along the Imperial fault, while to the north it is distributed over a region at least 50 km wide. Presumably, deformation is transferred from the Imperial fault, which acts as the primary strain release mechanism near the border, to distributed shear along the San Andreas, San Jacinto, and Elsinore faults.

4.3 Superstition Hills Earthquake Sequence

On November 24, 1987 (1:54 GMT), a large M_S 6.2 earthquake occurred along a northeast trending seismic lineament northeast of the Superstition Hills fault (Figure 4.2) [*Magistrale et al.*, 1988]. The focal mechanism and aftershock sequence, which extended for 26 km to the northeast and into the Brawley Seismic Zone, are consistent with left-lateral strike slip motion on a vertical fault. Seven foreshocks were recorded in the 22 minutes prior to the main event, including two with $M_L > 4.0$. Surface rupture consisted of a complex pattern of left-lateral northeast-trending offsets ranging in length from 1.5 to 10 km, and with maximum displacements between 3 and 13 cm [*Budding and Sharp*, 1988; *Hudnut et al.*, 1989a]. We refer to this northeast trending lineament as the Elmore Ranch fault, although more precisely this name refers only to the longest of the surface fractures.

Twelve hours after the Elmore Ranch event (13:15 GMT), a M_S 6.6 earthquake occurred along the northwest trending Superstition Hills fault. The epicenter was near the intersection of the Elmore Ranch and Superstition Hills faults. Strong ground motion and teleseismic data suggest the rupture process for this second event was somewhat complicated, consisting of

multiple sub-events [*Bent et al.*, 1989; *Frankel and Wennerberg*, 1989; *Hwang et al.*, 1990; *Wald et al.*, 1990]. Surface rupture extended 24 km along the previously mapped trace of the fault [*Williams and Magistrale*, 1989]. Up to 50 cm right-lateral displacement were measured immediately following the earthquake. The aftershock pattern was concentrated slightly to the west of the fault and did not extend the length of the surface rupture. *Magistrale et al.* [1989] suggested the aftershock sequence was highly correlated with basement structure. Both the Superstition Hills and Elmore Ranch events triggered sympathetic surface offsets along the Imperial, San Andreas, and Coyote Creek faults [*McGill et al.*, 1989; *Hudnut and Clark*, 1989].

Significant afterslip was recorded along the Superstition Hills fault following the second mainshock. No afterslip was measured along any of the surface ruptures associated with the Elmore Ranch event. In fact, all seismic activity essentially stopped along this segment after the initiation of the 2nd mainshock.

One of the most interesting aspects of this earthquake sequence is the conjugate nature of faulting. That is, two surface ruptures oriented nearly perpendicular to each other. As discussed below, this type of fault interaction may be typical of Imperial Valley tectonics and may dictate the mode of stress/strain transfer from one fault system to another.

What makes the Superstition Hills earthquake sequence unique from a GPS perspective is that it occurred within a preexisting GPS network. Stations located near the seismic rupture zone were displaced nearly 0.5 meters. These movements, as well as smaller displacements observed at

Figure 4.2: Seismicity and surface faulting associated with the November 24, 1987 Superstition Hills earthquake sequence. A M_S 6.2 event occurred along a northeast trending structure (referred to here as the Elmore Ranch fault) and was followed by 12 hours with a M_S 6.6 event along the northwest trending Superstition Hills fault. The focal mechanisms, aftershock distribution, and surface offset measurements are consistent with left-lateral strike-slip motion along the Elmore Ranch fault and right-lateral strike-slip motion along the Superstition Hills fault. A significant amount of postseismic slip was observed along the surface trace of the Superstition Hills fault, while activity essentially ceased on the Elmore Ranch fault after the M_S 6.6 event. The shaded strips along each fault indicate the geometrical extent of the dislocations used to model the geodetic displacements.

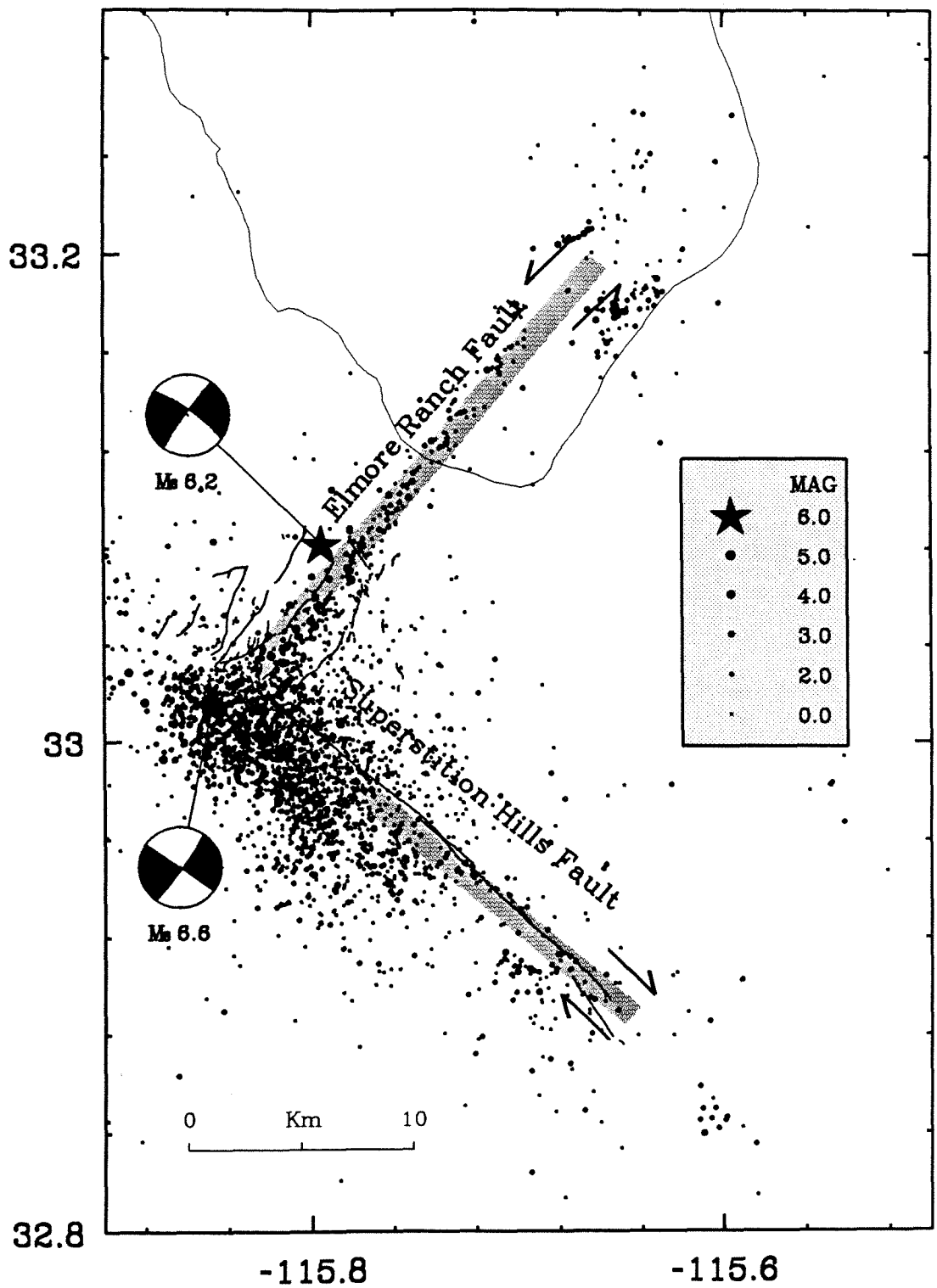
33.2
33
32.8
-115.8
-115.6
Elmore Ranch Fault
Superstition Hills Fault
Ms 6.2
Ms 6.6
MAG
6.0
5.0
4.0
3.0
2.0
0.0
0
Km
10

nearby stations can be inverted to infer properties of the rupture process. This is the first time GPS measurements have recorded the deformation from a large earthquake.

4.4 GPS Observations

After a brief introduction to the Global Positioning System, in this section we report how the GPS data were obtained from field campaigns in 1986, 1988, and 1990, as well as the processing methods used to obtain station coordinates. The GPS displacement vectors between surveys are presented and we discuss how measurement errors are handled for this study. More complete details about the Global Positioning System, including theoretical aspects and processing methods, are found in *King et al.* [1985], *Wells et al.* [1987], and *Rocken* [1988].

The signal structure broadcast from each GPS satellite consists of two carrier phase signals modulated by a navigational message as well as pseudo-random codes. The two carrier frequencies, known as the L1 and L2 phases, are broadcast at 1575.42 Mhz (L1) and 1227.60 Mhz (L2). This is equivalent to wavelengths of about 19 cm for the L1 and 24 cm for the L2. The navigational message contains the satellite coordinates (broadcast ephemeris), clock parameters, satellite health, and general system status. The pseudo-random codes are accurate time marks which allow a GPS receiver to determine the transmission time of the signal. When scaled by the speed of light, the pseudorange, or the satellite-receiver distance is computed. If measurements to at least 4 GPS satellites are available, and if satellite coordinates are known (usually with the broadcast ephemeris), the 3-

dimensional receiver position as well as the satellite-receiver time offset can be determined. The positioning accuracy with the pseudorange is 1 to 100 m, depending on whether the P or C/A code is used, the receiver type, length of observation, and the static or kinematic behavior of the instrument. It is the pseudorange which will be used for civilian and military navigation. For highly accurate geodetic positioning, however, it is necessary to use the carrier phase measurements in a post-processing mode. That is, the data collected in the field are brought back to the office or laboratory for analysis, usually with a fairly robust computer software system.

GPS Surveys -- Data Collection

The GPS data for this study were collected during 4 Imperial Valley field campaigns from 1986 to 1990 (Table 4.1). A total of 46 stations in or near the valley have been occupied at least once during this interval (Figure 4.3), while 30 sites have been reoccupied since 1986 (Figure 4.3, Table 4.2). TI-4100 GPS receivers supporting GESAR software were used during 1986 and 1988, while Trimble 4000SDT instruments were used during the 1990 survey As one of the first commercially available instruments, the TI-4100 is a code correlating receiver which allows the simultaneous tracking of up to 4 satellites at a time. This instrument records the L1 and L2 carrier signals, the P and C/A pseudo-codes, and the broadcast message. The Trimble 4000SDT is able to record the L1 and L2 phase components for up to 8 satellites at once, as well as the C/A code and the broadcast message

The National Geodetic Survey (NGS) occupied 54 sites in southern California in May/June 1986; 42 stations were located in or near the Imperial

Figure 4.3a: Imperial Valley and related GPS stations surveyed in 1986, 1988, and/or 1990. Station names for sites indicated in the shaded box are given in Figure 4.3b.

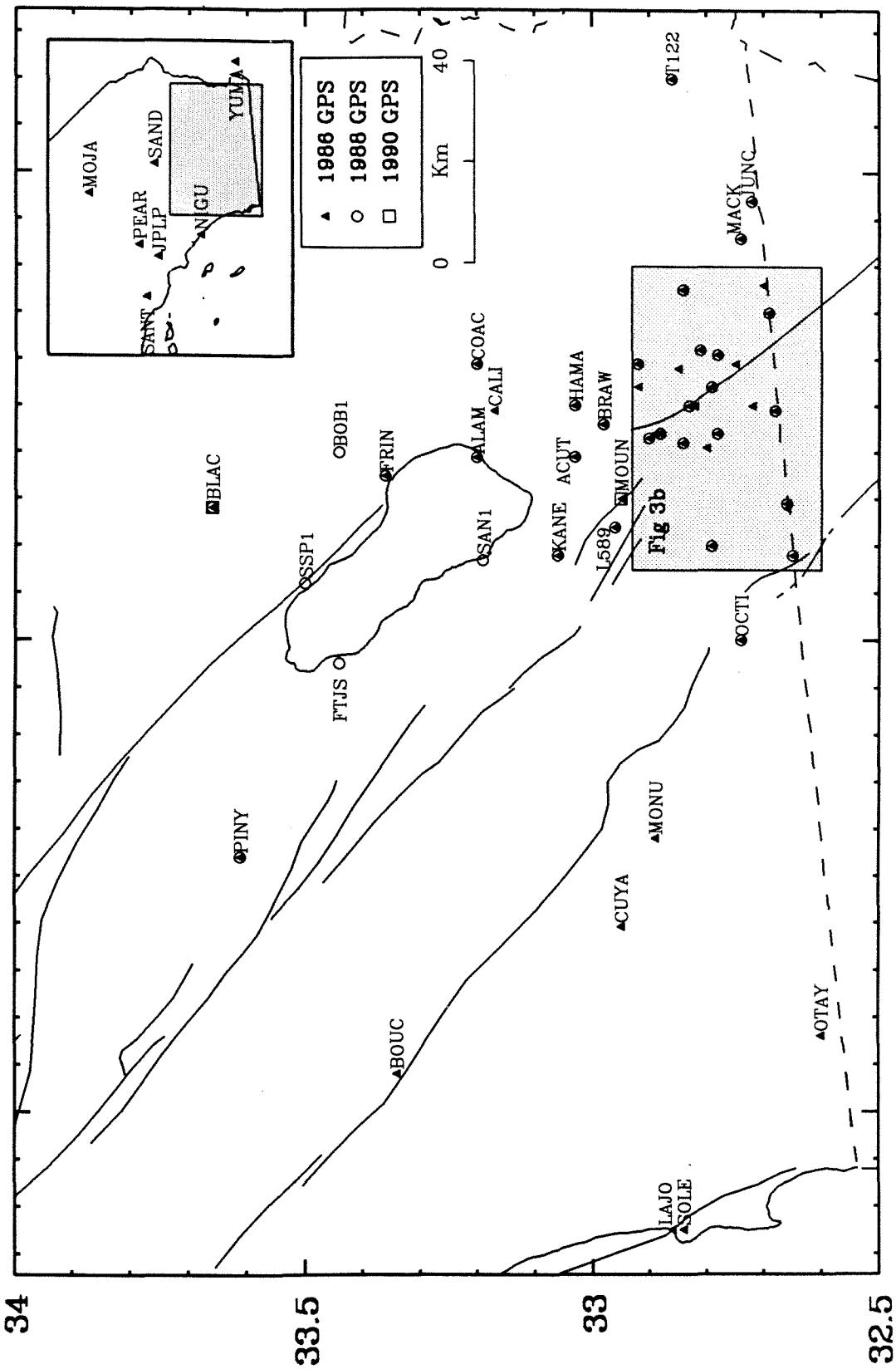
1986 GPS
1988 GPS
1990 GPS
0
40
Km
MOJA
PEAR
JPLP
SAND
YUMA
SANT
IGU
BLAC
PINY
BOUC
LAJO
SOLE
CUYA
MONU
OTAY
FTJS
OSSP1
OBOB1
FRIN
SAN1
ALAM
CALI
COAC
KANE
ACUT
HAMA
BRAW
MOUN
L589
OCTI
MACK
JUNC
T122
Fig 3b
34
33.5
33
32.5
-117
-116
-115

Figure 4.3b: Central-southern Imperial Valley and related GPS stations surveyed in 1986, 1988, and/or 1990.

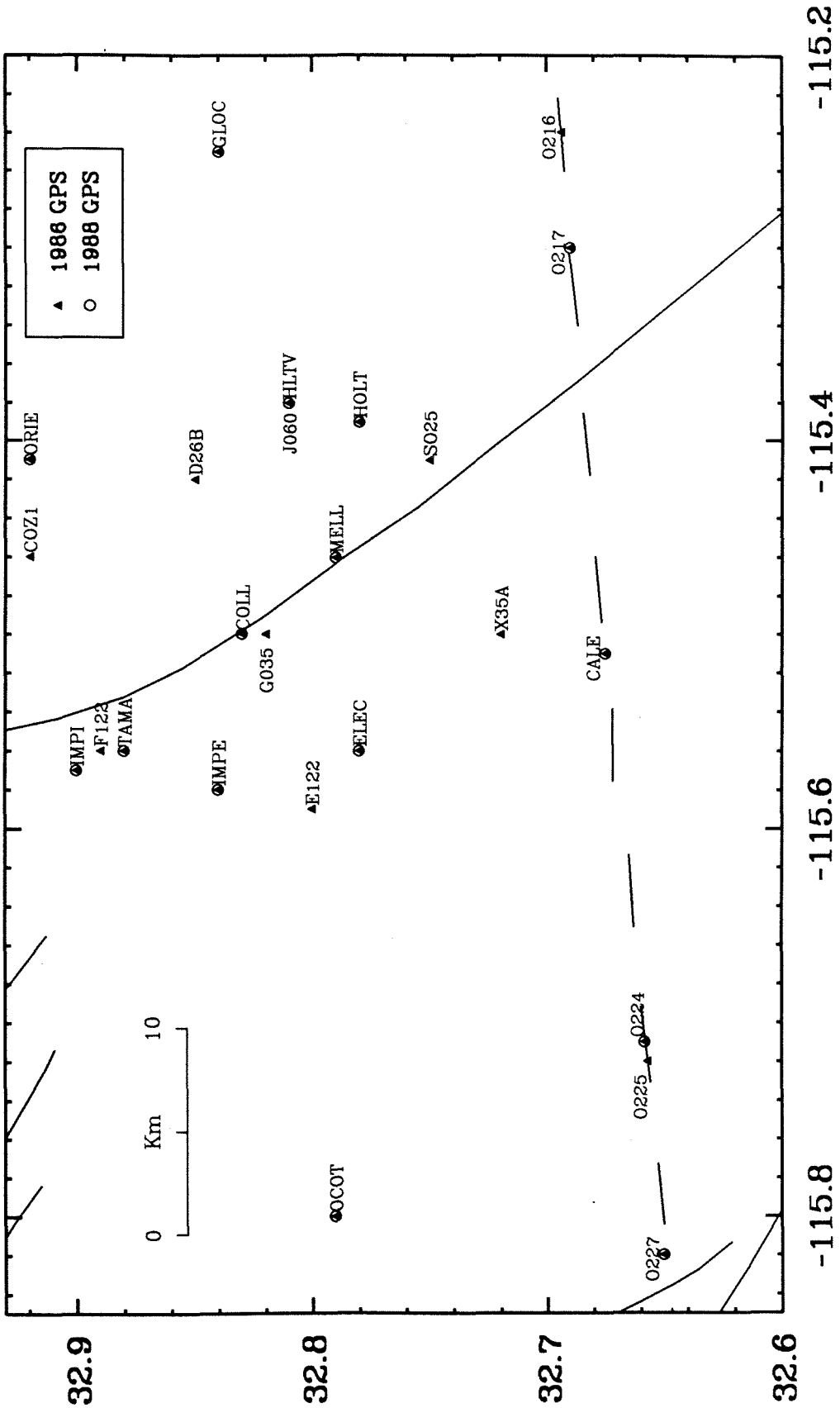
1986 GPS
1988 GPS
GLOC
0216
0217
ORIE
COZ1
D26B
J060
HLTV
HOLT
S025
MELL
COLL
G035
X35A
CALE
MPI
F122
TAMA
MPE
E122
ELEC
OCOT
0225
0224
0227
0
Km
10
32.9
32.8
32.7
32.6
-115.8
-115.6
-115.4
-115.2

Table 4.1 Imperial Valley GPS Campaign Summary

Year	Month	Days	Stations	Organization
1986	May/June	20	42	NGS
1988	February/March	9	19	UNAVCO
1988	March/April	6	21	NGS
1990	April	1	3	UNAVCO/RCFC

NGS - National Geodetic Survey
UNAVCO - University Navstar Consortium
RCFC - Riverside County Flood Control

Table 4.2 Reoccupied GPS Stations

Station Name	Abbr.	Occupation				Longitude	Latitude	Elevation
		1986	1988[1]	1988[2]	1990	°	°	(m)
Acute 1934	ACUT	•	•	•		-115.6093	33.0300	-80.91
Alamo	ALAM	•	•	•		-115.6111	33.1964	-72.91
Black Butte NCMN 1982	BLAC	•	•		•	-115.7198	33.6638	490.01
Brawley 2 rm 5	BRAW	•		•		-115.5434	32.9773	-66.78
Calexico 1954	CALE	•	•			-115.5064	32.6645	-34.07
Coach	COAC	•	•			-115.4070	33.1962	-8.40
College 1967	COLL	•	•			-115.5024	32.8269	-54.63
El Centro 2 1959	ELEC	•		•		-115.5622	32.7846	-45.76
Frink 1934	FRIN	•	•	•		-115.6470	33.3603	-85.39
GLO Cornew 1934	GLOC	•	•			-115.2465	32.8396	-15.46
Hamar 2 1967	HAMA	•	•	•		-115.5007	33.0375	-79.80
Holt 1924	HOLT	•		•		-115.3963	32.7814	-36.79
Holtville (Alt) 1934	HLTV	•		•		-115.3821	32.8084	-38.77
Imp 1934	IMPI	•		•		-115.5698	32.8982	-59.27
Imperial 1934	IMPE	•		•		-115.5788	32.8439	-51.85
Junction	JUNC	•		•		-115.0619	32.7092	8.35
Kane 1939	KANE	•	•	•		-115.8237	33.0614	10.05
L 589 1967	L589	•	•	•		-115.7611	32.9506	13.62
Mack 2 1967 bm reset	MACK	•		•		-115.1441	32.7288	1.20
Mello 3 1967	MELL	•		•		-115.4653	32.7961	-47.00
Mound 1934	MOUN	•			•	-115.6998	32.9502	3.40
Ocotillo NCMN 1982	OCOT	•	•	•		-115.7962	32.7901	-36.43
Ocotillo 1935	OCTI	•	•	•		-116.0017	32.7338	111.33
Offset 217	O217	•	•	•		-115.3131	32.6782	-17.16
Offset 224	O224	•		•		-115.7055	32.6493	50.00
Offset 227	O227	•		•		-115.8173	32.6414	70.64
Orient 1939	ORIE	•	•			-115.4064	32.9168	-61.36
Pinyon Flat	PINY	•		•		-116.4588	33.6093	1235.88
T 1226	T122	•		•		-114.8050	32.8583	141.19
Tamarisk 3 1967	TAMA	•	•			-115.4783	32.8829	-68.19

[1] UNAVCO
[2] NGS

Valley. Most marks were observed at least two days (Table 4.3), although redundant baselines were relatively uncommon (i.e., simultaneous occupation of the same station-station pair for two or more days). Unfortunately, the quality of the observations were very poor. The scheduled 4.5 hour daily occupations were somewhat less than the 6-8 hour sessions typical of other southern California campaigns. In addition, due to a variety of equipment and logistical problems, less than 2 hours of data were collected at several sites. In the observation scenario, there was less than a 2 hour period in which more than 3 satellites were simultaneously tracked. In fact, there was a scheduled 1 hour gap in Satellite 6 during the middle of the measurement session. The data were generally noisy and the final double difference phase observables may contain uncorrected cycle slips.

In February/March 1988 university field crews (UNAVCO) observing for 9 days reoccupied 15 of the Imperial Valley marks, as well as establishing 4 new stations along the Salton Sea. These new sites were installed at tide gauge monitoring facilities and will be used to constrain vertical GPS baseline components and for monitoring tectonic tilting in the Salton Trough. Most monuments were occupied for 2 days (Table 4.3) (1 was observed 3 days, 1 for 4 days, and 2 for 1 day). The scheduled nightly observation scenario lasted 7.5 hours, with a total of 7 satellites tracked.

In March/April 1988 the NGS reoccupied 21 of the 1986 stations (7 of which were observed by the university crews a month earlier). Most sites were occupied only 1 day (Table 4.3). The daily observation period of 6.0 hours was slightly shorter than the February/March survey, although 7 satellites were tracked each day.

Table 4.3 Imperial Valley GPS Occupation History

Year	Day	Stations							
1986	141	COLL	CALE	L589					
	142	O217	O216	MELL	E122	HOLT	ELEC	O227	
	143	COLL	CALE	TAMA	HLTV	MACK	O224	IMPE	O225
	144	OCTI	IMPI	F122	OCOT		O224	O227	O225
	145	HAMA	IMPI	ALAM			ACUT	MOUN	
	146	HAMA	CALE	TAMA	ORIE		GLOC	CO12	BRAW
	147	COAC	CALI	ALAM	ORIE	FRIN	BLAC	KANE	
	148	OCTI	MONU	L589	OCOT	FRIN	ACUT	KANE	BRAW
	149	O217	O216	J060	T122	MACK	GLOC	MOUN	YUMA
	150	COAC	MONU	MELL	T122	HOLT	BLAC	CO12	YUMA
	151	G035	S025	L589	D26B	HOLT	ACUT	X35A	JUNC
	153	G035	S025	J060	D26B			X35A	BRAW
	161	PINY		SAND	OCOT	PEAR	BLAC		
	162	PINY		SAND	OCOT	PEAR	BLAC		YUMA
	163	PINY		SAND	OCOT	SANT	BLAC		YUMA
	164	PINY		JPLP	OCOT		BLAC		YUMA
	167	PINY	MONU	MOJA	NIGU	SOLE			YUMA
	168	PINY	MONU	MOJA	NIGU	SOLE	OTAY		YUMA
	169	LAJO	MONU	MOJA	BOUC		OTAY		YUMA
	170	LAJO	MONU	MOJA	BOUC	CUYA			YUMA
1988[1]	55	L589	BLAC	FTJS	COAC	SAN1			
	56	ALAM	GLOC	OCOT	SSP1	SAN1			
	57	ALAM	GLOC	OCOT	SSP1	ORIE			
	58	L589	GLOC	BOB1	COAC	ORIE			
	59	L589	BLAC	FTJS	KANE	FRIN			
	60	L589	CALE	TAMA	KANE	FRIN			
	62	O217	CALE	TAMA					
	63	O217	COLL	OCTI					
	64	HAMA	COLL	OCTI					
1988[2]	88	PINY	OCOT	BRAW	HOLT	MELL			
	89	PINY	OCOT	IMPE	IMPI	O217			
	90	PINY	OCOT	ACUT	HAMA	KANE			
	91	PINY	OCOT	ELEC	HLTV	OCTI			
	92	PINY	OCOT	MACK	O227	T122			
	93	PINY	FRIN	JUNC	L589	O224			
1990	100	BLAC	MOUN	BC01					

Day is Julian day of year

[1] UNAVCO

[2] NGS

In addition to the UNAVCO and NGS campaigns, GPS observations in 1988 were made at Mojave (California), Westford (Massachusetts), and Richmond (Florida). These sites are continuously monitored as part of the Cooperative International GPS Network (CIGNET) [*Chin*, 1988]. Data from CIGNET stations are used to improve satellite orbits in the GPS processing. Unfortunately, these observations are frequently of poor quality and contain abundant cycle slips. During the 1988 campaign, observations were not always available or usable at all CIGNET sites on all days (Table 4.4).

Station MOUN (Mound), which was surveyed in 1986, was destroyed from the 1987 earthquake sequence. The site is located less than 1 km from the surface rupture of the Superstition Hills fault. Field investigation during early 1988 reveiled that the monument and supporting concrete base had been completely uprooted from the ground. Destroyed monuments usually can not be tied to previous surveys because of the high accuracy required for crustal motion research. If the suspected deformation is significantly large, however, some information may be recovered if the monument (or a substitute) is reset in approximately the same location. Site inspection at MOUN clearly showed where the old monument had been and in early April, 1990 a rebar rod acting as a temporary benchmark was set at approximately the same position. We estimate the temporary mark was set within 0.15 m of the previous monument. Because of its proximity to the 1987 rupture zone, the calculated seismic displacement at MOUN is about 0.5 m. Therefore, reoccupation of this site should retrieve a tectonic component larger than the expected uncertainty.

The 1990 survey was conducted to establish the displacement of MOUN

relative to its 1986 position. This "mini-campaign" (Table 4.3), which included stationary GPS receivers at only three sites (MOUN, BLAC, and BC01) was performed interactively with kinematic GPS transects along the southern San Andreas fault (K. Hudnut, personal communication, 1990). Data were collected for only one night; a total of 9 satellites were visible during the scheduled 7.0 hour experiment.

GPS Processing

The 1986 GPS observations were processed with the GPS22 software developed at the National Geodetic Survey. Satellite orbital information was provided by the NSWC (Naval Surface Weapons Center). A tropospheric delay parameter was solved at each station, constrained by surface meteorological measurements. Ambiguities were fixed to the nearest integer. Each of the 20 days of observation was processed separately, and the daily solutions were combined to form one set of station coordinates with the geodetic adjustment program DYNAP (DYNamic Adjustment Program) [*Drew and Snay*, 1989]. All coordinates were computed in the WGS-84 reference frame [*Defense Mapping Agency*, 1987]. Due to poor data quality and observation constraints, the accuracy of these measurements is believed to be on the order of 1 ppm (parts per million) [*Neugebauer*, 1988].

Data from both 1988 campaigns were processed with the Bernese GPS analysis software (version 3.0), from the University of Bern in Switzerland. (Preliminary processing such as data translation and cycle slip fixing were performed with an earlier version of the software.) The Bernese GPS analysis package allows 3-dimensional station coordinates to be determined from the

integration of carrier phase, pseudo-range, and orbital data [e.g., *Gurtner et al.*, 1985; *Beutler et al.*, 1985; *Rocken*, 1988]. In addition to measuring station coordinates, the double difference estimation algorithm can solve for adjustments to six Keplerian elements and two radiation pressure coefficients for each satellite, an atmospheric zenith delay parameter at each station, a clock error term at each site, ionospheric model coefficients, and cycle ambiguity terms [e.g., *Rocken*, 1988].

For each of the 1988 surveys, all data were combined into a simultaneous multi-day solution. Surface meteorologic data (temperature, pressure, relative humidity) were used to constrain a Saasmotonian atmospheric model, and independent tropospheric zenith delay parameters were estimated at each station. We experimented with fixing ambiguities but found mixed results, therefore, ambiguities were left unresolved in the final solutions.

In addition to station coordinates, satellite orbital parameters were estimated for both solutions. GPS observations from the CIGNET tracking sites were used to constrain the orbits. The Bernese software is able to combine ephemeris information from several days into a single multi-day arc. It has been suggested that multi-day satellite arcs significantly improve GPS precision [e.g., *Lichten*, 1987]. Typically, 6 Keplerian elements and 2 radiation pressure coefficients are estimated for each satellite. *Davis et al.* [1989] utilized 4-day arcs (72 hours plus the length of the daily observation session) to analyze GPS data from North America. A 5-day satellite arc was used to process GPS data off the southern California coast near Santa Barbara [*Larsen et al.*, 1990].

There comes a point, however, when the force model describing the satellite orbits begins to break down. It is unlikely that the 10-day interval of the February/March 1988 survey (9 observation days plus one day of no measurements) could be modeled from a 10-day satellite arc. For purposes of orbit determination, therefore, this campaign is divided into multiple 3-day arc segments (days 55-57, 58-60, and 62-64), each defined by its own initial conditions. The data are still processed simultaneously, except that independent satellite parameters are estimated for each 3-day arc. For the entire campaign, 18 Keplerian orbital elements and six radiation pressure terms are estimated for each satellite. A similar technique is used for the March/April survey. The satellite orbits for this campaign are defined by two 3-day arcs (days 88-90 and 91-93).

Orbits are improved by holding the coordinates of at least 3 CIGNET stations fixed, to values well determined from VLBI and satellite laser ranging [Murray and King, MIT interoffice memorandum, 1988]. The GPS phase observables from these fiducial sites constrain the orbits, which in turn improve the solution accuracy of the unfixed stations estimated as free parameters. Notice in Table 4.4 that there are several gaps in the fiducial coverage. Although it would be better to have complete data, in general, this is not a problem since there is always at least one day in each 3-day arc interval where observations from 3 fiducial sites are available.

After each 1988 campaign was processed separately, the Cartesian coordinate differences from the two solutions were adjusted by least squares to obtain one set of coordinates for that year.

Table 4.4 CIGNET Data Availability 1988

Day	MOJA	WEST	RICH
55	●	●	
56	●	●	
57	●	●	●
58	●	●	●
59	●	●	●
60	●	●	
62	●	●	●
63	●	●	●
64	●	●	●
88	□	●	●
89	●	●	●
90	●	●	●
91	●	●	●
92	□	●	●
93	●	●	●

Day is Julian day of year
● Good quality data
□ Poor quality data

The 1990 "mini-campaign" was processed with the Trimvec software, made available from the receiver manufacturer (Trimble Navigation, Sunnyvale, California). Recall that the purpose of this survey was to establish the displacement at station MOUN, presumed large because of its proximity to the 1987 seismic rupture. Since this mark had been reset between the 1986 and 1990 occupations, the error in the displacement estimate will be fairly large ($\sim$ 15 cm). Therefore, high accuracy from a GPS perspective is not required. Only stations BLAC and MOUN were included in the processing since BC01 was not occupied in 1986. The orbits were given by the broadcast ephemeris, and surface meteorological data were used to constrain a tropospheric delay model. (This line was processed by K. Hudnut.)

Station Displacements 1986-1988

GPS station displacements for the interval 1986 to 1988 are shown in Figure 4.4. All movements are made relative to station OCTI. Only horizontal components are shown. The method in which errors are formulated and utilized is disussed below. Generally, the observed displacements can be decomposed into 3 components: 1) seismic deformation due to the Superstition Hills earthquake sequence, 2) secular deformation due to the Pacific-North American relative plate motion, and 3) measurement error attributed to poor data quality from the 1986 survey, most notable in the east-west direction.

The GPS displacement vectors suggest considerable deformation between the 1986 and 1988 campaigns, of which a significant fraction is attributed to

Figure 4.4: Imperial Valley GPS station displacements between 1986 and 1988. All movements are relative to station OCTI. The observed displacements are attributed to the 1987 earthquake sequence, secular plate-boundary deformation across the Imperial Valley, and measurement error. Movements near the 1987 rupture zone approach 0.5 m. Error ellipses are determined by multiplying the formal errors by a variance factor, determined so the average error scales as 1 ppm (parts per million). The uncertainty in the east-west direction is about 4 time larger than that in the north-south direction. The anomalous southwest trending apparent movements for those stations to the southeast are attributed to measurement error.

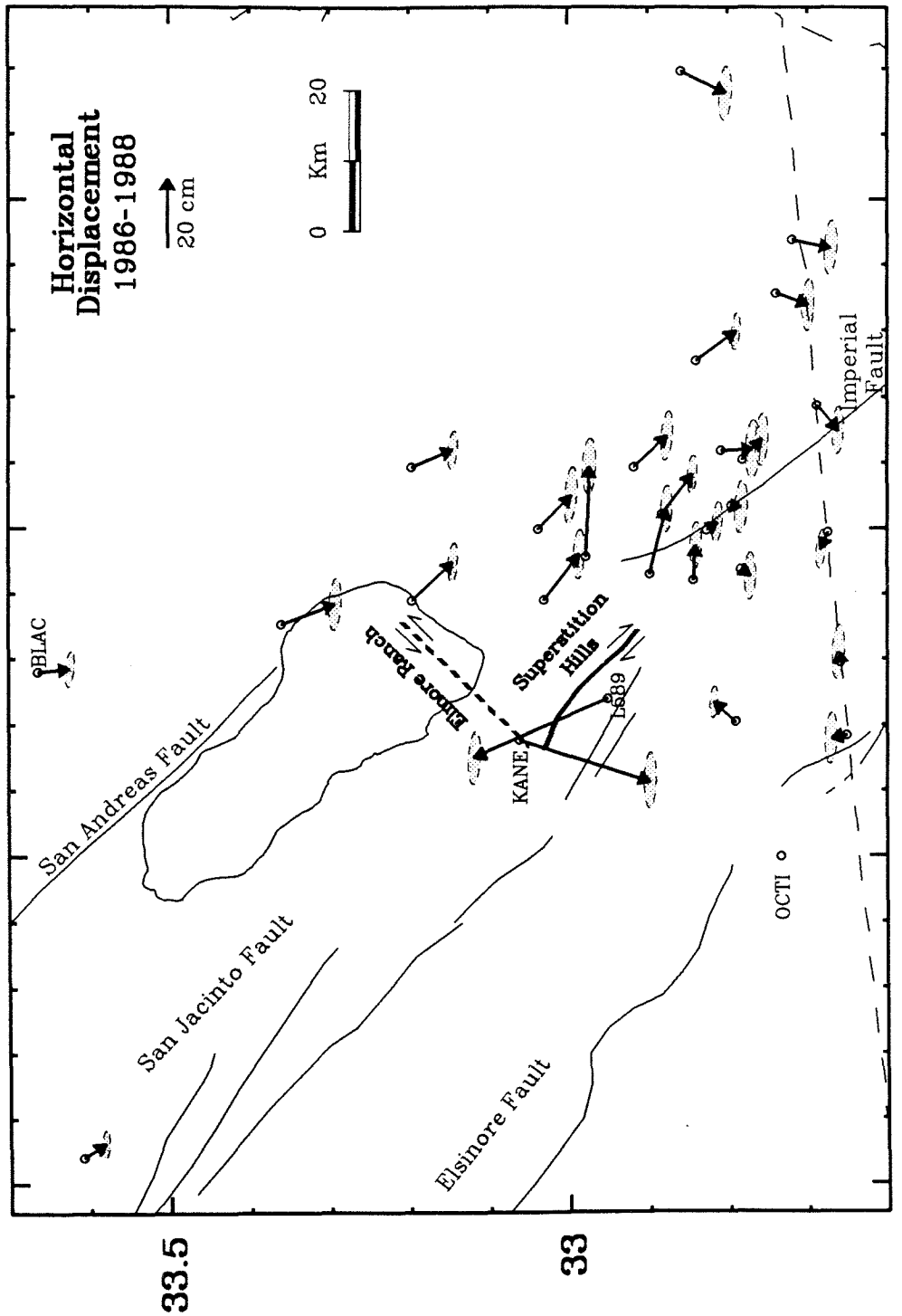
Horizontal
Displacement
1986-1988
20 cm
0 Km 20
PBLAC
San Andreas Fault
San Jacinto Fault
Elsinore Fault
Elmore Ranch
Superstition
Hills
KANE
Imperial
Fault
OCTI
33.5
33
-116.5
-116
-115.5
-115

the 1987 Superstition Hills earthquake sequence. Stations nearest the seismic rupture zone (KANE and L589) show movements on the order of 40 cm. In fact, the 13 km KANE-L589 baseline was shortened by 70 cm. The orientations of the displacements are consistent with the conjugate fault pattern indicated by the mapped surface offsets (i.e., right-lateral rupture on the Superstition Hills fault and left-lateral rupture along the Elmore Ranch fault). Other stations near the active fault system appear to have been affected by the 1987 event as well.

There is an additional component of displacement not readily explained by the seismic deformation. Stations east of the Imperial fault tend to be moving south or southeast relative to sites on the other side of the valley. This secular displacement is attributed to the relative motion between the North American and Pacific plates. Unfortunately, it is difficult to ascertain the magnitude of this deformation since station coverage west of the Imperial fault is somewhat lacking and many of these sites have rather large seismically induced displacements (recall that all GPS vectors are relative to OCTI). However, the plate-boundary deformation does appear to be considerable, which is not too surprising considering conventional geodesy indicates a significant fraction of relative plate motion is occurring across the Imperial Valley.

Also evident in Figure 4.4 are unusual movements which do not appear to be tectonically related. Most notable are the southwest trending vectors (as opposed to southeast) for those sites near the border east of the Imperial fault. It appears as if the entire network has undergone a systematic clockwise rotation. We have investigated this possibility by assuming the

network could be rotated (and translated) in terms of an outer coordinate solution by minimizing the displacement component perpendicular to the structural axis of the valley (N40°W) [e.g., *Prescott*, 1981]. Stations KANE and L589 were not included in the solution. However, the applied adjustment did not correct for the anomalous displacements, and in fact, made the apparent deformation less uniform. Although these unusual movements can not be attributed to a simple coordinate rotation, they can be explained by large east-west trending systematic measurement errors in the 1986 survey. This is consistent with the longitudinal orientation of the computed error ellipses (see below) and suggests the north-south displacement components may be a more reliable indicator of tectonic deformation.

Station Displacements 1986-1990

The 1986-1990 displacement of MOUN relative to BLAC is shown in Figure 4.5 (dashed arrow). Although the errors are large because MOUN was reset between surveys, the GPS data indicate significant movement attributed to the Superstition Hills events (recall MOUN is less than 1 km from the 1987 surface rupture). However, based on conventional geodesy as well as the 1986-1988 GPS movements, a non-seismic plate-boundary displacement component is suspected in the measurements. We attempt to remove this component by estimating the MOUN-BLAC secular displacement based on EDM observations. This is discussed in more detail below. We remove 2 years of the accumulated MOUN-BLAC secular movement, and then compute the displacement relative to station OCTI. Although the measurements still contain 2 years of non-seismic deformation, it places the displacements into the same reference frame as the 1986-1988 movements. The adjusted MOUN

Figure 4.5: Imperial Valley GPS station displacements between 1986 and 1990. The displacement at MOUN relative to BLAC is shown by the dashed arrow. For consistency with the 1986-1988 observations the estimated displacement at MOUN relative to OCTI is calculated by subtracting the estimated secular velocity of BLAC relative to OCTI obtained from conventional geodetic measurements (see Figure 4.9). Station MOUN was reset between surveys and site inspection during 1990 revealed a positioning error of about 15 cm.

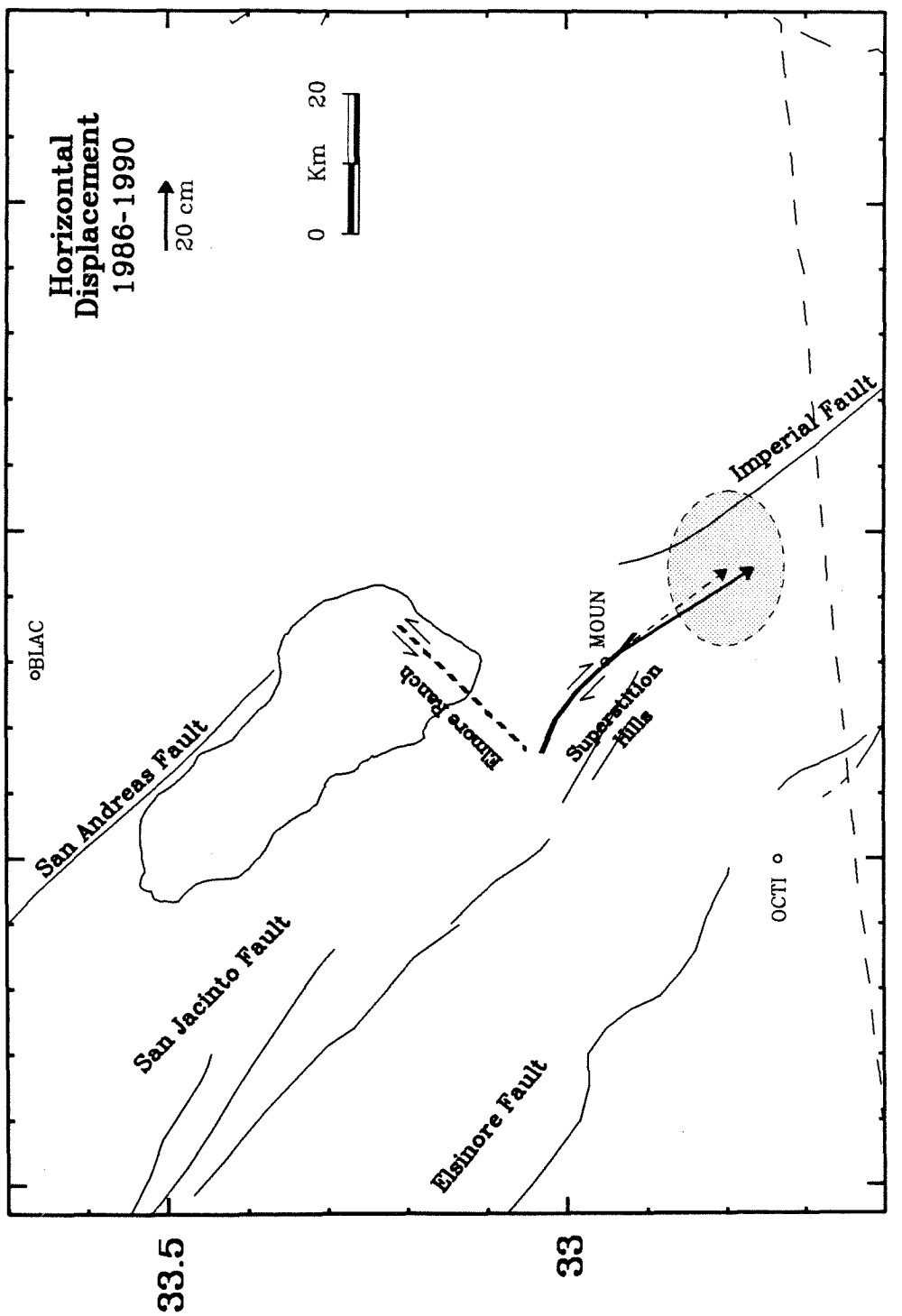
Horizontal
Displacement
1986-1990
20 cm
0 Km 20
BLAC
MOUN
OCTI
San Andreas Fault
San Jacinto Fault
Elsinore Fault
Elsinore Fault
Superstition
Hills
Imperial Fault
33.5
33
-116.5
-116
-115.5
-115

displacement is shown in Figure 4.5 (solid arrow).

Station Displacements 1988-1988 (February-April)

Seven GPS sites were occupied during both 1988 campaigns (Table 4.2). Calculated site displacements for this 1 month interval are shown in Figure 4.6. An adjustment (simple translation) was applied to all movements so that the sum of the vector displacements is zero. The magnitude of the apparent movements range from 0.9 to 2.9 cm, averaging 1.6 cm. It is interesting that the 2.9 cm displacement at KANE is to the west-southwest, more or less expected if left-lateral afterslip occurred along the Elmore Ranch fault. However, while postseismic offsets were significant along the Superstition Hills fault, almost all Elmore Ranch activity ceased after the initiation of the 2nd main event [*Williams and Magistrale*, 1989; *Magistrale*, 1989; *Hudnut et al.*, 1989a]. The observed displacements probably represent measurement error as opposed to real deformation. Note that the largest vector components are oriented in the east-west direction. Station O217 also exhibits a fairly large apparent east-west directed movement, although this is almost certainly not tectonically related.

Even if the displacements shown in Figure 4.6 are entirely measurement error, they do illustrate two points: 1) the accuracy with GPS is easily sufficient to monitor tectonic motions, and 2) the anomalous displacements for the 1986-1988 interval (Figure 4.4) are probably due to the poor quality of the 1986 data. Typical crustal deformation rates across major tectonic structures in southern California are between 1 and 5 cm/yr. At 1 to 2 cm GPS accuracy, such deformation would be resolvable in time scales as short as 1

year. Although the short baseline (~ 50 km) horizontal precisions computed from GPS repeatability studies are generally at the sub-centimeter level [e.g., *Dong and Bock*, 1989], these tests usually involve multiple occupations of the same network over a consecutive 4 to 5 day interval. Because the 7 stations shown in Figure 4.6 were not all observed simultaneously (Table 4.3), the repeatability is somewhat degraded since errors will tend to propagate through the solutions. However, the relatively good consistency suggested with the 1988 results suggest that some of the unusual movements observed with the 1986-1988 displacement vectors are probably due to poor data quality from the 1986 campaign.

GPS Errors

Formal estimates of GPS uncertainty almost always underestimate variances derived from repeatability studies. We attempt to determine more realistic and illustrative errors by multiplying the structure of the formal covariance matrix calculated with the GPS solution by an estimated variance factor, which scales as average baseline length. For the 1986-1988 displacements, the primary error source is presumably due to the 1986 survey, where the estimated accuracies are on the order of 1 ppm. We have chosen a variance factor so that the average baseline error scales as 1 ppm. Since the 1988 data were processed robustly utilizing orbit improvement techniques (not available with the 1986 data), we assume these errors are negligible. Although this method is somewhat ad hoc, it does illustrate an important fundamental. Notably, the error in the east-west component is about 4 times larger than the north-south uncertainty. This is attributed to the north-south ground-track of the satellite orbits.

Figure 4.6: Imperial Valley GPS station displacements between February/March 1988 and March/April 1988. The observed movements indicate the magnitude of errors due to the 1988 survey. The vector scale is twice that of Figures 4.4 and 4.5. The displacement at KANE could represent postseismic deformation from the 1987 earthquake sequence.

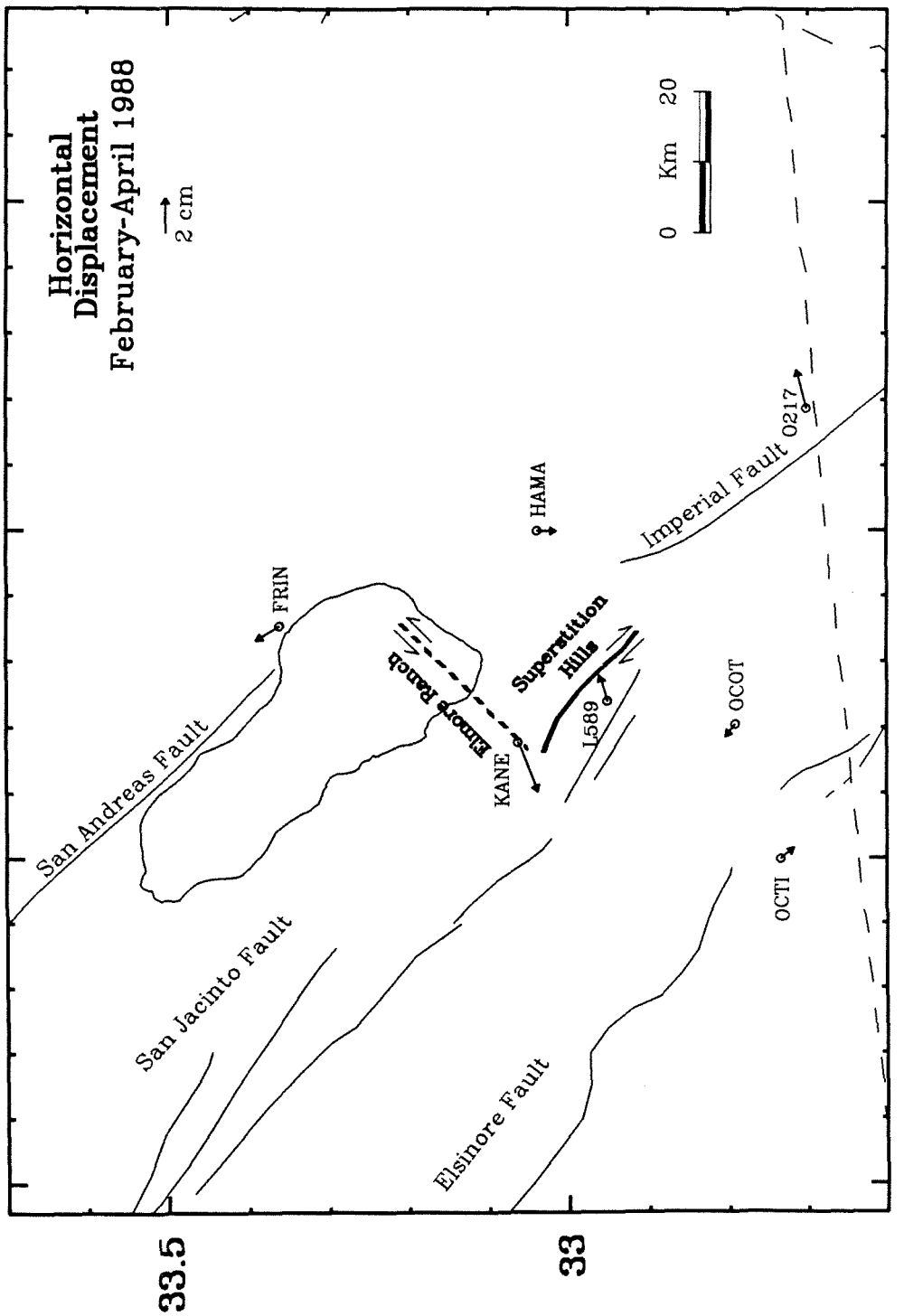
Horizontal
Displacement
February-April 1988
2 cm
0 Km 20
HAMA
FRIN
KANE
1589
OCOT
OCTI
0217
Superstition
Hills
Elmore Ranch
San Andreas Fault
San Jacinto Fault
Elsinore Fault
Imperial Fault
33.5
33
-116.5
-116
-115.5
-115

Because station MOUN was reset between the 1986 and 1990 surveys, the largest error source is due to the difficulty in establishing the new mark at the previous location. From field inspection, this uncertainty is estimated at 15 cm (in all directions) and is additive to the GPS measurement error.

4.5 Modeling

Theory

Simple dislocation theory is often used to model seismically induced geodetic deformation. The earth is considered a homogeneous isotropic elastic half-space with no stress applied to the free surface. The displacement field u_k for a dislocation Σ in the medium is given by

$$u_k = \frac{1}{8\pi\mu}\int\int_{\Sigma} \nabla u_i w_{ij}^k v_j d\Sigma \tag{4.1}$$

where ∇u_i is the discontinuity, w_{ij}^k are the displacement Green's functions due to a set of strain nuclei, and v_j are the direction cosines of the normal to the surface element $d\Sigma$ [*Steketee*, 1958; *Chinnery*, 1961]. Analytical solutions to this integral are rather complex, but have been simplified for special cases of dislocation or fault geometry [e.g., *Chinnery*, 1961; *Savage and Hastie*, 1966; *Mansinha and Smylie*, 1967]. General expressions of the displacement field for rectangular strike and dip-slip faults of arbitrary inclination have been computed by *Mansinha and Smylie* [1971] and *Okada* [1985]. Arbitrary slip directions can be designed by the superposition of strike and dip-slip dislocations.

The strain/stress within a medium is computed by differentiating the displacement field. For the displacement u_k where u is a function of the

geometrical coordinates x_i, the components of the strain tensor **E** are given by

$$\epsilon_{ij} = \frac{1}{2}\left(\frac{\partial u_i}{\partial x_j} + \frac{\partial u_j}{\partial x_i}\right) \tag{4.2}$$

In an isotropic medium the stress tensor σ is given by

$$\sigma_{ij} = \lambda\theta\delta_{ij} + 2\mu\epsilon_{ij} \tag{4.3}$$

where θ is the dilatation ($\theta = \sum_{i=1}^{3}\epsilon_{ii}$). We consider the medium as a Poisson solid with $\lambda = \mu = 2.8\text{x}10^{11}$ dyne-cm^{-2}.

A rectangular dislocation within an elastic half-space will create a spatially dependent stress tensor σ throughout the volume. The force acting at a point along an arbitrarily oriented plane in the medium is computed by multiplying σ by the outward normal vector to the plane ($\vec{N}_n$). That is, the traction vector $\vec{T}$ is given by

$$\vec{T} = \sigma\vec{N}_n \tag{4.4}$$

If we assume the plane is coincident with a fault, then the forces generated on this secondary structure due to the initial dislocation are determined by calculating the traction vectors at selected points along the fault. The normal (σ_n), strike-slip (σ_s), and dip-slip (σ_d) stresses on the fault plane are computed by

$$\sigma_n = \vec{T}\cdot\vec{N}_n \tag{4.5a}$$

$$\sigma_s = \vec{T}\cdot\vec{N}_s \tag{4.5b}$$

$$\sigma_d = \vec{T}\cdot\vec{N}_d \tag{4.5c}$$

where $\vec{N}_n$, $\vec{N}_s$, and $\vec{N}_d$ are the normalized vectors perpendicular to, along strike, and along dip to the fault plane. Analytic solutions for the dislocation generated stress and strain fields within a medium are given by *Iwasaki and Sato* [1979] and *Alewine* [1974].

Inverse Methods

Inversion of seismically generated geodetic displacements can yield fault-rupture parameters, such as the slip distribution along a fault plane [e.g., *Ward and Barrientos*, 1986; *Harris and Segall*, 1987; *Segall and Harris*, 1987; *Snay*, 1989]. We use a method similar to that outlined in *Segall and Harris* [1987]. Singular Value Decomposition (SVD) [e.g., *Lanczos*, 1961; *Jackson*, 1972; *Menke*, 1984] and elastic dislocation theory are used to invert the Imperial Valley GPS measurements for seismic slip along the Superstition Hills and Elmore Ranch faults.

The relationship between surface deformation and slip along a rectangular dislocation is defined by Equation (4.1). The rupture plane is modeled as a set of non-overlapping rectangular dislocations. That is, the fault plane is partitioned into multiple sub-elements or sub-faults. The slip distribution along the seismically active fault is given as the discreate approximation of slip along each sub-element. The normal equations which govern surface displacement resulting from such slip is given by

$$\mathbf{A}^g \mathbf{m}^f = \mathbf{d}^g \tag{4.6}$$

where the superscripts *g* and *f* refer to geodetic observation and fault slip, respectively. Each row of $\mathbf{A}^g$ is determined from (4.1), and is a function of sub-fault geometry and geodetic position. The slip distribution $\mathbf{m}^f$ is defined by $\mathbf{m}^f = [m_1, m_2, \cdots, m_n]^T$, where m_i is the slip along the *i*th sub-fault. The data vector $\mathbf{d}^g$ contains the geodetic observables. Each GPS station displacement will add 3 rows to $\mathbf{A}^g$ and 3 elements to $\mathbf{d}^g$, corresponding to the vertical and two horizontal components. In practice, we may choose to ignore the less accurate vertical observation. This is especially true in strike-slip

environments where the predominant displacement direction is horizontal.

Surface rupture is easily included into (4.6) by considering measurements of surface displacement as geodetic observation. The offsets are modeled as a priori slip information on the surface intersecting sub-faults. Equation (4.6) becomes

$$\mathbf{A}\mathbf{m}^f = \begin{bmatrix} \mathbf{A}^g \\ \mathbf{A}^s \end{bmatrix} \mathbf{m}^f = \begin{bmatrix} \mathbf{d}^g \\ \mathbf{d}^s \end{bmatrix} = \mathbf{d} \tag{4.7}$$

where d_i^s are the discreate approximations of surface slip along the fault trace and $\mathbf{A}_{ij}^s = 1$ if sub-fault element j corresponds to surface slip offset i; otherwise $\mathbf{A}_{ij}^s = 0$.

The GPS displacements shown in Figures 4.4 and 4.5 are not connected to an external reference but are defined relative to station OCTI. (Some geodetic measurements such as line-length change recorded by EDM observations are independent of an absolute reference.) The displacement at OCTI is assumed to be 0, which in fact may be true from a seismic standpoint since this site is far from the Superstition Hills rupture zone. However, any attempt to use the GPS displacements as a criteria for evaluating the effect of the earthquake sequence will be distorted by measurement error at OCTI and/or non-seismic deformation between this site and the other stations. This ambiguity is largely circumvented if displacement-offset terms are estimated in addition to the fault slip parameters. Equation (4.7) is then rewritten

$$\mathbf{A}\mathbf{m} = \mathbf{A} \begin{bmatrix} \mathbf{m}^f \\ \mathbf{m}^\circ \end{bmatrix} = \mathbf{d} \tag{4.8}$$

where m_i° is the ith non-seismic component (i.e., north-south, east-west, vertical) uniformly added to all station displacements.

The Singular Value Decomposition of $\mathbf{A}$ is given by

$$\mathbf{A} = \mathbf{U}\lambda\mathbf{V}^T \tag{4.9}$$

where $\mathbf{U}$ is a matrix of eigenvectors spanning the data space, $\mathbf{V}$ is a matrix of eigenvectors spanning the parameter space, and λ is a diagonal matrix of singular values. Without loss of generality this is written

$$\mathbf{A} = \mathbf{U}_p\lambda_p\mathbf{V}_p^T \tag{4.10}$$

where p refers to the non-zero singular values. If the normal equations of (4.8) are normalized to have unit variance [e.g., *Segall and Harris*, 1987], the generalized inverse of (4.8) and (4.10) is given by

$$\mathbf{A}^{-1} = \mathbf{V}_p\lambda_p^{-1}\mathbf{U}_p^T \tag{4.11}$$

[*Lanczos*, 1961; *Menke*, 1984]. In practice it is often necessary to restrict the volume of the parameter space by considering only the k largest singular values, setting all others to 0.

The generalized solution to (4.8) for the k largest singular values is given by

$$\mathbf{m} = \mathbf{A}_k^{-1}\mathbf{d} + \mathbf{V}_0\alpha_0 \tag{4.12}$$

where $\mathbf{V}_0$ are eigenvectors spanning the null space of the model and α_0 is a vector of arbitrary coefficients. The volume of the model space not constrained by observation is defined by $\mathbf{V}_0\alpha_0$. This term is not influenced by the geodetic data and is thus arbitrary. Often it is the minimum-length solution $\mathbf{m} = \mathbf{A}_k^{-1}\mathbf{d}$ which is of interest (the coefficients of α_0 are 0). However, some other solution criteria can be satisfied by carefully designating the coefficients of α_0.

For high resolution fault models where the rupture plane is partitioned into numerous sub-faults, it is necessary to apply some type of smoothing

constraint over the dislocation surface to prevent the slip distribution from taking on an oscillatory pattern. *Segall and Harris* [1987] showed that the "roughness" of fault slip could be minimized by considering smoothness as an a priori constraint utilized from the model null space through the coefficients of α_0 (Equation 4.12). They considered a smoothing matrix **T**, with coefficients determined from the discreate approximation of the Laplacian operator $\nabla^2 = \partial^2/\partial x^2 + \partial^2/\partial y^2$, where x and y are the fault distances along strike and dip, respectively. The boundary conditions around the lower and lateral edges of the dislocation are assumed to be null slip, so that the applied smoothing operator causes the calculated fault offset to tend toward zero along these boundarys. Because the Superstition Hills and Elmore Ranch faults ruptured the surface, the upper boundary is considered an unconstrained dislocation. The estimated fault slip is then given by

$$\mathbf{m} = [\mathbf{I} - \mathbf{V}_0(\mathbf{V}_0^T\mathbf{T}^T\mathbf{T}\mathbf{V}_0)^{-1}\mathbf{V}_0^T\mathbf{T}^T\mathbf{T}]\mathbf{A}_k^{-1}\mathbf{d} \qquad (4.13)$$

(Equation 13, [*Segall and Harris*, 1987]). A similar formulation for utilizing fault smoothness over the model null space is given by *Harris and Segall* [1987]; an alternate method considering fault smoothness as quasi-data is provided by *Snay* [1989].

For over-constrained solutions, where there are more independent data than parameters, if $k = p$ then SVD is equivalent to simple least-squares. This is advantageous since the solution provided by (4.12) can be utilized for either uniform dislocations or for detailed parameterizations where the fault plane is partitioned into multiple sub-elements.

Simple dislocation theory has the advantage that the displacement and stress/strain fields for simple fault ruptures can be computed almost

instantaneously. The inverse problem of using geodetic data to calculate the slip distribution along a fault plane is also straightforward. However, we have assumed the earth can be modeled as a homogeneous half-space. Crustal layering or inhomogeneities in the earth can introduce non-existent structure into half-space models [*Savage*, 1987]. While low-resolution schemes such as the average slip over the fault plane will not be seriously affected, attempts to resolve detailed properties may be badly contaminated by artifacts of earth structure.

Seismic Displacement

We model rupture along the Superstition Hills and Elmore Ranch faults as strike-slip dislocations along vertical planes extending from the surface to 10 km depth. Each dislocation approximately coincides with the mapped surface rupture and/or aftershock distribution. The geometrical parameters for the modeled faults are listed in Table 4.5. Initially, the Superstition Hills and Elmore Ranch faults are considered uniform dislocations, with no slip variation allowed on the rupture planes. The dislocations are then partitioned into multiple sub-elements and the slip distribution along the two faults is calculated from the discrete offset for each sub-fault.

For an initial estimate of slip along the two faults, we consider only the displacements at KANE, MOUN, and L589; the three GPS sites nearest the seismic rupture zone (Figure 4.7). Because the observed movements at these stations are relative to OCTI, we also solve for a uniform north-south and east-west offset in the displacements. This will remove any systematic distortion due to measurement error at OCTI. Both faults are regarded as

Table 4.5 Parameters for Modeled Dislocations

	Superstition Hills	Elmore Ranch
Length (km)	25	25
Width (km)	10	10
Strike	N50 ° W	N40 ° E
Dip	90	90
Depth (km)	0	0
Latitude (° N)	32.9569	33.1078
Longitude (° E)	-115.7431	-115.7505

Latitude and Longitude are coordinates
at top center of dislocation
Depth is depth to top of fault

Figure 4.7: The best-fit solution to Model 1 (3-station inversion). The solid arrows indicate the observed displacements, while the dashed arrows represent the computed displacement based on Model 1. The shaded region indicates where horizontal displacements are greater than 4 cm.

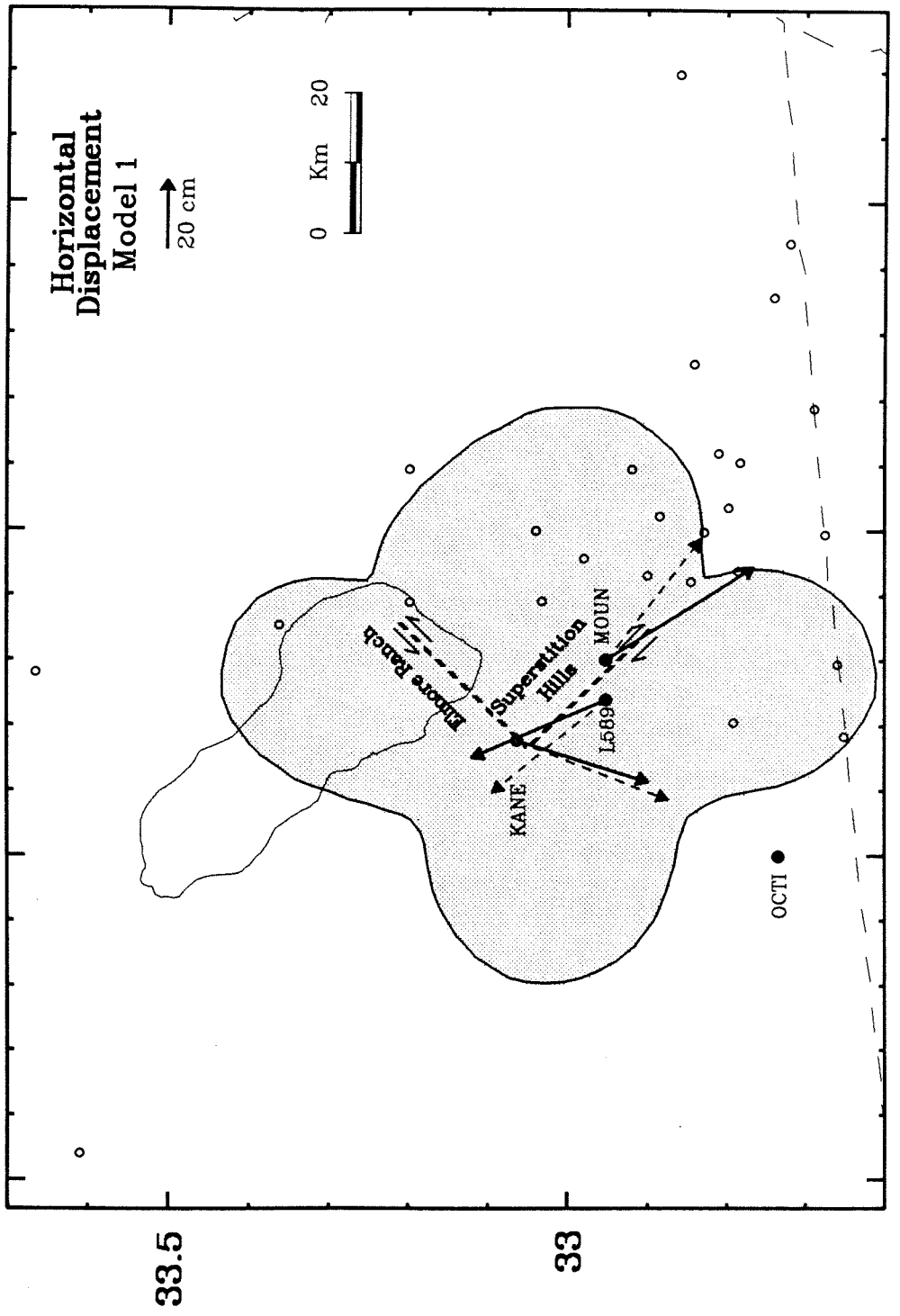
Horizontal
Displacement
Model 1
20 cm
0 Km 20
Superstition
Hills
MOUN
L589
KANE
OCTI
-116.5
-116
-115.5
-115
33.5
33

simple dislocations not segmented into sub-regions. The solution to this simple model is given in Table 4.6 (Model 1) and the observed vs. calculated displacements are shown in Figure 4.7. Generally, there is good agreement between model and observation. This is not altogether unexpected since we are solving for 4 parameters with 6 data. The large discrepancy at MOUN is presumably due to the uncertainty in relocating the 1990 reset monument at the 1986 position (recall the estimated error is 15 cm in each direction). The surface deformation pattern computed from Model I is fairly extensive; the 4 cm horizontal displacement contour is shown in Figure 4.7.

The north-south and east-west displacement components at each Imperial Valley site, plotted as a function of distance from a N40°W trending line through OCTI are shown in Figure 4.8. Shown are the non-seismic movements; that is, the seismic component computed from Model 1 is subtracted from the observed displacements (Figure 4.4). Stations where the seismic correction is greater than 4 cm (in the component plotted) are shown as open circles, other sites as filled circles. The displacements represent a cross-section of non-seismic deformation perpendicular to the plate motion direction.

A fairly consistent pattern is observed in the north-south components (Figure 4.8). Stations to the northeast have moved south (or southeast) about 8.1 cm relative to sites on the other side of the valley. Stations which display the largest deviation are for the most part those sites where the applied seismic correction is greater than 4 cm (open circles). This may indicate additional fault complexity not accounted for by the simple dislocation model used to remove the effects of the 1987 earthquake. The

Table 4.6 Inverse Models of Seismic Slip

Model	Fault	Sub-faults		Slip	Moment
		Strike	Dip	(cm)	($x10^{25}$ dyne-cm)
Model 1	SH	1	1	109. ± 13.	7.8
Model 1	ER	1	1	-45. ± 19.	3.4
Model 2	SH	1	1	130. ± 8.	9.4
Model 2	ER	1	1	-30. ± 10.	2.3
Model 3a	SH	10	5		9.9
Model 3a	ER	10	5		5.9
Model 3b	SH	10	5		8.4
Model 3b	ER	10	5		7.0
Model 3c	SH	10	5		6.2
Model 3c	ER	10	5		3.9
Model 3d	SH	10	5		9.2
Model 3d	ER	10	5		4.9

SH - Superstition Hills fault
ER - Elmore Ranch fault

Figure 4.8: The north-south and east-west GPS displacement components for the 1986-1988 interval. All distances are computed relative to OCTI on a cross section trending N50 ° E, perpendicular to the plate motion direction. The effects of the 1987 Superstition Hills earthquake sequence based on Model 1 are removed. Open circles indicate stations where the seismic correction is greater than 4 cm (for that component). The 8.1 cm north-south offset between stations on opposite sides of the valley is equivalent to 5.9 cm/yr displacement oriented N40 ° W. The large scatter for the east-west component is presumably due to large measurement errors in the 1986 survey.

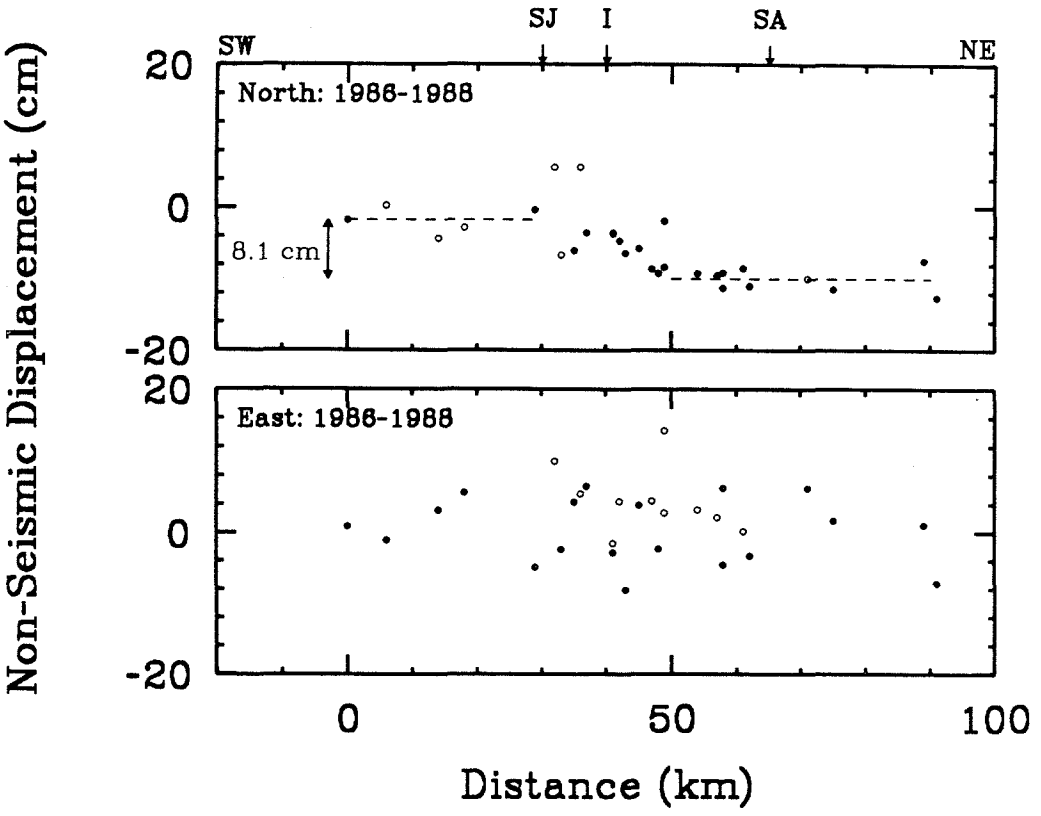
SJ
I
SA
SW
NE
20
0
-20
North: 1986-1988
8.1 cm
East: 1986-1988
0
50
100
Distance (km)
Non-Seismic Displacement (cm)

east-west oriented displacements, however, show large data scatter; no distinguishable pattern is readily visible across the valley. The scatter is not a function of the magnitude of the applied seismic correction, so presumably it represents the large measurement errors inherent in the east-west direction.

We assume the 8.1 cm north-south offset (Figure 4.8) is attributed to plate-boundary deformation between the North American and Pacific plates. Taking into account the orientation of the suspected deformation (N40 ° W), as well as the time interval between the 1986 and 1988 surveys (1.79 years), the north-south movements are consistent with 5.9 cm/yr displacement across the valley. This is significantly larger than the 3.45-4.3 cm/yr rates obtained from conventional surveys. Although accelerated deformation between the GPS campaigns can not be ruled out, there is relatively poor station coverage in the southwest portion of the valley so it is difficult to estimate the valley crossing displacement precisely. This is even more true considering most of the southwestern sites suffered large seismic displacements during 1987. If Model 1 (Table 4.6) does not accurately reflect the rupture process during the Superstition Hills earthquake sequence, the unmodeled effects will propagate into the non-seismic estimate.

The fault rupture calculated from Model 1 depends heavily on shallow slip since the three stations used are all within close proximity to the dislocation planes. While the observed surface offsets indicate rupture extends to the surface, greater slip at depth may go undetected. Therefore, it is necessary to examine the displacement at stations away from the fault to ascertain the depth extent of faulting.

To incorporate more GPS data into the fault-plane inversion, it is necessary to remove the non-seismic deformation from the displacement field. Perhaps the best example of secular deformation across the Imperial Valley is provided by U.S.G.S. trilateration measurements between 1972 and 1987 [e.g., *Prescott et al.*, 1987a; *Prescott et al.*, 1987b]. Computed station velocities for the Salton Trough EDM network (Figure 4.9) are roughly parallel to the direction of plate motion (N40°W), although to some degree the geodetic orientation is dictated by the outer coordinate solution imposed to transform EDM line-length changes into station displacements [*Prescott*, 1981]. The total differential velocity across the network is 3.45 cm/yr and is accommodated in a 50 km wide zone [*Prescott et al.*, 1987b]. Triangulation measurements suggest a larger rate between 1941-1986 (4.3 cm/yr) but these observations are not as accurate as the EDM measurements [*Snay and Drew*, 1988]. However, along the Imperial fault where EDM sites are sparse, the triangulation data suggest concentrated deformation in a narrow 20 km wide zone. The conventional geodetic data are modeled using the following empirical approach. The differential velocity across the valley is taken to be 3.45 cm/yr. Running along the axis of the valley is a transition zone(s) (Figure 4.9), where the strain gradient is defined by simple shear with the displacements oriented N40°W. The transition zone north of the Imperial fault is 50 km wide; to the south it is 20 km wide. The modeled station movements shown by the dashed arrows in Figure 4.9 fit the observed EDM displacements extremely well.

The secular deformation derived from the conventional measurements is removed from the observed GPS displacements (Figures 4.4 and 4.5) leaving

Figure 4.9: Imperial Valley EDM station velocities computed between 1972 and 1987 (solid arrows). The movements are largely attributed to secular deformation due to the relative motion between the North American and Pacific plates. The displacements are modeled (dashed arrows) by 3.45 cm/yr displacement across the valley, with right-lateral simple shear oriented N40 ° W occurring in a transition zones 50 km wide north of the Imperial Fault and 20 km wide to the south (shaded). The secular deformation is subtracted from the GPS displacements shown in Figures 4.4 and 4.5.

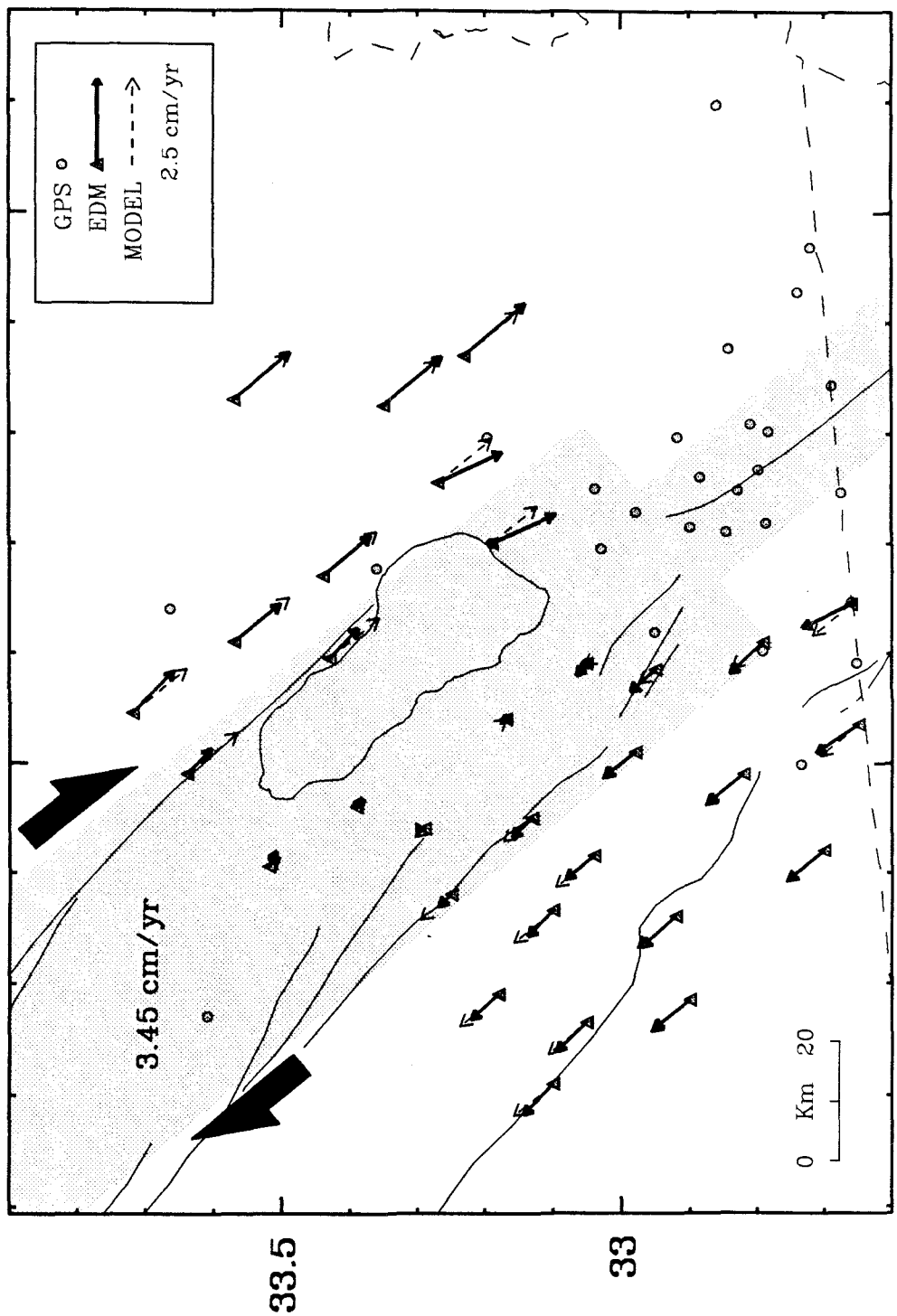
GPS
EDM
MODEL ----->
2.5 cm/yr
3.45 cm/yr
0 Km 20
33.5
33
-116
-115

the seismic component (and measurement error). For Model 2 (Table 4.6) the uniform slip along the Superstition Hills and Elmore Ranch faults is recomputed using all GPS data (without the secular deformation). The residuals (observed minus calculated) for this model are shown in Figure 4.10. The largest station discrepancies between model and observation trend in the longitudinal direction and are especially noticeable for those sites in the southeast. This simply reconfirms our speculation for large east-west trending errors. However, the residuals at the three stations nearest the seismogenic zone are unusually large. The large vector at MOUN is easily explained since this station was reset between surveys. The residuals at L589 and KANE, however, are significantly larger than the average discrepancy computed for the other stations. Because both sites are located in close proximity to the earthquake rupture zone, this suggests additional seismic slip not accounted for by the simple dislocation parameters used for Model 2.

Although the inversion results (Table 4.6) between Model 1 and 2 are marginally different (less slip on the Elmore Ranch fault; more on the Superstition Hills fault), this is not significant considering the estimated uncertainties. In fact, because the near-field (Model 1) and far-field (Model 2) solutions are similar, this suggests that to first order there is not significant slip dependence with depth (within a factor of 2 or 3). It is also noteworthy that the uncertainties improve by only $\sim$ 50 % with the additional data supplied with Model 2. This illustrates the necessity of measurements near the seismic rupture. For simple fault models, where uniform slip is constrained to a single dislocation plane (or two planes in the case of the Superstition Hills sequence), it is as important to have at least minimal

station coverage within a few kilometers of the seismogenic zone as it is to have many sites located away from the fault(s).

Seismic Slip Distribution

Uniform dislocations along the Superstition Hills and Elmore Ranch faults were utilized for Models 1 and 2. To estimate the seismic slip distribution, it is necessary to partition the rupture planes into multiple regions or sub-faults (Model 3). The divisions must be sufficiently dense as to provide reasonable slip resolution. We choose 10 sub-fault elements in the horizontal and 5 in the vertical, so that each fault is partitioned into 50 sub-regions. The dimensions of each dislocation element is 2.0 km in width (vertical) and 2.4-2.6 km in length (2.4 km for Superstition Hills and 2.6 km for the Elmore Ranch fault). The slip distribution along the two rupture planes is constrained to be sufficiently smooth (Equation 4.13). The GPS displacements are adjusted according the the estimated north-south and east-west offsets from Model 2.

In addition to the GPS data, a priori surface-slip information is added to the solution. Surface slip along the Superstition Hills fault (Figure 4.11) [*Williams and Magistrale*, 1989] extends (nearly) the entire length of the modeled fault plane. The surface rupture has been incremented into 2.4 km segments corresponding to the horizontal dimension of each sub-fault. The average slip over each segment is assigned as an a priori slip estimate for the surface fault element which it corresponds. Surface rupture along the Elmore Ranch fault is confined to the southwestern segment (Figure 4.11). Recall for this event that the mapped surface breaks occurred along several nearly

Figure 4.10: The residuals (observed minus calculated) for the best-fit solution to Model 2. The large residual components in the east-west direction are suggestive of measurement error. The residual at MOUN is likely attributed to the reset benchmark between surveys. The unusually large discrepancy at L589 (and KANE) suggest additional seismic deformation not accounted for by the simple uniform slip parameterization considered for Model 2.

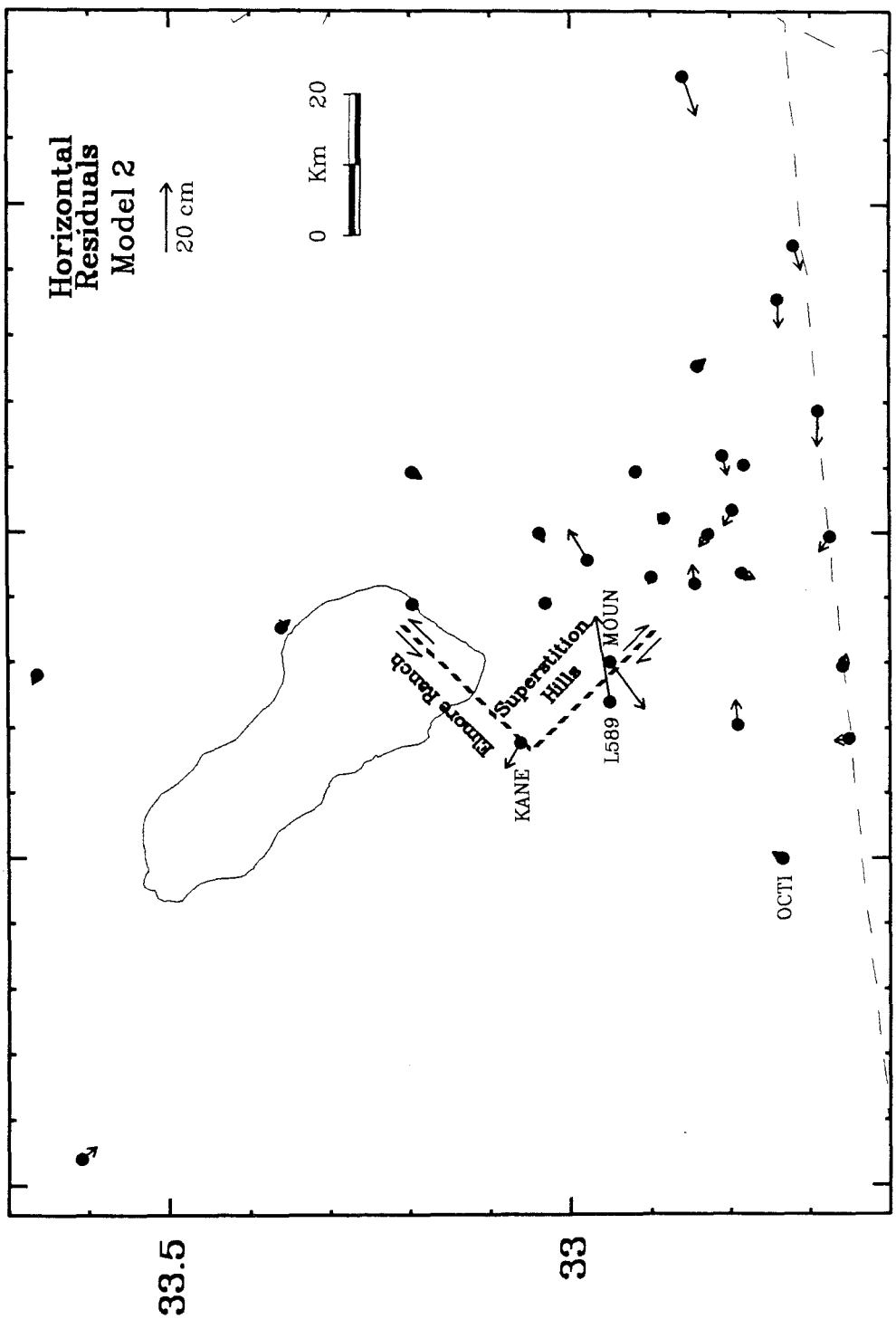
Horizontal
Residuals
Model 2
20 cm
0 Km 20
Superstition
Hills
Brawley Ranch
KANE
L589
MOUN
OCTI
33.5
33
-116.5
-116
-115.5
-115

Figure 4.11: Observed surface slip along the Superstition Hills and Elmore Ranch faults (dashed lines). The Superstition Hills offsets were measured on January 25 and 26, 1988 about 1 month before the GPS observations. Decaying afterslip is recorded up to nearly 1 year after the earthquake sequence. The Elmore Ranch measurements are the cumulative slip from multiple surface breaks across a 10 km wide zone, with no recorded postseismic offset after the earthquake. The discrete approximation to the surface slip used to constrain the uppermost subfault elements in Models 3a and 3b is shown by the solid lines.

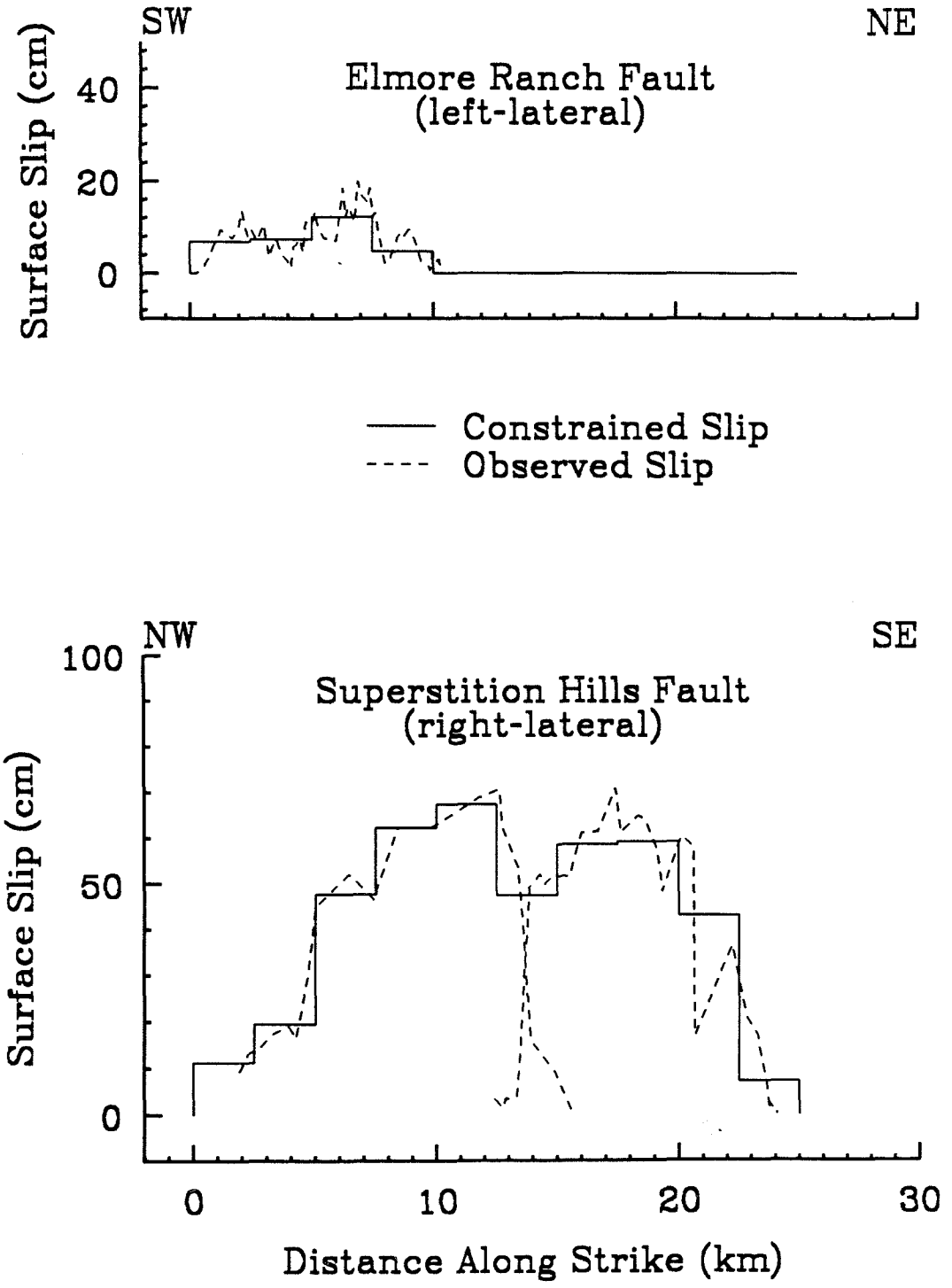
SW
NE
Elmore Ranch Fault
(left-lateral)
Surface Slip (cm)
40
20
0
Constrained Slip
Observed Slip
NW
SE
Superstition Hills Fault
(right-lateral)
Surface Slip (cm)
100
50
0
0
10
20
30
Distance Along Strike (km)

parallel strands (Figure 4.2). We take the cumulative surface offset for all strands [*Hudnut et al.*, 1989a] averaged over 2.6 km segments along the fault, and apply this as a priori slip information for the surface sub-fault elements. Where no rupture is mapped (to the northeast), the surface intersecting fault partitions are assigned 0 slip. The a priori uncertainty for each surface-slip estimate is assumed to be 10 cm.

The number of independent parameters estimated through singular value decomposition depends on the number of singular values k utilized in Equation (4.12). A trade-off exists between solution variance and resolution [e.g., *Menke*, 1984]. While large k produces highly resolved models, this is at the expense of increasing solution uncertainty. Correspondingly, small k yields low variance solutions but does not provide detailed resolution. A total of 100 sub-fault elements are incorporated into Model 3 (50 for each fault). If $k = 100$ then slip along each sub-fault will be determined uniquely. Because of limited geodetic coverage, however, it is practical to consider only the first few eigenvectors of the parameter space defined by the geodetic observations. Therefore, each solved parameter is a function of some average slip over multiple sub-fault elements. This is fundamental property of singular value decomposition when used to solve under-determined or poorly-determined problems [e.g., *Jackson*, 1972]. It is necessary to determine the k which maximizes the resolution without allowing the solution to become too oscillatory or unstable.

The geodetic moment, solution instability, and model residual calculated for different values of k are shown in Figure 4.12. The moment is a function of the average slip along the fault planes, while solution instability is

determined from the standard deviation of slip for each sub-fault element. An instability of 0 (stable) indicates uniform slip along the fault planes, while high values indicate an oscillatory or unstable solution. The RMS indicates the agreement between model and observation and is calculated by $RMS = \sum(o_i - c_i)^2/\sigma_i^2$ where o_i is the observed, c_i is the calculated, and σ_i is the uncertainty assigned to the ith observation.

With surface slip incorporated into the solution (Figure 4.12a), the first 20 singular values are well constrained by the measured offset along the fault, and are influenced little by the geodetic observations. The surface measurements reflect the dislocation on the uppermost fault elements, with little depth resolution. This is illustrated by the solution for $k = 20$. The calculated moments are significantly less than that for Model 2, presumably because the surface offset is not representative of the larger displacement along the rest of the fault plane(s). Consequently, in order to estimate the slip distribution with depth it is necessary to consider solutions where $k > 20$. After $k = 30$ the solution becomes very oscillatory as is indicated by the increasing instability value. The RMS is significantly reduced beyond $k = 20$ but only improves marginally with increasing k. The solution fit for $k > 20$ is slightly better than that for Model 2.

Also evident in Figure 4.12a are the large moment estimates for the Elmore Ranch fault, which are almost equal to the computed moments for the Superstition Hills fault. This is unexpected considering the latter event yielded a significantly greater surface wave magnitude, as well as a larger moment estimated from Model 2. It is difficult to distinguish slip between the two faults using SVD as is illustrated by Figure 4.13. The displacement

Figure 4.12a: The geodetic moment, standard deviation of sub-fault slip (instability), and solution RMS calculated for different singular values (k). Shown here are solutions constrained by surface slip measurements ($20 \leq k \leq 30$).

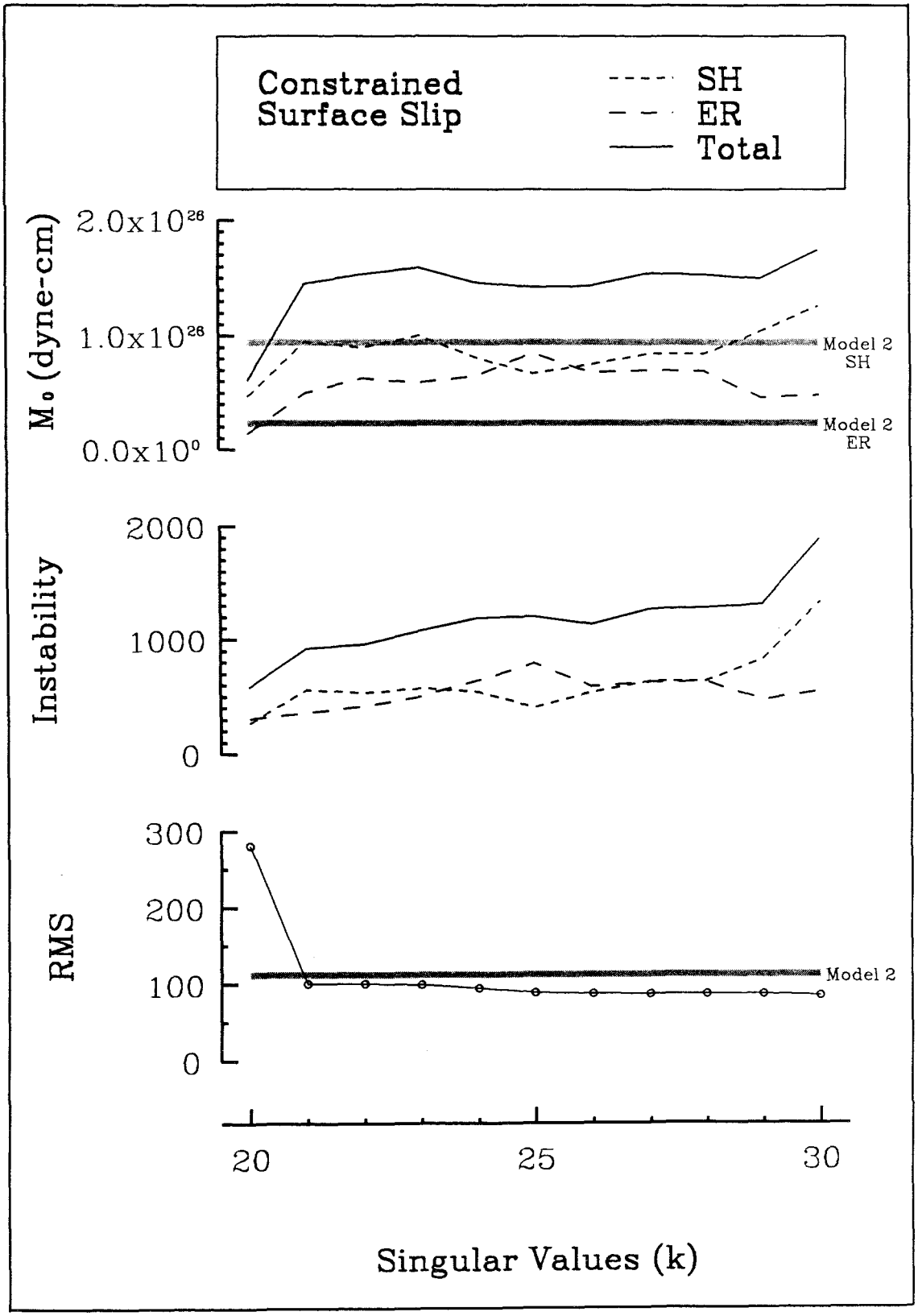
Constrained
Surface Slip
SH
ER
Total
M_o (dyne-cm)
$2.0x10^{26}$
$1.0x10^{26}$
$0.0x10^{0}$
Model 2
SH
Model 2
ER
Instability
2000
1000
0
RMS
300
200
100
0
Model 2
20
25
30
Singular Values (k)

Figure 4.12b: The geodetic moment, standard deviation of sub-fault slip (instability), and solution RMS calculated for different singular values (k). Shown here are solutions unconstrained by surface slip measurements ($1 \leq k \leq 10$).

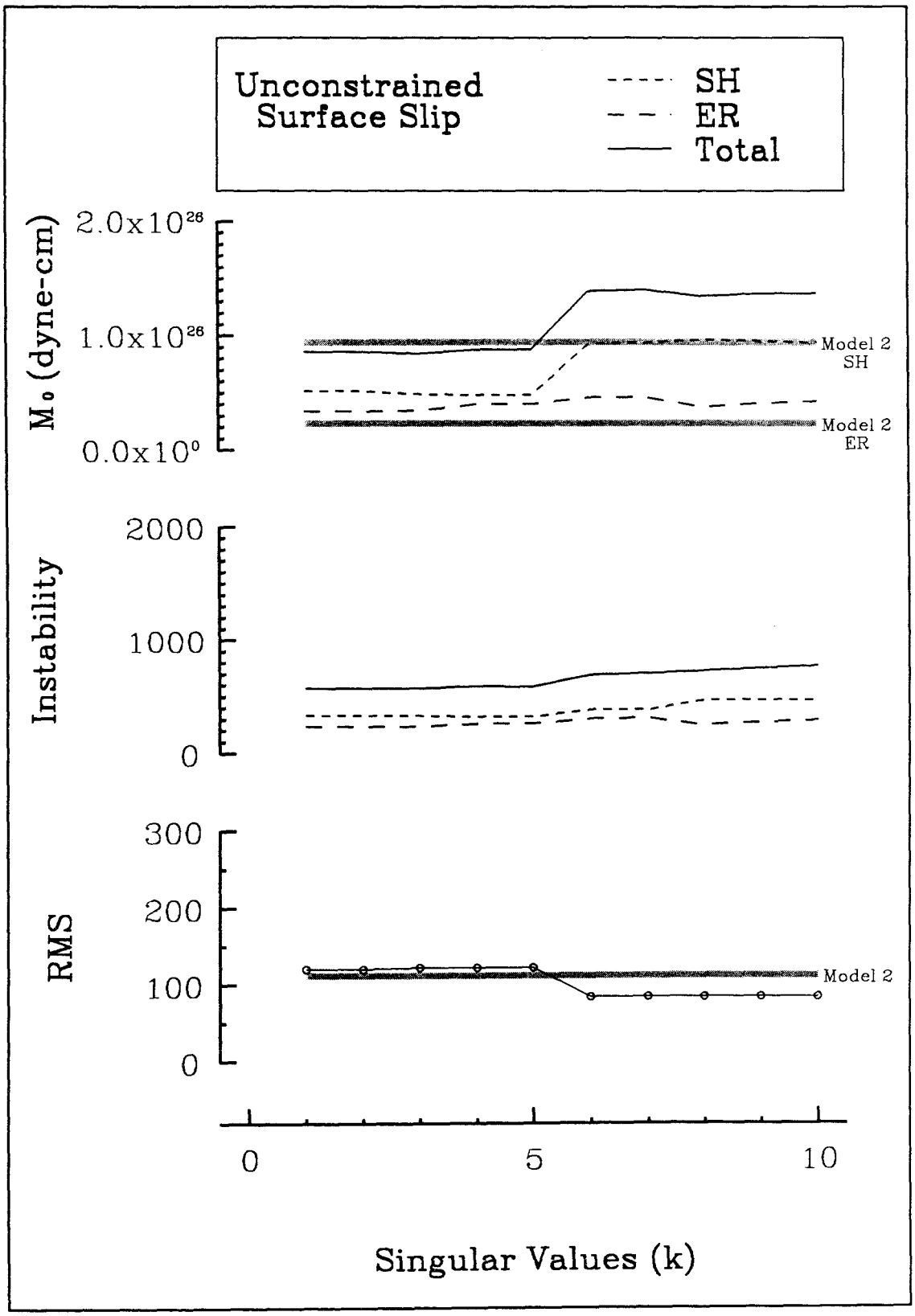
Unconstrained
Surface Slip
SH
ER
Total
M_o (dyne-cm)
$2.0x10^{26}$
$1.0x10^{26}$
$0.0x10^{0}$
Model 2
SH
Model 2
ER
Instability
2000
1000
0
RMS
300
200
100
0
Model 2
0
5
10
Singular Values (k)

Figure 4.13: The horizontal slip distribution calculated independently for the Superstition Hills and Elmore Ranch faults based on Model 2. The shaded region indicates where the horizontal deformation is greater than 2 cm for the Superstition Hills fault and 0.5 cm for the Elmore Ranch fault. The scale for the Elmore Ranch event is altered to account for the smaller dislocation. The deformation pattern is almost identical between the two faults, although the displacement magnitudes are larger for the Superstition Hills event. This illustrates the difficulty in using the GPS measurements to resolve slip between the two faults.

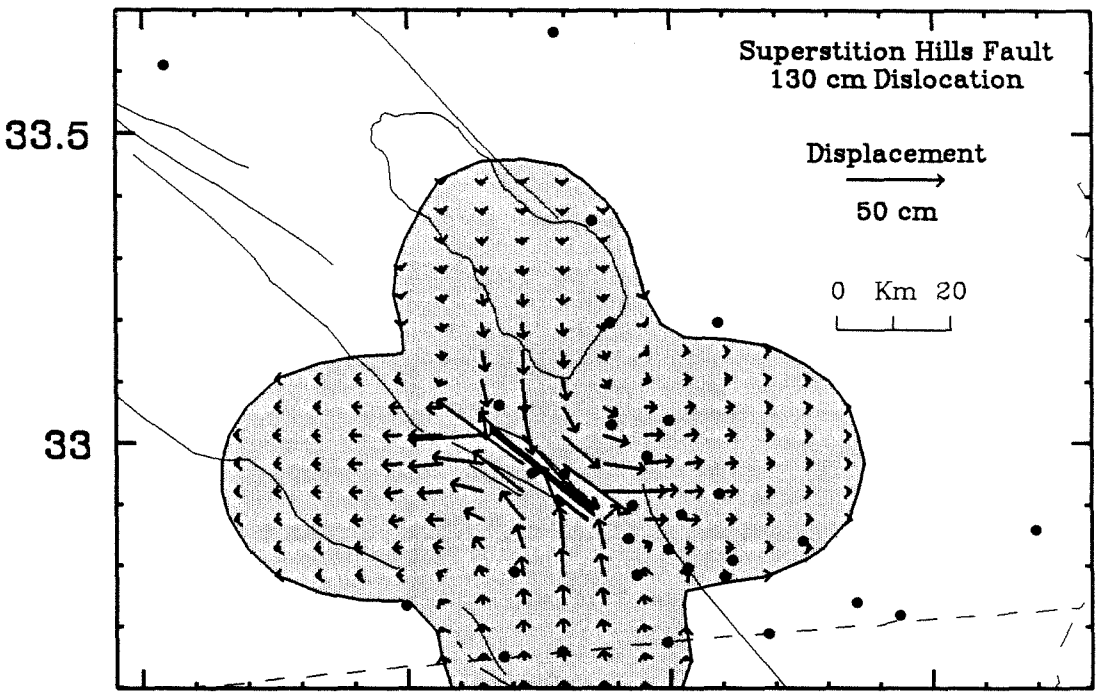
Superstition Hills Fault
130 cm Dislocation
Displacement
50 cm
0 Km 20
33.5
33

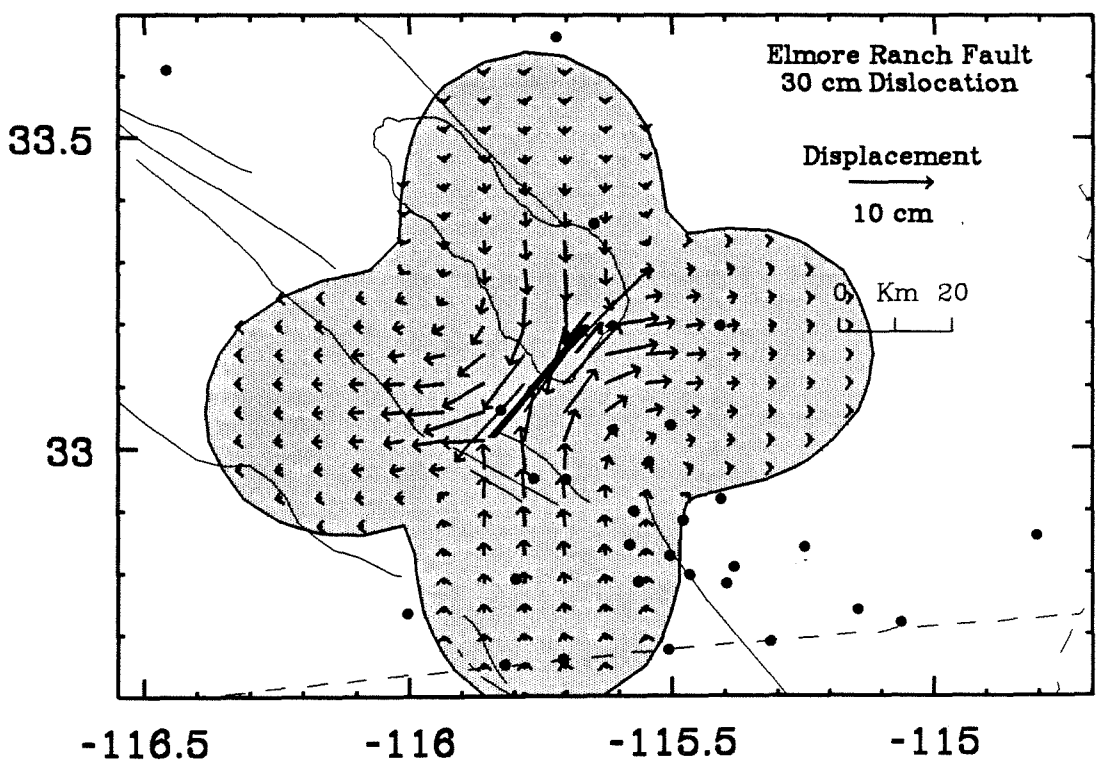
Elmore Ranch Fault
30 cm Dislocation
Displacement
10 cm
0 Km 20
33.5
33
-116.5
-116
-115.5
-115

pattern for a 130 cm rupture on the northwest trending right-lateral Superstition Hills fault is compared with a 30 cm rupture on the northeast trending left-lateral Elmore Ranch fault. Although the magnitude is different, the deformation pattern between the two dislocations is almost identical. As a result, the larger slip estimate along the Superstition Hills fault is being mapped onto the Elmore Ranch fault plane producing the higher moment. This is all the more true considering only the first few model-space eigenvectors are utilized, as is necessary since Model 3 is very underdetermined (more model parameters than data). Therefore, only linear combinations of model parameters are uniquely defined. The similar moments indicated by Figure 4.12a suggest slip between the two faults is strongly correlated in the solution.

The estimated seismic slip distribution along the Superstition Hills and Elmore Ranch faults for $k=23$ and $k=27$ are shown in Figure 4.14a. We refer to these solutions as Models 3a and 3b, respectively (Table 4.6). Although both faults are partitioned into 50 elements, the fault-rupture is not as resolved as the contours suggest since only the first few (non-surface) model-space eigenvectors are independently solved. For $k=23$ the solution suggests fairly uniform rupture along both fault planes. The dislocation may be slightly concentrated to the southwest along the Elmore Ranch fault. The apparent "bullseye" pattern is due to the smoothness constraints requiring the slip to tend towards 0 along the lateral edges and lower boundaries (the upper boundaries are constrained by the surface slip information). There is little difference in the slip distribution for $k=21$ through $k=26$. However, there is a noticeable change in the dislocation pattern starting with $k=27$. While slip

along the Elmore Ranch fault still appears fairly uniform, displacement along the Superstition Hills fault is concentrated to the northwest and to the southeast. This change is significant and is caused by the GPS displacement at one station. Recall the large residual for L589 in Model 2 (Figure 4.10). This discrepancy is nearly eliminated beginning with $k=27$. Therefore, in order to satisfy the observed displacement at L589, it is necessary to concentrate rupture at each end of the Superstition Hills fault. Of course this analysis assumes the observed GPS displacement at L589 is seismically generated, and not contaminated by unusually large measurement error. The dislocation null near the center of the fault roughly corresponds to the drop in fault offset measured at the surface (Figure 4.11).

Independent solutions are made without constraining the upper sub-fault elements by measurements of surface offset (Figure 4.12b). The unconstrained moments are generally smaller than when surface slip is incorporated into the model. This is because the surface measurements are less than the average slip estimate along the fault plane. Without surface constraint, the geodetic data are satisfied to a greater degree by slip near the surface; otherwise, it is necessary to compensate the small shallow offsets by increased slip at greater depths. The seismic slip distribution estimated without surface constraint along the Superstition Hills and Elmore Ranch faults for $k=3$ and $k=7$ are shown in Figure 4.14b. We refer to these solutions as Models 3c and 3d, respectively (Table 4.6). For these unconstrained solutions the slip distribution is confined to shallower depths. Slip concentration at each end of the Superstition Hills fault is suggested for $k=7$, although this division is not as pronounced as in Model 3b. We conclude that incorporating measurements

Figure 4.14a: Slip distribution along the Superstition Hills and Elmore Ranch faults computed from Singular Value Decomposition. Each fault is partitioned into the 50 sub-elements indicated by the grid spacing. Shown here are solutions for $k=23$ and $k=27$ constrained by measurements of surface offset.

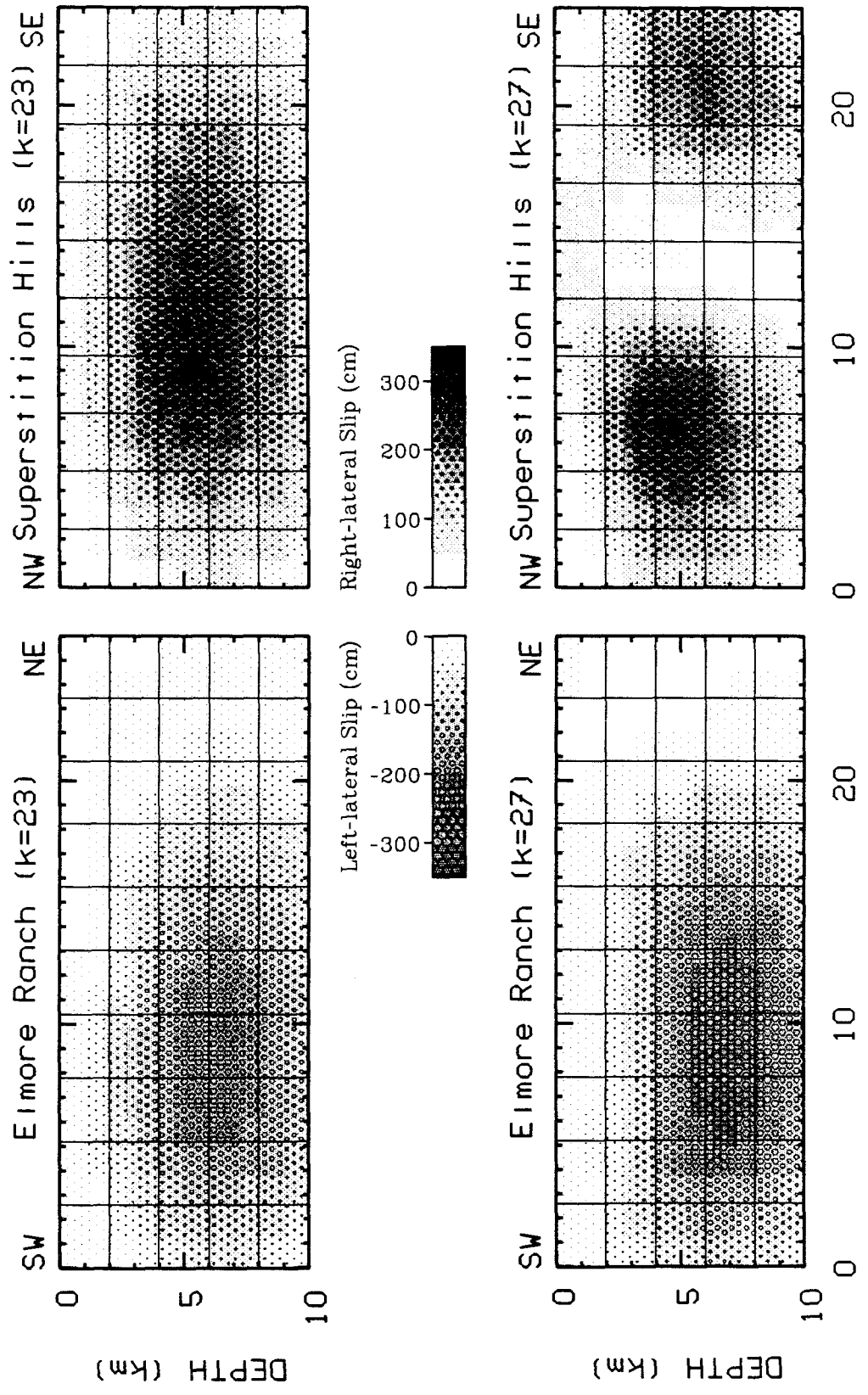
SW
Elmore Ranch (k=23)
NE
NW Superstition Hills (k=23) SE
SW
Elmore Ranch (k=27)
NE
NW Superstition Hills (k=27) SE
DEPTH (km)
0
5
10
LENGTH (km)
0
10
20
Left-lateral Slip (cm)
0
-100
-200
-300
Right-lateral Slip (cm)
0
100
200
300

Figure 4.14b: Slip distribution along the Superstition Hills and Elmore Ranch faults computed from Singular Value Decomposition. Each fault is partitioned into the 50 sub-elements indicated by the grid spacing. Shown here are solutions for $k = 3$ and $k = 7$ unconstrained by surface slip measurements.

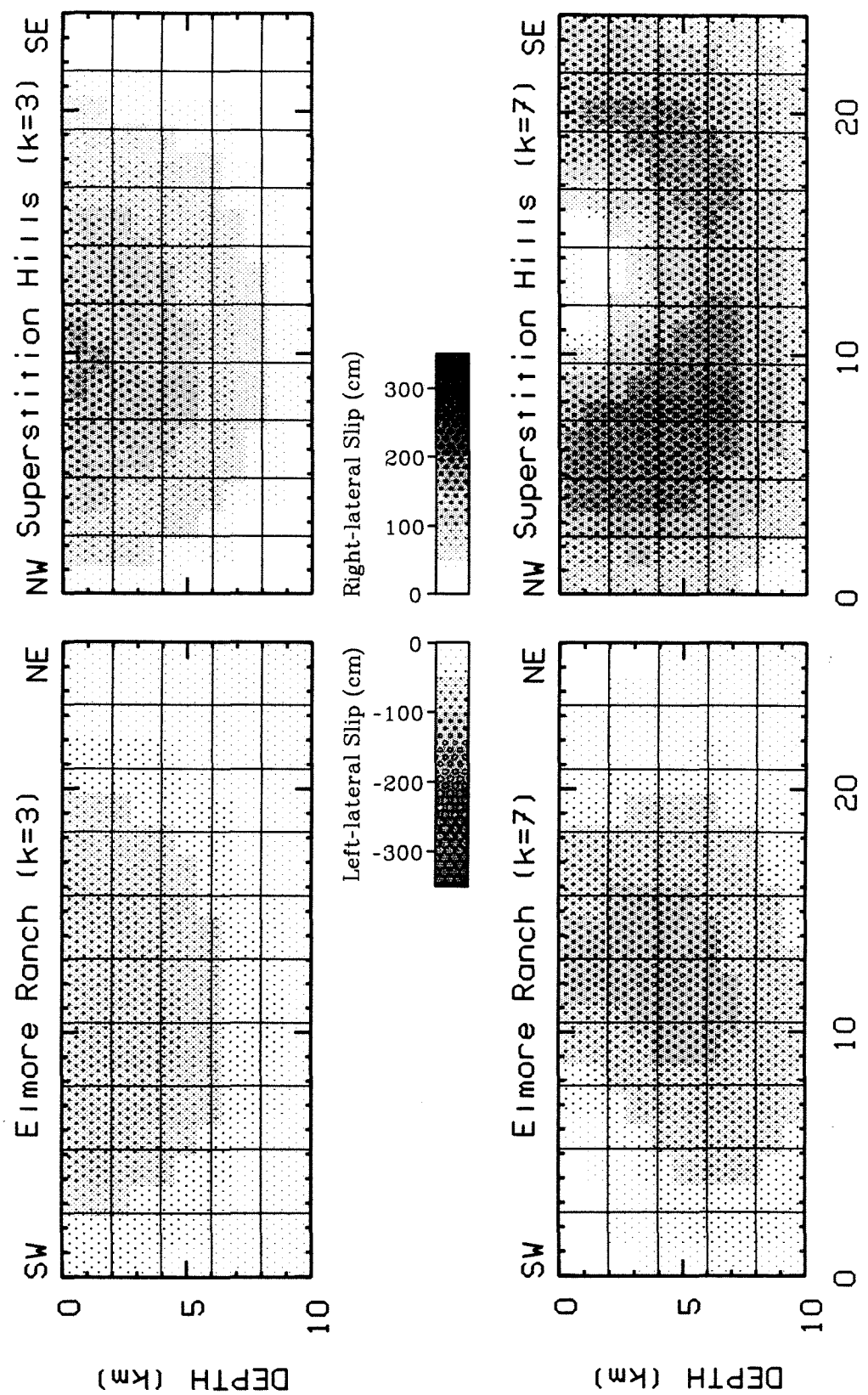
SW
Elmore Ranch (k=3)
NE
NW
Superstition Hills (k=3)
SE
SW
Elmore Ranch (k=7)
NE
NW
Superstition Hills (k=7)
SE
DEPTH (km)
0
5
10
LENGTH (km)
0
10
20
Left-lateral Slip (cm)
0
-100
-200
-300
Right-lateral Slip (cm)
0
100
200
300

of surface offset tends to change displacement magnitude by requiring slip at greater depths, however, it does not significantly alter estimates of slip distribution.

4.6 Geophysical Implications

Conjugate Faulting

The most prominent feature of the Superstition Hills earthquake sequence is the conjugate relationship exhibited by near-simultaneous ruptures along right-lateral northwest and left-lateral northeast trending faults. In the context of the Imperial Valley, the northeast trending structures are termed "cross-faults" [e.g., *Hudnut et al.*, 1989a]. Conjugate and cross-fault seismicity seems to be a fairly typical phenomenon for this region (Figure 4.15), and may dictate the strain transfer mechanism between faults. The 1981 Westmorland earthquake (M_L 4.1) is a prime example of cross-fault tectonics. The mainshock and aftershock sequence is clearly mapped onto a northeast trending lineament. Other examples are associated with the Imperial fault. The largest aftershock (M_L 5.8) following the 1979 Imperial Valley earthquake (M_L 6.6) was located near the town of Brawley [*Johnson and Hutton*, 1982]. The focal mechanism and following seismicity suggested left-lateral slip along a vertical northeast trending fault. *Reilinger and Larsen* [1986] found that rupture along an identical conjugate structure successfully modeled geodetic observations within the Brawley Seismic Zone. A large (M_L 5.5) aftershock was also recorded near Brawley following the 1940 earthquake [*Neumann*, 1942]. Due to the sparsity of seismic data, neither the mechanism nor location are precisely determined, although we speculate this event occurred

along the same northeast trending feature as the large 1979 aftershock. Of historical interest are Imperial Valley earthquake pairs during 1915 (M_L 6.3, M_L 6.3) and 1927 (M_L 5.8, M_L 5.5) [*Beal*, 1915; *Toppozada et al.*, 1978]. In each case the 2nd shock followed the first by about 1 hour, contrasting with the 12 hour interval between the 1987 events. It is not known which fault(s) ruptured during these earthquake sequences, but conjugate fault interaction is highly probable.

Rupture on the Superstition Hills fault was almost certainly triggered by the Elmore Ranch event (occurring 12 hours earlier) suggesting some mechanism of stress transfer between the two faults. Figure 4.16 shows the normal (σ_n) and strike-shear (σ_S) stress components instantaneously applied to the Superstition Hills fault due to a 30 cm left-lateral Elmore Ranch dislocation (Model 2). Tension and right-lateral shear are considered positive, both tending to induce failure on the rupture plane. Also shown is the Coulomb failure stress (σ_c), here given by $\sigma_c = \sigma_s + \mu\sigma_n$, where $\mu = 0.75$. Positive values indicate stress-loading leading toward shear failure.

The stress regime necessary for left-lateral rupture along a northeast trending fault is identical to that required for right-lateral failure along a northwest trending fault. Hence, we can assume that the Superstition Hills rupture plane was at or near failure at the time of the Elmore Ranch event. The initial shock generated an increase in the Coulomb failure potential along the Superstition Hills fault (Figure 4.16), possibly advancing it past its failure threshold. This is seen mostly as a combination of reduced compressive normal stress (earthquake inducing) countered by left-lateral shear (earthquake inhibiting). The increase is maximized along the northwest

Figure 4.15: Known and/or potential conjugate/cross-fault seismic episodes in the Imperial Valley since 1900. Seismic release on (left-lateral) northeast trending structures was observed in 1979, 1981, and 1987. Earthquake pairs or mainshock/aftershock sequences suggestive of conjugate faulting were observed in 1915, 1927, 1940. This suggests conjugate/cross-fault interaction is typical for the Imperial Valley.

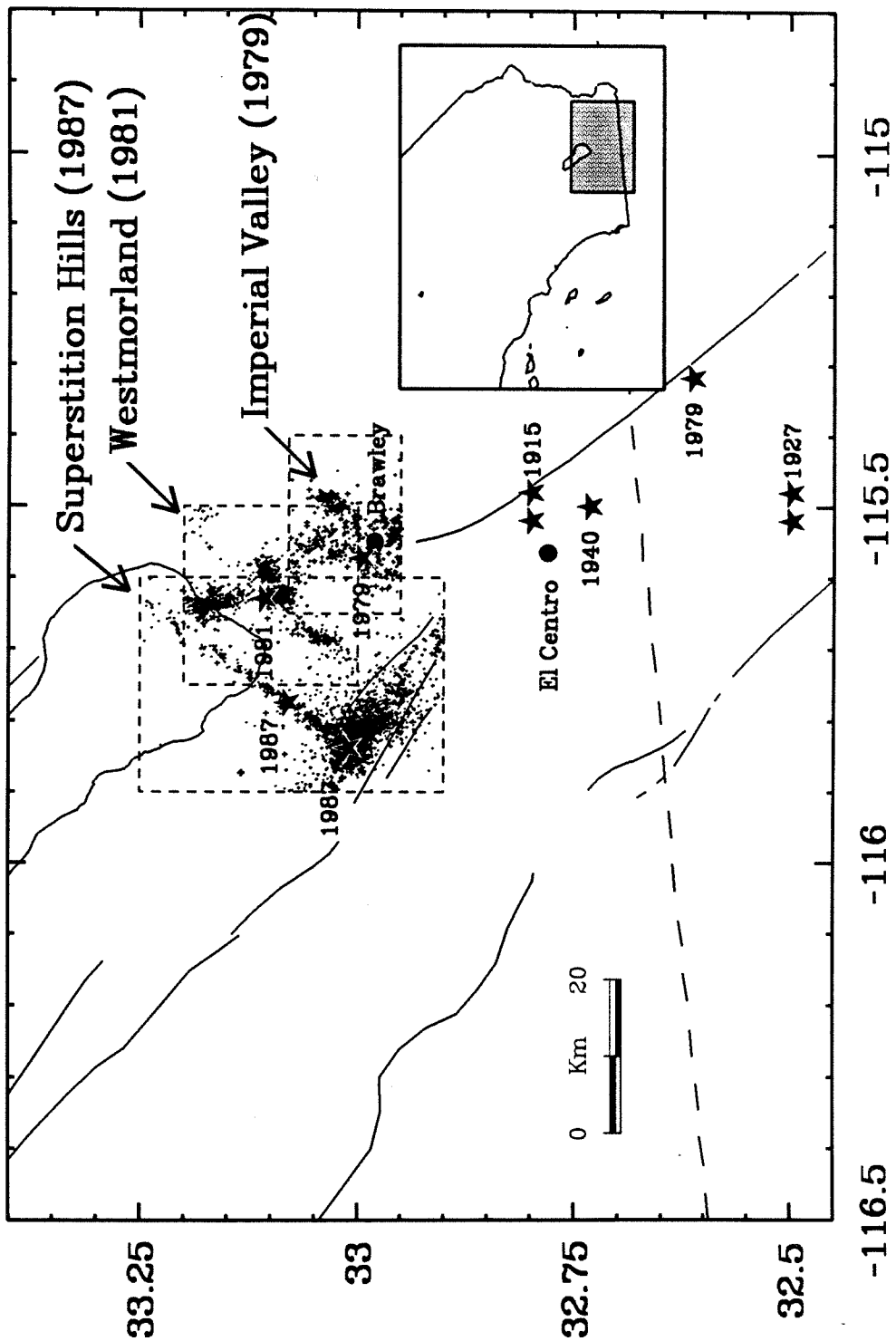
Superstition Hills (1987)
Westmorland (1981)
Imperial Valley (1979)
Brawley
El Centro
1915
1940
1979
1927
1981
1987
1979
1987
0 Km 20
33.25
33
32.75
32.5
-116.5
-116
-115.5
-115

Figure 4.16: Strike-shear (right-lateral positive) and normal stress change (dilatation positive) induced on the Superstition Hills fault due to a 30 cm left-lateral Elmore Ranch dislocation (Model 2). Also shown is the Coulomb failure stress change, where positive values indicate an increased potential for rupture (earthquake inducing stress). The northwest third of the 1987 Superstition Hills rupture plane underwent a stress change tending it toward failure with the maximum change calculated in the epicentral region near the intersection with the Elmore Ranch fault. There was no rupture to the northwest where the Coulomb failure stress was negative (reduced earthquake potential). The magnitude of the stress change (in bars) is in the range of typical earthquake stress drops.

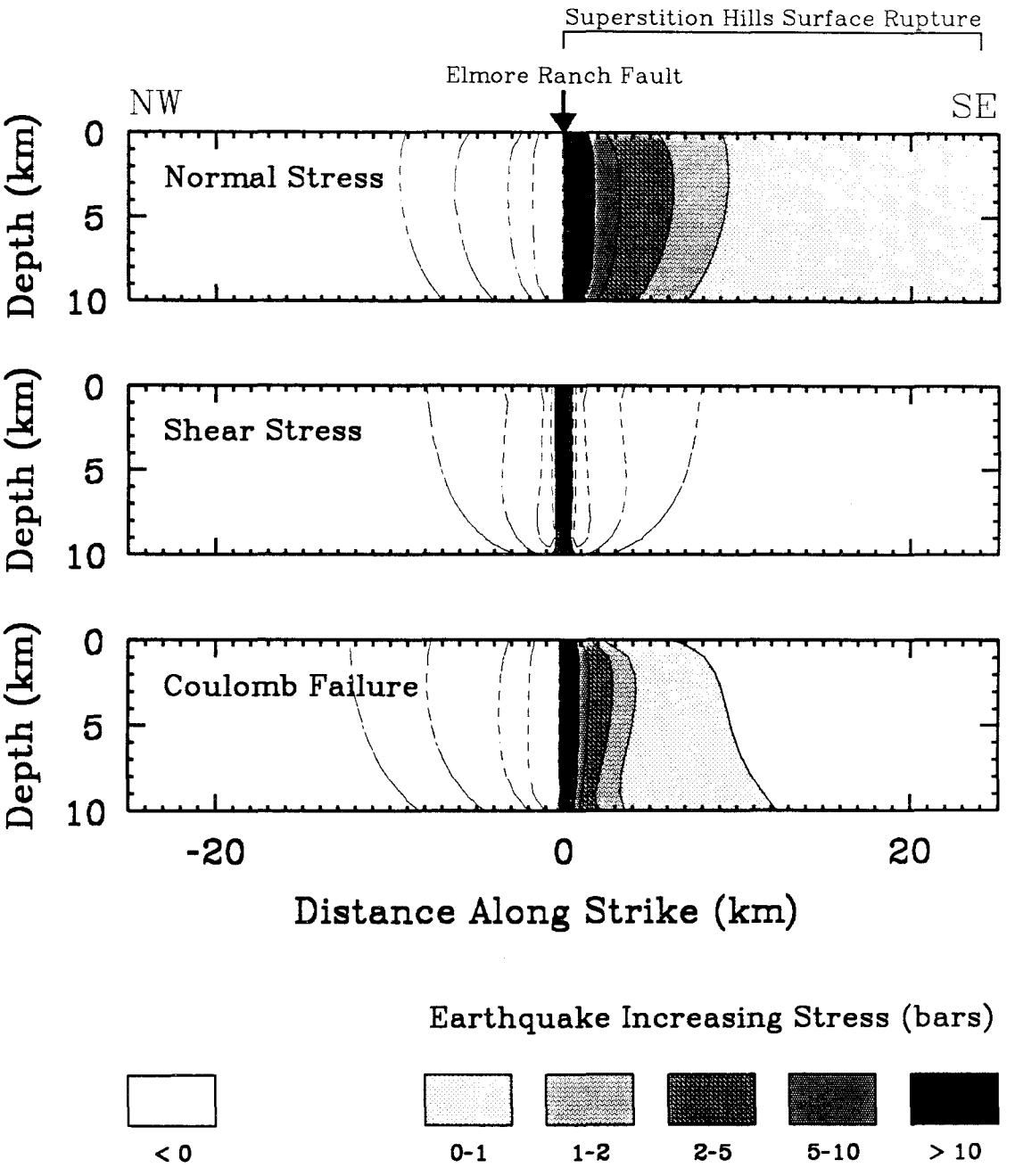
Superstition Hills Surface Rupture
Elmore Ranch Fault
NW
SE
Depth (km)
0
5
10
Normal Stress
Shear Stress
Coulomb Failure
-20
0
20
Distance Along Strike (km)
Earthquake Increasing Stress (bars)
< 0
0-1
1-2
2-5
5-10
> 10

boundary of the rupture plane, near the nucleation point of the second event. Presumably rupture began where the applied stress was greatest and then propagated to the southeast. Northwestward rupture is prohibited because the increase in compressive forces tends to inhibit shear failure along this segment of the fault. The magnitude of the Coulomb stress increase near the Superstition Hills epicentral zone ($\sim$ 10 bars) is comparable to typical earthquake stress drops.

The one to several hour delay recorded between events during observed and suspected conjugate episodes in the Imperial Valley is significant from an earthquake failure perspective. Shown in Figure 4.17 are potential scenario's for earthquake ruptures involving conjugate-mainshock interaction, such as that observed for the Superstition Hills events. We assume faults fail by an undefined mechanism when they are at or above some critical stress level. The regional strain acting over several years brings a given fault near this critical failure point. A stress increase is induced along part of the fault plane due to rupture on a conjugate structure (e.g., Figure 4.16), which may or may not be sufficient to push the stress state past its critical threshold. In the case of Earthquake 1 (Figure 4.17a), the stress change caused by the conjugate event is not enough to induce failure. Some form of time dependent stress transfer onto the fault is active and eventually the critical level is reached. Such a mechanism involving postseismic viscous creep along the Elmore Ranch fault has been suggested for the 1987 Superstition Hills sequence [*Given and Stuart*, 1988]. If this scenario is valid we would equally expect failure modes such as that indicated by Earthquake 2. Here the instantaneous stress applied to the fault from the conjugate event pushes the stress state past the

critical level and rupture is immediate. In this case failure along the two perpendicular fault planes will occur simultaneously. However, this behavior is not observed in the Imperial Valley. Conjugate episodes characteristically have been separated by one to several hours. This suggests that the critical stress level can be exceeded without immediate failure. Therefore, some time dependent mechanism must be active on the fault plane, as opposed to additional stress transfer through the crust. We loosely refer to this as "stress corrosion" (Figure 4.17b) [e.g., *Das and Scholz*, 1981]. In the case of Earthquakes 3 and 4, it is suggested that the critical stress level must be exceeded for a period of one to several hours before failure occurs. *Hudnut et al.* [1989b] proposed fluid diffusion as an alternate mechanism, whereby the effective normal stress was reduced (made more positive) due to pore-fluid infiltration into the rupture plane, thus increasing the Coulomb failure stress. This process still involves action on the fault plane rather than stress transfer. Regardless of cause, the temporal and geometric relationship exhibited by the conjugate fault interaction is seemingly typical of Imperial Valley tectonics and is thus an important factor for the potential prediction of large earthquakes and aftershocks.

Moment and slip distribution

The geodetic (GPS) source parameters for the Superstition Hills and Elmore Ranch earthquakes are listed in Table 4.6 and Figure 4.14. The seismic moment is best defined by Model 2, while the slip distribution is best expressed by Models 3a and 3b. Model 1 is constrained with minimal station coverage and Models 3c and 3d do not include the additional information supplied from surface slip measurements. The GPS observations are directly

Figure 4.17: Schematic of potential earthquake failure processes in the Imperial Valley. a) Earthquake failure occurs after some critical stress is reached. b) Earthquake failure occurs following a time dependent delay after critical stress is exceeded.

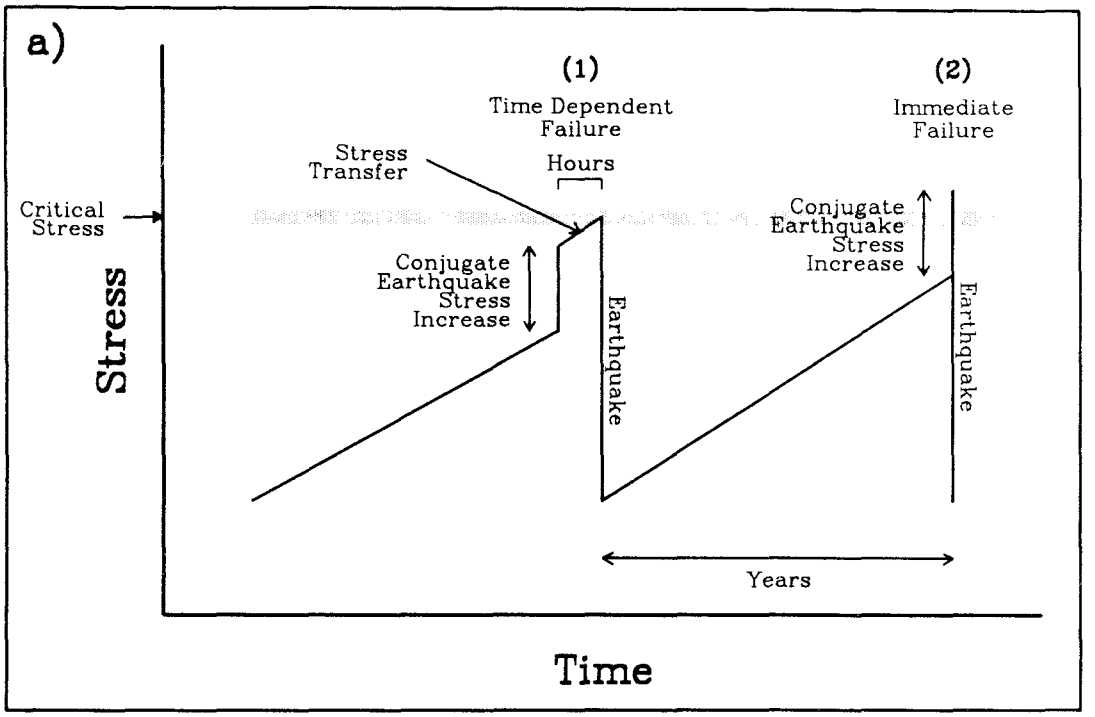
a)
(1)
Time Dependent
Failure
Hours
(2)
Immediate
Failure
Stress
Transfer
Critical
Stress
Conjugate
Earthquake
Stress
Increase
Earthquake
Conjugate
Earthquake
Stress
Increase
Earthquake
Years
Stress
Time

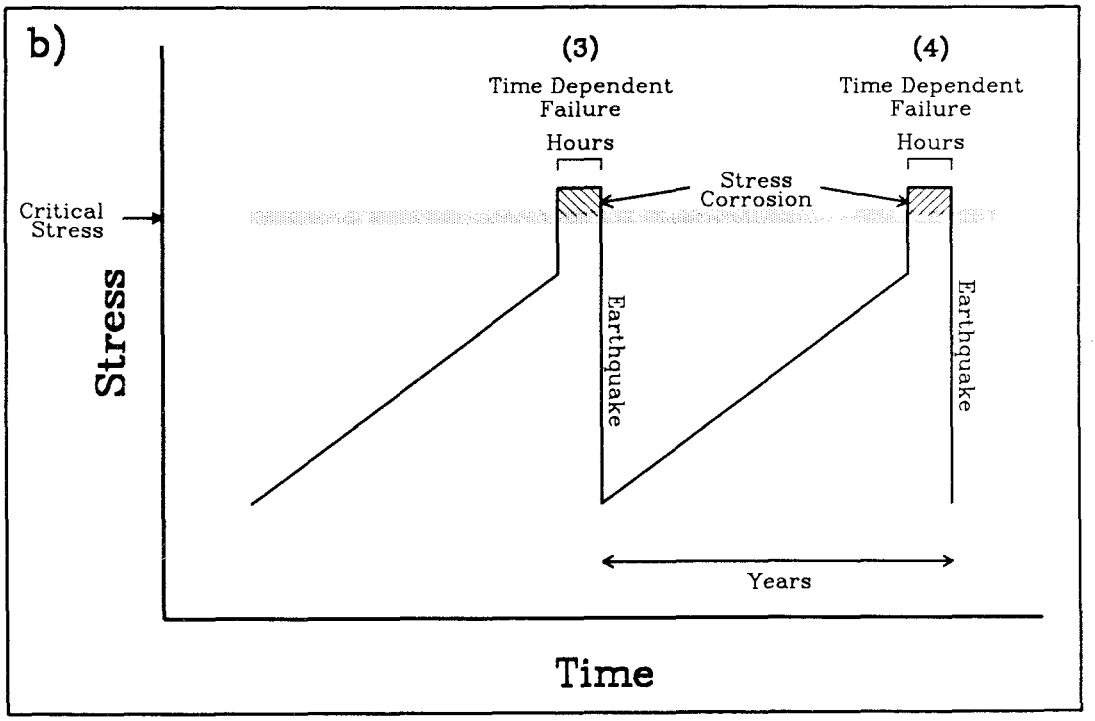
b)
(3)
Time Dependent
Failure
Hours
(4)
Time Dependent
Failure
Hours
Stress
Corrosion
Critical
Stress
Earthquake
Earthquake
Years
Stress
Time

proportional to the combined effect of the Elmore Ranch and Superstition Hills events, although we have attempted to resolve slip between each fault plane. The calculated parameters are a function of the coseismic offset, as well as 3-4 months of postseismic slip (plus 1.5 years of preseismic movement, if any). The average Elmore Ranch dislocation is about 30 cm (left-lateral) with fairly uniform distribution along the fault plane. In the case of the Superstition Hills fault, the average slip is estimated at 130 cm with concentrated deformation along the northwest and southeast sections of the fault. Because the GPS sampling frequency is so low (years), the calculated source parameters should contain the total coseismic moment release, which includes several months of postseismic slip.

In Table 4.7 the GPS moments are compared with estimates made through seismic and other geodetic studies. Forward and inverse models using teleseismic [*Dziewonski et al.*, 1989; *Bent et al.*, 1989; *Sipkin*, 1989; *Hwang et al.*, 1990] and strong-motion recordings [*Frankel and Wennerberg*, 1989; *Wald et al.*, 1990] are used to constrain source parameters, as well as investigate complexities of the Superstition Hills rupture process. The teleseismic moments agree fairly well with the GPS estimates, while the strong ground motion data yield significantly lower results. The high-frequency strong-motion measurements are dominated by energy around 1 second and conceivably miss a sizable portion of the long-period energy release recorded with the teleseismic and GPS data. Hence, the near field seismic solutions may underestimate the total moment release.

Geodetic measurements from Pinyon Flat observatory are used to constrain planer and curved dislocation models for the Superstition Hills and

Table 4.7 Moment Comparison

Method	Moment ($x10^{25}$ dyne-cm)				Reference
	SH	ER	Total	Ratio	
GPS (Model 2)	9.4	2.3	11.7	4.1	This Study
Teleseismic	7.2	1.4	8.6	5.1	*Dziewonski et al.* [1988]
Teleseismic	10.	2.3	12.	4.3	*Sipkin* [1989]
Teleseismic	10.8	2.7	13.5	4.0	*Bent et al.* [1989]
Teleseismic	8.				*Hwang et al.* [1990]
Strong Motion	5.2				*Wald et al.* [1989]
Strong Motion	1.8				*Frankell and Wennerberg* [1989]
Pinyon Flat (Planar-A)	3.7	0.8	4.3	4.6	*Agnew and Wyatt* [1989]
EDM	9.3				*Lisowski and Savage* [1988]

SH - Superstition Hills fault
ER - Elmore Ranch fault

Elmore Ranch faults [*Agnew and Wyatt*, 1989]. The data are obtained from long-base strain and tilt-meters, as well as a borehole dilatometer. The best-fit planer models to all observations (Table 4.7) are significantly lower than those calculated with the GPS and teleseismic data, although a 70 % moment increase for the Superstition Hills fault is obtained when the strainmeter data are excluded. The low moment estimate may be due to a number of factors [*Agnew and Wyatt*, 1989]: 1) measurement quality, particular with the strainmeter, 2) rheologic differences between Superstition Hills and Pinyon Flat, and 3) strainmeter-dilatometer sensitivity to the nodal deformation plane roughly on azimuth with the observatory.

Geodolite observations of the Salton Trough EDM network were made in early December (1987), several days after the two large earthquakes [*Lisowski and Savage*, 1988]; the last previous occupation was in January, 1987. Simple dislocation models with 40 cm left-lateral slip along the Elmore Ranch fault and 120 cm right-lateral slip along the Superstition Hills fault best-fit the observations. The estimated moment for the Superstition Hills event (Table 4.7) is comparable to that obtained with the GPS displacements.

The discrepancies in Table 4.7 are largely attributed to the alternate methodologies, observations, and parameters used to constrain each model. However, for those calculations which include moment estimates for both the Superstition Hills and Elmore Ranch events, the ratio between the two ruptures is fairly constant. This illustrates an internal consistency with each method. More importantly, it suggests that postseismic slip along the Superstition Hills fault is probably confined to the shallow segment of the rupture plane. Since seismic activity on the Elmore Ranch fault essentially

ceased after the 2nd main event, if postseismic slip were occurring in mass along a large fraction of the Superstition Hills rupture plane, the GPS moment ratio would be considerably larger.

While the epicenter and aftershock sequence for the Superstition Hills event were concentrated along the northwestern portion of the fault, strong ground motion, teleseismic, and surface offset data suggest significant moment release on the southern section of the Superstition Hills fault [*Wald et al.*, 1989; *Bent et al.*, 1989; *Hwang et al.*, 1990; *Williams and Magistrale*, 1989]. An exception is the strong ground motion study of *Frankel and Wennerberg* [1989] where slip is confined to the northwest. However, their low Superstition Hills moment (Table 4.7) suggests this analysis may be strongly susceptible to the high-frequency content of the data, indicating rupture along the southeast segment was dictated primarily by low-frequency energy release. The GPS data also reveal dislocation along the southeastern segment of the fault, and further suggests a displacement null near the faults mid-section. This slip deficiency may be related to the surface offset drop observed along the center of the fault (Figure 4.10).

Deformation across the Imperial Valley

The 1986-1988 GPS station displacements indicate a significant component of deformation across the Imperial Valley not associated with the 1987 Superstition Hills earthquake sequence (Figures 4.4 and 4.8). This motion is attributed to plate-boundary deformation due to the relative velocity between the Pacific and North American plates. From empirical evidence provided by Salton Trough EDM observations between 1972 and

1987, these non-seismic movements were modeled as 3.45 cm/yr differential velocity across the valley. However, after removing the seismic deformation predicted with a preliminary model (Model 1, Table 4.6) the calculated GPS displacements average 5.9 cm/yr (Figure 4.8), significantly larger than that obtained with the trilateration measurements over the last two decades. This GPS velocity is also larger than the 4.7 cm/yr plate motion predicted from global models (for Imperial Valley coordinates) [*DeMets et al.*, 1990]. Most likely the GPS rate is an overestimate, especially considering it contains large measurement uncertainty due to poor 1986 data quality, and is heavily influenced by seismic effects from the 1987 earthquake sequence. It is possible, however, that the 1986-1988 GPS rate could represent accelerated deformation. In fact, GPS observations between 1988 and 1989 indicate 5.2 $\pm$ 0.9 cm/yr displacement across the Imperial Valley [*Larsen and Reilinger*, 1990]. Accelerated deformation is not without precedence. Triangulation observations suggest a rate of 6.2 cm/yr between 1941 and 1954, although this is attributed to postseismic deformation following the 1940 Imperial Valley earthquake. Increased deformation following the 1979 earthquake is not observed in the EDM observations [*Savage et al.*, 1986]. Additional GPS measurements are necessary in the Imperial Valley in order to ascertain the current deformation rate.

4.7 Conclusions

Station movements computed from 4 Imperial Valley GPS campaigns indicate large crustal displacements during the periods 1986-1988 and 1986-1990. Much of the deformation is attributed to the 1987 Superstition Hills

earthquake sequence. Ten sites near the seismic rupture zone are displaced at least 10 cm, although the GPS observations contain large uncertainties due to poor data quality from the initial (1986) survey. This is the first occurrence of a large earthquake within a preexisting GPS network.

The 1987 earthquake sequence is initially modeled as uniform offsets along rectangular dislocations in an elastic half-space. The best-fit model to the GPS observations requires 130 cm right-lateral slip along the northwest trending Superstition Hills fault and 30 cm left-lateral motion along the conjugate northeast trending Elmore Ranch fault. The slip distribution along each fault is investigated by partitioning the rupture planes into 50 sub-elements and utilizing Singular Value Decomposition to estimate the slip along each sub-fault. Measurements of surface offset are used to constrain the shallow elements of the fault plane. The estimated slip distribution along the Elmore Ranch fault is fairly uniform. Slip along the Superstition Hills fault appears to be concentrated to the northwest and the southeast with a displacement drop indicated near the faults midsection. There is some evidence that postseismic slip along the Superstition Hills fault was concentrated near the surface. The estimated moments are 9.4×10^{25} dyne-cm and 2.3×10^{25} dyne-cm for the Superstition Hills and Elmore Ranch faults, respectively, which are consistent with moments obtained from teleseismic data.

In addition, the 1986-1988 GPS observations suggest non-seismic movements across the Imperial Valley of up to 5.9 cm/yr. These secular displacements are attributed to plate-boundary deformation due to the relative motion between the North American and Pacific plates. The observed

rate is probably an overestimate, however, as it is heavily influenced by unmodeled seismic effects and measurement error. Regardless, the observed seismic and secular deformations clearly emphasize the importance of future GPS study in the Imperial Valley.

Acknowledgements

This research was a collaborative effort conducted under the auspices of Robert Reilinger (MIT). The field support provided by so many people has proven invaluable. William Young and Gerald Dole at the Riverside County Flood Control District and Gerald Stayner at the Riverside County Survey Department provided support for the 1990 mini-campaign. I am especially grateful to the support provided by Hiroo Kanamori. This work is supported by U.S.G.S. grants 14-08-0001-61679 (MIT) and 14-08-001-61354 (Caltech), and by NASA contracts NAG-5-842 (Caltech) and NAG-5-814 (MIT).

References

Agnew, D. C., and F. K. Wyatt, The 1987 Superstition Hills earthquake sequence: Strains and tilts at Pinon Flat observatory, *Bull. Seismol. Soc. Am.*, *79*, 480-492, 1989.

Alewine, R. W., Application of linear inversion theory toward the estimation of seismic source parameters, Ph.D. Thesis, California Institute of Technology, Pasadena, 303 pp., 1974.

Beal, C. H., The earthquake in the Imperial Valley, California, June 22, 1915, *Bull. Seismol. Soc. Am.*, *5*, 130-149, 1915.

Bent, A. L., D. V. Helmberger, R. J. Stead, and P. Ho-Liu, Waveform modeling of the November 1987 Superstition Hills earthquakes, *Bull. Seismol. Soc. Am.*, *79*, 500-514, 1989.

Beutler, G., W. Gurtner, I. Bauersima, and R. Langley, Modeling and estimating the orbits of GPS satellites, paper presented at First International Symposium on Precise Positioning with the Global Positioning System, Int. Assoc. of Geod., Rockville, Md., April 15-19, 1985.

Budding, K. E., and R. V. Sharp, Surface faulting associated with the Elmore Ranch and Superstition Hills, California, earthquake of 24 November 1987, *Seismol. Res. Letts.*, *59*, p. 49, 1988.

Chinnery, M. A., The deformation of the ground around surface faults, *Bull. Seismol. Soc. Am.*, *51*, 355-372, 1961.

Chinnery, M. A., The stress changes that accompany strike-slip faulting, *Bull. Seismol. Soc. Am.*, *53*, 921-932, 1963.

Das, S., and C. H. Scholz, Off-fault aftershock clusters caused by shear stress increase?, *Bull. Seismol. Soc. Am.*, *71*, 1669-1675, 1981.

Davis, J. L., W. H. Prescott, J. L. Svarc, and K. J. Wendt, Assessment of global positioning system measurements for studies of crustal deformation, *J. Geophys. Res.*, *94*, 13,635-13,650, 1989.

Defense Mapping Agency, Department of Defense world geodetic system 1984, *DMA TR 8350.2*, D.M.A. Washington, D. C., 122 pp., 1987.

DeMets, C., R. G. Gordon, S. Stein, and D. F. Argus, A revised estimate of Pacific-North America motion and implications for western North America plate boundary zone tectonics, *Geophys. Res. Letts.*, *14*, 911-914, 1987.

DeMets, C., R. G. Gordon, D. F. Argus, and S. Stein, Current plate motions, *Geophys. J. Inter.*, *101*, 425-478, 1990.

Dong, D., and Y. Bock, Global positioning system network analysis with phase ambiguity resolution applied to crustal deformation studies in California, *J. Geophys. Res.*, *94*, 3949-3966, 1989.

Drew, A. R., and R. A. Snay, DYNAP: software for estimating crustal deformation from geodetic data, *Tectonophysics*, *162*, 331-343, 1989.

Dziewonski, A. M., G. Ekstrom, J. H. Woodhouse, and G. Zwart, Centroid-moment tensor solutions for October-December 1987, *Phys. Earth Planet.*

Inter., *54*, 10-21, 1989.

Elders, W. A., R. W. Rex, T. Meidav, P. T. Robinson, and S. Biehler, Crustal spreading in southern California, *Science*, *178*, 15-24, 1972.

Frankel, A., and L. Wennerberg, Rupture process of the M_S 6.6 Superstition Hills earthquake determined from strong-motion recordings: Application of tomographic source inversion, *Bull. Seismol. Soc. Am.*, *79*, 515-541, 1989.

Fuis, G. S., W. D. Mooney, J. H. Healey, G. A. McMechan, and W. J. Lutter, Crustal structure of the Imperial Valley region, *U.S. Geol. Surv. Prof. Pap.*, *1254*, 25-50, 1982.

Given, D. D., and W. D. Stuart, A fault interaction model for triggering of the Superstition Hills earthquake of November 24, 1987, *Seismol. Res. Letts.*, *59*, p. 48, 1988.

Gurtner, W., G. Beutler, I. Bauersima, and T. Schildknecht, Evaluation of GPS carrier difference observations: The Bernese second generation software package, paper presented at First International Symposium on Precise Positioning With the Global Positioning System, Int. Assoc. of Geod., Rockville, Md., April 15-19, 1985.

Harris, R. A., and P. Segall, Detection of a locked zone at depth on the Parkfield segment of the San Andreas fault, *J. Geophys. Res.*, *92*, 7945-7962, 1987.

Hudnut, K. W., L. Seeber, T. Rockwell, J. Goddmacher, R. Klinger, S.

Lindvall, and R. McElwain, Surface ruptures on cross-faults in the 24 November 1987 Superstition Hills, California, earthquake sequence, *Bull. Seismol. Soc. Am.*, *79*, 282-296, 1989a.

Hudnut, K. W., L. Seeber, and J. Pacheco, Cross-fault triggering in the November 1987 Superstition Hills earthquake sequence, southern California, *Geophys. Res. Letts.*, *16*, 199-202, 1989b.

Hudnut, K., and M. Clark, New slip along parts of the 1968 Coyote Creek fault rupture, California, *Bull. Seismol. Soc. Am.*, *79*, 451-465, 1989.

Hwang, L. J., H. Magistrale, and H. Kanamori, Teleseismic source parameters and rupture characteristics of the 24 November 1987, Superstition Hills earthquake, *Bull. Seismol. Soc. Am.*, *80*, 43-56, 1990.

Iwasaki, T., and R. Sato, Strain field in a semi-infinite medium due to an inclined rectangular fault, *J. Phys. Earth*, *27*, 285-314, 1979.

Jackson, D. D., Interpretation of inaccurate, insufficient and inconsistent data, *Geophys. J. R. Astron. Soc.*, *28*, 97-107, 1972.

Johnson, C. E., and D. P. Hill, Seismicity of the Imperial Valley, *U.S. Geol. Surv. Prof. Pap.*, *1254*, 14-24, 1982.

Johnson, C. E., and L. K. Hutton, Tectonic implications of the November 24, 1987, Superstition Hills earthquakes, Imperial Valley, CA, *Seismol. Res. Letts.*, *59*, p. 48, 1988.

King, R. W., E. G. Masters, C. Rizos, A. Stolz, and J. Collins, *Surveying with GPS, Monograph 9*, School of Surveying, The University of New South

Wales, Kensington, Australia, 128 pp., 1985.

Lanczos, C., *Linear Differential Operators*, D. Van Nostrand, New York, 1961.

Larsen, S. C., R. E. Reilinger, GPS measurements of strain accumulation across the Imperial Valley, California: 1986-1989, in preparation, 1990.

Larsen, S. C., D. C. Agnew, B. H. Hager, Strain accumulation in the Santa Barbara channel: 1971-1987, in preparation, 1990.

Lichten, S. M., and J. S. Border, Strategies for high-precision Global Positioning Systems orbit determination, *J. Geophys. Res.*, *92*, 12,751-12,762, 1987.

Lisowski, M., and J. C. Savage, Deformation associated with the Superstition Hills, California, earthquakes of November 1987, *Seismol. Res. Letts.*, *59*, p. 35, 1988.

Lomnitz, C., F. Mooser, C. R. Allen, J. N. Brune, and W. Thatcher, Seismicity and tectonics of northern Gulf of California region, Mexico: Preliminary results, *Geofis. Int.*, *10*, 34-48, 1970.

Magistrale, H., L. Jones, and H. Kanamori, The Superstition Hills, California, earthquakes of 24 November, 1987, *Bull. Seismol. Soc. Am.*, *79*, 239-251, 1989.

Mansinha, L., and D. E. Smylie, Effect of earthquakes on the Chandler wobble and the secular polar shift, *J. Geophys. Res.*, *72*, 4731-4743, 1967.

Mansinha, L., and D. E. Smylie, The displacement fields of inclined faults,

Bull. Seismol. Soc. Am., *61*, 1433-1440, 1971.

McGill, S. F., C. R. Allen, K. W. Hudnut, D. C. Johnson, W. F. Miller, and K. E. Sieh, Slip on the Superstition Hills fault and on nearby faults associated with the 24 November 1987 Elmore Desert Ranch and Superstition Hills earthquakes, southern California, *Bull. Seismol. Soc. Am.*, *79*, 362-375, 1989.

Menke, W., *Geophysical Data Analysis: Discrete Inverse Theory*, Academic, Orlando, Fla., 1984.

Neugebauer, H. C., The 1986 Salton trough GPS survey and data processing results, National Geodetic Survey (unpublished report), 1988.

Neumann, F., United States earthquakes, 1940, *U.S. Coast and Geod. Sur. Serial*, *647*, 74 pp., 1942.

Okada, Y., Surface deformation due to shear and tensile faults in a half-space, *Bull. Seismol. Soc. Am.*, *75*, 1135-1134, 1985.

Prescott, W. H., The determination of displacement fields from geodetic data along a strike slip fault, *J. Geophys. Res.*, *86*, 6067-6072, 1981.

Prescott, W. H., J. C. Savage, and M. Lisowski, Crustal strain, in National Earthquake Hazards Reduction Program, Summaries of Technical Reports, *U.S. Geological Survey Open-File Report*, *87-374*, 272-280, 1987a.

Prescott, W. H., M. Lisowski, and J. C. Savage, Velocity field along the San Andreas fault in southern California, *EOS Trans.*, *68*, p. 1506, 1987b.

Reilinger, R. E., and S. C. Larsen, Vertical crustal deformation associated with the 1979 M=6.6 Imperial Valley, California earthquake: Implications for fault behavior, *J. Geophys. Res.*, *91*, 14,044-14,056, 1986.

Rocken, C., The global positioning system: A new tool for tectonic studies, Ph.D. Thesis, University of Colorado, Boulder, 365 pp., 1988.

Savage, J. C., and L. M. Hastie, Surface deformation associated with dip-slip faulting, *J. Geophys. Res.*, *71*, 4897-4904, 1966.

Savage, J. C., W. H. Prescott, and G. Gu, Strain accumulation in southern California, 1973-1984, *J. Geophys. Res.*, *91*, 7455-7473, 1986.

Savage, J. C., Effect of crustal layering upon dislocation modeling, *J. Geophys. Res.*, *92*, 10,595-10,600, 1987.

Segall, P., and R. Harris, Earthquake deformation cycle on the San Andreas fault near Parkfield, California, *J. Geophys. Res.*, *92*, 10,511-10,525, 1987.

Sipkin, S. A., Moment-tensor solutions for the 24 November 1987 Superstition Hills, California earthquake, *Bull. Seismol. Soc. Am.*, *79*, 493-499, 1989.

Snay, R. A., Enhancing the geodetic resolution of fault slip by introducing prior information, *Manuscripta Geodaetica*, *14*, 391-403, 1989.

Snay, R. A., and A. R. Drew, Supplementing geodetic data with prior information for crustal deformation in the Imperial Valley, California, Technical Report Series, University of Stuttgart, 30 pp., 1988.

Steketee, J. A., On Volterra's dislocations in a semi-infinite medium, *Can.*

Jour. Phys., *36*, 192-205, 1958.

Toppozada, T. R., D. L. Parke, and C. T. Higgins, Seismicity of California 1900-1931, *Calif. Div. of Mines and Geol Spec. Rep.*, *135*, 39 pp., 1978.

U.S. Geological Survey, The Imperial Valley, California, earthquake of October 15, 1979, *U.S. Geol. Surv. Prof. Pap.*, *1254*, 451 pp., 1982.

Wald, D. J., D. V. Helmberger, S. H. Hartzell, Rupture process of the 1987 Superstition Hills earthquake from the inversion of strong motion data, *Bull. Seismol. Soc. Am.*, in press, 1990.

Ward, S. N., and S. E. Barrientos, An inversion for slip distribution and fault shape from geodetic data observations of the 1983, Borah Peak, Idaho, earthquake, *J. Geophys. Res.*, *91*, 4909-4919, 1986.

Wells, D., N. Beck, D. Delikaraoglou, A. Kleusberg, E. J. Krakiwsky, G. Lachapelle, R. B. Langley, M. Nakiboglu, K. Schwarz, J. M. Tranquilla, and P. Vanicek, *Guide to GPS Positioning*, Canadian GPS Associates, Fredericton, N. B., Canada, 1987.

Williams, P. L., and H. W. Magistrale, Slip along the Superstition Hills fault associated with the 24 November 1987 Superstition Hills, California, earthquake, *Bull. Seismol. Soc. Am.*, *79*, 390-410, 1989.

Chapter 5

GPS Measurements of Strain Accumulation Across the Imperial Valley, California: 1986-1989

Abstract

GPS data collected in southern California from 1986 to 1989 indicate considerable strain accumulation across the Imperial Valley. Displacements are computed at 29 stations in and near the valley from 1986 to 1988, and at 11 sites from 1988 to 1989. The earlier measurements indicate 5.9 $\pm$ 1.0 cm/yr right-lateral differential velocity across the valley, although the data are heavily influenced by the 1987 Superstition Hills earthquake sequence. Some measurements, especially the east-west trending displacements, are suspect for large errors. The 1988-1989 GPS displacements are best modeled by 5.2 $\pm$ 0.9 cm/yr of plate-boundary deformation, but rates calculated from conventional geodetic measurements (3.4-4.3 cm/yr) fit the data nearly as well. There is evidence from GPS and VLBI observations that the present slip rate along the southern San Andreas fault is smaller than the long-term geologic estimate, suggesting a lower earthquake potential than is currently assumed. The Imperial Valley GPS sites form part of a larger network of 183 stations spanning an entire cross-section of southern California and northern Mexico. Once data from a recent 1990 campaign are fully analyzed and integrated with the previous measurements, the strain distribution across the San Andreas, San Jacinto, and Elsinore faults will be well established.

5.1 Introduction

The Global Positioning System (GPS) is rapidly becoming one of the most important tools to study tectonic deformation. Signals from earth-orbiting NAVSTAR satellites (NAVigation Satellite Time And Ranging) are inverted to obtain 3-dimensional coordinates of geodetic monuments with high precision. For crustal deformation studies, the relative position (or baseline) between stations is often measured. Under optimal conditions, the typical accuracy for a 50 km baseline is about 1 cm in the horizontal and 3 cm in the vertical [e.g., *Davis et al.*, 1989]. The accuracy is significantly degraded from poor observing conditions. GPS measurements are used to monitor secular deformation such as that associated with plate motion, or to record rapid strain fluctuations such as those due to seismic and volcanic activity.

A prime location for GPS studies is the Imperial Valley of southern-most California (Figure 5.1). The valley is one of the most tectonically active regions in the state and has been the site of several large earthquakes. In fact, GPS monitoring was initiated in 1986 with resurveys in 1988 and 1989. GPS station displacements from 1986 to 1988 have been discussed by *Larsen et al.* [1990]. These measurements illustrate the effect of the 1987 Superstition Hills earthquake sequence, as well as nonseismic displacement components attributed to interplate deformation. In the present study we incorporate the 1989 GPS observations. Station displacements from 1986-1988 and 1988-1989 are computed and these movements are related to the relative motion between the North American and Pacific plates.

5.2 Seismicity and Tectonics

Figure 5.1: Major faults and seismicity from 1932 to 1990 (Caltech Catalog) in the Imperial Valley. Large earthquakes are shown as stars. The Brawley Seismic Zone is the region of anomalously high activity between the Imperial and San Andreas faults. Major earthquakes include the 1940 and 1979 events along the Imperial fault, the 1954 and 1968 events along the San Jacinto fault, and the 1987 Superstition Hills earthquake sequence along the Superstition Hills and Elmore Ranch faults.

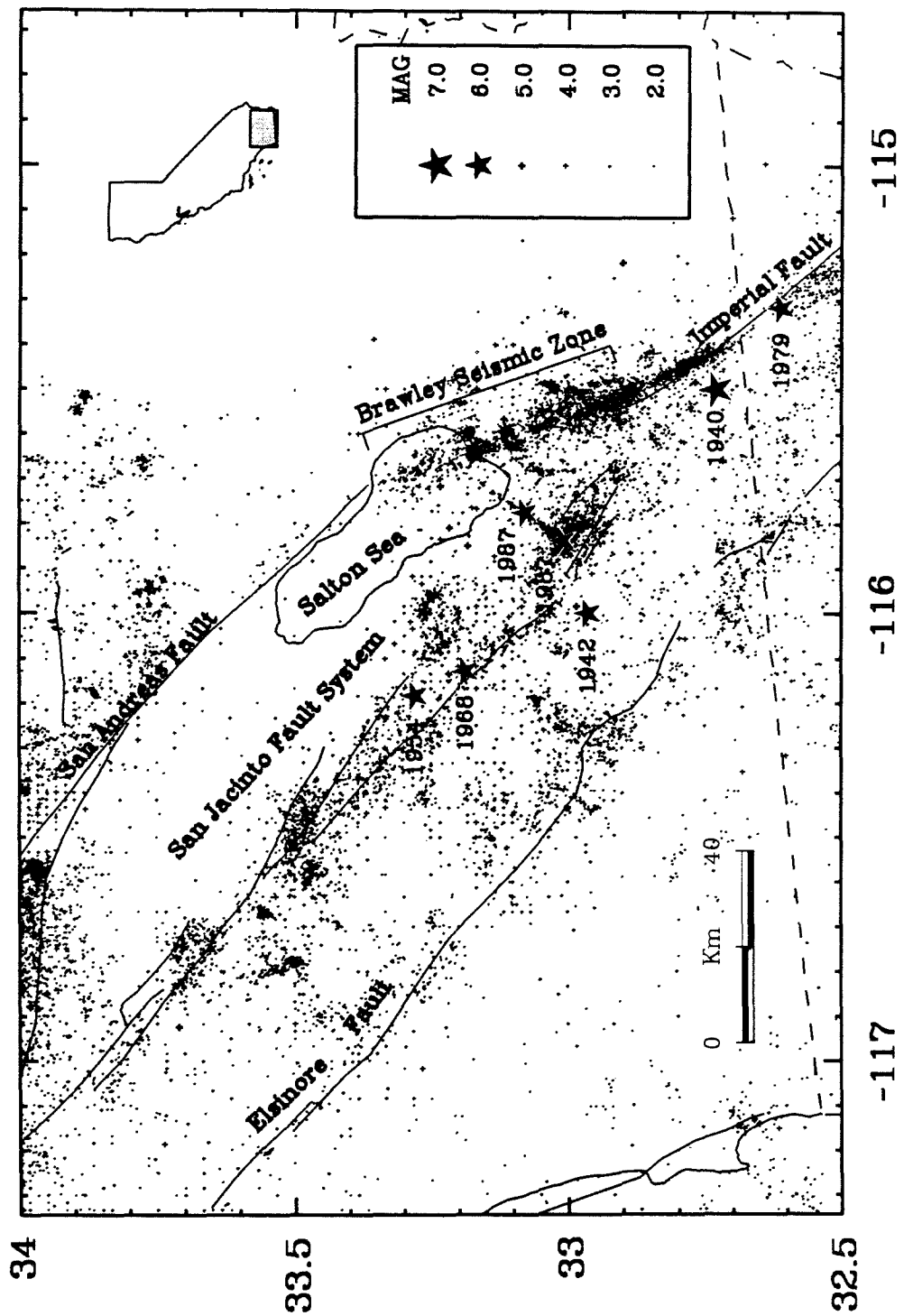
MAG
7.0
6.0
5.0
4.0
3.0
2.0
Brawley Seismic Zone
Imperial Fault
Salton Sea
San Andreas Fault
San Jacinto Fault System
Elsinore Fault
1940
1979
1987
1968
1942
0
Km
40
34
33.5
33
32.5
-117
-116
-115

The Imperial Valley (Figure 5.1) is a complex transition zone between crustal spreading in the Gulf of California and right-lateral transform motion along the San Andreas fault [*Lomnitz et al.*, 1970; *Elders et al.*, 1972]. The valley is 4-5 million years old and has been filled by up to 5 km of late Cenozoic sediments [*Fuis et al.*, 1982]. The structural axis of the valley and its major fault systems trend to the northwest, roughly parallel to the Pacific-North American plate motion. A significant fraction of the relative plate displacement may be accommodated across the valley.

The Imperial Valley is one of the most seismically active regions of California with much of the activity occurring along the Imperial fault and in the Brawley Seismic Zone [*Johnson and Hill*, 1982]. Several large earthquakes have occurred in and near the Imperial Valley since 1940. The Imperial fault ruptured with a M_S 7.1 event in 1940 and a M_L 6.6 event in 1979 [*U. S. G. S.*, 1982]. Segments of the San Jacinto fault system broke with a M_L 6.2 earthquake in 1954 (Clark segment) and the 1968 M_L 6.5 Borrego Mountain event (Coyote Creek segment). The most GPS relevant episode of seismic activity occurred recently along the Superstition Hills segment of the San Jacinto fault system [e.g., *Magistrale et al.*, 1989]. On November 24, 1987, a large (M_S 6.2) earthquake occurred along a northeast trending seismic lineament, and was followed 12 hours by a larger event (M_S 6.6) along the Superstition Hills fault.

Conventional geodetic measurements indicate significant displacements across the Imperial Valley, inferred to represent interplate deformation. Triangulation data averaged from 1941 to 1986 suggest 4.3 cm/yr plate-boundary movement oriented N40°W [*Snay and Drew*, 1988]. The observed

deformation is time dependent, with rates of 6.1, 2.1, and 4.5 cm/yr for the intervals 1941-1954, 1954-1967, and 1967-1979, respectively. The high velocity for the earliest period supports the hypothesis of northwestward strain migration following the 1940 earthquake [*Thatcher*, 1979; *Reilinger*, 1984]. Furthermore, the computed station displacements indicate that north of the Imperial fault interplate deformation is distributed over a zone at least 50 km wide whereas to the south interplate deformation is concentrated within a 20 km wide band centered along the Imperial fault. Trilateration measurements made by the U.S. Geological Survey from 1972 to 1987 [*Prescott et al.*, 1987a; *Prescott et al.*, 1987b] indicate 3.45 cm/yr differential displacement oriented roughly N40°W between stations on opposite sides of the valley. Unlike the increased rate following the 1940 earthquake, these measurements reveal no significant change in station velocity after the 1979 event [*Savage et al.*, 1986].

New global plate models (NUVEL-1) [*DeMets et al.*, 1987; *DeMets et al.*, 1990] predict the Pacific-North American relative velocity at Imperial Valley coordinates (longitude 115.5°W, latitude 33.0°N) averaged over the last several million years to be 4.7 cm/yr oriented N39.6°W. VLBI observations during the 1980's suggest a similar present-day rate [e.g., *Clark et al.*, 1987; *Kroger et al.*, 1987]. A significant fraction of this motion may be distributed along faults in and near the Imperial Valley.

5.3 GPS Observations

The data presented here were obtained in a series of GPS field campaigns in 1986, 1988, and 1989. Here we provide summaries regarding the collection

and processing of the 1986 and 1988 surveys, discussed in more detail by *Larsen et al.* [1990], and present a more detailed account of the most recent campaign. In all, a total of 32 Imperial Valley stations have been occupied more than once between 1986 and 1989 (Table 5.1).

The National Geodetic Survey (NGS) began GPS observations in southern California with a 54 station network in 1986; 42 stations are located in or near the Imperial Valley (Figure 5.2). TI-4100 GPS receivers were used for all data collection. Each of the 20 days of observation are processed independently utilizing the GPS22 software developed at the NGS, with satellite orbit parameters provided by the NSWC (Naval Surface Weapons Center). The day to day solutions are integrated into one set of station coordinates with the geodetic adjustment program DYNAP (DYNamic Adjustment Program) [*Drew and Snay*, 1989]. Due to insufficient coverage and poor data quality during the 1986 survey, uncertainties are suggested to be approximately 1 ppm (parts per million) [*Neugebauer*, 1988].

During late February and early March, 1988, university GPS crews (UNAVCO) occupied 19 sites in the Imperial Valley, including 15 marks observed in 1986 (Figure 5.2). The following month, the NGS returned to the Imperial Valley and reoccupied 21 previously established monuments. TI-4100 receivers were used for all measurements. Data from both surveys are processed independently with the Bernese GPS software package from the University of Bern in Switzerland. For each campaign, the data are combined into one multiday solution. Satellite orbits are improved with the aid of fiducial observations from Mojave (California), Westford (Massachusetts), and Richmond (Florida), made as part of the Cooperative International GPS

Table 5.1 Reoccupied Stations (1986-1989)

Station Name	Abbr.	Occupation			Longitude	Latitude	Elevation
		1986	1988	1989	°	°	(m)
Acute 1934	ACUT	•	•		-115.6093	33.0300	-80.91
Alamo	ALAM	•	•	•	-115.6111	33.1964	-72.91
Black Butte NCMN 1982	BLAC	•	•	•	-115.7198	33.6638	490.01
Brawley 2 rm 5	BRAW	•	•		-115.5434	32.9773	-66.78
Calexico 1954	CALE	•	•		-115.5064	32.6645	-34.07
Calipatria 2	CALI	•		•	-115.5088	33.1690	-89.03
Coach	COAC	•	•		-115.4070	33.1962	-8.40
College 1967	COLL	•	•	•	-115.5024	32.8269	-54.63
El Centro 2 1959	ELEC	•	•		-115.5622	32.7846	-45.76
Frink 1934	FRIN	•	•	•	-115.6470	33.3603	-85.39
GLO Cornew 1934	GLOC	•	•		-115.2465	32.8396	-15.46
Hamar 2 1967	HAMA	•	•		-115.5007	33.0375	-79.80
Holt 1924	HOLT	•	•		-115.3963	32.7814	-36.79
Holtville (Alt) 1934	HLTV	•	•		-115.3821	32.8084	-38.77
Imp 1934	IMPI	•	•		-115.5698	32.8982	-59.27
Imperial 1934	IMPE	•	•		-115.5788	32.8439	-51.85
Junction	JUNC	•	•	•	-115.0619	32.7092	8.35
Kane 1939	KANE	•	•	•	-115.8237	33.0614	10.05
L 589 1967	L589	•	•	•	-115.7611	32.9506	13.62
Mack 2 1967 bm reset	MACK	•	•		-115.1441	32.7288	1.20
Mello 3 1967	MELL	•	•		-115.4653	32.7961	-47.00
Monument Peak NCMN 1983	MONU	•		•	-116.4228	32.8918	1839.41
Ocotillo NCMN 1982	OCOT	•	•	•	-115.7962	32.7901	-36.43
Ocotillo 1935	OCTI	•	•	•	-116.0017	32.7338	111.33
Offset 217	O217	•	•		-115.3131	32.6782	-17.16
Offset 224	O224	•	•		-115.7055	32.6493	50.00
Offset 227	O227	•	•		-115.8173	32.6414	70.64
Orient 1939	ORIE	•	•	•	-115.4064	32.9168	-61.36
Pinyon Flat	PINY	•	•		-116.4588	33.6093	1235.88
Sandy Beach	SAN1		•	•	-115.8344	33.1929	-99.92
T 1226	T122	•	•		-114.8050	32.8583	141.19
Tamarisk 3 1967	TAMA	•	•		-115.4783	32.8829	-68.19

Figure 5.2: GPS stations surveyed in 1986 and 1988. The 1986 campaign was conducted by the National Geodetic Survey and included 42 stations in and near the Imperial Valley. The 1988 observations consisted of two campaigns, the first by university groups in February/March and the second by the National Geodetic Survey in March/April. A total of 32 stations were occupied in 1988, of which 29 were repeat measurements from 1986. Stations mentioned in text are indicated.

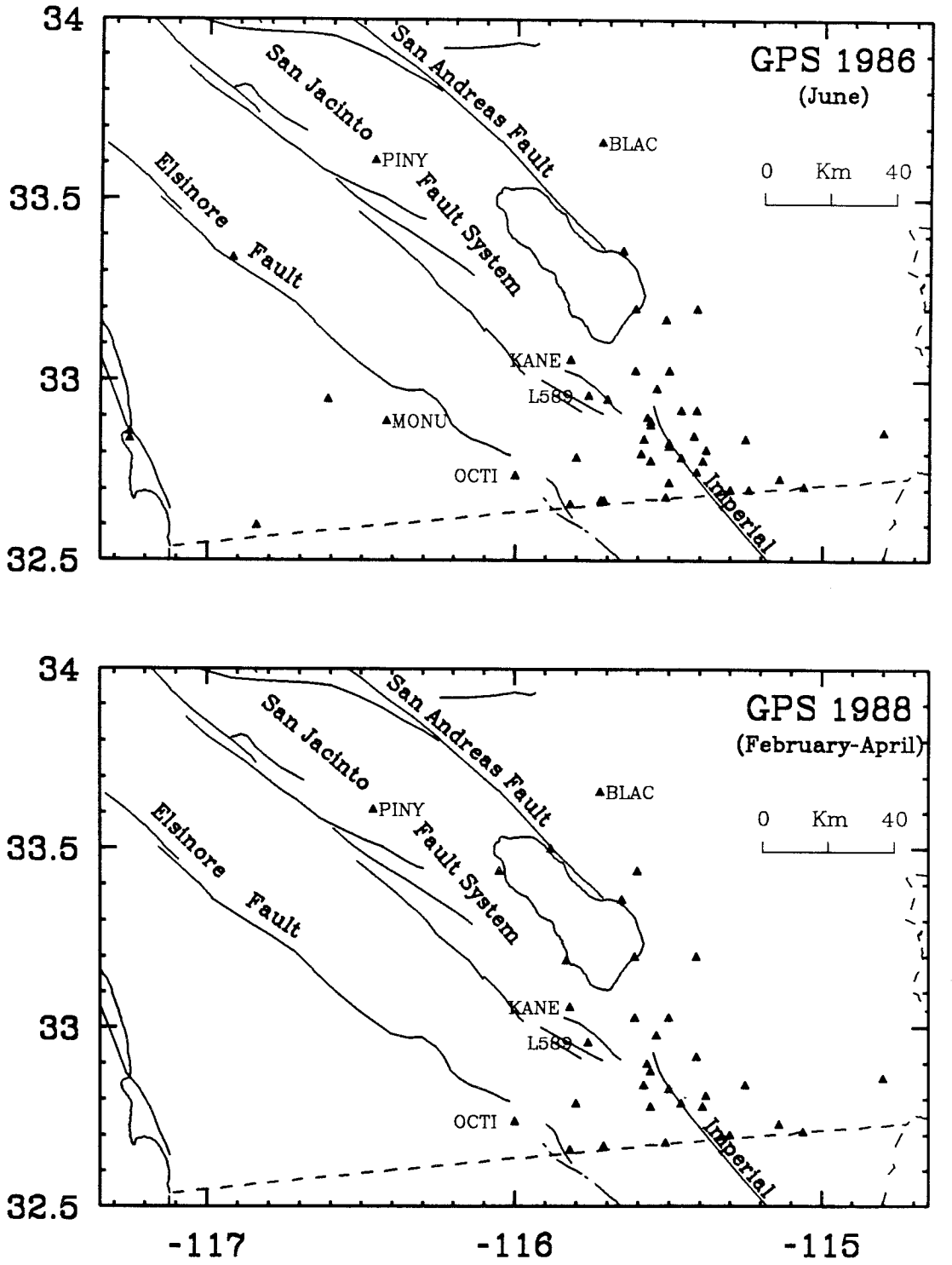
GPS 1986
(June)
0 Km 40
San Andreas Fault
San Jacinto
Fault System
Elsinore Fault
Imperial
BLAC
PINY
KANE
L589
MONU
OCTI
34
33.5
33
32.5
GPS 1988
(February-April)
0 Km 40
San Andreas Fault
San Jacinto
Fault System
Elsinore Fault
Imperial
BLAC
PINY
KANE
L589
OCTI
34
33.5
33
32.5
-117
-116
-115

Network (CIGNET) [*Chin*, 1987]. Since orbit improvement techniques are used, the (horizontal) precision for each survey is about $\sim$ 0.03 ppm (sub-centimeter) [e.g., *Davis et al.*, 1989; *Dong and Bock*, 1989]. The Cartesian coordinate differences from the university and NGS surveys are adjusted by least squares to obtain station positions for 1988.

During March, 1989, university groups occupied 28 geodetic marks in the vicinity of the Imperial Valley, 19 of which were previously surveyed in 1986 or 1988 (Table 5.2, Figure 5.3). Several new marks were established north of the Salton Sea in the Coachella Valley. While most data were collected with TI-4100 GPS instruments, this campaign differed from previous surveys in that Trimble-4000SD receivers were used at some sites. The field experiment was conducted at a time of anomalously high solar flare activity which created large ionospheric disturbances [*Jackson et al.*, 1989]. The ionosphere creates a frequency dependent delay for the GPS multi-signal structure, composed of two carrier phase transmissions at 1575.42 MHz (L1) and 1227.60 MHz (L2) [e.g., *King et al.*, 1985]. For dual frequency observations (L1 and L2) the ionospheric contribution (error) is removed by an appropriate combination of the two phase observables. However, if only single frequency measurements are available (either intentionally or due to poor observing conditions), the positioning accuracy on all but the shortest baselines will be seriously degraded. The 1989 phase observations contain a disproportionate number of cycle slips and data gaps, presumably due to the poor ionospheric conditions. The TI-4100 instruments generally collected both the L1 and L2 phase signals, so the ionospheric effect could be eliminated. The Trimble 4000SD receivers, however, experienced significant difficulty maintaining

Table 5.2 Imperial Valley GPS Occupation History (1989)

Day	Stations						
65	OCOT	PINY[1]	MONU	BLAC	ROBO	EXTR[1]	COAC[1]
66	OCOT	PINY[1]	MONU	BLAC	ROBO	EXTR[1]	COAC[1]
67	OCOT	PINY[1]	MONU	BLAC		VARN	SAN1[1]
68	OCOT	TRAN[1]	FRIN		COCH	VARN	SAN1[1]
69	OCOT	TRAN[1]	FRIN	DUNP	COCH	GLOC[1]	VORO[1]
70	OCOT	TRAN[1]	ALAM	DUNP	ROBO	GLOC[1]	VORO[1]
72	OCOT	KANE	ALAM	L589	TAMA[1]	GLOC[1]	
73	OCOT	KANE	O217[1]	L589	TAMA[1]		ACUT[1]
74	OCOT	BORD	O217[1]	ORIE		SIPH	ACUT[1]
75	OCOT	BORD[1]	CALI	ORIE	TAMA[1]	SIPH	
76	OCOT	JUNC	COLL[1]	HAMA[1]	TAMA[1]	SIPH	SAN1
77		JUNC	COLL	ORIE[1]	TAMA[1]	GLOC[1]	SAN1

Day is Julian day of year
[1] Trimble 4000SD

Figure 5.3: Imperial Valley GPS stations surveyed in 1989. TI-4100 GPS receivers (triangles) were used at most sites. Trimble 4000sd receivers (open circles) were also used. Thirty sites were occupied; 10 for the first time. Due to very poor ionospheric conditions, data collected with the Trimble 4000SD receivers are not discussed here.

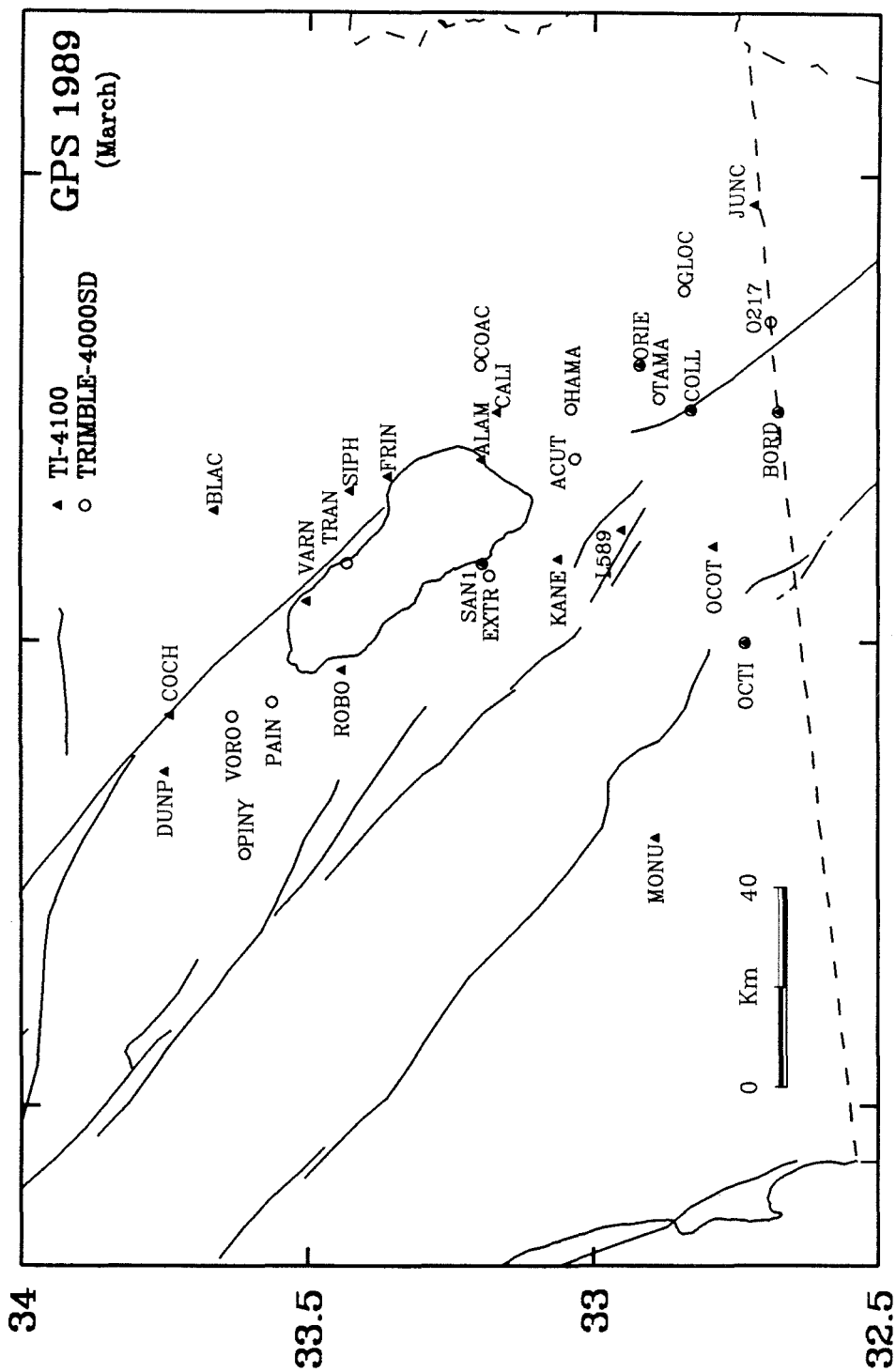
GPS 1989
(March)
TI-4100
TRIMBLE-4000SD
BLAC
COCH
DUNP
VORO
PAIN
PINY
ROBO
VARN
TRAN
SIPH
FRIN
ALAM
COAC
CALI
SAN1
EXTR
ACUT
HAMA
KANE
1589
ORIE
TAMA
COLL
GLOC
JUNC
0217
BORD
OCOT
OCTI
MONU
0
Km
40
34
33.5
33
32.5
-117
-116
-115

phase-lock on the L2 frequency (it is found that newer Trimble models, specifically the 4000SDT, are not as susceptible to solar activity). In fact, between 30-60 percent of the L2 data (Trimble 4000SD) was lost. It is unlikely that the centimeter level accuracy required for this study could be achieved solely with the L1 frequency. Therefore, data collected with Trimble 4000SD instruments are not considered, although we are currently working on schemes to utilize these measurements through ionospheric modeling constrained by the dual frequency TI-4100 data. Continental fiducial phase observations from the CIGNET tracking sites were either nonexistent or of extremely poor quality, presumably due to the unfortunate ionospheric conditions. We were therefore not able to apply orbit improvement techniques so a multiday solution is obtained with the Bernese software utilizing the broadcast orbits. Positioning errors from the broadcast ephemerides are believed to be 0.1-1.0 ppm.

5.4 GPS Displacements

GPS vector displacements for the intervals 1986-1988 and 1988-1989 are shown in Figures 5.4 and 5.5, respectively. All measurements are made relative to station OCTI. Formal estimates of GPS uncertainty almost always underestimate variances derived from repeatability studies. We attempt to define more realistic errors by multiplying the structure of the formal covariance matrix calculated with the GPS solution by an estimated variance factor, which scales as the average baseline length. For the 1986-1988 displacements, we assume a variance factor so that the average baseline error is 5 cm, or 1 ppm for a 50 km baseline. The large uncertainty is due to

the poor quality of the 1986 data. For the 1988-1989 displacements, the average baseline error is assumed 2 cm, or 0.4 ppm for a 50 km baseline. The largest component of uncertainty is attributed to the broadcast orbits used for the 1989 solution. *Larsen et al.* [1990] found 1-3 cm discrepancies between broadcast and improved-orbit solutions in a similar sized network spanning the Santa Barbara channel. This approach, albeit somewhat ad hoc, allows for self consistent relative errors and it illustrates the much larger uncertainties in the east-west direction ($\sim$ 4 times larger than the north-south uncertainties). This distortion is primarily due to the north-south ground track of the satellite orbits, which significantly improves solution constraint along this orientation.

Displacements for the 1986-1988 interval (Figure 5.4) are complicated by the 1987 Superstition Hills earthquake sequence, as well as large measurement uncertainties. Effects of the earthquake sequence are clearly demonstrated in the GPS vectors; displacements at KANE and L589 approach 0.5 meters. Estimates of fault rupture suggest 10 stations near the seismic rupture zone moved at least 5 cm [*Larsen et al.*, 1990]. The displacements are consistent with right-lateral slip along the Superstition Hills fault and left-lateral slip along the Elmore Ranch fault. Still, there is a considerable component of southeast trending movement which can not be explained as seismic deformation or measurement uncertainty. The relative displacement between stations on opposite sides of the valley averages 5-6 cm/yr. We take this motion to represent continuous strain accumulation due to plate motion.

The 1988-1989 station displacements clearly demonstrate the right-lateral southeast trending movement across the GPS network. Stations furthest to

Figure 5.4: GPS station displacements for the interval 1986-1988 (1.8 years). All measurements are made relative to station OCTI. Errors are determined by multiplying the formal uncertainties from the GPS solution by a variance factor so that the average baseline error scales as 1 ppm. The east-west uncertainties are about 4 times larger then the north-south. Seismically induced displacements from the 1987 Superstition Hills earthquake sequence are most apparent at stations KANE and L589. The large non-seismic displacements are assumed to represent relative motion between the Pacific and North American plates, which is concentrated across the valley.

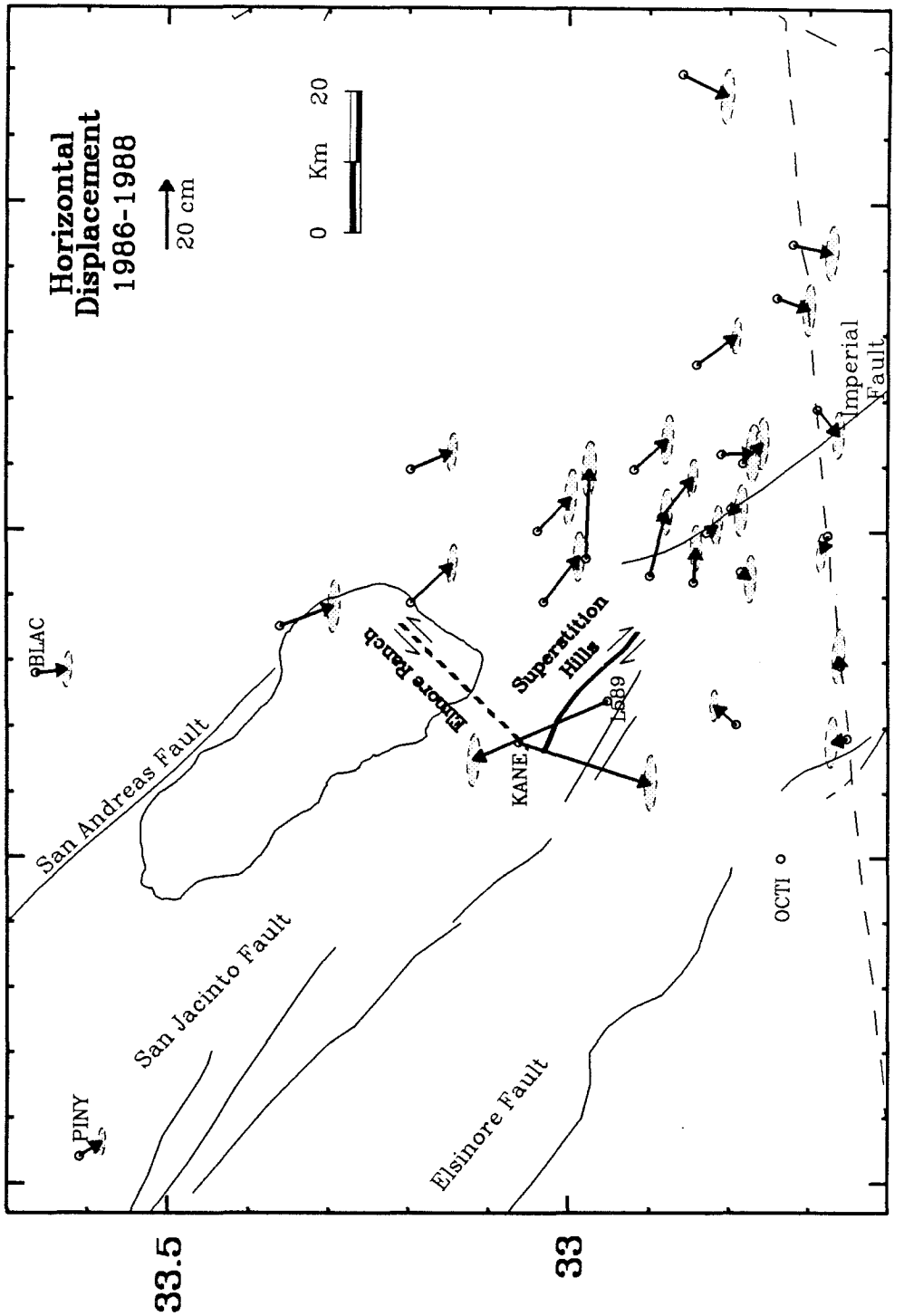
Horizontal
Displacement
1986-1988
20 cm
0 Km 20
BLAC
PINY
KANE
OCTI
San Andreas Fault
San Jacinto Fault
Elsinore Fault
Superstition
Hills
Imperial
Fault
33.5
33
-116.5
-116
-115.5
-115

Figure 5.5: GPS station displacements for the interval 1988-1989 (1.0 years). All measurements are made relative to station OCTI. Errors are determined by multiplying the formal uncertainties from the GPS solution by a variance factor so that the average baseline error scales as 0.5 ppm. Stations to the northeast moved about 5 cm southwest relative to stations on the other side of the valley.

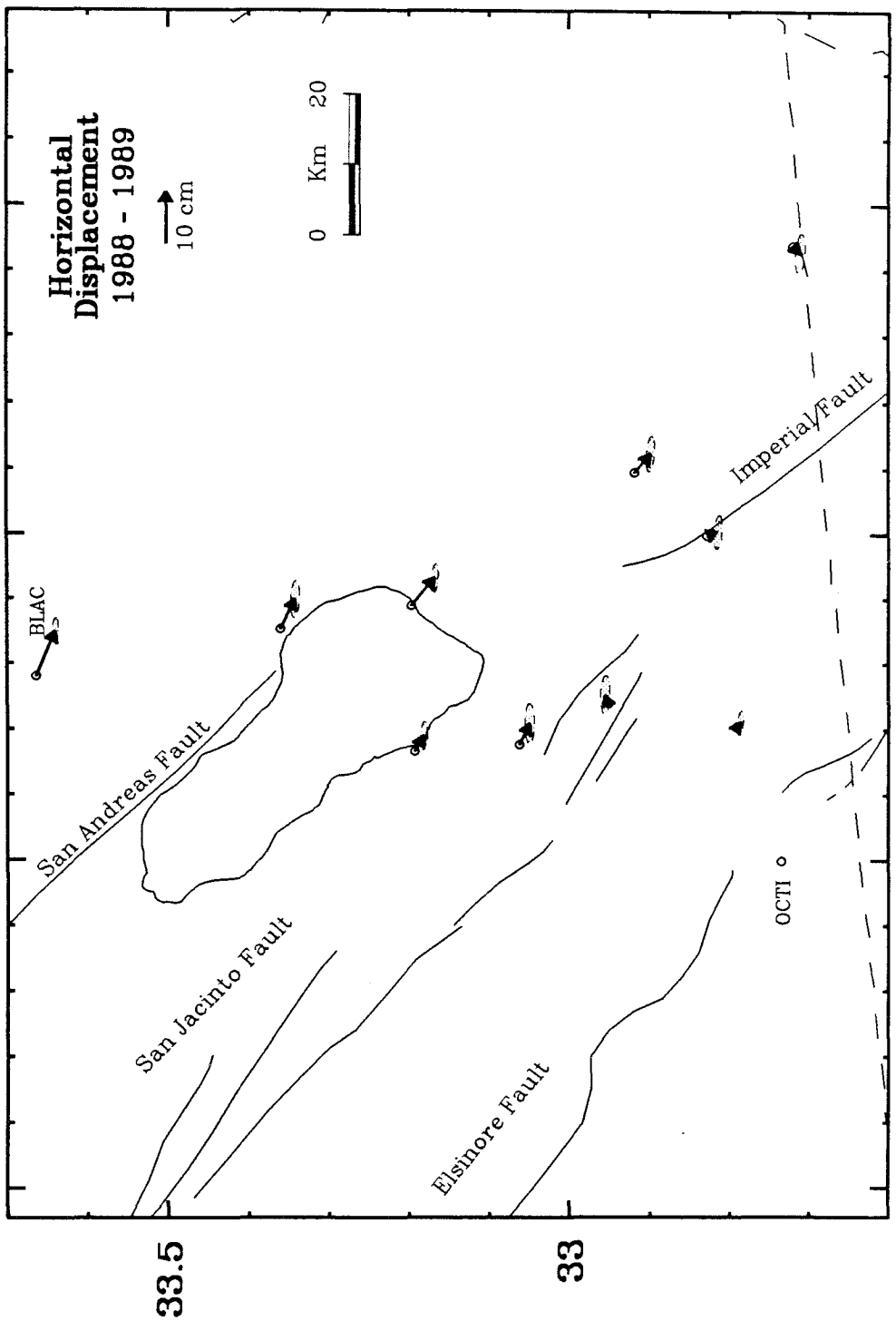
Horizontal
Displacement
1988 - 1989
10 cm
0 Km 20
BLAC
San Andreas Fault
San Jacinto Fault
Elsinore Fault
Imperial Fault
OCTI
33.5
33
-116.5
-116
-115.5
-115

the northeast are displaced approximately 5 cm to the southeast relative to sites on the other side of the valley, although some of the observed motion (e.g., BLAC) may be distortion from the larger east-west uncertainties. In addition, Figure 5.5 demonstrates how easily GPS can monitor tectonic deformation even over time scales as short as 1 year.

The 1986-1988 and 1988-1989 displacements are decomposed into their north-south and east-west components, corresponding to the directions of minimum and maximum error, respectively (Figure 5.6 and 5.7). Each component is plotted as the distance from OCTI on a cross section trending N50°E, perpendicular to the predicted plate motion orientation (N40°W) (Figure 5.8). Simple dislocation theory [e.g., *Mansinha and Smylie*, 1971] is used to remove the effect of the 1987 Superstition Hills earthquake sequence from the observed 1986-1988 displacement field, following fault models suggested by *Larsen et al.* [1990] (approximately 109 cm right-lateral slip on the Superstition Hills fault and 45 cm left-lateral slip on the Elmore Ranch fault).

Decomposing the vector displacements into geographic components tends to separate the uncertainties which are magnified along the longitudinal direction. The north-south movements clearly exhibit right-lateral displacement for both intervals; stations to the northeast display southerly offsets relative to sites on the other side of the valley. The magnitude of the displacement is roughly proportional to the time interval spanned by the measurements, suggesting continuous strain accumulation. Stations which display the largest scatter in Figure 5.6 are for the most part those sites where the applied seismic correction is greater than 4 cm (open circles). This may

indicate additional fault complexity not accounted for by the dislocation model used to remove the effects of the 1987 earthquake.

The east-west movements for the 1986-1988 interval exhibit large scatter with no discernible trend across the valley. This is invariant of the seismic correction, so the scatter is not explained simply as unmodeled effects from the Superstition Hills earthquakes. Presumably, the large deviations are due to fairly significant east-west oriented errors from the 1986 survey. This may explain the anomalous vector displacements observed in Figure 5.4, especially noticeable for those sites near the border east of the Imperial fault. On the other hand, the 1988-1989 displacements clearly show large east directed movements for stations furthest to the northeast, consistent with southeast trending deformation across the valley.

5.5 Discussion

Deformation across valley

The 1986-1988 measurements are concentrated along the Imperial fault (Figure 5.4). The nonseismic displacements reveal a sharp boundary 15-20 km wide between deformation on either side of the valley (Figure 5.6). This suggests that in the southern half of the Imperial Valley strain is being accommodated exclusively along the Imperial fault. The 1988-1989 measurements are distributed more uniformly throughout the region (Figure 5.5), and indicate a broader strain-transition zone (Figure 5.7). This implies that deformation may be occurring along several structures to the north, including the San Andreas, San Jacinto, and Elsinore faults. The same

Figure 5.6: The north-south and east-west displacement components for the 1986-1988 interval. All distances are relative to OCTI on a cross section trending N50°E, perpendicular to the plate motion (see Figure 5.8). The effect of the 1987 Superstition Hills earthquake sequence is removed. Open circles indicate stations where the seismic correction is greater than 4 cm. The north-south offset between stations on opposite sides of the valley is 8.1 cm. The large scatter for the east-west components are presumably due to errors in the 1986 survey. The average uncertainty for each displacement component is shown.

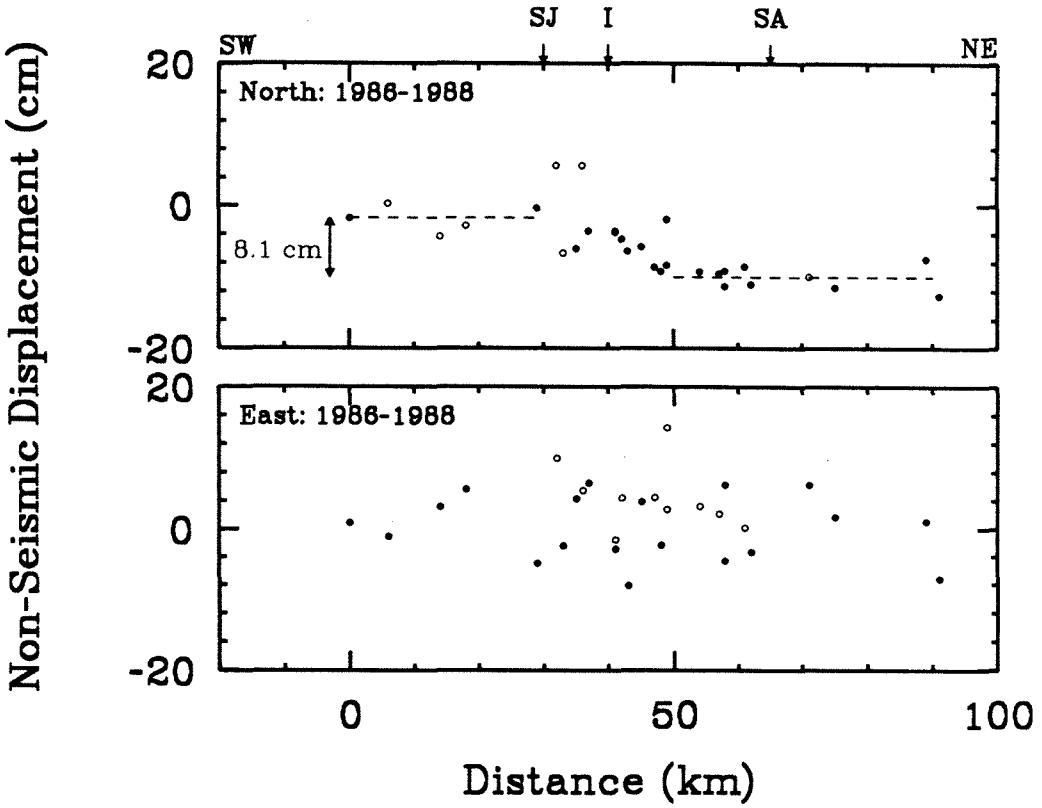
SJ
I
SA
SW
NE
North: 1986-1988
8.1 cm
East: 1986-1988
20
0
-20
20
0
-20
0
50
100
Non-Seismic Displacement (cm)
Distance (km)

Figure 5.7: The north-south and east-west displacement components for the 1988-1989 interval. All distances are relative to OCTI on a cross section trending N50 ° E, perpendicular to the plate motion direction. The data are best-fit by 5.2 cm/yr displacement across the valley (solid line), although a rate of 3.4 cm/yr fit the data nearly as well (dashed line). The average uncertainty for each displacement component is shown.

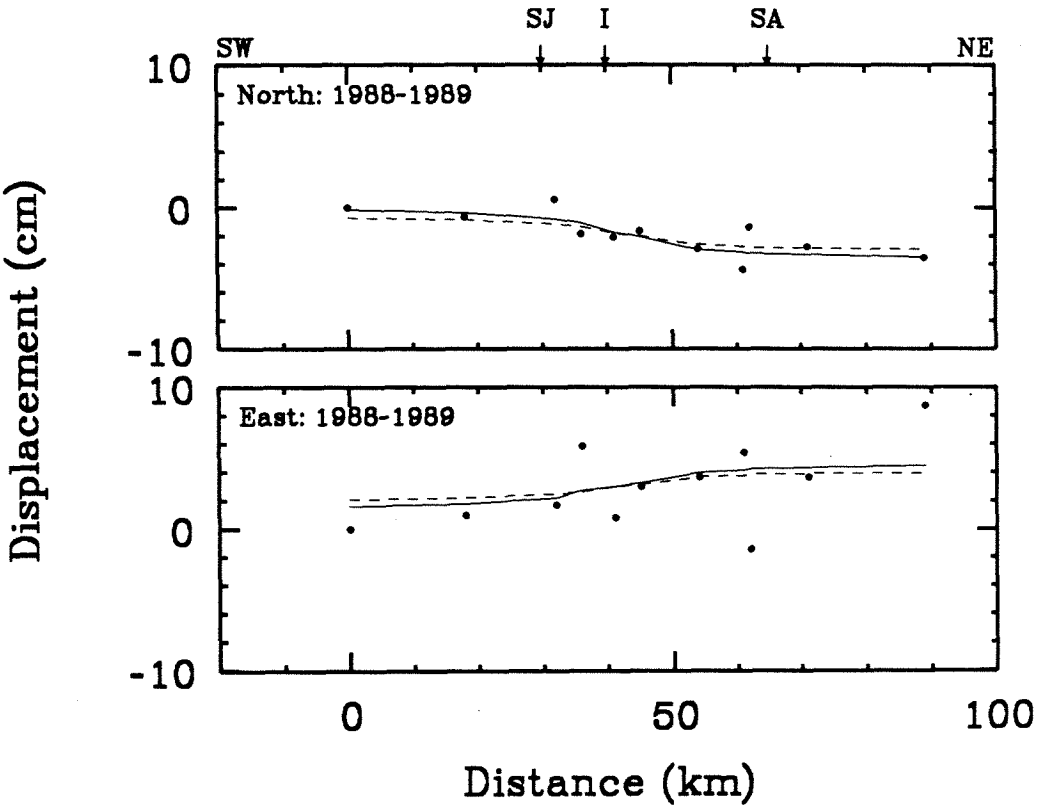
SJ
I
SA
SW
NE
North: 1988-1989
East: 1988-1989
10
0
-10
10
0
-10
0
50
100
Displacement (cm)
Distance (km)

Figure 5.8: Shear plane (10 km depth) used to model the 1988-1989 displacements (shaded band); cross section used in Figures 5.6 and 5.7; and stations surveyed at least twice between 1986 and 1989. Considerable strain is observed across the GPS network, which is attributed to plate-boundary deformation between the North American and Pacific plates.

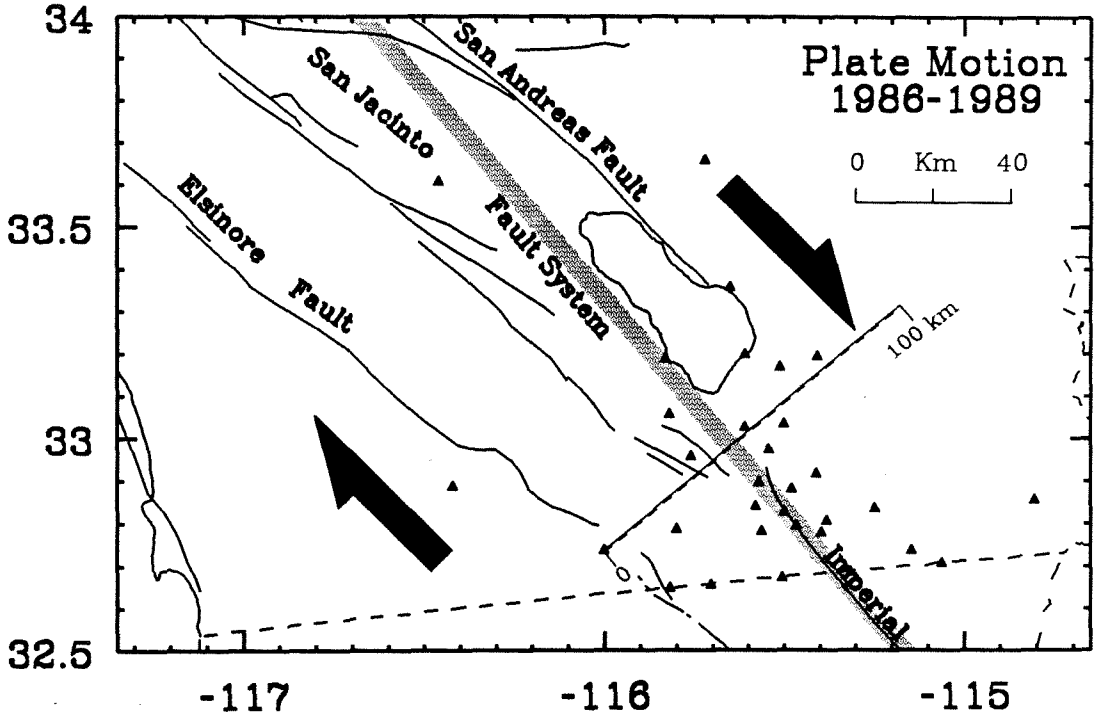
34
33.5
33
32.5
-117
-116
-115
San Andreas Fault
San Jacinto
Fault System
Elsinore
Fault
Imperial
Plate Motion
1986-1989
0 Km 40
100 km

pattern is observed in the conventional geodetic measurements, which indicate concentrated strain in a narrow 20 km wide zone about the Imperial fault, and diffuse deformation of at least 50 km wide to the north [*Snay and Drew*, 1988; *Prescott et al.*, 1987b].

The 1986-1988 displacements (Figure 5.4) have been modeled by *Larsen et al.* [1990]. The station movements are consistent with right-lateral slip along the Superstition Hills fault and left-lateral offset along the Elmore ranch fault. The nonseismic residuals indicate remaining deformation across the valley, evidenced by the 8.1 $\pm$ 1.3 cm offset in the north-south displacement component (Figure 5.6). The differential movement is calculated by linearly fitting those data furthest to the southwest and northeast. The data errors are increased by 0.33 times the estimated seismic displacements, giving less weight to those stations most affected by the 1987 earthquakes. The east-west components are not used due of the large data scatter. The observed movement is taken to represent plate-boundary deformation due to the relative motion between the North American and Pacific plates. The calculated north-south differential displacement averaged over the 1.8 year observation interval, is equivalent to 5.9 $\pm$ 1.0 cm/yr right-lateral movement oriented N40 $^\circ$ W, assuming a uniform velocity field parallel to the direction of plate motion. Conventional geodetic data are consistent with the assumed orientation [*Prescott et al.*, 1987a; *Snay et al.*, 1988].

The differential movement across the Imperial Valley is clearly visible in the 1988-1989 displacements (Figure 5.5 and 5.7), and is observed in both the north-south *and* east-west components. The movement is smaller than the earlier interval because of the shorter observation period (1.0 years).

However, the most recent measurements are not influenced by seismic activity and contain smaller experimental error. Since the 1988-1989 station displacements are more uniformly distributed across the valley, it is difficult to constrain an absolute differential offset. Instead, the measurements are modeled assuming a semi-infinite right-lateral shear plane at depth representing the Pacific-North American plate margin (Figure 5.8). The plane is oriented N40°W about coordinates 32.796°N, 115.454°W, almost congruent with the Imperial fault and the axis of the valley. The upper depth is constrained at 10 km and uniform slip is assumed over the entire shear boundary. *Snay and Drew* [1988] incorporate a similar model to explain triangulation observations from 1941 to 1986, but allow additional slip along the Imperial fault necessitated by the detailed station coverage in this region. More complex models assuming distributed offset along the Imperial, San Andreas, San Jacinto, and Elsinore faults, and within the Brawley Seismic Zone have been used to explain other geodetic measurements in the valley [e.g., *Savage et al.*, 1979]. The measurements presented here are not of sufficient resolution or accuracy (due to the short time coverage) to warrant such detail. The 1988-1989 GPS displacement vectors are best constrained by 5.2 ± 0.9 cm/yr plate-boundary deformation. The best-fit solution to the observed GPS movements is shown in Figure 5.7. Additional solutions are obtained by varying the depth to the upper boundary of the shear plane from 5 to 15 km. The calculated displacement rates range from 4.4 (5 km) to 6.0 cm/yr (15 km), while the minimum residual solution is obtained at 10 km depth (5.2 cm/yr).

Because the 1988-1989 displacements are not affected by seismic

deformation, we speculate this interval yields a more reliable GPS estimate of strain across the Imperial Valley. The GPS rates, as well as those derived through conventional geodetic techniques, are listed in Table 5.3. These are compared with the predicted relative velocity between the Pacific and North American plates (NUVEL-1), and rates derived from VLBI measurements between stations along the western coast of California and the stable North American continent. The 1988-1989 GPS rate is comparable to the plate velocity estimates, while the earlier GPS interval is somewhat higher. This suggests that all plate motion is concentrated across the valley, with little or no deformation west of the Elsinore fault. Conventional measurements taken over the last 50 years indicate significantly smaller rates (3.4-4.3 cm/yr), and thus require additional slip on faults not spanned by the networks to satisfy the plate velocity. GPS and trilateration (EDM) provide comparable accuracies, and both are considerably more precise than triangulation (although GPS yields 3-dimensional positions whereas the conventional methods do not). Since the EDM observations span a 15 year period compared to the 3 year GPS coverage, the trilateration rate should more accurately reflect the deformation across the valley, which suggests the GPS measurements over-estimate the true displacement. In fact, a 3.4 cm/yr deformation rate fits the 1988-1989 observations nearly as well (Figure 5.7). An alternate explanation is accelerated deformation between 1986 and 1989. The triangulation data indicate highly time-dependent displacements. Between 1941 and 1954 the calculated rate is significantly greater than the average between 1941 and 1986, although this is attributed to post-seismic effects following the 1940 Imperial Valley earthquake. No increased rate is observed following the 1979 earthquake [*Savage et al.*, 1986]. There is

Table 5.3 Displacement Rates

Method	Region	Interval	Rate (cm/yr)	Reference
GPS	Imperial Valley	1986-1988	4.8	This Study
		1988-1989	5.2	
Triangulation	Imperial Valley	1941-1986	4.3	*Snay and Drew* [1988]
		1941-1954	6.1	
		1954-1967	2.1	
		1967-1986	4.5	
Trilateration	Imperial Valley	1972-1987	3.4	*Prescott et al.* [1987b]
Plate Model	Plate boundary	$\sim$ 3 m.y.	4.7	*DeMets et al.* [1990]
VLBI	Continental	1979-1987	4.8-5.1	*Clark et al.* [1987]
				Kroger et al. [1987]

marginal evidence for a regional strain fluctuation (increase) during 1978 and 1979 throughout southern California, but the nature of this apparent deformation is uncertain [*Savage et al.*, 1981; *Savage et al.*, 1986]. Given the large uncertainties for the GPS estimates ($\sim$ 1 cm), it is not possible with the available data to distinguish if there has been increased deformation over the last several years.

Imperial and southern San Andreas fault earthquake potential

The earthquake recurrence interval along the Imperial fault is estimated using the geodetically determined strain rates. The 1940 Imperial Valley earthquake ruptured the entire length of the Imperial fault. Approximately 3.0 and 4.5 m slip (coseismic plus postseismic) are estimated for the northern and southern segments of the fault, respectively [*Reilinger*, 1984]. Surface offsets were as great as 6 m south of the border with displacements tapering off rapidly to the north [*Trifunac and Brune*, 1970; *Sharp*, 1982]. Surface rupture was confined to the fault north of the border during the 1979 earthquake. Geodetic and strong ground motion modeling suggest an average slip of about 1 m along the 1979 rupture plane, with patches of higher displacement (asperities) [e.g., *Hartzell and Heaton*, 1983; *Archuleta*, 1984; *Reilinger and Larsen*, 1986]

Triangulation measurements along the Imperial fault and north of the U.S.-Mexico border indicate concentrated deformation in a narrow 20 km wide zone. At an observed strain rate of 4-5 cm/yr and per event ruptures between 1 and 3 m, a 20-75 year earthquake recurrence interval is calculated for the northern Imperial fault. This assumes total strain release during seismic

episodes. The estimated recurrence rate is comparable to the 32 year earthquake repeat time suggested by *Sykes and Nishenko* [1984] and the $\sim$ 50 year interval predicted by *Anderson and Bodin* [1987].

Conventional geodetic data north of the Imperial fault indicate distributed deformation over a fairly wide region ($\geq$ 50 km wide) [*Snay and Drew*, 1988]. Presumably the strain that occurs almost exclusively along the Imperial fault in the south is transferred by some mechanism to the San Andreas, San Jacinto, and Elsinore faults. The slip distribution across each fault segment is important from an earthquake hazard standpoint.

Three Imperial Valley GPS sites have well determined VLBI solutions (Very Long Baseline Interferometry) from observations since 1979 [*Clark et al.*, 1987; *Sauber et al.*, 1989; *Ma et al.*, 1989]. Relative velocities of BLAC-PINY and BLAC-MONU for the GPS and VLBI analyses are listed in Table 5.4 and illustrated in Figure 5.9. The VLBI velocities vary depending on the continental or global nature of each solution and the extent of data availability. Only the north-south GPS displacements are considered because of the large east-west errors inherent in the 1986 survey. The fault parallel velocities are right-lateral assuming relative motions are oriented N40°W. The calculated effect from the 1987 Superstition Hills earthquake sequence is removed from the GPS data. The VLBI measurements indicate 1.5 to 2.1 cm/yr fault-parallel (right-lateral) displacement across the San Andreas fault (BLAC-PINY) and 3.0 to 3.5 cm/yr across the valley (BLAC-MONU). The GPS measurements suggest 1.4 cm/yr displacement across the fault and 3.2 cm/yr across the valley (Table 5.3 rates are different since they represent averages over the entire network). While the BLAC-MONU velocities roughly

Table 5.4 Displacement Rates Across San Andreas Fault

Baseline	Method	Interval	North (cm/yr)	East (cm/yr)	Fault Parallel (cm/yr)
BLAC-PINY	VLBI[1]	1982-1987	1.8	-1.1	2.1
	VLBI[2]	1979-1988	1.5	-1.0	1.8
	VLBI[3]	1982-1988	1.2	-0.9	1.5
	GPS	1986-1988	1.1		1.4
BLAC-MONU	VLBI[1]	1982-1987	2.3	-2.7	3.2
	VLBI[2]	1979-1988	2.5	-2.5	3.5
	VLBI[3]	1982-1988	2.4	-1.8	3.0
	GPS	1986-1989	2.5		3.2

[1] *Clark et al.* [1987]
[2] *Ma* [1988]
[3] *Sauber* [1989]

agree with the conventional geodetic measurements (3.4-4.3 cm/yr), the fault-crossing displacements are somewhat surprising as they are lower than geologic evidence. The long-term geomorphological slip rate along the southern San Andreas fault over the last 10,000-30,000 years is estimated between 2.3 and 3.5 cm/yr [*Keller et al.*, 1982; *Weldon and Sieh*, 1985], with 2.5 cm/yr a commonly accepted average [e.g., *Sieh and Williams*, 1990]. The geologic slip rate and radiocarbon dating of Holocene offsets along the fault suggest a recurrence interval of about 300 years with the last major event in 1680 [*Sieh*, 1986]. This logic leads to the conclusion that the potential for a major earthquake along the southern San Andreas is high. However, the geodetic evidence reported here indicates a smaller strain accumulation rate during the last decade, suggesting decreased earthquake potential assuming these measurements are indicative of the last few hundred years. This will be observed either as a longer recurrence interval or less slip per event. The geodetic data are supported by geologic trenching studies which suggest a decreasing southern San Andreas slip rate during the past 1000 years *Sieh* [1986]. If this is true, the San Jacinto fault should play a more active role in regional tectonics. In fact, the shear strain along the fault determined from EDM observations between 1973 and 1984 is nearly the same as that for networks which lie on the San Andreas fault *Savage et al.* [1986]. The two fault systems may alternately assume dominant roles in absorbing plate motions, as is suggested by variable Quaternary slip rates along the San Jacinto fault [*Sharp*, 1981].

Future analyses

The 1986, 1988, and 1989 Imperial Valley GPS observations are not

Figure 5.9: VLBI (solid arrows) and GPS (dashed arrows) velocities at stations PINY and MONU relative to station BLAC (Table 5.4). The GPS vectors contain large uncertainty in the east-west direction. The fault-parallel geodetic velocities across the San Andreas fault are less than geologic estimates.

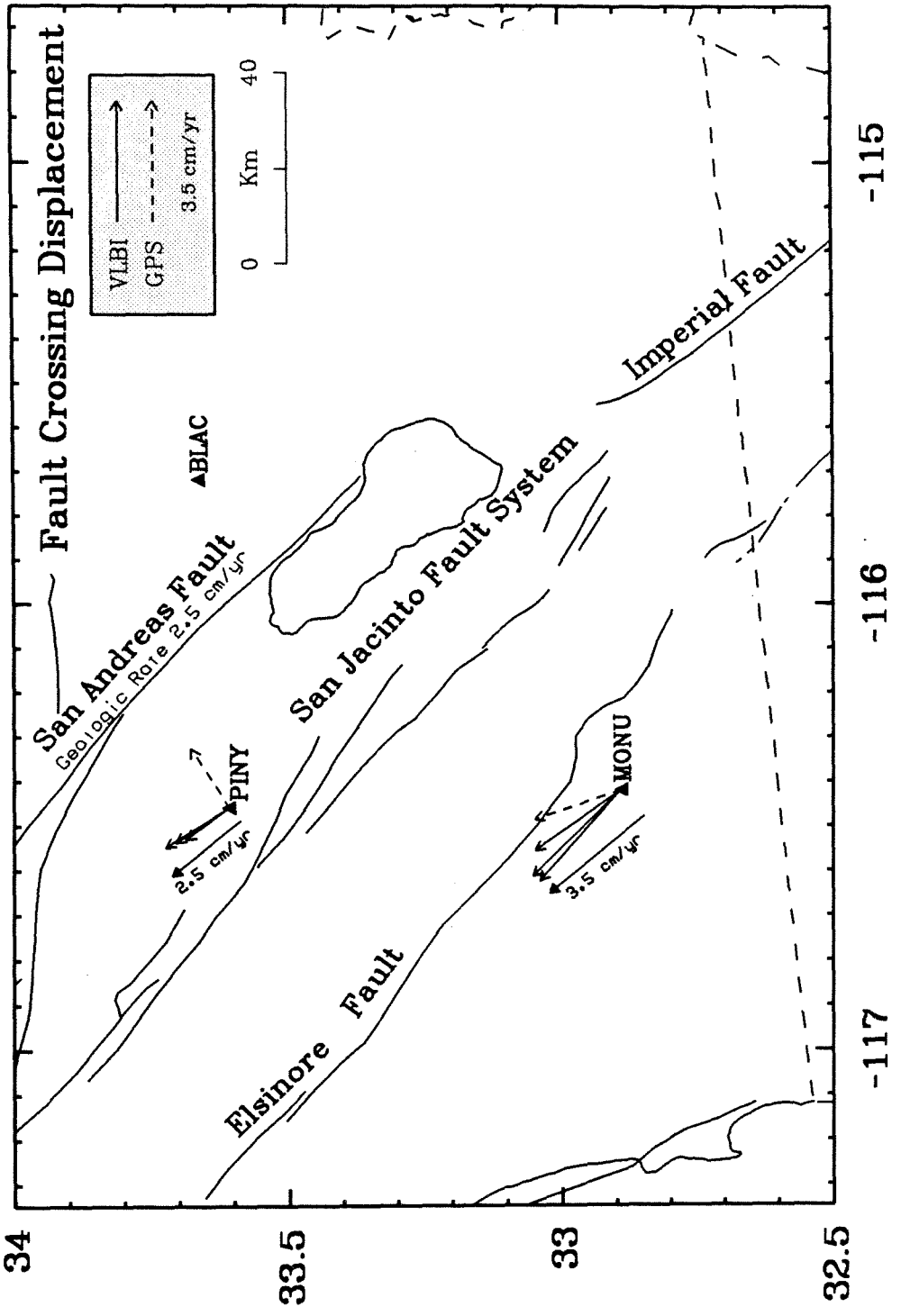
Fault Crossing Displacement
VLBI
GPS
3.5 cm/yr
0
Km
40
San Andreas Fault
Geologic Rate 2.5 cm/yr
BLAC
PINY
2.5 cm/yr
San Jacinto Fault System
MONU
3.5 cm/yr
Imperial Fault
Elsinore Fault
34
33.5
33
32.5
-117
-116
-115

sufficiently resolved to accurately map details of the strain distribution in this portion of southern California. This is due to poor data quality from the 1986 measurements, complications due to the 1987 Superstition Hills earthquake sequence, the inability to incorporate L2 phase data from several sites during 1989, and the short interval spanned by the observations (1 year of nonseismic displacement). However, additional GPS data have been collected in southern California in March/April 1988 and again in February/March 1990 (Figure 5.10). The 1988 measurements were made in conjunction with the Riverside County (California) Flood Control District and the Riverside County Survey Department. In a network of 62 stations spanning an entire cross section of southern California, a maximum of 8 TI-4100 GPS receivers were deployed each day over the two week survey. The daily observation period was about 4.5 hours. Although the instruments collected data every 3 seconds, during the download from receiver to floppy disk only every 10th measurement was recorded (30 second epochs). Unfortunately, the receivers were not synchronized and the recorded time-tags were randomly distributed at 30-second intervals. These data have been subsequently processed with the Bernese software. The day to day baseline repeatability on the 18 lines with multiple observations is 1.1 cm, suggesting that the receiver time-tag offsets are not a serious source of solution error considering the 3 to 5 cm tectonic movements expected in southern California.

During 1990, a high precision GPS network was established along a 400 km segment of the Pacific-North American plate-boundary from the Gulf of California in northern Mexico to just south of the junction of the San Andreas and San Jacinto faults ($\sim 34^\circ$ N) [*Reilinger et al.*, 1990]. Twenty-

three receivers were used for approximately two weeks including the TI-4100, Trimble 4000SD, and Trimble 4000SDT models. A total of 134 stations were occupied during the campaign. Data collection at 103 sites lasted 6 to 7 hours each day, while the daily observation interval at 31 stations was 3 to 4 hours (half-sessions). The following month (April 1990), 3 additional monuments near Upland, California, were established and surveyed by the Riverside County Flood Control District in support of university research associated with the February 28 (1990) M_L 5.5 Upland earthquake. The 1990 observations are in the process of being analyzed, although obtaining geodetic coordinates for the entire survey will be time consuming due to the enormity of the data set and the uncertainty in correlating GPS measurements from different receivers.

The 1986-1990 GPS occupation summary for the Imperial Valley, Riverside County, and Baja California is listed in Table 5.5. A total of 183 stations have been occupied at least once (Figure 5.10), and of these 85 have been occupied at least twice with most dating back to 1986 or 1988. The station coverage does not include kinematic GPS measurements made on relatively short transects (few kilometer) crossing the southern San Andreas fault [K. Hudnut, personal communication, 1990]. In addition to the dense distribution within the Imperial Valley and Baja California, the established network north of the Salton Sea provides station coverage extending from the California-Arizona border to near the Pacific Ocean. This network will be used to constrain the slip distribution along the major fault systems in southern California. When combined with geologic data of fault activity, the strain estimates will better define the earthquake potential in this region. The

Figure 5.10: GPS stations occupied from 1986 to 1990 in Riverside County, the Imperial Valley, and northern Baja California. Triangles inside circles indicate stations with multiple occupations. The network is composed of 183 stations, of which 85 have repeated observations.

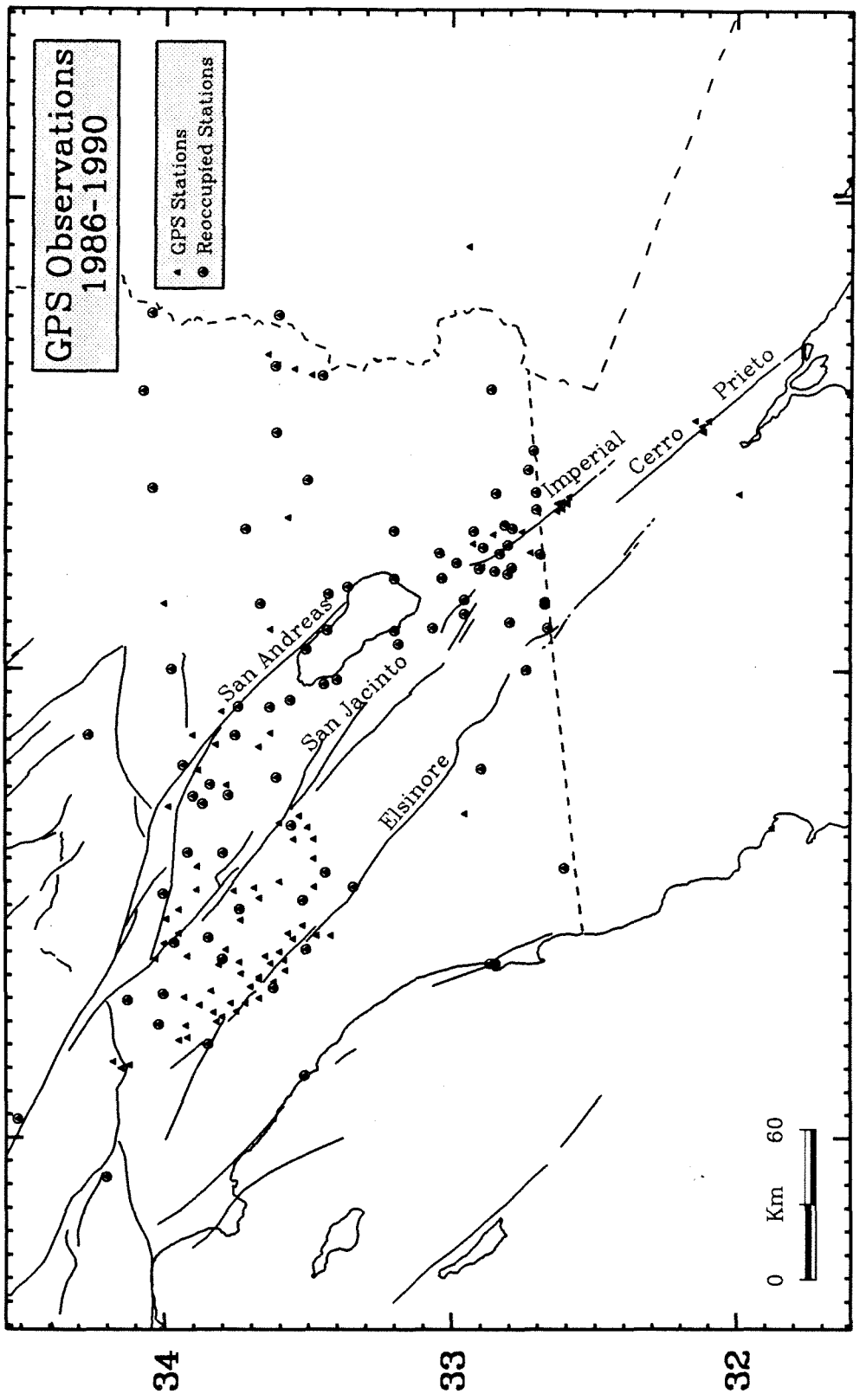
GPS Observations
1986-1990
GPS Stations
Reoccupied Stations
San Andreas
San Jacinto
Elsinore
Imperial
Cerro Prieto
0 Km 60
34
33
32
-118
-116
-114

Table 5.5 GPS Campaign Summary

Year	Stations	Region	Organization
1986	42	Imperial Valley	NGS
1988	15	Imperial Valley	UNAVCO
1988	62	Riverside County	RCFC/RCSD
1988	21	Imperial Valley	NGS
1989	28	Imperial Valley	UNAVCO
1990	134	Imperial Valley/Riverside County	UNAVCO/RCFC/RCSD/NGS

NGS - National Geodetic Survey
UNAVCO - University Navstar Consortium
RCFC - Riverside County Flood Control
RCSD - Riverside County Survey District

best GPS estimate of secular strain to date is provided by the 11 displacement vectors obtain from the 1988 and 1989 surveys. Once the 1990 data are fully analyzed, the increased station density (85 stations) and longer measurement interval (at least 2 years) will yield an order of magnitude increase in deformation extent and resolution. It should be possible to assess the present-day strain accumulation rates on the major fault systems in southern California to within a few millimeters per year. The network also provides good coverage along the southern San Andreas fault, which will be used to constrain fault rupture parameters in the likely event of a large earthquake within the next several decades [*Larsen*, 1990].

5.6 Conclusions

GPS measurements from southern California indicate 5.9 $\pm$ 1.0 and 5.2 $\pm$ 0.9 cm/yr right-lateral southeast trending displacement across the Imperial Valley for the intervals 1986-1988 and 1988-1989, respectively. These rates are significantly larger than those obtained from conventional geodetic surveys (3.4-4.3 cm/yr), suggesting the GPS observations may overestimate the true deformation. The earlier measurements contain relatively large errors, and are influenced by the 1987 Superstition Hills earthquake sequence. The 1988-1989 data are modeled nearly as well by 3.4 cm/yr of valley crossing movement. Regardless, a significant secular deformation component is clearly observed in the GPS displacements, which is attributed to the relative movement between the Pacific and North American plates. There is evidence from VLBI and GPS measurements that the strain accumulation rate along the southern-most San Andreas fault is smaller than the calculated long-term

geologic estimate. This indicates a lower earthquake potential for this segment of the fault than is presently assumed, and suggests that the San Jacinto system plays a more dominant role for relieving the strain accumulation in this region. The measurements discussed here are part of a larger 183 station GPS network which spans an entire cross section of southern California. A total of 134 stations were observed during a recent 1990 campaign; many of these sites were previously occupied in 1986 and/or 1988. An order of magnitude increase in resolution and detail regarding the strain accumulation rates along the San Andreas, San Jacinto, and Elsinore faults is expected once the 1990 GPS data are integrated with the previous surveys.

Acknowledgements

This research is a collaborative effort conducted jointly with Robert Reilinger at MIT. Helen Neugebauer and Bill Strange provided coordinate solutions from the 1986 NGS GPS survey. This research could not have taken place without the invaluable field support provided by many people. I thank my advisor Hiroo Kanamori for his support. This work is supported by U.S. Geological Survey contracts 14-08-0001-61679 (MIT) and 14-08-001-61354 (Caltech), and by NASA grant NAG-5-814 (MIT).

References

Anderson, J. G., and P. Bodin, Earthquake recurrence models and historical seismicity in the Mexicali-Imperial Valley, *Bull. Seismol. Soc. Am.*, *77*, 562-578, 1987.

Archuleta, R. J., A faulting model for the 1979 Imperial Valley earthquake, *J. Geophys. Res.*, *89*, 4559-4585, 1984.

Chin, M., CIGNET report, *GPS Bull.*, Global Positioning System Subcomm. of Comm. VIII, Int. Coord. of Space Tech. for Geod. and Geodyn., Natl. Geod. Surv., Rockville, Md., 1988.

Clark, T. A., D. Gordon, W. E. Himwich, C. Ma, A. Mallama, and J. W. Ryan, Determination of relative site motions in the western United States using Mark III very long baseline interferometry, *J. Geophys. Res.*, *92*, 12,741-12,750, 1987.

Davis, J. L., W. H. Prescott, J. L. Svarc, and K. J. Wendt, Assessment of global positioning system measurements for studies of crustal deformation, *J. Geophys. Res.*, *94*, 13,635-13,650, 1989.

DeMets, C., R. G. Gordon, S. Stein, and D. F. Argus, A revised estimate of Pacific-North America motion and implications for western North America plate boundary zone tectonics, *Geophys. Res. Letts.*, *14*, 911-914, 1987.

DeMets, C., R. G. Gordon, D. F. Argus, and S. Stein, Current plate motions, *Geophys. J. Inter.*, *101*, 425-478, 1990.

Dong, D., and Y. Bock, Global Positioning System network analysis with phase ambiguity resolution applied to crustal deformation studies in California, *J. Geophys. Res.*, *94*, 3949-3966, 1989.

Drew, A. R., and R. A. Snay, DYNAP: software for estimating crustal deformation from geodetic data, *Tectonophysics*, *162*, 331-343, 1989.

Elders, W. A., R. W. Rex, T. Meidav, P. T. Robinson, and S. Biehler, Crustal spreading in southern California, *Science*, *178*, 15-24, 1972.

Fuis, G. S., W. D. Mooney, J. H. Healey, G. A. McMechan, and W. J. Lutter, Crustal structure of the Imperial Valley region, *U.S. Geol. Surv. Prof. Pap.*, *1254*, 25-50, 1982.

Hartzell, S. H., and T. H. Heaton, Inversion of strong ground motion and teleseismic waveform data for the fault rupture history of the 1979 Imperial Valley, California, earthquake, *Bull. Seis. Soc. Am.*, *73*, 1553-1583, 1983.

Jackson, M., R. Reilinger, M. Bevis, B. Perin, C. Rocken, B. Stephens, and J. Stowell, Impact of ionospheric effects on GPS campaigns in southern California and the South Pacific, *EOS Trans.*, *70*, p. 1049, 1989.

Johnson, C. E., and D. P. Hill, Seismicity of the Imperial Valley, *U.S. Geol. Surv. Prof. Pap.*, *1254*, 14-24, 1982.

Keller, E. A., M. S. Bonkowski, R. J. Korsch, and R. J. Shiemon, Tectonic geomorphology of the San Andreas fault zone in the southern Indio Hills, Coachella Valley, California, *Geol. Soc. Am. Bull.*, *93*, 46-56, 1982.

King, R. W., E. G. Masters, C. Rizos, A. Stolz, and J. Collins, *Surveying with GPS, Monograph 9,* School of Surveying, The University of New South Wales, Kensington, Australia, 1985.

Kroger, P. M., G. A. Lyzenga, K. S. Wallace, and J. M. Davidson, Tectonic motion in the western United States inferred from very long baseline interferometry measurements, 1980-1986, *J. Geophys. Res., 92,* 14,151-14163, 1987.

Larsen, S. C., Inverting GPS displacement vectors for seismic slip distribution: Implications for network geometry along the southern San Andreas fault, paper presented at NSF/USGS joint workshop: crustal deformation measurement and earthquake mechanics, Morro Bay, California, 1990.

Larsen, S. C., R. E. Reilinger, H. Neugebauer, W. Strange, GPS measurements of deformation associated with the 1987 Superstition Hills earthquake, Imperial Valley, California: Evidence for conjugate faulting, *J. Geophys. Res.*, in preparation, 1990.

Lomnitz, C., F. Mooser, C. R. Allen, J. N. Brune, and W. Thatcher, Seismicity and tectonics of northern Gulf of California region, Mexico: Preliminary results, *Geofis. Int., 10,* 34-48, 1970.

Ma, C., J. W. Ryan, D. Caprette, Crustal dynamics project data analysis -- 1988, VLBI geodetic results 1979-1988, *NASA Technical Memorandum, 100723,* 1989.

Magistrale, H., L. Jones, and H. Kanamori, The Superstition Hills, California, earthquakes of 24 November, 1987, *Bull. Seismol. Soc. Am., 79,* 239-251,

1989.

Mansinha, L., and D. E. Smylie, The displacement fields of inclined faults, *Bull. Seismol. Soc. Am.*, *61*, 1433-1440, 1971.

Neugebauer, H. C., The 1986 Salton trough GPS survey and data processing results, National Geodetic Survey (unpublished report), 1988.

Prescott, W. H., J. C. Savage, and M. Lisowski, Crustal strain, in National Earthquake Hazards Reduction Program, Summaries of Technical Reports, *U.S. Geol. Surv. Open-File Rep.*, *87-374*, 272-280, 1987a.

Prescott, W. H., M. Lisowski, and J. C. Savage, Velocity field along the San Andreas fault in southern California, *EOS Trans.*, *68*, p. 1506, 1987b.

Reilinger, R., Coseismic and postseismic vertical movements associated with the 1940 M7.1 Imperial Valley, California, earthquake, *J. Geophys. Res.*, *89*, 4531-4537, 1984.

Reilinger, R. E., and S. C. Larsen, Vertical crustal deformation associated with the 1979 M = 6.6 Imperial Valley, California earthquake: Implications for fault behavior, *J. Geophys. Res.*, *91*, 14,044-14,056, 1986.

Reilinger, R., J. Beavan, L. Gilbert, S. Larsen, K. Hudnut, C. Aiken, D. Ziegler, B. Strange, M. F. de la Fuente, J. G. Garcia, J. Stowell, W. Young, G. Doyle, and G. Stayner, 1990 Salton Trough-Riverside County GPS Network, *EOS Trans. abst.*, *71*, p. 447, 1990.

Sauber, J., Geodetic measurement of deformation in California, Ph.D. Thesis, Massachusetts Institute of Technology, 1989.

Savage, J. C., W. H. Prescott, M. Lisowski, and N. King, Deformation across the Salton Trough, California, 1973-1977, *J. Geophys. Res.*, *84*, 3069-3079, 1979.

Savage, J. C., W. H. Prescott, M. Lisowski, and N. E. King, Strain accumulation in Southern California, 1973-1980, *J. Geophys. Res.*, *86*, 6991-7001, 1981.

Savage, J. C., W. H. Prescott, and G. Gu, Strain accumulation in southern California, 1973-1984, *J. Geophys. Res.*, *91*, 7455-7473, 1986.

Sharp, R. V., Variable rates of late Quaternary strike slip on the San Jacinto fault zone, southern California, *J. Geophys. Res.*, *86*, 1754-1762, 1981.

Sharp, R. V., Comparison of 1979 surface faulting with earlier displacements in the Imperial Valley, *U.S. Geol. Surv. Prof. Pap.*, *1254*, 213-221, 1982.

Sieh, K. E., Slip rate across the San Andreas fault and prehistoric earthquakes at Indio, California, *Eos Trans. abst.*, *67*, p. 1200, 1986.

Sieh, K. E., and P. L. Williams, Behavior of the southernmost San Andreas fault during the past 300 years, *J. Geophys. Res.*, *95*, 6629-6645, 1990.

Snay, R. A., and A. R. Drew, Supplementing geodetic data with prior information for crustal deformation in the Imperial Valley, California, Technical Report Series, University of Stuttgart, 30 p., 1988.

Sykes, L. R., and S. P. Nishenko, Probabilities of occurrence of large plate rupturing earthquakes for the San Andreas, San Jacinto, and Imperial faults, California, 1983-2003, *J. Geophys. Res.*, *89*, 5905-5927, 1984.

Thatcher, W., Horizontal crustal deformation from historic geodetic measurements in southern California, *J. Geophys. Res.*, *84*, 2351-2370, 1979.

Trifunac, M. D., and J. N. Brune, Complexity of energy release during the Imperial Valley, California, earthquake of 1940, *Bull. Seismol. Soc. Am.*, *60*, 137-160, 1970.

Weldon, R. J., and K. E. Sieh, Holocene rate of slip and tentative recurrence interval for large earthquakes on the San Andreas fault, Cajon Pass, southern California, *Geol. Soc. Am. Bull.*, *96*, 793-812, 1985.

U. S. G. S., The Imperial Valley, California, earthquake of October 15, 1979, *U.S. Geol. Surv. Prof. Pap.*, *1254*, 451 p., 1982.

Chapter 6

Age Constraints for the Present Fault Configuration in the Imperial Valley, California: Evidence for Northwestward Propagation of the Gulf of California Rift System

Abstract

Releveling and other geophysical data for the Imperial Valley of southern California suggest the northern section of the Imperial-Brawley fault system, which includes the Mesquite Basin and Brawley Seismic Zone, is much younger than the 4 to 5 million year age of the valley itself. A minimum age of 3000 years is calculated for the northern segment of the Imperial fault from correlations between surface topography and geodetically observed seismic/interseismic vertical movements. Calculation of a maximum age of 80,000 years is based upon displacements in the crystalline basement along the Imperial fault, inferred from seismic refraction surveys. This young age supports recent interpretations of heat flow measurements, which also suggest that the current patterns of seismicity and faults in the Imperial Valley are not long lived. The current fault geometry and basement morphology suggest northwestward growth of the Imperial fault and migration of the Brawley Seismic Zone. We suggest this migration is a manifestation of the propagation of the Gulf of California rift system into the North American continent.

6.1 Introduction

The Salton Trough is a complex transition zone between crustal spreading in the Gulf of California and right-lateral transform motion along the San Andreas fault system (Figure 6.1). The Imperial Valley is that section of the Salton Trough north of the U.S.-Mexico border and south of the Salton Sea (Figure 6.2). The Trough is characterized by predominately right-stepping, right-lateral en echelon faults, presumably linked by zones of crustal extension [*Lomnitz et al.*, 1970; *Elders et al.*, 1972]. It is a 150 by 300 km structural depression, 4 to 5 million years old, and filled by up to 15 km of late Cenozoic sediments. The seismic velocity of the lower 5-10 km (V_p = 5.7 km/s) suggests they are greenschist-facies, metasedimentary rocks [*Fuis et al.*, 1984].

The Imperial Valley and its major fault systems trend northwesterly, nearly parallel to the relative motion between the North American and Pacific plates. Dextral faulting predominates, although northeast trending left-lateral structures, as well as dip-slip motion along north-south surface breaks, play a significant role in the regional tectonics [*Johnson and Hutton*, 1982; *Nicholson et al.*, 1986; *Reilinger and Larsen*, 1986].

The Mesquite Basin is a subaerial topographic low bounded on the west by the northern Imperial fault and on the east by the Brawley fault (Figure 6.2). Maximum basin relief is about 10 m relative to its periphery. Evidence that the Mesquite Basin is actively subsiding includes geodetic measurements of surface deformation and measurements of vertical slip along the Imperial and Brawley faults. We provide evidence that the Mesquite Basin is extremely young compared to the age of the Imperial Valley, suggesting this

Figure 6.1: The Salton Trough (hatch pattern) is a transition zone between crustal spreading in the Gulf of California and right-lateral transform motion along the San Andreas fault. The Imperial Valley is that portion of the Salton Trough north of the U.S.-Mexico border and south of the Salton Sea. Abbreviations are S.F., San Francisco; L.A., Los Angeles. Map modified from Lachenbruch *et al.* [1985].

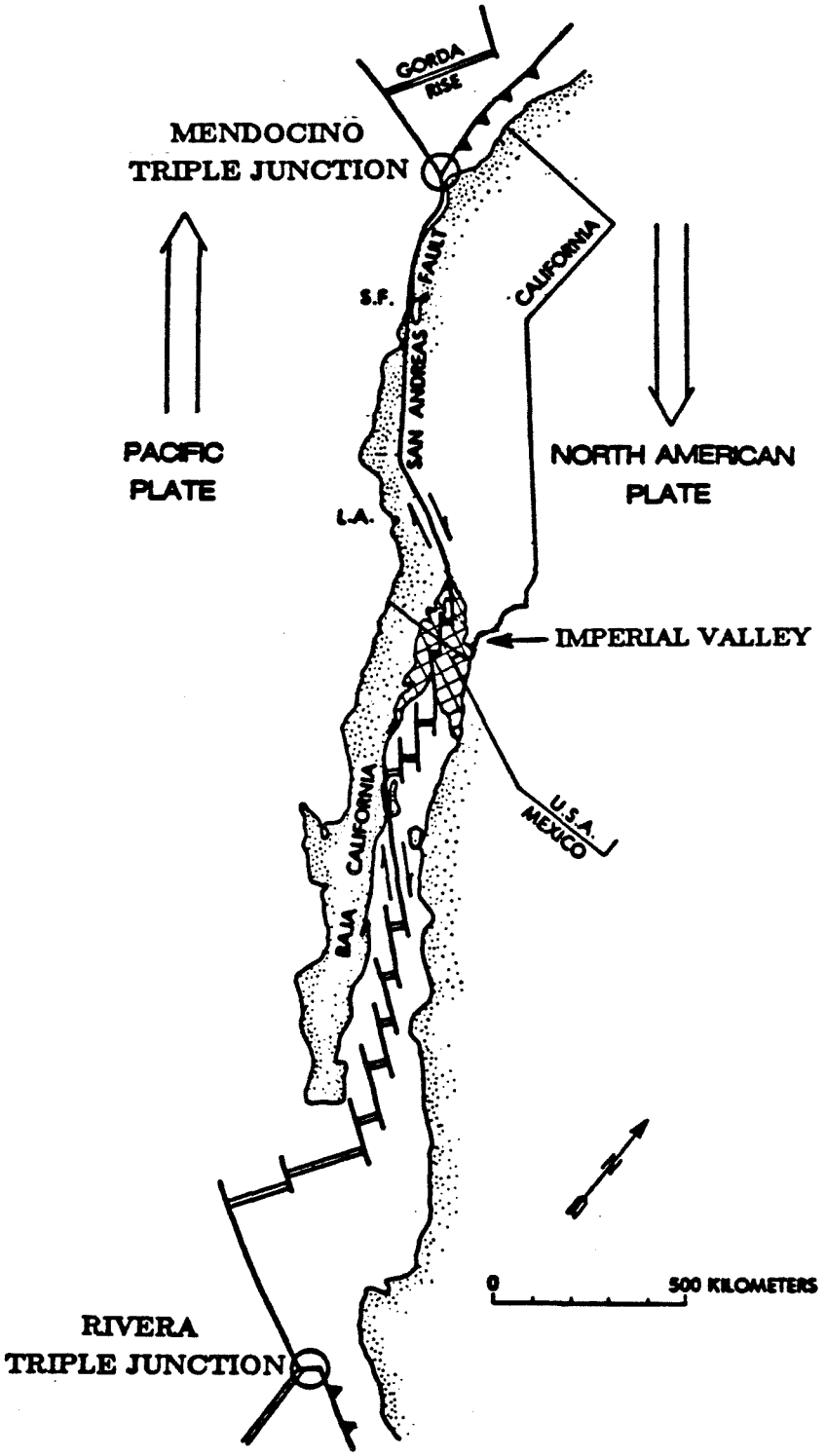
GORDA
RISE
MENDOCINO
TRIPLE JUNCTION
PACIFIC
PLATE
S.F.
SAN ANDREAS FAULT
CALIFORNIA
NORTH AMERICAN
PLATE
L.A.
IMPERIAL VALLEY
U.S.A.
MEXICO
BAJA CALIFORNIA
0
500 KILOMETERS
RIVERA
TRIPLE JUNCTION

Figure 6.2: The Imperial Valley and important faults. The Mesquite Basin is a subaerial topographic depression of about 10 meters between the Imperial and Brawley faults.

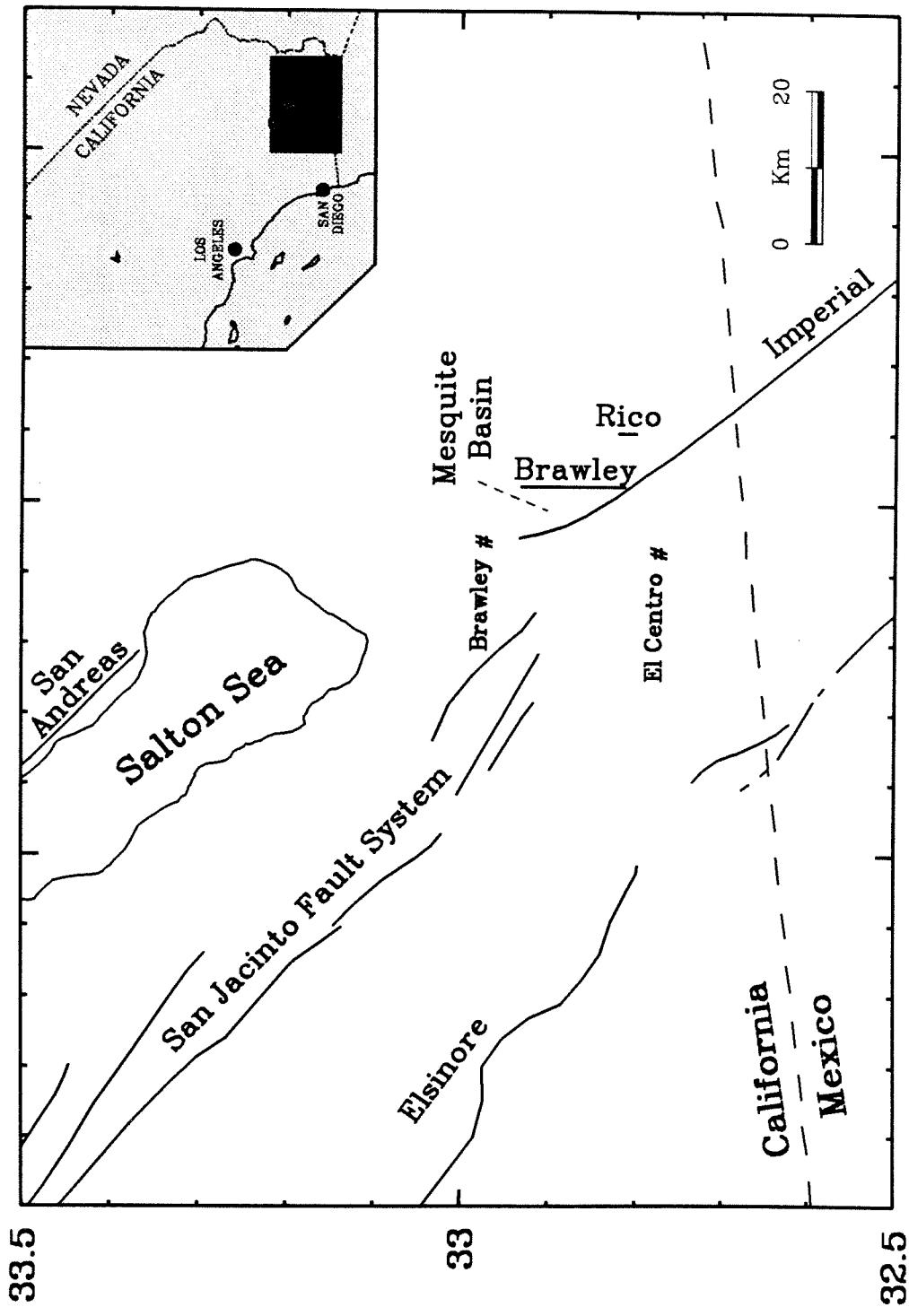
NEVADA
CALIFORNIA
LOS ANGELES
SAN DIEGO
0 Km 20
Mesquite Basin
Rico
Brawley
Imperial
Brawley #
El Centro #
San Andreas
Salton Sea
San Jacinto Fault System
Elsinore
California
Mexico
33.5
33
32.5
-116.5
-116
-115.5
-115

section of the Imperial-Brawley fault system is at an early stage of tectonic development. We extend this hypothesis and suggest ongoing northwestward propagation of the Gulf of California rift system.

6.2 Imperial Valley Seismicity and Faulting

The Imperial Valley is one of the most seismically active regions of California (Figure 6.3). A significant fraction of this seismicity occurs within the Brawley Seismic Zone, a region of high activity between the northern Imperial and southern San Andreas faults [*Johnson*, 1979; *Johnson and Hill*, 1982]. The Imperial fault has ruptured historically, in 1940 (M_L 6.4, M_S 7.1) and in 1979 (M_L 6.6, M_S 6.9); episodes of creep have been recognized along the fault since 1966 [*Allen et al.*, 1972]. The seismic moment of the 1979 earthquake is well determined (6×10^{25} dyne-cm) [e.g., *Kanamori and Regan*, 1982], while that for the 1940 event ranges between $10 - 80 \times 10^{25}$ dyne-cm [*Trifunac and Brune*, 1970; *Hanks et al.*, 1975] although the 48×10^{25} dyne-cm moment estimated from long-period surface waves is preferred [*Doser and Kanamori*, 1987]. Other major earthquakes in the Imperial Valley include the recent 1987 Superstition Hills earthquake sequence: a M_S 6.2 event produced by slip along a northeast trending seismic lineament, followed 12 hours by a M_S 6.6 earthquake produced by slip along the Superstition Hills fault [*Magistrale et al.*, 1989; *Williams and Magistrale*, 1989].

The 1979 surfacial rupture of the Imperial fault extended northwestward 33.1 km from a point 5 km north of the border to a point south of Brawley (Figure 6.4). The predominate strike of the Imperial fault is N37 °W. Along the northwestern most 5 km, however, the fault bends and trends north-

south. We refer to this segment as the north extension. Parallel and 6 km east of the north extension, the Brawley fault ruptured in 1979 along a 13 km surface break. The rupture pattern generally featured left-stepping en echelon cracks that extended a few millimeters to a few centimeters [*Sharp el al.*, 1982]. A third, yet relatively minor 1 km north-south break named the Rico fault was mapped 6-7 km east of the Brawley fault (Figure 6.4). The surface breakage along this structure resembled that of the Brawley fault zone. The geometrical similarity in strike and separation shown by the north extension, Brawley, and Rico faults, suggest a similar tectonic origin.

The epicenter of the 1940 earthquake was north of the U.S. border, but right-lateral surfacial offsets were larger in Mexico (Figure 6.3). A maximum surface offset of 6 meters was recorded near the border, with displacement tapering off rapidly to the north [*Trifunac and Brune*, 1972; *Sharp*, 1982]. Geodetic measurements indicate 4.5 and 3.0 m of right lateral slip (coseismic plus postseismic) along the southern and northern halves of the Imperial Fault, respectively (i.e., north and south of the epicenter), with 2.0 m postseismic slip along a northwest extension of the Brawley fault [*Reilinger*, 1984]. The 1979 epicenter was south of the border, although surfacial displacement was observed only in the United States. Maximum coseismic surfacial offset was 55-60 cm, with considerable afterslip ($\sim$ 30 cm) during the following 6 months [*Sharp et al.*, 1982]. Strong ground motion and geodetic modeling [*Archuleta*, 1984; *Hartzell and Heaton*, 1983; *Reilinger and Larsen*, 1986] suggest an average slip of about 1 m along the fault plane, with small patches of higher displacement (asperities).

The mechanism of strain transfer between the Imperial and San Andreas

Figure 6.3: Seismicity in the Imperial Valley between 1932 and 1989 (Caltech/USGS Catalog). Major events include the 1940 Imperial Valley (M_S 7.1), 1968 Borrego Mountain (M_L 6.5), 1979 Imperial Valley (M_S 6.6), and the 1987 Superstition Hills (M_S 6.6, M_S 6.2) earthquakes. The Brawley Seismic Zone is the active region between the northern reach of the Imperial fault and the southern extent of the San Andreas. The Sand Hills Seismic Lineament is shown by the shaded strip outlining earthquakes trending southeast from the southern end of the San Andreas fault. Shown in the inset are aftershocks of the 1979 earthquake which have been relocated following the methods outlined in Doser and Kanamori [1986]. The dashed lines represent orthogonal faults used to satisfy the observed vertical deformation from the 1979 event [Reilinger and Larsen, 1986]. Focal mechanisms (lower hemisphere, equal area projections [Reasenberg and Oppenheimer, 1985]) for events defining a northwest trend indicate right-lateral strike slip motion.

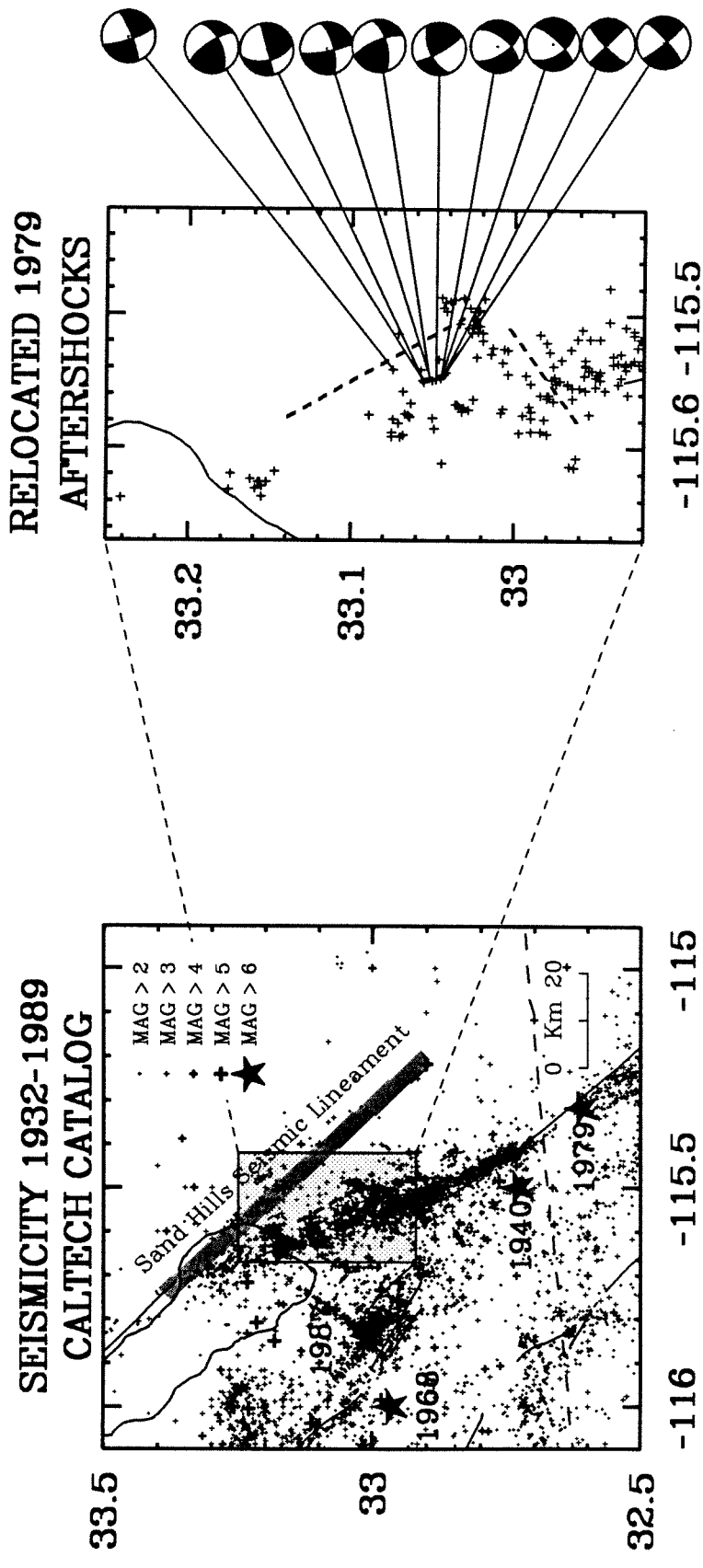
SEISMICITY 1932-1989
CALTECH CATALOG
MAG > 2
MAG > 3
MAG > 4
MAG > 5
MAG > 6
Sand Hills Seismic Lineament
1968
1940
1979
0 Km 20
33.5
33
32.5
-116
-115.5
-115
RELOCATED 1979
AFTERSHOCKS
33.2
33.1
33
-115.6 -115.5

Figure 6.4: Map of the Imperial Valley and important tectonic features. Abbreviations are RF, Rico Fault; BF, Brawley Fault; NE, North Extension. The shaded pattern along each fault indicates the surface rupture from the 1979 earthquake. The Brawley Seismic Zone (hatched) is the region of high seismicity extending northwest from the northern reach of the Imperial fault. The Salton Sea Geothermal Field is the shaded pattern along the southern section of the Salton Sea. Refraction surveys [Fuis *et al.*, 1984] cross the Imperial fault at RL-1, RL-2, RL-3. The leveling route is shown by the series of dots from the central Imperial Valley to the eastern border of the Salton Sea (each dot representing a benchmark).

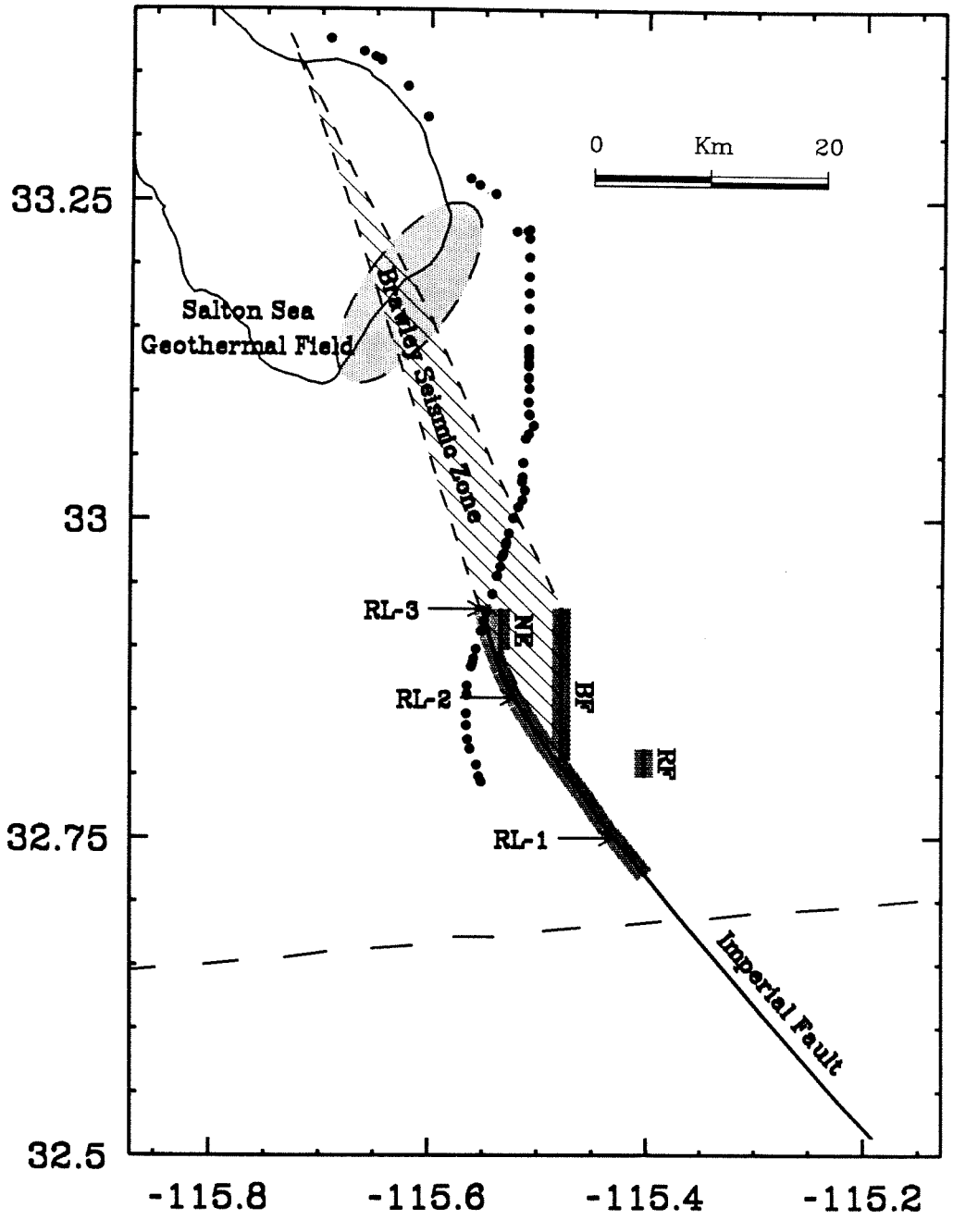
0
Km
20
33.25
33
32.75
32.5
-115.8
-115.6
-115.4
-115.2
Salton Sea
Geothermal Field
Brawley Seismic Zone
RL-3
RL-2
RL-1
NF
BF
RF
Imperial Fault

faults within the Brawley Seismic Zone has been the focus of considerable investigation [e.g., *Johnson*, 1979]. A conjugate relationship of right-lateral, northwest trending faults perpendicular to left-lateral, northeast trending structures may play a significant role in the regional tectonics [*Nicholson et al.*, 1986]. Although the Imperial and San Andreas faults strike predominately northwest (right-lateral), a left-lateral structure extending northeast from the northern terminus of the Imperial fault is indicated from focal mechanisms and the aftershock pattern of the 1979 earthquake [*Johnson and Hutton*, 1982]. A conjugate fault mechanism is supported by *Reilinger and Larsen* [1986], who suggested several tectonic models in the Brawley Seismic Zone satisfying geodetically determined measurements of vertical surface displacement. The preferred model consists of a northeast trending left-lateral fault conjugate to a right-lateral northwest trending structure dipping 70° to the southwest (Figure 6.3, dashed lines). Neither fault broke the surface but roughly 1 m slip at depth was required to fit the geodetic measurements. A similar conjugate fault relationship was observed for the 1987 Superstition Hills earthquake sequence [e.g., *Magistrale et al.*, 1989].

Aftershocks from the 1979 earthquake have been relocated following the methods of *Doser and Kanamori* [1986] and *Klein* [1985] (Figure 6.3). The northeast trending seismic lineament first identified by *Johnson and Hutton* [1982] is clearly defined. To the north, a tightly constrained group of events following a northwesterly direction is indicated. Epicentral depths for this cluster range from 5 to 11 km, possibly putting them on the 70° west dipping structure suggested by *Reilinger and Larsen* [1986]. We have computed focal mechanisms for these events and find them consistent with a northwest-

trending right-lateral fault (Figure 6.3). Thus, both seismic and geodetic data suggest the tectonic framework of the Brawley Seismic Zone is marked by en echelon northwest-trending right-lateral faults linked by conjugate left-lateral structures.

Extending southeast from the southern tip of the San Andreas fault is a linear alignment of earthquakes (Figure 6.3), here referred to as the Sand Hills seismicity lineament. This feature may signify the southeasterly extension of the San Andreas fault, although there is no surfacial geological evidence to support this hypothesis [*Sharp*, 1982].

The earthquake recurrence interval along the Imperial fault is not well constrained. *Sykes and Nishenko* [1984] use the 39 year interval separating the 1940 and 1979 shocks as well as a 1915 earthquake sequence located near El Centro [*Beal*, 1915] to estimate a 32 year recurrence rate. Anderson and Bodin [1987] suggest the fault north of the border will next rupture between 2010 and 2050 (50 year recurrence), and the next break along the southern segment to occur between 2170 and 2290 (300 year recurrence). Measurements of surface offset, as well as seismic and geodetically determined estimates of fault slip at depth, indicate the 1940 fault rupture was several times larger than in 1979, in agreement with the larger moment for the 1940 event. North of the border, however, the magnitude of horizontal surface displacement was relatively constant for the two earthquakes. One explanation is that the fault north of the border may rupture more frequently but with smaller events. Alternatively, the large postseismic slip following the 1940 earthquake indicated by geodetic data, suggests that a significant fraction of strain buildup may be relieved aseismically.

If the entire 49 mm/yr movement between the Pacific and North American plates predicted by new global plate models (NUVEL-1) [*DeMets et al.*, 1987] is accommodated across the Imperial fault, 1.0 meter of seismic or aseismic fault slip would require a 20 year interval of strain buildup. More likely, however, a significant component of plate motion is distributed along the Elsinore and San Jacinto fault systems [*Sharp*, 1981; *Pinault and Rockwell*, 1984; *Snay et al.*, 1986], as well as faults off the coast of southern California [e.g., *Weldon and Humphreys*, 1986]. Triangulation and trilateration measurements from 1941 to 1981 in the central Imperial Valley indicate an average displacement across the Imperial fault of 40 mm/yr [*Snay and Drew*, 1988]. Preliminary results utilizing the Global Positioning System (GPS) suggest a similar rate between 1986 and 1988, although interpretation of these measurements have been complicated by large displacements from the 1987 Superstition Hills earthquake sequence [*Larsen et al.*, 1988].

Assuming 40 mm/yr of plate motion across the Imperial fault, 1.0 m of potential slip will accumulate in 25 years. This will be equivalent to the earthquake recurrence interval, at least for the northern segment of the Imperial fault, if the $\sim$ 1.0 m surface displacement measured in 1940 and 1979 is characteristic of fault displacement and if all slip is generated seismically. Considering the likelihood of aseismic deformation, as well as the seismic and geodetic models indicating asperities along the 1979 rupture plane, it is reasonable to expect that the average slip generated along the northern Imperial fault during each earthquake (or earthquake cycle) is somewhat greater than 1.0 m. Assuming 2-3 m of slip (based on the seismic plus postseismic offset estimated for the 1940 earthquake and the maximum

slip observed for the 1979 earthquake), more reasonable estimates of earthquake recurrence would be 50 to 75 years for this segment of the Imperial fault.

6.3 Subsidence of the Mesquite Basin

First-order leveling surveys crossing the northern Mesquite Basin were conducted by the National Geodetic Survey (NGS) in 1931, 1941, 1974, 1978, and 1980 (Figure 6.4). Profiles of elevation change from 1931 to 1941, 1941 to 1974, and 1978 to 1980 are shown in Figure 6.5. The procedure used to determine these crustal movement profiles is described in *Brown and Oliver* [1976]. Briefly, an estimate of relative elevation change between successive benchmarks is obtained by subtracting the elevation difference between benchmarks measured at some reference time from the difference measured at some later time. These movement profiles have not been connected to any external reference. Therefore, only relative movements along the level lines are significant.

The random error for these measurements is comparatively small, less than 1 cm. In addition, elevation-correlated errors (i.e., rod calibration and atmospheric refraction) which can obscure or be mistaken for real tectonic deformation, will not seriously affect the data because of negligible topographic variation along the leveling route (Figure 6.5a).

The 1931-1941 and 1941-1974 profiles have been modeled as coseismic and postseismic deformation from the 1940 Imperial Valley earthquake [*Reilinger*, 1984]. Displacements for the most recent interval (1978 to 1980) have been

Figure 6.5: Shown in a) is the elevation (dashed line) along the releveling route between El Centro and the Salton Sea. The adjusted topography (solid line) is the elevation with the northward tilt of -0.0011 radians removed. The 10 meter depression between 9 and 22 km is the surfacial expression of the Mesquite Basin. Shown in b) are the elevation changes along the leveling route from 1931 to 1941, 1941 to 1974, and 1978 to 1980. Note the strong correlation between deformation and the surface expression of the Mesquite Basin.

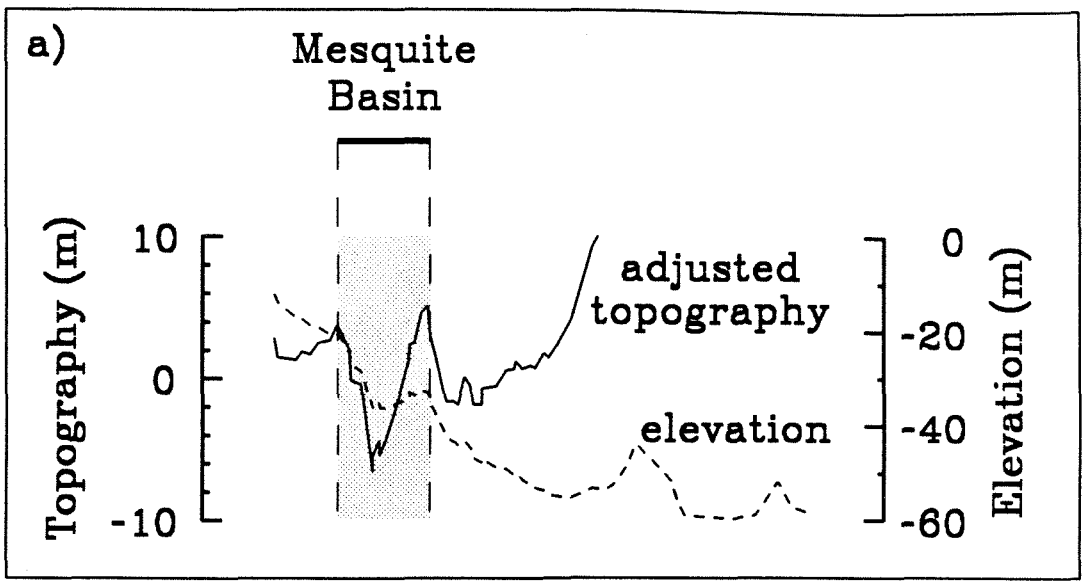
a)
Mesquite
Basin
Topography (m)
10
0
-10
adjusted
topography
elevation
0
-20
-40
-60
Elevation (m)

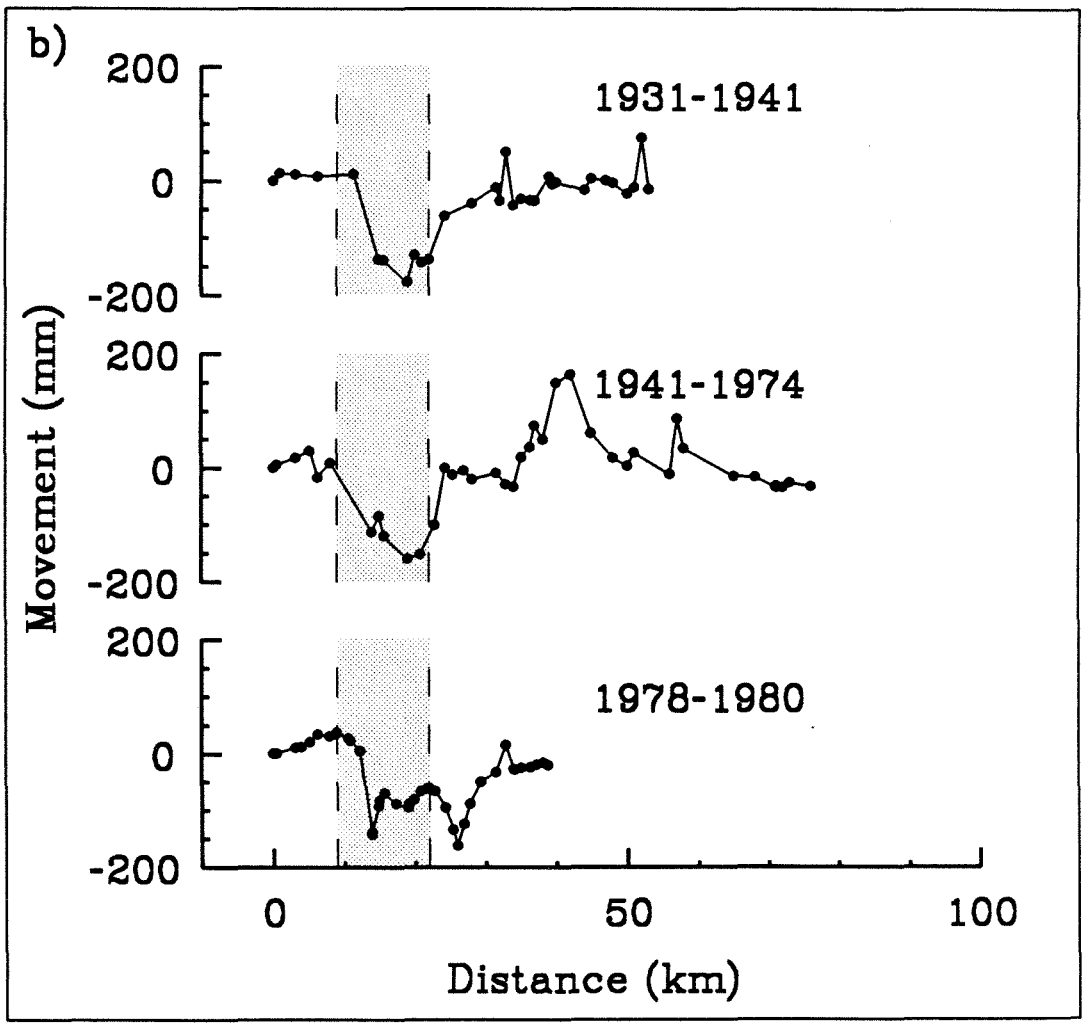
b)
200
0
-200
1931-1941
1941-1974
1978-1980
Movement (mm)
0
50
100
Distance (km)

modeled as surface deformation from the 1979 earthquake [*Reilinger and Larsen*, 1986]. The most striking feature of the leveling data is the similar pattern of subsidence across the Mesquite Basin observed on all three profiles, suggesting this deformation style is characteristic for the region. Coseismic subsidence for the 1940 and 1979 events are on the order of 10-15 cm, with an additional 15 cm following the 1940 earthquake. Total subsidence for the period 1931 to 1980 is about 40 cm.

Elevation along the leveling route is shown in Figure 6.5a (dashed line). A relatively constant northward slope of -0.0011 radians is observed. This long-wavelength trend may mask small scale variations, so we construct a modified topographic profile by removing this regional slope (we add 0.0011 radians to the true profile). The modified profile, or adjusted topography, is shown as the solid line in Figure 6.5a. The 10-meter depression between 9 and 22 km marks the boundary and surface relief along the northern part of the Mesquite Basin. The topographic relief is well correlated with the seismically generated subsidence, strongly suggesting the Mesquite Basin formed by many episodes of seismic activity similar to the 1940 and 1979 events.

Vertical surface slip along the northern section of the 1979 rupture plane ranged from 0 to 30 cm (including 6 months afterslip), while vertical offset along the Brawley fault was 0 to 24 cm [*Sharp et al.*, 1982]. Measurements of vertical slip following the 1940 earthquake were sparse, although the sense of displacement was generally the same as in 1979 [*Sharp*, 1982]. During an earthquake swarm in 1975, up to 20 cm of vertical displacement was observed along the Brawley fault and an additional 20 cm possibly occurred between

1960 and 1975 [*Sharp*, 1976]. In each case, slip was down to the east along the Imperial fault and down to the west along the Brawley fault. That is, the Mesquite Basin underwent subsidence during each event.

Perhaps the most puzzling and intriguing aspect of deformation in the Mesquite Basin is shown by the offset pattern recorded in the crystalline basement along the Imperial fault. Seismic refraction experiments were conducted by the U.S. Geological Survey in the Imperial Valley during 1979 [*Fuis et al.*, 1984]. Three refraction lines RL-1, RL-2, and RL-3 cross the Imperial fault where shown in Figure 6.4. (These correspond to *Fuis et al.* [1984] lines 6NW-1SE-1NW, 1ESE, 1E-2W.) The seismic measurements indicate a 1000 m basement offset across the Imperial fault at RL-1, a 500 m offset at RL-2, whereas no basement offset is observed at RL-3. That is, the offset increases to the southeast. Where detectable, the subsurface morphology is down to the east. The basement is defined as rock with V_p = 5.6 km/sec, which approximately corresponds to 5 km depth. What makes the basement structure so unusual is its opposite arrangement to the deformation displayed at the surface, where vertical fault offsets measured for the 1940 and 1979 earthquakes generally increased to the northwest. In fact, where the basement structure is maximum (at RL-1), the coseismic vertical surface displacements were either small or non-existent. Presumably, this apparent discrepancy between surface and sub-surface structure must illustrate an important tectonic feature.

6.4 Age of Faulting

The correlation between geodetically measured subsidence and the

topographic expression shown in Figure 6.5 strongly suggests this region developed from episodes of seismic activity similar to the 1940 and 1979 earthquakes. In fact, this example clearly illustrates that earthquakes are a fundamental building block of tectonic structures. The 10 m surface depression, together with the subsidence rate and basement morphology, places constraints on the age of the Mesquite Basin, and correspondingly the northern segment of the Imperial fault.

About 5 m of seismic and postseismic slip along the Imperial fault north of the border is required to form the 40 cm subsidence between the earliest and most recent levelings across the Mesquite Basin (1931-1980) [*Reilinger*, 1984; *Reilinger and Larsen*, 1986] (additional slip is required to the northest of the basin and along the Brawley fault to produce the detailed deformation pattern). At a plate motion rate of 40 mm/yr across the Imperial fault, 5 m of potential slip will accumulate in 125 years. The equivalent basin subsidence rate is thus about 3 mm/yr. While depending heavily on the rate of strain accumulation, this analysis is invariant to the earthquake recurrence interval.

At a tectonic subsidence rate of 3 mm/yr, the 10 m depression which outlines the Mesquite Basin would form in 3000 years. This suggests that the tectonic framework underlying the basin, namely the northern Imperial and Brawley faults, is extremely young compared to the 4 to 5 million year age of the Imperial Valley. However, this estimate does not include sediment influx into the Mesquite Basin. While the measured seismic subsidence is about an order of magnitude larger than typical fill rates in arid regions [*Ollier*, 1978], the basin is located in one of the largest river deltas in the United States;

presumably sediment influx is high. In fact, the average rate of deposit in the central Imperial Valley is about 1 mm/yr (5 km over the last 5 million years), only slightly smaller than the rate of tectonic subsidence. Overlying sediments may mask a deeper basin, so 3000 years is an extreme minimum time for basin development.

The lack of an observed basement offset at RL-3 places further constraint on fault age. The geometry and dextral motion of the San Andreas and Imperial faults require extension in the Brawley Seismic Zone. Dip-slip motion along the northern Imperial and Brawley faults helps to fill this requirement. Although geodetic, geologic, and strong-motion data indicate significant vertical displacements along the northern segment of the Imperial fault (north of its intersection with the Brawley fault), apparently insufficient time has elapsed to allow the formation of a detectable basement offset at its northern extent. The lack of offset suggests this region formed relatively recently and is at its earliest stage of tectonic development. Assuming the refraction data can resolve offsets of 250 m (1/2 the offset measured at RL-2), at a tectonic subsidence rate of 3 mm/yr the maximum age for the northern Imperial fault is about 80,000 years; again very young compared to the 4-5 million year age of the Imperial Valley.

Other evidence support a young age for this segment of the Imperial fault. Models of heat transfer mechanisms suggest the Salton Sea geothermal field (Figure 6.4) formed within the last 3500 to 12,000 years [*Kasameyer et al.*, 1980], consistent with the 3000 to 80,000 year age range calculated for the Mesquite Basin. If representative of central Imperial Valley tectonics, the geothermal field likely formed contemporaneously with the Brawley Seismic

Zone, and correspondingly with the northern Imperial fault. To achieve a balance between thermal constraints and the current composition of the crust, heat flow measurements within the Imperial Valley indicate an average extension rate of $\sim 10^{-14}s^{-1}$ since the formation of the Salton Trough [*Lachenbruch et al.*, 1985]. At this rate, the differential velocity between the Pacific and North American plates requires that extension and faulting must have been distributed over a relatively wide region ($\sim$ 150 km) during the last 4-5 million years. Presumably, tectonic and seismic activity, which is presently highly concentrated along the Imperial fault and within the Brawley Seismic Zone, is part of an evolutionary process in which tectonic activity is shifted from one region of the valley to another. The northern Imperial and Brawley faults, Mesquite Basin, and Brawley Seismic Zone may represent the most recent epoch of activity in a rapidly changing fault geometry.

6.5 Propagating Rift

The relationship between seismicity, dip-slip faulting, and basement offset indicates a young age for the northern segment of the Imperial fault. Similarly, the larger basement offset along the central section of the fault (at RL-1) suggests significant vertical slip along this segment in the past.

We suggest a scenario for the recent history of the Imperial fault and Brawley Seismic Zone, which is consistent with the notion of northwestward propagation of the Gulf of California oceanic rift system. Although rupture along the Imperial fault is predominately strike slip, the large component of normal motion along the northern segment of the fault is presumably in response to the en echelon geometry of the San Andreas and Imperial faults.

These faults may act as transforms associated with a spreading center beneath the Brawley Seismic Zone [*Elders et al.*, 1972; *Johnson*, 1979]. If the northern extent of the Imperial fault, as well as the Brawley Seismic Zone were previously further south (perhaps southeast of El Centro), dip slip motion would be expected along this segment of the fault. Eventually, a detectable offset would develop in the crystalline basement. As the spreading center (Brawley Seismic Zone) migrated northwest to its present position, so would the vertical movements during seismic events. Although rupture along the older section of the fault would change to strike slip, a vertical offset would be recorded in the basement. This model can account for the apparent disparity between long-term vertical offsets on the Imperial fault (increasing basement offset to the southeast) and present-day seismic fault slip (maximum dip-slip along the northern segment of the fault).

The rupture pattern for the 1979 earthquake supports this hypothesis (Figure 6.4). Clearly the northern Imperial and Brawley faults are active components in the stress/strain transfer mechanism between the Imperial and San Andreas faults. Both structures show significant seismic displacements at the surface and at depth. Although displacement along the Rico fault was approximately 10 cm vertical with no horizontal offset [*Sharp et al.*, 1982; *Reilinger and Larsen*, 1986], the 1 km rupture length suggests it is only a minor constituent in the regional tectonics. In fact, the Rico fault may be an older structure reactivated during the 1979 earthquake. The Rico, Brawley, and the north extension of the Imperial fault, each follow a north-south trend and are uniformly spaced at distances of 6 to 7 km. This strong geometrical relationship among the three faults suggest a similar tectonic origin. A

schematic illustration of the temporal evolution of this region is shown in Figure 6.6. If the Brawley Seismic Zone was further southeast than at present, the Rico fault may have acted as the Brawley fault does today. Similarly, the Brawley fault would have been the northern splay of the Imperial fault, identical to the present north extension. A prehistoric basin would have developed between the Rico and Brawley faults (forming the observed fault offset), similar to the Mesquite Basin. Presumably, as the Imperial fault lengthened to the northwest, the Rico-Brawley fault system no longer influenced the stress/strain distribution between the northern Imperial and southern San Andreas faults. As a result, a new fault developed (north extension) and the Rico fault died out. Continued migration of the Brawley Seismic Zone may in the future create a new north-south trending structure northwest of the present terminus of the Imperial fault. As the Brawley Seismic Zone shifted to the northwest, so did the southern terminus of the San Andreas fault (Figure 6.6). The Sand Hills lineament may be the remnant of an older segment of the San Andreas, and except for residual seismic activity, left dormant with the northwest passage of the Brawley Seismic Zone.

It is possible to make a rough estimate for the migration rate of the Imperial fault and Brawley Seismic Zone. Assuming a dip-slip offset rate of 3 mm/yr (estimated above), approximately 330,000 years are required to form the 1000 m basement offset measured along the Imperial fault at RL-1. The 3000 to 80,000 year age for the fault segment 20 km to the northwest (at RL-3), indicates that the Brawley Seismic Zone has migrated about 20 km over the last 250,000 to 300,000 years. This yields a migration rate of about 7

cm/yr. While this rate is only a very crude estimate, it is significant to note that it is quite comparable to the 4.8 cm/yr spreading rate in the Gulf of California averaged over the last 3 million years [*DeMets et al.*, 1987]. In fact, the northwesterly migration of the Brawley Seismic Zone, and its underlying spreading center, may be directly associated with propagation of the Gulf of California rift system into the North American continent.

6.6 Conclusions

Geodetic, seismic, tectonic, and heat flow data in the Imperial Valley suggest that the northern segment of the Imperial-Brawley fault system is extremely young compared to the 4 to 5 million year age of the Imperial Valley. We find a minimum age of 3000 years based upon the relationship between topography and earthquake induced geodetic displacements, and a maximum age of 80,000 years based upon observed basement offsets across the Imperial fault determined from seismic refraction surveys. A young age is consistent with heat flow data which indicate a distributed and ephemeral pattern of faulting in the Imperial Valley [*Lachenbruch et al.*, 1985].

In addition, we speculate that a disparity along the Imperial fault between the observed seismic vertical displacements (maximum to the north) and the offset recorded in the crystalline basement (maximum to the south) is a direct result of the northwestward propagation of the Imperial fault and Brawley Seismic Zone. A series of evenly spaced north-south surface ruptures and the Sand Hills seismicity lineament are consistent with this hypothesis. A 7 cm/yr migration rate, similar to the rate of oceanic spreading in the Gulf of California, is calculated from measured surface displacements and from

Figure 6.6: Schematic diagram of past and present fault configurations in the Imperial Valley illustrating the hypothesized northwesterly migration of the Brawley Seismic Zone. In this model the Sand Hills Seismicity Lineament is the extension of the San Andreas, left dormant after the passage of the Brawley Seismic Zone.

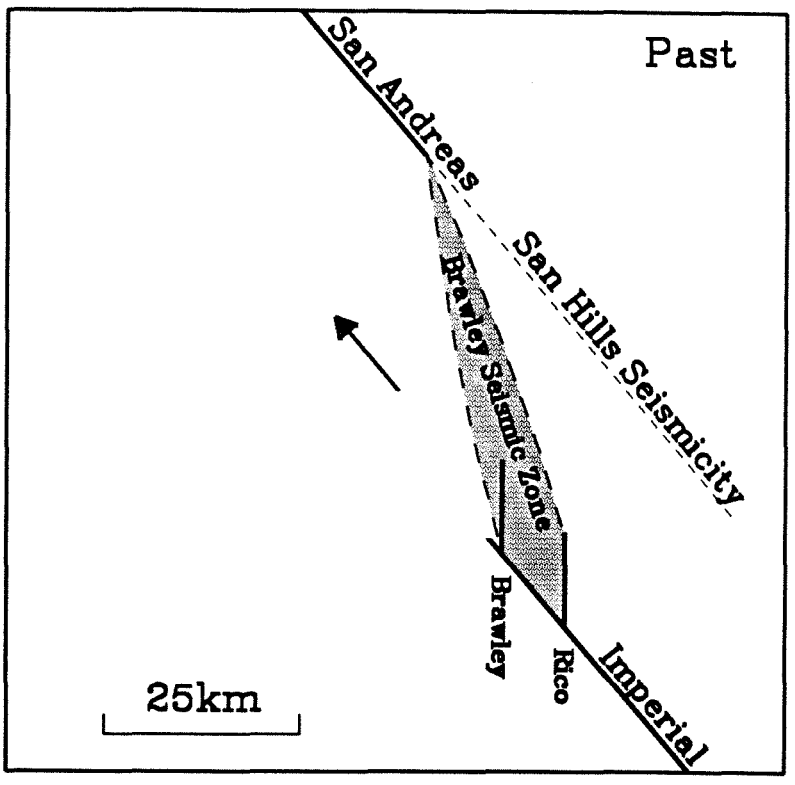
Past
San Andreas
San Hills Seismicity
Brawley Seismic Zone
Brawley
Rico
Imperial
25km

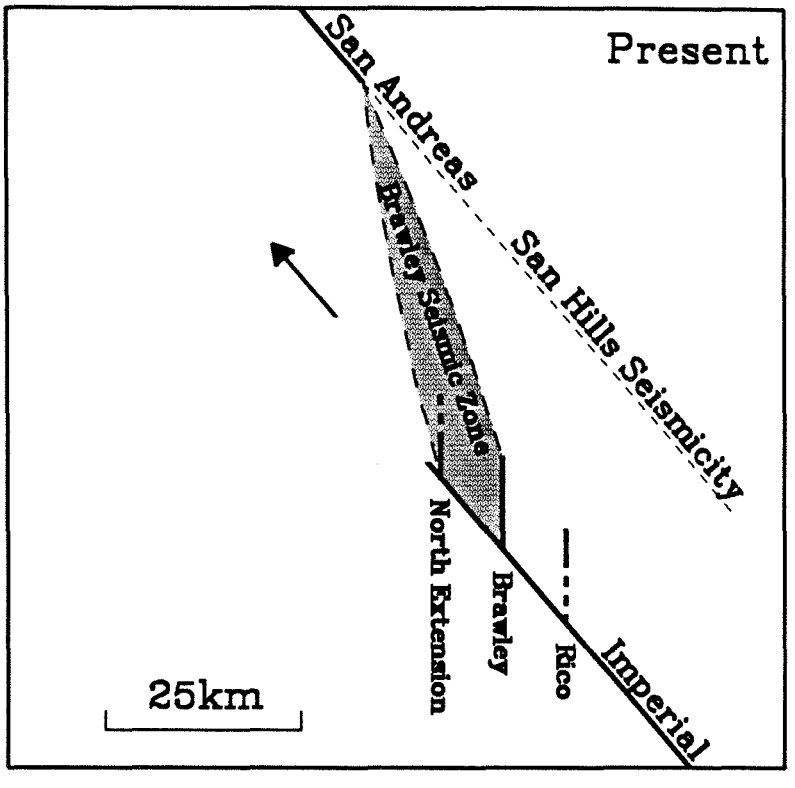
Present
San Andreas
San Hills Seismicity
Brawley Seismic Zone
North Extension
Brawley
Rico
Imperial
25km

variations in basement morphology along the Imperial fault. The migration of the Brawley Seismic Zone and Imperial fault may be associated with the propagation of the Gulf of California rift system into the North American continent.

Acknowledgments

This work was a collaborative effort with Robert Reilinger (MIT). I thank the National Geodetic Survey and in particular Emery Balazs for providing the leveling data reported here. Comments by Kerry Sieh and Hiroo Kanamori substantially improved the present manuscript, as was a review by Gary Fuis on a much earlier version. This work was supported in part by NASA grant NAG 5-814 and by U.S. Geological Survey contracts 14-08-0001-61679 (MIT) and 14-08-0001-61354 (Caltech).

References

Allen, C. R., M. Wyss, J. N. Brune, A. Grantz, and R. E. Wallace, Displacements on the Imperial, Superstition Hills, and San Andreas faults triggered by the Borrego Mountain earthquake, *U.S. Geol. Surv. Prof. Pap.*, *787*, 84-104, 1972.

Anderson, J. G., and P. Bodin, Earthquake recurrence models and historical seismicity in the Mexicali-Imperial Valley, *Bull. Seismol. Soc. Am.*, *77*, 562-578, 1987.

Archuleta, R. J., A faulting model for the 1979 Imperial Valley Earthquake, *J. Geophys. Res.*, *89*, 4559-4585, 1984.

Beal, C. H., The earthquake in the Imperial Valley, California, July 22, 1915, *Bull. Seismol. Soc. Am.*, *5*, 130-149, 1915.

Brown, L. D., J. E. Oliver, Vertical crustal movements from leveling data and their relations to geologic structure in the eastern United States, *Rev. Geophys. Space Phys.*, *14*, 13-35, 1976.

DeMets, C., R. G. Gordon, S. Stein, and D. F. Argus, A revised estimate of Pacific-North America motion and implications for western North America plate boundary zone tectonics, *Geophys. Res. Letts.*, *14*, 911-914, 1987.

Doser, D. I., and H. Kanamori, Depth of seismicity in the Imperial Valley region (1977-1983) and its relationship to heat flow, crustal structure, and the October 15, 1979, earthquake, *J. Geophys. Res.*, *91*, 675-688, 1986.

Doser, D. I., and H. Kanamori, Long-period surface waves of four western United States earthquakes recorded by the Pasadena strainmeter, *Bull. Seis. Soc. Am.*, *77*, 236-243, 1987.

Elders, W. A., R. W. Rex, T. Meidav, P. T. Robinson, and S. Bieher, Crustal spreading in southern California, *Science*, *178*, 15-24, 1972.

Fuis, G. S., W. D. Mooney, J. H. Healy, G. A. McMechan, and W. J. Lutter, A seismic refraction survey of the Imperial Valley region, California, *J. Geophys. Res.*, *89*, 1165-1189, 1984.

Hanks, T. C., J. A. Hileman, and W. Thatcher, Seismic moments of the larger earthquakes of the southern California region, *Geol. Soc. Am. Bull.*, *86*, 1131-1139, 1975.

Hartzell, S. H., and T. H. Heaton, Inversion of strong ground motion and teleseismic waveform data for the fault rupture history of the 1979 Imperial Valley, California, earthquake, *Bull. Seis. Soc. Am.*, *73*, 1553-1583, 1983.

Johnson, C. E., CEDAR-An approach to the computer automation of short-period local seismic networks; seismotectonics of the Imperial Valley of southern California, California Institute of Technology, Ph.D. thesis, Pasadena, 343 pp., 1979.

Johnson, C. E., and D. P. Hill, Seismicity of the Imperial Valley, The Imperial Valley, California, earthquake of October 15, 1979, *U.S. Geol. Surv. Prof. Pap.*, *1254*, 14-22, 1982.

Johnson, C. E., and L. K. Hutton, Aftershocks and preearthquake seismicity, *U.S. Geol. Surv. Prof. Pap., 1254*, 59-76, 1982.

Kanamori, H., and J. Regan, Long-period surface waves, *U.S. Geol. Surv. Prof. Pap., 1254*, 55-58, 1982.

Kasameyer, P. W., L. W. Younker, and J. M. Hanson, Age of the Salton Sea geothermal system as inferred from the thermal data, *Geol. Soc. Am. Abst. Prog., 12*, 458, 1980.

Klein, F. W., User's guide to HYPOINVERSE, a program for VAX and PC350 computers to solve for earthquake locations, *U.S. Geol. Surv. Open-File Rep., 85-515*, 24 pp., 1985.

Lachenbruch, A. H., J. H. Sass, and S. P. Galanis, Jr., Heat flow in southernmost California and the origin of the Salton Trough, *J. Geophys. Res., 90*, 6709-6736, 1985.

Larsen, S. C., R. E. Reilinger, H. Neugebauer, and W. Strange, GPS measurements of deformation associated with the 1987 Superstition Hills earthquake, Imperial Valley, California: Evidence for conjugate faulting, AGU Chapman conference on GPS measurements for geodynamics, 1988.

Lomnitz, C., F. Mooser, C. R. Allen, J. N. Brune, and W. Thatcher, Seismicity and tectonics of northern Gulf of California region, Mexico: Preliminary results, *Geofis. Int., 10*, 34-48, 1970.

Magistrale, H., L. Jones, and H. Kanamori, The Superstition Hills, California, earthquakes of 24 November, 1987, *Bull. Seismol. Soc. Am., 79*, 239-251,

1989.

Nicholson, C., L. Seeber, P. Williams, and L. R. Sykes, Seismic evidence for conjugate slip and block rotation within the San Andreas fault system, southern California, *Tectonics, 89*, 629-648, 1986.

Ollier, C., Tectonics and Landforms, Longman Group Limited, 324 pp., 1981.

Pinault, C. T., and T. K. Rockwell, Rates and sense of Holocene faulting on the Elsinore fault: Further constraints on the distribution of dextral shear between the Pacific and North American plates, *Geol. Soc. Am. Abst. Prog., 16*, 624, 1984.

Reasenberg, P., and D. Oppenheimer, FPFIT, FPPLOT, FPPAGE: computer programs for calculating and displaying earthquake fault-plane solutions, *U.S. Geol. Surv. Open-File Rep., 85-739*, 46 pp., 1985.

Reilinger, R. E., Coseismic and postseismic vertical movements associated with the 1940 Imperial Valley, California earthquake, *J. Geophys. Res., 89*, 4531-4537, 1984.

Reilinger, R. E., and S. C. Larsen, Vertical crustal deformation associated with the 1979 M_L = 6.6 Imperial Valley, California earthquake: Implications for fault behavior, *J. Geophys. Res., 91*, 14,044-14,056, 1986.

Sharp, R. V., Surface faulting in Imperial Valley during the Earthquake swarm of January-February, 1975, *Bull. Seismol. Soc. Am., 66*, 1145-1154, 1976.

Sharp, R. V., Variable rates of late Quaternary strike slip on the San Jacinto

fault zone, southern California, *J. Geophys. Res.*, *86*, 1754-1762, 1981.

Sharp, R. V., Comparison of 1979 surface faulting with earlier displacements in the Imperial Valley, *U.S. Geol. Surv. Prof. Pap.*, *1254*, 213-221, 1982.

Sharp, R. V., J. J. Lienkaemper, M. G. Bonilla, D. B. Burke, B. F. Fox, D. G. Herd, D. M. Miller, D. M. Morton, D. J. Ponti, M. J. Rymer, J. C. Tinsley, J. C. Yount, J. E. Kahle, E. W. Hart, and K. E. Sieh, Surface faulting in the central Imperial Valley, *U.S. Geol. Surv. Prof. Pap.*, *1254*, 119-143, 1982.

Snay, R. A., M. W. Cline, and E. L. Timmerman, Horizontal crustal deformation models for California from historical geodetic data, *Royal Society of New Zealand Bulletin*, *24*, 131-140, 1986.

Snay, R. A. and A. R. Drew, Supplementing geodetic data with prior information for crustal deformation in the Imperial Valley, California, Technical Report Series, Geodetic Institute, University of Stuttgart, 1988.

Sykes, L. R., and S. P. Nishenko, Probabilities of occurrence of large plate rupturing earthquakes for the San Andreas, San Jacinto, and Imperial faults, California, 1983-2003, *J. Geophys. Res.*, *89*, 5905-5927, 1984.

Trifunac, M. D., and J. N. Brune, Complexity of energy release during the Imperial Valley, California, earthquake of 1940, *Bull. Seismol. Soc. Am.*, *60*, 137-160, 1970.

Weldon, R., and E. Humphreys, A kinematic model of southern California, *Tectonics*, *5*, 33-48, 1986.

Williams, P. L., and H. W. Magistrale, Slip along the Superstition Hills fault associated with the 24 November 1987 Superstition Hills, California, Earthquake, *Bull. Seismol. Soc. Am.*, *79*, 390-410, 1989.